Contrôle de santé des structures en béton armé à partir des équations de Maxwell : inversion et traitement des signaux

Sima Kadkhodazadeh

COLLEGE ED MATHEMATIQUES
DOCTORAL STIC
PAYS DE LA LOIRE

Nantes Université

THÈSE DE DOCTORAT DE

NANTES UNIVERSITE

ÉCOLE DOCTORALE N° 641
Mathématiques et Sciences et Technologies du numérique, de l'Information et de la Communication
Spécialité: Télécommunications

Par
Sima KADKHODAZADEH

Contrôle de santé des structures en béton armé à partir des équations de Maxwell : inversion et traitement des signaux magnétiques

Thèse présentée et soutenue à « Nantes », le « 08 September 2023 »
Unité de recherche : Cerema- Non Destructive Assessment of Structures and Materials (ENDSUM)

Rapporteurs avant soutenance :

Véronique BOUTEILLER	Directrice de Recherche à Université Gustave Eiffel - Campus de Marne-la-Vallée
Stéphane RIOUAL	Maître de conférences HDR à Université Bretagne Occidentale

Composition du Jury :

Attention, en cas d'absence d'un des membres du Jury le jour de la soutenance, la composition du jury doit être revue pour s'assurer qu'elle est conforme et devra être répercutée sur la couverture de thèse

Président :	Sylvie YOTTE	Professeur de Université Limoges - Egletons, Génie Civil, Diagnostic et Durabilité
Examinateurs :	Sylvie YOTTE	Professeur de Université Limoges - Egletons, Génie Civil, Diagnostic et Durabilité
	Abdelhafid KHELIDJ	Professeur de Nantes Université - GEM UMR-CNRS N° 6183
	Laurent FERRO-FAMIL	Professeur de Université Fédérale Toulouse Midi-Pyrénées - ISAE-SUPAERO / CESBIO
Dir. de thèse :	Amine IHAMOUTEN	IDTPE - HDR chercheur senior à l'Université Gustave Eiffel /MAST - LAMES
Co-dir. de thèse :	Xavier DÉROBERT	IDTPE - HDR chercheur senior à l'Université Gustave Eiffel /GERS - GeoEND

Invité(s) :

Elisabeth HAZA-ROZIER	Chargée de Recherche à Direction Recherche, Innovation et International Cerema
David SOURIOU	Ingenieur de recherche à FI-NDT

ACKNOWLEDGEMENT

I would like to express my deepest gratitude and appreciation to the individuals who have contributed significantly to the completion of this thesis. Their guidance, support, and dedication have been invaluable throughout this research journey.

First and foremost, I extend my heartfelt thanks to my thesis director, Amine Ihamouten. I am immensely grateful to him for providing me with the opportunity to be a part of this thesis and for his rigorous and scientific approach to work. His expertise and knowledge have been instrumental in shaping the direction of this study.

I would also like to acknowledge Xavier Derobert, my co-director of thesis, whose hard work and unwavering commitment have played a pivotal role in the successful completion of this thesis. His extensive knowledge and years of experience in the field of Non-Destructive Testing (NDT) have been invaluable. I am grateful for his constant guidance, patience, and the fundamental understanding of NDT that he imparted to me, from begining of the project.

I extend my sincere appreciation to David Souriou, my third supervisor, for his exceptional efforts in the experimental sections, which greatly accelerated the results of this research. His dedication and contributions have significantly enhanced the quality of this thesis.

Moreover, I would like to extend my heartfelt appreciation to the thesis reporters, Professors Véronique BOUTEILLER and Stéphane RIOUAL. Their dedicated efforts, valuable time to review my manuscript and providing invaluable feedback and evaluation of my thesis have been invaluable to me. Additionally, I extend my heartfelt thanks to the jury members, Professors Sylvie YOTTE, Abdelhafid KHELIDJ, and Laurent FERRO-FAMIL, for dedicating their time to my defense, posing thought-provoking questions, and graciously serving as members of the jury. Their contributions have significantly enhanced the quality of my doctoral research. Thank you wholeheartedly.

Furthermore, I am deeply grateful to the laboratory Cerema for funding this project and for their unwavering support, particularly in the context of the ANR project of Labcome OHMIGOD. I would like to express my sincere gratitude to Cyrille Fauchard , the director of the ENDSUM group and LABCOM project, as well as direction of Cerema l'ouest Guénaëlle Bernard and Jean-Christophe Villemeaud, the direction of Cerema Angers Patrick Ingless, Mathieu Le Feuvre, and also members of Cerema research direction (DRII). I also extend my thanks to all the colleagues and engineers at Cerema of Angers and Nantes for their valuable time, kindness and support.

I would like to acknowledge the University Gustave Eiffel (UGE), specifically the laboratory of

LAMS-Mast, for hosting me in an excellent environment for one and a half years. My sincere thanks go to Philippe Tamagny, the president of UGE, and Jean-Michel Simonin , the director of LAMS at the Nantes campus, for their support and great academic environments that provide for research.
I would like to extend a special thanks to Professor Yannick Aoustin, the president of école doctorale MaSTIC, for his kind support and invaluable advice.
I am grateful to all my friends, colleagues, and research directors at UGE and also at ENDSUM group of Cerema in different cities (Rouen, Strasbourg, Angers), who have made my time there memorable and enriching.
At this moment, I want to express my profound appreciation to my family—my father, sister, and brother—for their unwavering love, encouragement, and support throughout my life. I am eternally grateful for their warmth and presence. I dedicate this thesis to the loving memory of my beloved mother, whose unwavering support and encouragement have been the guiding force behind my journey. She was a woman of incredible courage and dedication, devoting her life to the pursuit of science. Her tireless efforts and passion for knowledge have instilled in me the values of bravery and strength. I am forever grateful for the invaluable lessons she taught me and the inspiration she continues to provide.
I dedicate my thesis work to all the brilliant and tenacious women scientists and engineers who, for years, have made invaluable contributions to their respective fields. It is a tribute to their unwavering determination, resilience, and groundbreaking discoveries that have paved the way for progress and innovation. In the face of adversity and societal barriers, these extraordinary women have challenged the status quo, shattered glass ceilings, and continue to inspire future generations. May their remarkable achievements serve as a testament to the limitless potential of women in science and engineering, and may their trailblazing efforts be celebrated and acknowledged for eternity.
This thesis is dedicated, above all, to the movement of Women life freedom at Iran. It is a heartfelt tribute to the courageous women who have fought tirelessly for gender equality, empowerment, and the right to lead lives of their choosing. Their unwavering determination and spirit have challenged societal norms, shattered barriers, and paved the way for a more inclusive and just world. This dedication is a reminder of the ongoing struggle for women's rights, and a call to action to continue supporting and advocating for the freedom, dignity, and equality of all women, everywhere. May their voices be heard, their stories be shared, and their vision for a better future be realize.
In conclusion, I would like to express my heartfelt gratitude to everyone mentioned above (and also everyone whom I may forget), as well as to all those who have played a part in this thesis. Without their contributions and support, this research would not have been possible.

Résumé en français

Le Béton Armé (B.A.) est le matériau composite fondamental le plus largement utilisé dans la construction de structures et d'infrastructures du Génie Civil. Cependant, dans un environnement marin et en raison de la présence d'agents agressifs, la durabilité des structures en béton armé est fortement affectée par la corrosion des armatures métallique. Ce phénomène est essentiellement dû aux réactions chimiques et électrochimiques du fer avec l'humidité, l'oxygène et les agents agressifs, qui pénètrent depuis l'environnement dans le réseau poreux de béton. Il est donc nécessaire d'effectuer une surveillance régulière de l'état du béton pour détecter la corrosion des armatures à un stade précoce et éviter l'effondrement de la structure avec des conséquences dangereuses et coûteuses. En particulier, des techniques d'inspection fiables sont nécessaires pour se concentrer sur le niveau de contamination du béton armé, principalement dans les zones à risque (comme la zone de marnage des structures dans les zones maritimes) afin de prévenir la corrosion des armatures. Ainsi, il serait possible d'économiser les coûts de maintenance, voire estimer le risque d'effondrement.

Au cours des dernières décennies, plusieurs méthodes de surveillance ont été développées pour résoudre le problème de la corrosion des armatures, avec des tests destructifs ou non destructifs (ND). Les tests destructifs (TD) comprennent le carottage des structures de béton en service pour effectuer des tests chimiques en laboratoire. Ces méthodes sont très utiles pour évaluer la vitesse de pénétration des agents agressifs, mais elles endommagent la structure et ne sont utiles que pour les premières décennies de service, ce qui est hors sujet pour cette thèse.

Les techniques de Contrôle Non destructif (CND) sont d'autres méthodes d'inspection qui permettent d'évaluer la durée de vie résiduelle des structures à partir d'indicateurs de durabilité liés à l'état physique de la structure à travers une phase de calibration des résultats. À cet égard, il existe une variété de tests ND qui utilisent des ondes électriques, électromagnétiques ou mécaniques qui permettent d'évaluer les propriétés du béton à partir de vitesse de propagation, d'atténuation ou de résistivité électrique, etc. Les résultats correspondants sont calibrés pour évaluer les défauts du béton tels que les fissures ou la teneur volumique en eau résultant de la corrosion. Ces méthodes sont généralement peu coûteuses, rapides et facilement reproductibles sur une grande surface. Cependant, les résultats souffrent d'incertitude, en raison de la sensibilité à l'état et nature du béton, au niveau d'humidité, à la température, etc. Par conséquent, ces techniques doivent souvent être répétées plusieurs fois en raison du niveau d'incertitude. Dans le cas de la corrosion des armatures, la plupart des méthodes de CND existantes détectent généralement ce phénomène après son apparition et ne peuvent pas la prédire, elles ne sont donc

pas proposées comme solution de pronostic.
Une autre catégorie de CND est connue sous le nom de contrôle de santé des structures (SHM). Elle utilise des dispositifs et des capteurs intégrés dans le béton et, à l'aide d'un interrogateur externe, surveillent la variation de la signature de sortie des capteurs intégrés pour diagnostiquer la pathologie. Les techniques SHM sont principalement recommandées pour l'inspection des nouvelles structures et sont généralement intégrés dans les zones à risque des structures. Elles ont l'avantage de fournir des informations continues en un point précis de la structure. Les dispositifs embarqués peuvent être alimentés par des batteries intégrées, avec ou sans fil. Le principal défi des dispositifs embarqués SHM est de fournir une alimentation fiable les maintenant pendant une longue période dans le béton. Cependant, avec les progrès des technologies de communication telles que le WIFI, les dispositifs intégrés SHM peuvent être connectés en interne et également avec des interrogateurs de surveillance externes.
En ce qui concerne l'avancement de la technologie dans les communications sans fil, les dispositifs embarqués peuvent être connectés à distance à l'interrogateur qui peut fournir l'énergie nécessaire pour travailler pendant une longue période de temps. Considérant les avantages des techniques SHM, dans le cadre du projet ANR français LabCom OHMIGOD, dans cette thèse, nous nous intéressons à une technologie magnétique SHM innovante qui pourrait fonctionner de manière autonome, à faible coût, sans batterie et utile pour la surveillance continue du front d'ions chlorure dans le béton de peau. La technologie proposée est appelée Fonctionnel Magnétique Matériel (FMM) et pourrait être intégrée dans le béton de peau afin d'être exposée au front d'agents agressifs. Le FMM est composé de deux parties : premièrement, une partie permanente qui sert de source magnétique (faite de matériaux magnétiques) protégée par une couche de revêtement contre la corrosion, et deuxièmement, la partie réactive, qui sert de blindage magnétique, faite de matériaux ferromagnétiques qui sont très sensibles à la corrosion. La partie réactive serait en contact avec les fronts de corrosion. La signature de sortie du FMM est la densité de flux magnétique qui sera utilisée comme observable magnétique (OM). L'hypothèse est que l'évolution de la corrosion sur la partie réactive affecterait sa géométrie et sa nature, ce qui aurait pour conséquence de modifier ses propriétés magnétiques. Par conséquent, l'OM générée par le FMM serait modifiée en fonction de l'état de dégradation de la partie réactive. En utilisant un interrogateur externe, il serait possible de mesurer la variation de l'OM en fonction de l'évolution de la corrosion sur la partie réactive et, indirectement, de la corréler avec le niveau de l'agent agressif. Ainsi, la présence d'agents agressifs dans le béton de peau pourrait être indirectement évaluée de manière ND. L'avantage de ce dispositif intégré au SHM est que l'OM n'est pas sensible aux modifications de l'environnement, à la teneur en eau ou à la formulation du béton, qui sont des paramètres non magnétiques. De plus, le nouveau dispositif est fabriqué à partir de matériaux disponibles, bon marché et n'a pas besoin d'énergie pour fonctionner, et pourrait être maintenu pendant une longue période dans le béton de peau des structures.

A cet égard, l'objectif principal de cette thèse est de développer une méthode de traitement du signal liée aux performances du FMM. La méthode proposée utilise l'équation de Biot Savart (comme modèle direct) et l'inversion qui évalue quantitativement la variation des propriétés magnétiques de la partie réactive (c'est-à-dire le moment dipolaire magnétique) en fonction des variations de l'OM et, éventuellement, le lien avec l'état de corrosion induit par les chlorures. La raison du choix des moments dipolaires magnétiques est de représenter des informations quantitatives sur les matériaux et la géométrie de la partie réactive ferromagnétique, qui sont soumis à des changements d'états dus à la corrosion. Pour atteindre cet objectif, un modèle numérique du dispositif FMM, développé avec le logiciel Ansys Maxwell et la méthode des éléments finis (MEF) est présenté dans cette thèse. Grâce à cette modélisation numérique, la tendance et la plage de variation de l'OM seraient obtenues en fonction de la perte de géométrie de la partie réactive, en tant qu'indice de corrosion. Ces informations seront utilisées comme données de référence. Ensuite, en utilisant des méthodes de traitement du signal, des techniques d'optimisation ainsi que les équations de Biot-Savart, le moment dipolaire magnétique serait étudié en fonction des variations de l'OM. Pour valider la méthode analytique proposée, une large gamme d'essais expérimentaux sur les milieux de béton armé en laboratoire à différents états physiques et hydriques, est réalisée. A terme, il serait possible de corréler quantitativement les variations estimées du moment dipolaire magnétique aux changements de l'OM et indirectement, à l'état de corrosion induit par les chlorures, de manière ND.

Le premier chapitre de cette thèse contribue à l'état de l'art de la thématique étudiée. A cet égard, les différents types de béton, tels que le béton hydraulique qui sont largement utilisés dans les constructions en milieu marin ainsi que les propriétés associées sont d'abord passés en revue. Puis, les mécanismes de corrosion et les facteurs contributifs connexes qui pourraient conduire à la corrosion sont présentés. Pour poursuivre, les indicateurs de durabilité de la structure liés à la corrosion et à la pénétration de chlorure pour évaluer les modèles de durée de vie restante sont rapidement étudiés. Ensuite, à travers une étude bibliographique, les différents CND disponibles associés à la corrosion des armatures ainsi que les méthodes d'évaluation du niveau d'ions chlorure dans le béton et également les différentes techniques SHM sont passées en revue à travers leurs avantages et inconvénients. Enfin, les orientations de la thèse, l'hypothèse, les objectifs et la méthodologie sont expliqués de manière exhaustive.

Dans le deuxième chapitre, l'objectif principal est de concevoir le FMM à l'aide d'un modèle numérique et d'une étude paramétrique sur les matériaux et la géométrie de la partie réactive. Pour la partie permanente, L'aimant rare est constitué de NdFeB, tandis que les matériaux ferromagnétiques de la partie réactive sont en fer pur à 99.99%, avec un taux de pureté et une perméabilité relative de 50. Ensuite, en utilisant ces informations comme entrée dans le modèle numérique, la tendance de l'OM due à la perte de géométrie de la partie réactive, en tant qu'indice de corrosion, est étudiée. Les recherches montrent que l'OM aurait une tendance à la

hausse avec la perte de géométrie (soit la surface ou l'épaisseur) de la partie réactive, en raison de la modification de la propriété d'écrantage à la suite de la corrosion. De plus, grâce à une étude expérimentale avec une corrosion accélérée sur les matériaux en fer de la partie réactive, les produits de corrosion qui sont générés à partir de la partie réactive pendant le processus de corrosion ont été caractérisés avec la technique DRX. Les résultats montrent que les principaux produits de corrosion de la partie réactive sont l'hématite et la magnétite qui ont toutes deux des propriétés antiferromagnétique et ferrimagnétique. La perméabilité relative pour le mélange de produits de corrosion (tous les produits identifiés) a également été obtenue expérimentalement et est égale à 5. En utilisant cette valeur dans la modélisation numérique, les performances du FMM avec la perte d'épaisseur de la partie réactive et l'évolution de la couche de produits de corrosion ont été étudiées et les résultats montrent que l'OM augmenterait avec la corrosion.

Dans le chapitre 3 de cette thèse, l'objectif principal est de quantifier les variations de l'OM avec la corrosion. Pour atteindre cet objectif, dans un premier temps, la quantité de géométrie effective de la partie réactive a été étudiée par une étude paramétrique et une modélisation numérique. La géométrie effective de la partie réactive s'est avérée égale à 25 mm 25 mm 1 mm identifiée en raison des variations rapides et significatives de l'OM en fonction de la perte de géométrie. De plus, toute la modélisation numérique a également été effectuée en fonction de la distance relative entre le FMM et l'interrogateur externe afin de trouver la position optimale du FMM dans le béton, les résultats obtenus étant très sensibles à ce paramètre. De plus, dans ce chapitre, la présence de produits de corrosion sur la valeur de l'OM a été modélisée numériquement et comparée à celle due à la perte d'épaisseur de la partie réactive. Les résultats numériques montrent que la quantité de la couche de produits de corrosion a un effet négligeable sur la plage de variation de l'OM. Ainsi, la perte de géométrie de la partie réactive est plus représentative de l'évolution de la corrosion. Compte tenu du niveau d'incertitude de la modélisation numérique dû au maillage et au bruit de l'environnement, d'un point de vue pratique, la différence que les produits de corrosion pourraient causer sur la variation de l'OM, est considérée comme un effet négligeable.

Par la suite, dans ce chapitre, la possibilité d'utiliser des configurations multi-FMM qui seraient intégrés dans différentes profondeurs de béton sera étudiée. Grâce à des études paramétriques et à la modélisation numérique, l'effet de couplage possible entre les dispositifs FMM et les armatures dans le modèle de béton est également étudié. Enfin, la distance latérale minimale entre les dispositifs FMM ainsi que la position optimale du FMM dans le béton, pour éviter le couplage, sont estimées. Il a été conclu qu'en plaçant le FMM au centre du maillage des armatures, l'effet de couplage serait minimal.

Dans le quatrième chapitre de cette thèse, le modèle avancé et la méthode d'inversion proposés, basés sur le moment dipolaire magnétique en fonction de la géométrie du dispositif FMM, sont évalués. A cette étape, l'OM généré par le modèle numérique et la réduction d'épaisseur de la

partie réactive, ont été utilisés comme modèle de référence. Dans cet ordre, le modèle analytique et la méthode d'inversion ont été étudiés avec une variété de configurations numériques du FMM. En considérant les étapes d'inversion, deux modèles analytiques ainsi que deux techniques d'optimisation de Levenberg-Marquardt de la méthode NLS et également l'algorithme simplex de Nelder-Mead de la méthode Fminsearch, ont été étudiés et comparés. Sur la base des résultats, l'équation de Biot-Savart a été sélectionnée comme l'expression analytique appropriée en raison de la faible erreur d'estimation. En ce qui concerne la technique d'optimisation, les deux algorithmes mentionnés expriment des performances similaires, et nous n'avons utilisé que le Levenberg-Marquardt de NLS dans les étapes suivantes pour éviter de répéter les résultats.
Finalement, les résultats montrent que les moments dipolaires magnétiques ont une tendance ascendante avec la corrosion (en accord avec la tendance de l'OM). Les résultats ont été comparés avec des configurations à un, deux et trois dipôles et il a été conclu qu'un et deux dipôles ont des résultats similaires pour représenter un modèle approprié de FMM. Les résultats de l'inversion ont permis de conclure que la quantité de moment dipolaire magnétique dépend fortement de la géométrie de la partie permanente choisie. Par conséquent, le FMM avec une partie permanente de grande taille, a une quantité plus élevée de moment dipolaire magnétique. La méthode d'inversion est comparée pour la surveillance dans l'axe horizontal et vertical. Dans les deux directions, les résultats montrent approximativement la même quantité de variations dipolaires magnétiques.
Les courbes de corrélation correspondantes sont obtenues sur la base d'une corrélation entre la quantité de moment dipolaire magnétique et les valeurs de MO correspondantes. Les courbes de corrélation montrent une tendance à la hausse dont la non-linéarité augmente avec la variation de l'OM. Ainsi, la quantité de moment dipolaire magnétique est directement liée à la quantité de l'OM et elle pourrait fonctionner comme une fonction non linéaire, puisque la perte de géométrie totale de la partie réactive est due à un taux de corrosion élevé. Les résultats montrent que la méthode proposée pourrait être utilisée comme une nouvelle méthode ND pour évaluer le niveau du front d'ions chlorure qui provoque la corrosion et la réduction de la partie réactive, indirectement. Dans le chapitre 3, la méthode proposée a également été vérifiée de manière inverse et en utilisant une variété de configurations numériques FMM différentes. Les résultats montrent que la méthode proposée fonctionne comme une méthode bilatérale (elle peut donner le moment dipolaire magnétique en entrée et identifier la géométrie correspondante de la partie réactive et vice versa). On peut donc conclure que les moments dipolaires magnétiques estimés sont obtenus de manière unique pour chaque géométrie de partie réactive du FMM et que les valeurs sont indépendantes de la distance relative à l'interrogateur qui mesure l'OM. Dans la cinquième chapitre, le modèle analytique proposé et les méthodes d'inversion ont été évalués avec des données expérimentales pour valider les résultats numériques. Une campagne expérimentale a donc été menée pour évaluer la méthode proposée ainsi que la performance et la

précision du dispositif FMM dans des milieux réels en béton. Ainsi, les performances du FMM sur différents types de béton ont été étudiées et la MO a été mesurée en fonction d'un taux de corrosion de la partie réactive compris entre 10 et 50 %. Dans cette campagne expérimentale, la valeur de l'OM générée par la partie permanente du FMM (partie de référence) et le niveau de bruit magnétique environnemental ont été mesurés séparément. Ainsi, le rapport signal/bruit des mesures est évalué expérimentalement. De plus, grâce à une variété de mesures de l'OM dans l'espace libre, la quantité moyenne de variations de l'OM dues à des facteurs environnementaux (comme le bruit de fond ou le changement du champ magnétique de la terre comme biais) a été déterminée. Ensuite, la plage de variation de l'OM en fonction de la modification du mélange de béton, de l'état hydrique et de l'épaisseur a été testée séparément sur 27 dalles de béton. Dans cet ordre, des dalles de béton de différentes épaisseurs de 3 cm, 4 cm et 5 cm ont été utilisées pour combler l'espace entre l'interrogateur et le FMM. De plus, trois mélanges de béton avec rapport eau/béton de 0,38, 0,50 et 0,78, à l'état sec et saturé, ont été utilisés. Le béton saturé a été placé pendant deux ans dans des bassines contenant des solutions de NaCl de concentration 0, 30 et 120 g/L. En utilisant toutes ces dalles de béton, les mesures expérimentales ont montré que l'OM a des variations très négligeables dues au changement des conditions du milieu du béton. Cette plage est également considérée comme la plus importante en raison de la plage de variation de l'interrogateur (due au traitement à chaud) et du changement du niveau de bruit de fond. Ainsi, l'hypothèse selon laquelle l'OM n'est pas sensible aux variations du béton ou de l'environnement, de la teneur en eau, etc. a été validée expérimentalement comme l'avantage du dispositif FMM et de la technologie magnétique proposée.

En outre, différents échantillons FMM avec des épaisseurs de partie réactive de 1 mm, 0.5 mm, 0.2 mm et 0.1 mm, qui sont corrodés séparément avec une solution de NaCl de 30 g/L et une technique de corrosion accélérée, ont été utilisés pour trouver les variations de MO en fonction de leur état de corrosion (10 à 50% de perte de masse). Les résultats expérimentaux confirment les données numériques selon lesquelles l'OM aurait une tendance à la hausse avec la corrosion (précédemment obtenues dans les chapitres 2, 3 et 4). Les résultats montrent également que la norme ($\mathbf{m}$), a une tendance à la hausse similaire. De plus, l'importance des variations de la norme ($\mathbf{m}$), dépend fortement de la distance relative à l'interrogateur et aussi de la géométrie de la partie réactive. Enfin, les graphiques de corrélation entre les moments dipolaires magnétiques et les variations d'OM ont été obtenus. Étant donné que dans les essais expérimentaux, la corrosion atteint 50 % (phase linéaire), les variations du moment dipolaire magnétique présentent également une tendance linéaire à la hausse en fonction de l'OM. Ainsi, la méthode proposée a été validée expérimentalement comme une nouvelle méthode ND pour trouver le niveau d'agents agressifs à travers la quantité de moments dipolaires magnétiques qui augmentent. De plus, la pente de la courbe de corrélation pourrait déterminer le risque de corrosion. En raison de l'augmentation non linéaire du niveau des graphiques de corrélation, on peut conclure que le niveau de contam-

ination augmente fortement, ce qui pourrait être une alerte pour le risque d'effondrement des structures en béton armé. Par conséquent, la méthode proposée pourrait être utilisée à l'avenir comme une nouvelle méthode de pronostic pour la corrosion des armatures et mettre à jour les modèles de durée de vie.

Abstract in English

Reinforced Concrete (RC) is the most fundamental composite material which is extensively used in the construction of civil engineering structures and infrastructures. However, in a marine environment and due to the availability of aggressive agents, the durability of RC structures is strongly affected by rebar corrosion. Rebar corrosion is basically, the chemical and electrochemical reactions of iron with moisture, oxygen, and aggressive agents, penetrating from the environment into a porous network of concrete. Due to the rebar degradation, the ultimate strength and serviceability of the RC structures would be highly reduced therefore, it is a necessity to develop inspection methods related to this pathology. For many decades, lots of destructive and Non Destructive Testing (NDT) methods have been developed to detect rebar corrosion at its early stages.

Among NDT, the techniques such as electrochemical, electrical, elastic wave, or Electromagnetic (EM) methods wave have shown successful results to evaluate the corrosion state of rebar through different principles, related to rebar electrochemical features or concrete electrical or mechanical properties changing, as consequences of corrosion. However, most of their results suffer from huge uncertainty level due to sensitivity to environmental parameter variations, so it is very difficult to interpret their results and, basically, they require a calibration phase. Moreover, these methods are mostly useful to detect rebar corrosion after it emerges and cannot provide any information about the probability of rebar corrosion or estimate the corrosion risk, in advance. Thus, the is a lack of reliable and robust prognostic methods that could predict rebar corrosion before it emerges as a preventive method.

To address this problem and under the framework of the national French project (ANR) of Labcom OHMIGOD, we propose a novel magnetic embedded device as Structural Health Monitoring (SHM) technique, to evaluate the contamination level of cover concrete due to the presence of aggressive agents, as a preventive ND method. This innovative device would be referred as Functional Magnetic Materials (FMM) and could work as an autonomous, low-cost, and battery-less device. It involves two parts: first, a reactive part (made of ferromagnetic materials that are very sensitive to corrosion) and the second is a permanent part that is made of magnetic materials. The FMM assumes to be embedded in cover concrete, exposed to chloride ion front. The reactive part would be in touch with the media and assumed to be rusted with available aggressive agents in media, however, the permanent part would be intact from corrosion by using a coating layer. In addition, the FMM device would induce a magnetic flux density ($\mathbf{B}$) that serves as Magnetic Observable (MO) for monitoring.

The hypothesis is that, due to the corrosion evolution on the reactive part, the generated MO would be varied during the time, thus, it is possible to correlate the amount of MO variation range with the aggressive agents level that results in the corrosion of the reactive part. Compared to other conventional ND methods, the MO is not sensitive to media and environmental variations. Moreover, the FMM doesn't need the power to work (battery-less technology) and could be used for real-time monitoring for a long time.

In this regard, the main objective of this thesis is to develop a signal-processing method related to FMM performance. The proposed method would use the Maxwell equations and inversion technique that estimate the amount of magnetic properties variation of the reactive part (*i.e.*, magnetic dipolar moment) caused by chloride-induced corrosion.

To reach this objective a numerical model of the FMM device would be used as reference. For numerical modeling the Ansys Maxwell Software and the Finite Element Method (FEM) would be used to solve the Maxwell equations in magnetostaic domain. Using numerical modeling, the tendency and MO range would be obtained as a function of the reactive part's corrosion. This information would be served as reference. Then, by using Biot-Savart equation as forward model, the amount of magnetic dipolar moment would be estimated inversely, through solving the optimization problem minimizing the cost function error. Moreover, through a wide range of experimental tests of FMM on the concrete media with different physical properties and hydric states, as reference data, the analytical approach would be evaluated to validate the hypothesis. Eventually, with this proposed signal processing method, it would be possible to correlate the MO changing with the amount of estimated magnetic properties variations and indirectly, the chloride-induced corrosion state, in ND way.

The results of numerical modeling and experimental tests show that the MO and also estimated magnetic dipolar moment has an upward tendency with corrosion. Thus at a high contamination level of cover concrete, the amount of MO and magnetic dipolar moments would rise rapidly, with significant relative variations. Therefore, the fast ad significant magnetic dipolar variations could be served as alert which indicated that the contamination level of the cover concrete is raised and thus, the rebar are at corrosion. In addition, the proposed novel method could be used as a preventive ND method of rebar corrosion, for the infrastructure managers and could be helpful to reduce the collapsing risk and save maintenance costs.

Table of Contents

List of acronyms

RC	Reinforced Concrete
NDT	Non Destructive Tests
DT	Destructive Tests
SHM	Structural Health Monitoring
DT	Destructive Tests
FMM	Functional Magnetic Materials
MO	Magnetic Observable
XRD	X-ray Diffraction Analysis
RMSE	Root Mean Square Error
NRMSE	Normalized Root Mean Square Error
NLS	None Linear Square

MATHEMATICAL NOTATIONS

$\mathbf{A}$	Vector
$\lvert\mathbf{A}\rvert$	Magnitude of vector
$\hat{\mathbf{a}}$ or $\frac{\mathbf{A}}{\lvert\mathbf{A}\rvert}$	Dimensionless unit vector
$\nabla \times \mathbf{A}$	Curl of vector
$\lvert\lvert\mathbf{A}\rvert\rvert$ or norm $(\mathbf{A})$	Norm of vector $\mathbf{A}$
$\mathbf{A} \cdot \mathbf{B}$	Dot or scalar product of two vectors $\mathbf{A}$ and $\mathbf{B}$
$\mathbf{A} \otimes \mathbf{B}$	Cross or Vector product of two vectors $\mathbf{A}$ and $\mathbf{B}$
$\nabla \cdot \mathbf{A}$	Divergence of vector
$\mathbf{A}^T$	Transpose of vector $\mathbf{A}$
$\mathbf{A}(\mathbf{r})$	Vector field in direction of $\mathbf{r}$
$f(\mathbf{r})$	Scalar field in direction of $\mathbf{r}$
$d\ell$	Differential element of length
$d\mathbf{s}$	Differential element of surface
dv	Differential element of volume
$(\mathbf{a}_x, \mathbf{a}_y, \mathbf{a}_z)$	Base vectors in Cartesian coordinate system
$(\mathbf{a}_\rho, \mathbf{a}_\varphi,, \mathbf{a}_z)$	Base vectors in cylindrical coordinate system
$(\mathbf{a}_r, \mathbf{a}_\theta, \mathbf{a}_\phi)$	Base vectors in spherical coordinate system
$\mathbf{A}_x, \mathbf{A}_y, \mathbf{A}_z$	Vectors components in Cartesian coordinate system

List of Figures

List of Tables

GENERAL INTRODUCTION

0.1 Context and objectives

Concrete is a fundamental material in the construction of many civil engineering structures and infrastructures. Due to its relatively low tensile strength, steel rebars have been introduced to raw concrete and the Reinforced Concrete (RC) composite has been developed. Basically, RC composites effectively improve the mechanical properties of raw concrete and specifically, increase the durability of RC infrastructures. However, RC suffers from a variety of defects caused by the environment such as freeze-thaw loads, non-uniform volume changes, temperature gradients, abrasion, erosion, or cavitation could strongly damage it and result in the development of internal and external cracks or micro cracks [1]. Furthermore, through the porous network of concrete and also the available micro cracks, moisture, oxygen, and aggressive agents from the environment could penetrate through the structure, during the time. Since aggressive agents reach the steel materials such as rebar, it would result in slow natural degradation, referred as corrosion, which is the most critical threat to the durability, safety, and sustainability of RC structures [2, 3, 4].

Generally, corrosion is caused by a series of chemical and electrochemical reactions of iron with oxygen and moisture content such as water, chloride ions, sulfate, alkalies, acids, and *etc.* The reaction of steel rebars with these aggressive agents (whether they penetrate from the environment to concrete or are available in concrete mixture and aggregates as contamination) would result in deterioration which could expand very fast to all sides of rebar. Consequently, the iron materials of rebar would be transformed into corrosion products (a series of oxides and hydroxides). Accumulation of corrosion products would result in increasing the rebar volume and eventually could cause concrete swelling, widening the cracks, inducing spalling and make serious damage to the concrete cross-section. Since these corrosive agents are typically available in the maritime environment, the RC structures which are constructed in sea areas are mostly subjected to corrosion (see Figure 1). Meanwhile, France is a country that takes advantage of a long coastline (more than 5000 km [5] coastline, considering the mainland), thereby, it is a necessity to develop specific methodologies for the sustainable infrastructure management of the RC structure and infrastructures, specifically in such areas.

According to [6], the RC structures located in sea areas are mainly exposed to three different environmental conditions, including atmospheric, tidal, and submerged zones. Different exposure conditions are shown in Figure 2. The tidal zone refers to the range of seawater between

(a) **(b)**

Figure 1 – Degradation of rebar in reinforced concrete structure at sea area

the mean low and high tides, it is exposed to both seawater and air. Generally, due to wet/dry cycles (caused by tides), this area is subjected to visible or non-visible cracks and micro-cracks. Consequently, the aggressive agents from seawater and the atmosphere could easily penetrate through these cracks and emerge corrosion. Therefore, the tidal zone is generally considered as the riskiest zone, in terms of rebar deterioration [6].

Generally, in healthy concretes, due to the Portland cement's reaction with water during the hydration phase, the pH of the media would be around 12 which results in concrete alkalinity. It induces the formation of a protective film around the rebar that protect it from moisture and oxygen attacks as well as chemical reactions. Meanwhile, due to carbonation (penetration of CO_2 and its reaction with concrete) and also chloride ions ingress, the pH of media will be dropped due to producing some acidic combinations. Thus, the protective film could not resist more and would be attenuated [7, 8]. Studies [9, 10] show that the chloride ions are the most reputed aggressive agents which can easily break the attenuated protective film and cause a local breakdown, referred as pits. Eventually, the oxygen and moisture could reach rebar through generated pits and the electrochemical reactions of corrosion would be emerged [11, 12, 13].

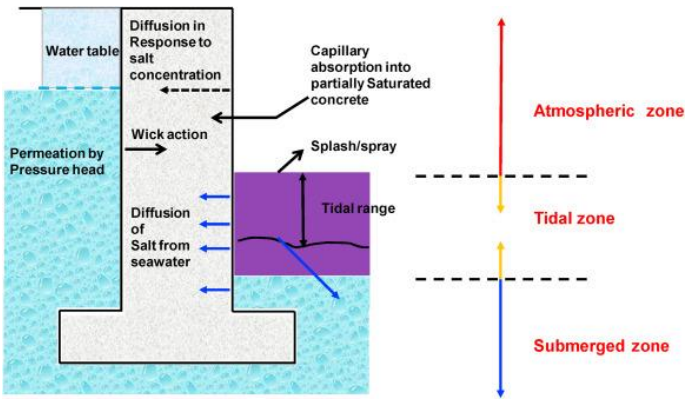

Figure 2 – Different exposure conditions under marine environment [6]

As mentioned, rebar corrosion leads to concrete swelling, facilitating more aggressive agents to ingress and the corrosion would be more accelerated.
Therefore, regular (or periodical) concrete inspection is required and quite necessary to detect rebar corrosion (as hidden pathology) at an early stage to avoid dangerous and costly consequences.
The main goal of this periodical inspection, is to evaluate the general health statement of structure by visual techniques. By detecting some trace of rust or unusual cracks, it would suggest for more complementary inspection to find the origin of this pathology, its extension as well as the possible velocity of evolution. However, the visual inspections are remain limited to surface damages of the concrete structure, mainly in the cover concrete thickness. Focusing on corrosion pathology, it is possible to carry out the other complementary inspections, in order to determine precisely the extend of damages, the active or passive type of corrosion and the corrosion rate [14].
During the decades, several complementary inspection methods have been developed to address the rebar corrosion problem involving destructive or Non-Destructive (ND) tests [15, 16, 17].
Firstly, the Destructive Tests (DT) include extracting the concrete cores from in-service structures for performing some laboratory tests. These methods are quite useful to estimate a variety of parameters such as the velocity of aggressive agent ingress, the porosity, and *etc.* (list not exhausting). However DT techniques are most useful for the first decades of service life, but they would damage the structure and thus, they can not provide the punctual and reproduced results. In addition, these techniques are not able to provide reliable representative information about the problematic of corrosion [18, 19].
The second category are ND techniques that are typically used to evaluate the state or the internal geometry of structures. These methods apply the electromagnetic or mechanical waves, while measuring parameters related to wave propagation such as the velocity or attenuation. As these methods provide indirect information, they could require some calibration phase to link the measured data to the durability indicators of surveyed structure [20, 21]. Focusing on rebar corrosion, a variety of ND tests have been developed as complementary techniques. Based on the principle of each method, the measurement have different sensitivity level to the indicators. These methods are divided into different categories such as low frequencies (*e.g.* resistivity methods [22]), high frequency (*e.g.* Electromagnetic such as Ground Penetrating Radar (GPR) [23, 24]), mechanical methods (*e.g.* Ultrasonic Pulse Velocity (UPV) [25, 26] or Impact Echo (IE) [27]) and *etc.*
Typically low frequency methods are useful to evaluate the chloride ion ingress, water content, and also porosity of media. The high frequency, techniques are usually apply to investigate the water content and the media porosity. The mechanical techniques are more significant to measure the comprehensive strength of media and its porosity level. In application rebar corrosion,

it is possible to use one or some of these techniques, simultaneously to evaluate the pathology, through a variety of indicators and make more accurate interpretation. The these methods are taken advantage from proposing inexpensive, quick, and easily reproducible information over a large area. However, the results obtained from these methods often suffer from a high degree of uncertainty, primarily due to their sensitivity to various factors such as the concrete's structural state (including cracks and defects), variations in environmental conditions (humidity and temperature), moisture gradients within the concrete, and the complex interplay of these factors [15, 17]. This uncertainty can result in variations in the obtained data and may require careful interpretation and additional verification measures to ensure accurate assessments. Moreover, it is a necessity to carry out the regular inspection to investigate the evolution of such pathologies. The last category of ND methods is referred as Structure Health Monitoring (SHM). The SHM techniques are typically useful for the punctual and long-term monitoring of specific parameters associated with concrete properties or structural behaviour. The SHM techniques involve monitoring equipment such as surface or embedded sensors.

The SHM techniques are generally divided into two main categories of wired or wireless methods. The wired methods such Ag/AgCl electrodes [28], they involves cables to connect the embedded devices with external equipment and also providing the power. The wireless methods such as Wireless Smart Sensors (WSS) [29] use advancement of technology mainly in communications systems to link external monitoring equipment with the embedded tools via WiFi or Bluetooth standards. Their main significance is related to providing the possibility to distribute multi-embedded devices in different locations of structures. Thus, it could provide the possibility to acquire data from many different risky zones as well as continuous and punctual monitoring at a certain point of the structure.

Focusing on rebar corrosion, the embedded devices are usually integrated into the areas of structures that are highly subjected to aggressive agent penetration [30]. Thus, any change in chloride ions level, as an example of aggressive agents, would result in a variation of the output signature of the embedded device and eventually, the monitoring system can record such variations to evaluate the health condition of structure.

Among two categories of SHM devices, the main drawback of wired SHM techniques is related to using long cables. In fact, if the cables have faced to any physical damages (such damaged or incorrect placement during installation or over time), they can potentially make a weak zone in their surrounding area through some cracks and openings and eventually allow the water and other aggressive agents penetrate into the concrete and reach the rebar. Moreover, the repairing and also replacing of damages cables, need to destruct the structure. At last but not least, the wired equipment are limited to being embedded in deep concrete depths. Therefore, the wireless SHM methods were proposed to solve the problems related to limitations of cables, however the most important challenge is providing reliable source of power for distributed wireless embedded

devices.

Wireless equipment could be divided into battery-powered and battery-less. The battery-powered embedded devices suffer from the disadvantage related to the requirement of battery replacement in the long term and also the limitation of geometrical designing due to battery size. Nowadays, battery-less embedded devices such as Radio Frequency Identification (RFID) have been developed to address this problem [31, 32]. RFID technologies encompass a spectrum of systems using radio waves to identify and track objects, including passive RFID tags relying on external readers for power and active RFID tags equipped with their power sources, each suited to various applications and operational ranges. Chipless RFID tags offer a promising electronics-free alternative, although they face limitations in read distance and coding capabilities. Research is ongoing to improve their performance and expand their applications in inspection and other fields [33].

Considering the existing NDT inspection and monitoring techniques, there is still a lack of reliable, low cost and accurate techniques that is not sensible to environmental condition and could provide punctual monitoring as well as low power and small size which eventually, propose a preventive method associated with the rebar corrosion issue.

Under the framework of the French national research project (ANR) LabCom OHMIGOD, in this research study, we are interested in proposing a technological solution related to rebar corrosion pathology as a preventive ND method. Using the advantages of SHM techniques, the technological solution would be an embedded SHM device in cover concrete, made of ferromagnetic and magnetic materials that are very sensitive to corrosion and not to environment. The proposed solution to be studied is exposed to the aggressive agents in cover concrete, as a battery-less device that has small geometry and generates magnetic flux density, using as Magnetic Observable (MO) to detect the availability of aggressive agent front. The MO remain insensitive to environmental conditions; consequently, its output signatures exclusively reflect the degradation of the reactive part caused by corrosion, including changes in its geometrical properties. The proposed magnetic innovation could be embedded as multi-embedded devices at several depths in different risk areas of RC structure.

Using an external interrogator, the variation of MO due to corrosion of the device materials during the time, could be measured and indirectly, correlates with the aggressive agent's availability. Thus, the corrosion risk of rebar corrosion due to aggressive agents, could be evaluated in an ND way, as well.

Considering the proposed technological solution, the objective of this research study is to propose a forward method, use to quantify the amount the magnetic property of embedded device, as magnetic source. The forward method includes an analytical model, based on traditional Maxwell equations in the magnetic domain. The hypothesis is that, since the corrosion evolution on embedded device, would leads to material transformation and its general degradation,

thus, the magnetic properties of device would be altered by rusting progress. To accurately evaluate the amount of device's magnetic properties in relation to its corroded state (self-corrosion), the proposed method would use the optimization technique and inversion approach. Thereby, the main goal of this thesis is to use the forward method, and find and the mentioned link between the amount of magnetic property variation in this device and the corrosion evolution. Thus, through this method, we would be able to assess the corrosion progress in device, in ND way and ultimately, evaluate the availability of aggressive agents that made the device rusted. It would allows to send on time alarm to infrastructure managers about the contamination level of cover concrete and prevent the collapsing risk of structure, before it emerges.
To use the forward method, a reference model is required to resolve the inverse problem. The methodology involves using reference data from numerical modeling of the embedded device through Ansys Maxwell software and the Finite Element Method (FEM) to obtain the MO changes due to degradation of the device. By minimizing the error between the MO of the reference and forward model, the amount of magnetic properties of the device are estimated. To validate these results, some laboratory tests are conducted using an accelerated corrosion technique in NaCl saline solution as a controlled aggressive agent medium to obtain MO variations as a function of device corrosion with different levels of rusting. Then, the proposed method will be evaluated with experimental tests as well to validate the hypothesis.

0.2 Chapters plan:

Chapter 1 contributes to the thesis state of the art. In this regard, initially, the different concrete types, such as hydraulic concrete that are widely used in marine environments constructions as well as the concrete properties are reviewed. Then corrosion mechanisms and the contributing factors that could lead to corrosion would be studied. Then, the RC durability indicators associated with chloride ion ingress to evaluate the service life models would be quickly studied. Moreover, through a bibliography study, different available NDT associated with rebar corrosion as well as the methods for evaluating the chloride ions level in concrete and also various SHM techniques would be reviewed through their advantages and disadvantages. In this chapter, the thesis orientation, including the proposed technology principle, the hypothesis, objectives, and methodology would be discussed, extensively.
In Chapter 2, the theory of magnetism and the governing constitutive Maxwell equations in the magnetostatic domain will be reviewed. A numerical model of the proposed technology will be created using Ansys Maxwell software. A parametric study will be conducted to determine the suitable materials for the embedded device's manufacturing. Using the parametric study with modelings, the feasibility studies will also be performed to maximize the MO range and analyze

the MO variation range based on the device's geometry and the evolution of corrosion product layers. To evaluate this, the corrosion products of the device are separately characterized through experimental tests and the results have been applied in the numerical models of this chapter.

In Chapter 3, the effective geometry of the embedded device would be studied with numerical models and parametric studies. Subsequently, the possibility of using the multi-embedded device in cover concrete would be investigated as a function of relative distance. The objective is to find the efficient location of the device and also find the lateral distance among devices to avoid internal magnetic coupling. Moreover, the possible coupling effect between this device and rebar in the concrete model would be also investigated, in this chapter.

In Chapter 4, the focus is on investigating the forward method to estimate the variations in the magnetic properties of the device caused by corrosion using numerical configurations. The chapter begins by considering two different analytical expressions as well as two algorithms to solve the nonlinear optimization problem. These options will be compared to determine the most effective solution for each step of the forward method. Then, using the numerical modelings and parametric study on altering the device dimensions, the generate MO variations are planned to obtained. This will enable the evaluation the proposed method, which correlates the variations in magnetic property changes of device and the degradation state due to changing the device geometry. For numerical modelings, we will use ANSYS Maxwell software is based on its recommendation as a powerful tool for electromagnetic modeling and analysis using FEM.

Finally, in Chapter 5, through an experimental campaign, the performance of the embedded device would be evaluated on real concrete media. The objective is initially to assess the hypothesis that MO is independent of environmental variations, such as concrete mixing, water content, and *etc.* Therefore, in this chapter, initially, through a variety of concrete slabs, with different concrete characteristics, the amount of MO variations would be evaluated. It would allow us to experimentally validate the hypothesis related to MO independence related to environmental factors. Similarly, the amount of MO variations in free space would be evaluated by experiments on different days to find the minimum uncertainty level of MO. The amount of MO variance would represent the stability level of measurement as well as the minimum magnetic background noise level (bias magnetic field) that could also alter MO. Secondly, the proposed forward method would be investigated with an experimental test, as reference data. through accelerating corrosion, the MO variations would be experimentally measured as a function of the corrosion state. Using these results as reference data, the proposed forward method would be experimentally checked to obtain the amount of estimated magnetic property variation as a function of corrosion to validate the numerical results.

Eventually, by analyzing and comparing the results of Chapter 5 with Chapter 4 as well as the numerical modelings in Chapters 2 and 3, the proposed method's effectiveness and robustness

can be assessed, highlighting its advantages such as sensitivity to corrosion induced MO variations and its potential as a reliable means of monitoring aggressive agents in the cover concrete and providing timely alerts for the risk of rebar corrosion.

Chapter 1

State of art

1.1 Introduction

Reinforced concrete is considered a durable composite material compared to raw concrete because it has reinforcing steel bars (rebars) embedded in it. The rebars provide additional strength and support to the concrete, which increases its ability to resist cracking, bending, and other forms of deformation. This reinforcement helps extend the life of the structure and prevents premature failure. Additionally, he presence of the rebars facilitates the even distribution of stress and load throughout the structure, thereby reducing the concentration of stress at specific points, which can lead to cracking or failure.

Although the presence of rebar would highly improve the tensile strength of concrete, the rebar suffers from corrosion. Rebar corrosion is a natural process caused by their exposure to the environment and aggressive agents such as oxygen, carbon dioxide, and chloride ions. It leads to series of electrochemical reactions between the steel and the surrounding environment. The concrete acts as an electrolyte and allows the transfer of ions, leading to the formation of an anode and cathode on the steel surface. The anode undergoes oxidation and corrodes, while the cathode remains protected from corrosion due to various factors, such as the formation of a passive film on the steel surface. This passive film acts as a barrier that impedes further corrosion reactions, preserving the integrity of the rebar. This corrosion process could be accelerated in the presence of moisture and contaminants, such as chloride ions. Chlorides can come from sources such as seawater, de-icing salts, and contaminated groundwater or could be present at the aggregates. Specifically, in marine environments due to availability of such corrosive agents, the RC structures are highly subjected to rebar deterioration. Consequently, rebar corrosion can lead to structural failure and the need for expensive repairs or replacement.

To prevent the negative effects of rebar corrosion, it is important to monitor its progression and detect it at an early stage. In this regard, many techniques such as periodical inspections, Destructive Testings (DT) and Non Destructive Testings (NDT) have been developed with great focusing on the rebar corrosion evaluation and also the estimate the aggressive agent level as preventive methods. Nevertheless, some of these methods show successful results in evaluating rebar corrosion state, but there is still a lack of reliable preventive ND method that could assess the probability of rebar corrosion before it emerges. In this purpose, it is important to initially

study the RC basic materials and consequently, the phenomenology of corrosion as well as the mains environmental reasons that could lead to rebar corrosion.
This chapter will begin by discussing the primary components of concrete material, particularly Portland cement, which is widely used in reinforced concrete structures for coastal engineering. The discussion will then turn to the durability and serviceability of reinforced concrete structures. The chapter will delve into the potential threats to concrete durability and the significance of using durability indicators to predict its service life. At this step, rebar corrosion, the most critical issue in terms of reinforced concrete durability, will be explored in detail. The mechanisms of corrosion and the key factors that contribute to its acceleration will be discussed. The chapter will also cover the most reliable durability indicator for measuring the ingress of aggressive agents, particularly chloride ions. A comparison of various inspection techniques such as DT, NDT, and Structural Health Monitoring (SHM technique which is a subcategory of NDT) will be presented, including an overview of their principles, advantages, and limitations. Then, it would focus on the remaining challenges in this field and provide a technological solution to address these issues. Finally, the thesis orientation including the hypothesis, objectives, and methodology will be discussed

1.2 Concrete

Concrete, a combination of cement, water, and aggregates, is a widely used material in civil construction projects such as tunnels, bridges, and highways [34]. Aggregates, which make up 60-80% of concrete's volume, are divided into fine and coarse groups [35]. The paste, made up of cement, water, and air, constitutes 20-40% of concrete's total volume [36]. Therefore, it is essential to examine the fundamental materials and their mix proportions to fully comprehend concrete's properties and characteristics [35].

1.2.1 Cement

Cement, a key component in concrete, is a finely ground powder that hardens when mixed with water [36]. In marine structures, Portland Cement or hydraulic cement is commonly used as it can harden even when submerged in water [37]. The chemical reaction between cement and water results in the formation of submicroscopic crystals or a high-surface-area gel-like material. This hydrating property makes Portland Cement suitable for curing under water [36, 38]. Hydraulic cement is composed of four mineral components: Tricalcium Silicate (C_3S), Dicalcium Silicate (C_2S), Tricalcium Aluminate (C_3A), and Tetracalcium Aluminoferrite (C_4AF), each with its own hydration properties [36]. By blending these raw materials through various dry/wet processes, a range of mixtures can be produced. The International Association Society for Testing and Materials (ASTM) defines five types of Portland cement (Types I, II, III, IV,

V) [36], each designed to meet specific physical and chemical requirements for various purpose. The five types of Portland cement are ordinary (Type I), modified (Type II), high-early-strength (Type III), low-heat (Type IV), and sulfate-resistant (Type V). Type I cement is the most widely used, while Type III is used for rapid strength development, where it is available. Types IV and V are differentiated by their lower heat of hydration and improved sulfate resistance, respectively [39]. In France, the different types were confirmed by the French Commission of Testing Methods and later standardized by the French Association for Standardization (AFNOR) [40].

1.2.2 Aggregates

The aggregates are usually composed of geological materials such as sand, gravel, crushed stone, or iron-blast furnace slag which, in mixing with a binder, could make concrete mixes more compact [34]. They are graded by passing them through a set of sieves with progressively smaller mesh sizes. For instance, by using a 4.75 mm sieve and retaining on a 0.075 mm sieve, fine aggregates would be produced. Consequently, the coarse aggregates that have a bigger size compared to fine aggregates, must retain on 4.75 mm sieve [36]. By carefully grading the material and selecting an optimal particle size distribution, a maximum packing density can be achieved, where the smaller particles fill the void spaces between the larger particles. The importance of using the proper aggregate size in concrete mixing is that such precise dense packing, could minimize the amount of essential cement paste and generally leads to improve the mechanical and durability properties of the concrete [41].

1.3 Concrete properties

1.3.1 Phase relationship in concrete

The properties of concrete are largely influenced by the proportions of its components - cement, water, coarse, and fine aggregates. Hence, it's important to examine the relationship between the volume and mass of solid (aggregates and binder), liquid (water), and gaseous (air) phases in concrete during the mixing process [42]. Typically, concrete can be in three states: partially saturated, saturated, and dried, as shown in Figure 1.1. In this diagram, m is used for mass in which m_a, m_w and m_s are indicating masses of air, water and solid, respectively. Moreover, the term of v indicates the volume unit where v_a, v_w and v_s are for volumes of air, water and solid in the concrete, respectively.
The most important ratio, defined by these three phases is the portion of water and cement, referred to as the Water to Cement (W/C) ratio. In this case, the difference between partially saturated and fully saturated phases, (Figure 1.1a and b), is determined by this value. Adding a huge amount of water to the mix would reduce the strength of concrete as a function of increasing the W/C ratio. On the other hand, too low W/C ratios cause poor workability of

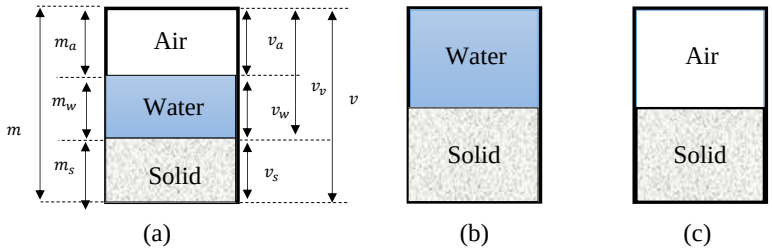

Figure 1.1 – Concrete materials phase relationship (a) partially saturated state (b) fully saturated state (c) dry state [42]

the concrete. While aggregate, cement, and water are the main ingredients, there are a large number of mineral and chemical admixtures that may be added to the concrete [36]. Some of these admixture allow the use of less water in the mix design and results in increasing the strength and durability of the concrete. Moreover, the other fundamental properties of concrete such as porosity, density, or saturation degree are defined through these relation phases. In the following, we would review these properties.

1.3.2 Concrete's porosity

The porosity is an intrinsic property of cement paste, depends on many factors related to the micro-structure of concrete and material's phase relations, illustrated in Figure 1.1. Basically, the porosity decreases with the W/C ratio. Porosity also increases with curing temperature during producing the concrete and the differences mostly concern the volume of large pores [43]. The type of cement also influences porosity, although it is more important in pastes than in mortar [1] and concrete. The determination of porosity and pore size distribution is an important means of characterizing cement pastes and is widely used as an indicator of concrete quality and durability. According to [44], the porosity of concrete, ϕ [-], is quantified by the ratio of void's volume v_v $[m^3]$ (water and air components at Figure 1.1a), over the total volume of concrete v $[m^3]$ given by:

$$\phi = \frac{v_v}{v} \tag{1.1}$$

Moreover, the void ratio η [-] could be express as the ratio of void volume v_v over solid volume v_s by:

$$\eta = \frac{v_v}{v_s} \tag{1.2}$$

1. Composition of cement, which is mixed with fine sands and water, with lime added to improve the durability of the product

Thereby, the amount of porosity could be expressed in function of concrete's void ratio through:

$$\phi = \frac{\eta}{1+\eta} \tag{1.3}$$

1.3.3 Concrete's density

The density of concrete is a specific property of concrete that is related to mechanical properties of concrete such as its strength and hardness. Concrete's density varies by the number of raw materials used in the manufacturing process, dried or saturated state, and volume of concrete sample. According to [42], the density of concrete γ [kg/m^3] for partially saturated concretes state, illustrated at Figure 1.1, express by:

$$\gamma = \frac{m}{v} \tag{1.4}$$

which m is mass of concrete [kg] and v is total volume of concrete [m^3].
Consequently, for density of saturated concrete in Figure 1.1b could be defined as γ_{sat} [kg/m^3] thorough:

$$\gamma_{sat} = \frac{m_s + m_w}{v} \tag{1.5}$$

In this case, the solid and liquid mass would be considered for measuring of density.
Finally, for dry state concrete in Figure 1.1c, the density of dired concrete (γ_{dry} [kg/m^3]) would be calculated by:

$$\gamma_{dry} = \frac{m_s}{v} \tag{1.6}$$

1.3.4 Moisture condition of concrete

The pore network of concrete has water from its manufacturing process which has been dried slowly only on its outer surfaces. The water amount can be defined by the porosity (quantity of pores, their distributions in the structure as well as the age of the concrete) and the saturation rate [45].
Monitoring the concrete properties associated with the moisture condition of concrete can be a critical issue that could avoid disastrous flooring failures, resulting in costly damages and repair fees.
In this case, there are different definitions related to moisture condition of concrete as: saturation degree S [-], volumetric water content w [-], gravimetric water content w_g [-], and relative humidity (RH [%]) could be used.
The saturation state degree is expressed as the fraction between water volume over void volume. The saturation ratio range is between 0 (totally dried) to 1 (totally saturated) and define

by [46, 47]:

$$S = \frac{v_w}{v_v} \tag{1.7}$$

Subsequently, the volumetric water content ratio w is defined by:

$$w = \frac{v_w}{v} \tag{1.8}$$

which express the ratio of water volume over total volume of concrete. Considering the Eq. 1.1 and Eq. 1.7, the volumetric water could be defined in function of saturation degree and porosity by:

$$w = \phi S \tag{1.9}$$

Moreover, the gravimetric water content w_g defines a ratio between masses of water and solid through:

$$w_g = \frac{m_w}{m_s} \tag{1.10}$$

Finally, the relative humidity (RH) represents the amount of water vapor in the air, compared to the amount that the air can hold [48]. The significance of this ratio is due to the fact that even though the concrete visual inspection, might be looks dried on the surface, that doesn't necessarily mean that it is totally in dried state. It is usually happen during concrete's drying process while the surface of concrete is apparently dried, however, the higher level of moisture is still the bottom of the slab. The RH ratio is usually defined as partial pressure of water vapour in pore space $\mathfrak{p}_w$ [kg/m^2] over saturated vapour pressure of water $\mathfrak{p}_w^*$ [kg/m^2] at a given temperature.

$$RH = \frac{\mathfrak{p}_w}{\mathfrak{p}_w^*} \times 100 \tag{1.11}$$

As mentioned, the evaluation of water level in concrete is very important. The significance is rather about providing the possibility of pathogens transferring assessment, such as chloride ions or carbon dioxide or other aggressive agents penetration, into the structure. These pathogen agents are responsible for the degradation of the concrete which could highly affect the structure's durability. The penetration of aggressive agents, particularly, is important in RC construction which could lead to the rebar deterioration [49]. With the extension of rebar's corrosion and increasing the volume of rebars, the cracking or spelling of concrete is inevitable. In section 1.4, we will describe the rebar's corrosion caused by pathogens.

1.4 Corrosion in reinforced concrete civil structures

As it's mentioned, steel rebars are embedded in concrete to increase its strength and tension, with the steel primarily responsible for resisting tensile forces and the concrete resisting com-

pressive forces. The alkalinity of the concrete typically protects the steel from corrosion, but this can be compromised in marine environments where chloride ions are present and can accelerate corrosion.
Corrosion can significantly reduce the structural strength of a building, causing the rebar to lose mass and expand in volume. This, in turn, can lead to the appearance of cracks in the concrete and gradual deterioration of the structure. In order to provide a solution to prevent the risks of collapse and associated repair and maintenance costs, a reliable inspection method is required. To develop such a method, it is essential to have a comprehensive understanding of the corrosion mechanism and the factors that significantly accelerate this corrosion process. Once this understanding is established, a cost-effective and reliable preventive solution can be proposed to evaluate the possibility of corrosion in the structure at an early stage.
This section aims to tackle the problem of rebar corrosion by following a three-step approach. Firstly, we will review the process of rebar corrosion, specifically caused by aggressive agents like chloride ions. Secondly, we will discuss and compare existing RC health statement's evaluation techniques associated with corrosion including: Destructive Testings (DT) and Non Destructive Testings (NDT) related to rebar corrosion, including both preventive and evaluation methods. Finally, we will explain the remaining challenges in this area before introducing the proposed solution of this thesis.

1.4.1 Corrosion process

Corrosion is the process of deterioration of metals caused by chemical reactions with their environment. In RC structures, the presence of aggressive agents, such as chloride ions, in the environment can initiate and accelerate the corrosion process of the embedded steel rebars. These agents penetrate the concrete cover, break down the protective oxide layer on the rebar's surface, and eventually lead to the rebar's mass loss and cracking of the concrete [51, 52]. The partial or complete loss of the passive layer, known as depassivation, leads to the active corrosion

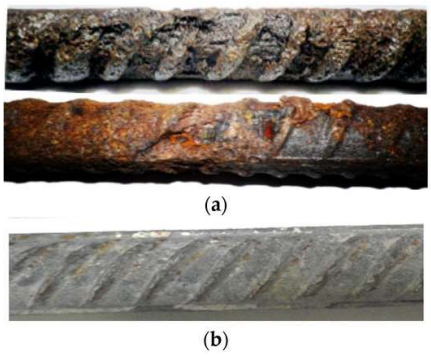

Figure 1.2 – Physical variations of rebar after corrosion (a): a rebar after corrosion, (b): a rebar before corrosion [50]

of steel bars. Some research has been carried out to understand the formation and breakdown of the passive layer [10]. Generally, chloride ions that come mostly from deicing salts or seawater, and carbon dioxide from the atmosphere, are the two most well-known factors that can break the passive film on the surface of steel, according to [10]. Finally, the corrosive products of iron would be formed due to electrochemical and chemical reactions of corrosion, and their formation can cause cracking and further deterioration in concrete. The corrosion products have different chemical formula, volume, density and color compare to the origin iron atoms. Figure 1.2 shows a part of rebar, before and after corrosion. The rebar color is changed and also its physical shape has been affected by corrosion.

As mentioned earlier, the accumulation of corrosion products on the rebar surface creates internal pressure on concrete, damaging structures. Porous concrete networks and the hidden micro-cracks allow more corrosive elements, moisture, and oxygen to penetrate. Since, steel rebar is composed mainly of iron, it can easily undergoes chemical reactions with water and oxygen. Thus, adequate moisture and oxygen create the initial conditions for the electrochemical reaction of corrosion [54, 55]. Figure 1.3 represents a schematic of a rebar corrosion process. At this point, one side of rebar becomes an anode and the other side, where the water and oxygen are available, would be the cathodic area. It leads to generating a differential potential between anode and cathode that is enough to emerge an electrochemical process. The iron atoms lose electrons and transform into ferrous ions which would move around concrete on the anode side of the rebar [22]. Then, the generated free electrons will move to the cathodic side. They would combine with water and oxygen and result in the generation of hydroxide ions OH^-. The main chemical reaction at anodic and cathodic sides of rebar are:

$$2\,\mathrm{Fe} \longrightarrow 2\,\mathrm{Fe}^{2+} + 4\,\mathrm{e}^- \tag{1.12}$$

$$\mathrm{O_2} + 2\,\mathrm{H_2O} + 4\,\mathrm{e}^- \longrightarrow 4\,\mathrm{OH}^- \tag{1.13}$$

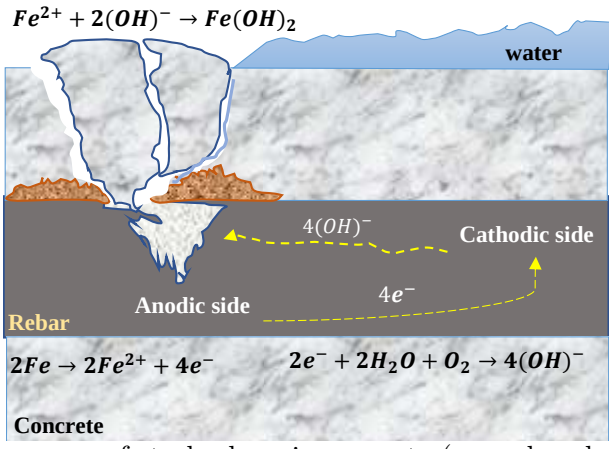

Figure 1.3 – Corrosion process of steel rebars in concrete (reproduced and modified from [53])

Then, they combine with hydroxide ions and form iron hydroxides like such as $Fe(OH)_2$.

$$Fe^{2+} + 2\,OH^- \longrightarrow Fe(OH)_2 \tag{1.14}$$

In fact, $Fe(OH)_2$ is one of the most typical iron corrosion products. If the oxygen around rebar is sufficient, iron hydroxides could transform into different iron oxides such as Fe_2O_3 or Fe_3O_4 which are all other corrosion product types [56].
Usually, the alkaline environment of concrete (pH of 12 to 13) naturally provides a passive oxide layer around steel, protecting it against corrosive elements despite its tendency to corrode. However, this layer is not entirely resistant to corrosion and can only slightly delay the process. Carbonation and aggressive agents, such as chloride ions, are two factors that can damage the passive layer and initiate corrosion [57]. Next, their role in initiation of rebar corrosion will be reviewed.

1.4.2 Carbonation induced corrosion in concrete

In fact, carbon dioxide present in the atmosphere could penetrate into the concrete through the voids of concrete. The carbon dioxide does not attack the cement paste, however, it would affect the pH of media through combination with the calcium hydroxide ($Ca(OH)_2$) in concrete and eventually, forming $CaCO_3$ (calcium carbonate) in the pore media [58], by the following equation:

$$Ca(OH)_2 + CO_2 \longrightarrow CaCO_3 + CaO_2 \tag{1.15}$$

Moreover, the water penetrated into the concrete would also react with carbon dioxide and form carbonic acid H_2CO_3 via the following equation:

$$H_2O + CO_2 \longrightarrow H_2CO_3 \tag{1.16}$$

Then, the carbonic acid reacts with $Ca(OH)_2$ from concrete's substance, which results in more carbonation by producing $CaCO_3$ and water, in the media:

$$H_2CO_3 + Ca(OH)_2 \longrightarrow CaCO_3 + 2\,H_2O \tag{1.17}$$

Moreover, by consuming the $Ca(OH)_2$ in the Eq. 1.17, the calcium silicate hydrate (CSH) from concrete's substance, would be released in form of CaO. It would also react with H_2CO_3 and pursue carbonation by production of $CaCO_3$.

$$H_2CO_3 + CaO \longrightarrow CaCO_3 + H_2O \tag{1.18}$$

More carbonation would lead to more production of acids, thus, the alkalinity of concrete media would be reduced, as well. Thereby, the pH of the pore solution would drop to 8-8.5 which at this level, the passive film can not resist against corrosion process [59]. Hereinafter, corrosive agents such as water and oxygen can penetrate through the attenuated passive layer, and dissolved aggressive agents like chloride ions can accelerate the process, which will be further discussed.

1.4.3 Chloride induced corrosion in concrete

Chloride ions are recognized as the most well-known aggressive agent which, easier than the others, could pass through the passive layer around steel rebars and cause localized breakdowns on it [60]. The destruction of the passive layer would provide suitable conditions for moisture and oxygen to reach the rebars and eventually accelerate the corrosion process [61].
In fact, the chloride ions are not consumed in the electrochemical and chemical reactions of the corrosion but act mostly like a catalyst.
According to [62], the ferrous ions produced from the Eq. 1.12, would react with the penetrated chloride ions and result in the formation of ferrous chloride $FeCl_2$ via Eq. 1.19:

$$2\,Fe^{2+} + 4\,Cl^{-} \longrightarrow 2\,FeCl_2 \tag{1.19}$$

Through reaction of ferrous chloride with water H_2O, the concrete's pH would be dropped due to producing acidic solution of HCl through Eq. 1.20:

$$FeCl_2 + 2\,H_2O \longrightarrow Fe(OH)_2 + 2\,HCl \tag{1.20}$$

Moreover, the produced OH^- from Eq. 1.13, could react with produced $FeCl_2$. Then, by breaking downs of $FeCl_2$, more ferrous ions would be involved in oxidation and formation of $Fe(OH)_2$ with Eq. 1.21:

$$2\,Fe + O_2 + 2\,H_2O \longrightarrow 2\,Fe(OH)_2 \tag{1.21}$$

Iron corrosion products include $Fe(OH)_2$ and FeO. The corrosion product types can change due to environmental factors such as aggressive agents, temperature, oxygen, or carbon dioxide. In high concentrations of chloride ions, Akaganeite (β-FeOOH) is the most common corrosion product found in reinforced concrete, increasing the rebar volume [10, 63].
Pitting corrosion caused by localized breakdowns of the passive layer with chloride attack is the most possible type of corrosion. However, determining chloride threshold values is complicated due to several reasons, such as varying concrete pH, chloride binding in concrete, and the presence of moisture and oxygen [62]. Corrosion can be observed at a threshold level of 0.2% chloride by weight of cement if the water and oxygen are available, or up to 1.0% or more if water and oxygen are excluded [64].

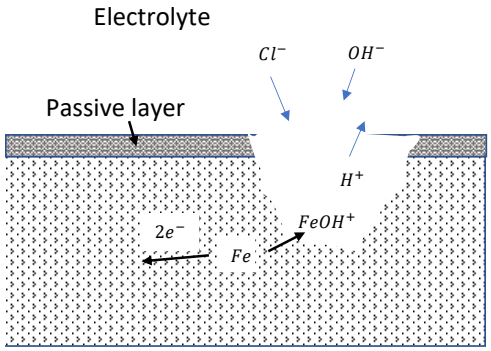

Figure 1.4 – Schematic of localized corrosion (pitting corrosion) of steel rebars in concrete, due to chloride attack (reproduced and modified from [65])

Figure 1.4 illustrates a schematic representation of pitting corrosion occurrence in rebar. The carbonation-induced corrosion could be detected through the cracking and spalling of concrete which serve as an early indicator. In chloride-induced problems, pitting corrosion could be considered as primary evidence. However, since the pits could be filled quickly with rusting products, they are identified as dangerous hidden defects which would extend rapidly to all sides of the rebar and it is very difficult to detect them during visual inspections (Figure 1.5). Hence, it is very important to develop reliable and accurate inspection methods to detect corrosion induced by chloride at early stages.

Much research in recent years has focused on developing durability indicators and NDT related to rebar corrosion detection. Moreover, there are also evaluation techniques associated with this problem which are used to monitor corrosion progress through indicators such as electrochemical properties of corrosion, corrosion state of rebar and *etc.* Eventually, there are also monitoring techniques related to chloride ions availability in the concrete. In the following, firstly, the most reputed durability indicators of chloride ion penetration in concrete would be reviewed. Then, some existing DT and NDT techniques, related to corrosion would be discussed and compared.

Figure 1.5 – Pitting corrosion on a side of rebar due to chloride attack
Source: `https://www.shutterstock.com`

1.5 Durability indicators related to chloride penetration

Detecting chloride-induced corrosion in RC structures is crucial for ensuring their safety and durability, especially in maritime zones where the problem is particularly prevalent. To achieve this, it is important to study available durability indicators related to chloride ion migration and develop effective inspection techniques. Concerning chloride ion penetration level, a variety of durability indicators associated with this issue are available. Typically, by using two or three of these related indicators, the RC durability and the service life could be evaluated [66].
Such durability indicators, which are usually related to the transport of gases, liquids, and ions, have been identified as key parameters in the estimation of the time to corrosion initiation and rate of corrosion propagation resulting from chloride ion penetration, according to [22]. The application of these indicators is crucial in various phases, including:

- During the design phase as input for service life and probabilistic models to relate concrete durability to service life.
- During the construction phase as part of the quality assurance regime to ensure that the specified durability is in fact attained on site.
- During the service life of the structure for regular condition assessment as part of a structural health monitoring regime.
- For updating the service life models in order to reassess the estimated life of the structure due to the time-dependency of the durability indicators.
- For the determination of the residual life of existing structures that were not necessarily designed and built using a performance-based approach and durability specifications.

Typically, the corrosion initiation and propagation is linked to penetrability concrete properties, in terms of aggressive agents. Usually, the aggressive agents penetration into concrete could be expressed by diffusion, migration, permeation and capillary suction, depending on the mechanism of chloride ingress [67]. The permeation is the process of chloride ion penetration into the concrete substance. According to Darcy's law for steady state condition, the flow rate at any point in the reservoir is directly determine by the fluid pressure gradient, the viscosity of the fluid, and the effective fluid permeability, in which it is express by [68]:

$$\vartheta = -\frac{K}{\eta}\frac{d\mathfrak{p}}{dx} \tag{1.22}$$

Here, ϑ $[m/s]$ is the flow velocity [m/s], K $[m^2]$ is the medium's permeability , η $[N_s/m^2]$ is the liquid's dynamic viscosity and $d\mathfrak{p}$ $[N_s/m^2]$ is the differential element of applied pressure which flow in distance of dx $[m]$.
Furthermore, fluids can transport through porous network of media, with or without gradient pressure, due to the surface tension that exits in the capillary pores. Therefore, the porosity and also the moisture condition could determine capillary suction [69]. It is directly associated to

dry/wet cycles of concrete.
Another important property of chloride ion penetration is diffusion coefficient. The Fick's first law of diffusion for steady state condition express by the concentration gradient and the proportionality diffusion coefficient through [70]:

$$\mathfrak{J} = -\mathfrak{D}\frac{dc}{dx} \tag{1.23}$$

Here, $\mathfrak{J}$ $[mol/m_s^2]$ is the flux and c $[mol/m^3]$ is concentration , $\mathfrak{D}$ $[m^2/s]$ is diffusion coefficient at the distance of x $[m]$.
Consequently, the Fick's second law [71] describes the rate of accumulation (or depletion) for concentration through the volume as proportional to the curvature coefficient of the concentration gradient. In this regards, the equation which could explain non-steady state conditions known as Crank's solution that is use to determine the diffusion coefficient through [70]:

$$c(x,t) = c_0[1 - erf(\frac{x}{2\sqrt{\mathfrak{D}t}})] \tag{1.24}$$

Here, *erf* is the error function. Here, t is time and at initial condition for $t = 0$ and $x > 0$, $c = 0$ and for $x = 0$, $c = c_0$.
Migration is the movement of ions into the solution or media under an electrical potential gradient. In this case, the migration coefficient of all ions is not the same in the porous media. When the potential difference is sufficient, the diffusion of ions would be accelerated and lead to generating of an electrical current that would refer to migration. The equations of Nernst-Planck [72] are usually used to describe the motion of chemical species that are charged in a fluid medium through the sum of pure diffusion, electrical migration, gradients pressure, and moisture that express through [73]:

$$-\mathfrak{J}_i = \mathfrak{D}_i\frac{\partial c_i(x)}{\partial x} + \frac{Z_i F}{UT}\mathfrak{D}c_i\frac{\partial q(x)}{\partial x} + c_i q_i(x) \tag{1.25}$$

Here, $\mathfrak{J}_i$ [mol/$m^2 s$] is the molar flux of ionic species i (chloride ions in our case), $\mathfrak{D}_i$ $[mol^2/s]$ is the diffusion coefficient of species, $c_i(x)$ $[mol/m^3]$ is the concentration of i as a function of location in x_i [m], Z is the valence number of species, F is the Faraday's constant (96485 C/mol), U is universal gas constant (8.314 J/mol/K), T is temperature in kelvin [K], *V(x)* is applied electrical potential as function of distance x and finally, $q_i(x)[m^2/s]$ is the velocity of species. The transport mechanism of corrosion, induced by chloride is related to diffusion and ions migrations which these two factors are particularly used as durability indicators in this case.
The transport of chloride ions is complex and influenced by environmental conditions. Diffusion dominates in the submerged marine structures, while capillary suction governs in the splash zone or tidal area. For structures exposed to de-icing salts, ingress is a combination of diffusion,

permeation, and capillary suction [68]. Variations in concrete resistivity are also significant durability indicators for identifying chloride diffusion [74]. Using a combination of these indicators can monitor the health of RC structures, and traditional inspection techniques associated with these indicators exist.

One of the testing groups are laboratory techniques. These methods are quite useful for decision-making in the long run way test with more accurate information on the initial material. The most reputed laboratory methods related to chloride ingress are:

- Rapid Chloride Permeability (RCP) (use migration diffusion. This method relates charge passed through a concrete slab to chloride penetrability in order to define the permeability of the material, test) [75],
- Nonsteady state diffusion test [76]. This method use diffusion models and complementary chemical techniques for characterizing the material,
- Ponding test [77] and impedance test [78] These methods accelerate diffusion processes for determining diffusion coefficient and chloride ingress profile.

However, these techniques can not provide any information for the in-service structures because they are design to evaluate the structure's performance before construction. Nevertheless, several ND methods related to natural diffusion tests, and migration tests have been suggested for in-service RC structures such as concrete electrical resistivity or conductivity evaluations.

In the next section, the evaluation techniques of concrete health statements, either the NDT techniques related to chloride ion ingress and eventually, rebar corrosion assessment, will be reviewed.

1.6 Review of concrete's health evaluation techniques: advantages and disadvantages

Generally, concrete health inspection refers to the group of assessment techniques which perform regularly to identify and determine many of the various concrete defects may occurred during its service life. In the case of rebar's corrosion, the inspection are usually categorized to:

- **Destructive Testings (DT)**
- **None Destructive Testings (NDT)** which are divided into two sub-categories:
  - Inspection methods
  - Structural Health Monitoring (SHM)

Each category is associated with a group of techniques, each with specific principles designed to provide information about the health statement of in-service RC structures.

Table 1.1 summarized the general existing inspection techniques during service life of RC structures, related to rebar corrosion. The first category of concrete health evaluation is Destructive Testings (DT). These methods are usually carried out on the inspection through coring of in-

Table 1.1 – Examples of concrete evaluation techniques

Techniques		**General principle**	**Main applications and advantages**	**Limitations**	**Examples**
Destructive Testings (DT)		Extracted core/concrete samples from structure for laboratory tests	Main applications: -Mechanical characterisation -Determine chloride ions profile Advantage: -Evaluation of in-place the structure's condition for decision making (*e.g.*, repairing or maintenance)	-Damage the structure -Cause under or over estimation of results due to differences between theoretical and measured data -can't provide punctual information	Volhard method [79] Mohr method [80] Fajans method [81]
None Destructive Testings (NDT)	Inspection methods	Structure's surface testing (external inspection tools and devices)	Main applications: -Concrete evaluation -Corrosion detection -Structural integrity assessment -Material characterization Advantages: - Don't cause damage -Relatively cost-effective -Can be customized -Possible to repeat -Rapid	-Require of calibration -Need to be repeated -Uncertainty in results due to environment variations such as temperature, humidity, quality of soil, water level - Some of them use expensive instruments - Sub surface monitoring	-GPR [20, 82] -Resistivity method [22] -Capacitive method [24, 83] -Magnetic Flux Leakage (MFL) [84] -Ultrasonic wave [85] -Impact Echo [86] -Half-cell potential [87]
	Structural Health Monitoring (SHM)	Using monitoring equipment	Main applications: monitoring the health statement of structures like: Bridge, buildings, dam and *etc.* Advantages: -Provide long term and continues monitoring -Provide early detection -Provide real time data -Safety enhancement	Stability of connection (wired or wireless to avoid data recording interruption -Need to damage concrete in case of problem in sensors	-RFID tag [32] -Fiber-optic sensors [88] -Piezoelectric sensors [89] -Acoustic emission [90]

service structures. Then, the samples would be taken to the laboratory to perform some chemical or physical testings to determine their different concrete properties related to mechanical characterization of structure (such as compressive strength, tensile strength, modulus of elasticity, and Poisson's ratio). Focusing in contaminant penetration, the concrete cores can be extracted from the structure at different depths and analyze them for chloride ion content. The depth of each core and its corresponding chloride ion content can be plotted to generate a chloride ion profile. Although these techniques are quite simple and useful for short decision-making, the main issue is the lack of possibility to perform punctual tests of concrete profiles during a time. The second category of concrete evaluation is NDT techniques, which have gained popularity in recent years due to their ability to rapidly assess concrete without causing damage to the structure. These techniques can be divided into the inspection and SHM methods. Both sub categories, can be used for several applications, such as assessment the concrete statement, corrosion detection, aggressive agent's ingress evaluations and *etc.* Additionally, SHM techniques can provide remote and real-time monitoring through the embedded devices in the concrete. However, both traditional NDT subcategories have their drawbacks, such as measurement uncertainties due to environmental variations in the former and high installation and maintenance costs, as well as the need for a reliable power source for long-term monitoring. In the following, some popular methods related to each main category would be discussed.

1.6.1 Destructive techniques

Core samples are often essential in structural investigations, and are extracted through destructive methods such as diamond drilling. The obtained samples are then analyzed in the laboratory, typically for a durability indicator specific to the investigation. For measuring chloride ingress, two common laboratory methods for determining chloride content are the Mohr [80] and Fajans [81] methods. Both methods involve the precipitation reaction of a solution containing chloride ions of sediment with a silver nitrate solution via known concentration. The Mohr method uses potassium chromate as the indicator and is conducted in a neutral or weakly alkaline environment, while the Fajans method uses fluorescein sodium as the indicator and is conducted in neutral solutions [91]. Another similar method is the Volhard method [79], which determines halide concentration through back titration with silver ions in an acidic medium. The Volhard method is the most commonly used for determining total chloride content in concrete. In France, there are various techniques used to evaluate the strength and quality of concrete, including methods that involve scraping or scratching the surface of the concrete. These techniques are also used to collect samples for further analysis, such as chemical analysis to determine contamination levels, moisture penetration, and chloride ion ingress [92]. Regarding chloride ion evaluation tests, the scraped material is collected and ground into a fine powder. The powder is then mixed with a solvent to extract the chloride ions, which are analyzed using a titration method. Finally, through a direct measurement of the amount of chloride ions, it could be possible to determine the extent of chloride ion penetration and assess the durability of the concrete structure [93].

One advantage of these methods is their direct and accurate way of determining the chloride content in concrete samples. They are well-established and widely used in practice.This helps in understanding the behavior of materials under load and the mechanisms of material failure. It also provides accurate and reliable data on the structural integrity of the component or structure being tested, allowing for a better assessment of the quality of construction and workmanship during and after construction.

However, with destructive testing, there is a risk of damage to the concrete such as popping, spalling, and delamination of concrete is likely to occur during the sampling process. Additionally, the results of destructive testing can be affected by sample size, sample preparation, and the testing procedure used. For instance, if the water used during drilling contains salt, the penetration of the salt into the concrete can also affect the accuracy of the test results. Finally, there is a risk of safety hazards associated with destructive testing, such as debris and flying particles, which need to be carefully managed to ensure the safety of personnel and surrounding structures.

Therefore, NDT methods have become a good alternative solution for traditional DT techniques. NDT methods have a wide range of applications, and some methods that focus on the evaluation

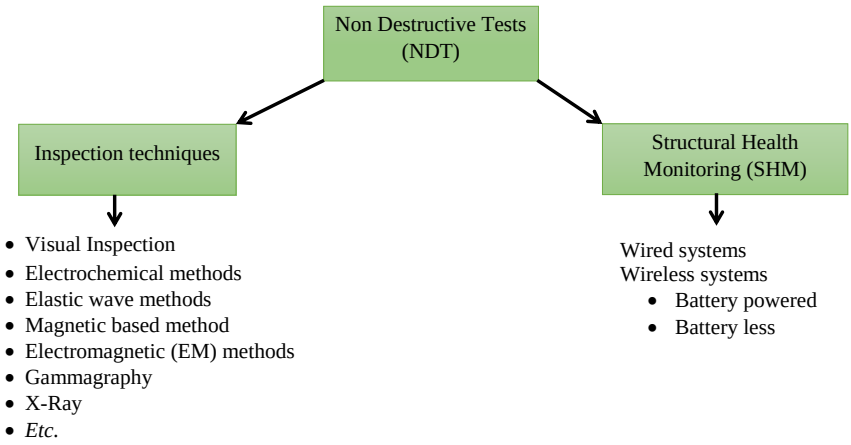

Figure 1.6 – Example of NDT techniques in inspection and SHM subcategories for rebar corrosion assessment and aggressive agent evaluations

of corrosion by chloride ions in reinforced concrete will be reviewed in the following section.

1.6.2 Non Destructive Testings (NDT)

As mentioned NDT are beneficial for assessing the RC structures health conditions, by evaluating material properties, components, or entire process units without destroying structure. NDT methods can be used to evaluate the condition of a structure, and the results of these evaluations can be used to determine the durability indicator for that structure. This can help to identify any potential problems with the structure and allow for maintenance and repair work to be carried out before any serious damage occurs. Therefore, it is essential to develop reliable NDT methods which could put precise diagnosis on the infrastructures pathologies during service life.

Over several decades, numerous studies have concentrated on creating reliable techniques for assessing the state of concrete structures and implementing long-term structural health monitoring. These studies have targeted various concrete structure pathologies. Diagram in Figure 1.6 illustrates two main categories of NDT methods, including inspection techniques and also SHM methods. For each of these groups, several traditional techniques are available that have their own advantages and disadvantages.

The primary objective of this research is to utilize a novel NDT techniques to establish a link between the degradation level of embedded devices (which can be quantified through changes in their geometry or mass loss), a consequence of exposure to contaminants in RC structures, and finally, estimate the potential risk of rebar corrosion induced by those aggressive agents. Therefore, this study will review several well-established NDT methods for evaluating RC contamination, such as chloride ion ingress, and for assessing rebar corrosion.

Generally, the NDT techniques could be categorized into two groups:

— The first category of NDT methods, inspection techniques including visual, electrochemical, mechanical wave, magnetic base, Electromagnetic (EM) wave methods, will be reviewed with some examples, highlighting their associated principles, advantages, and disadvantages.
— Similarly, some techniques related to SHM, such as acoustic emission, wired and wireless systems will be examined with their principles, benefits, and limitations.

In the following, both categories will be discussed through some technique's examples, their benefits, and drawbacks.

1.6.3 Non-Destructive Testings (NDT): Inspection methods

Visual inspection

Visual inspection is a periodical ND method to identify the possible visual signs of damage or degradation in RC structures, such as cracks or spalling. This method can help to detect the areas of the structure that require maintenance or repair and can prevent further extensive damage or failure of the structure. During a periodic visual inspection, the inspector looks for the visible signs of corrosion on the surface of the reinforced concrete structure, such as rust stains, cracking, or spalling. Corrosion on the surface of the rebar can also cause the surrounding concrete to crack and break away, revealing the corroded rebar underneath. By identifying these visible signs of corrosion, the inspector can recommend further testing or repairs to prevent the corrosion from spreading and potentially compromising the structural integrity of the reinforced concrete. Figure 1.7 shows a corroded area in reinforced concrete that is under inspection by measuring devices (a vernier caliper).
The advantages of periodic visual inspection for identifying rebar corrosion in reinforced concrete structures include that it is a relatively low-cost and simple method that can be carried out by trained personnel, and it can provide a qualitative assessment of the severity and extent of corrosion.
The disadvantages of this method include that it is generally limited to the detection of corrosion that has progressed to the point where it is visible, and it may not be sensitive enough to detect corrosion in its early stages. Additionally, the interpretation of visual inspection results can be subjective and may vary depending on the experience and training of the inspector. Finally, visual inspection does not provide any quantitative information about the degree of corrosion or the remaining service life of the structure. In addition, complementary inspection techniques are required to determine the origin of defect [94, 95]. In the next section, the complementary NDT methods related to rebar corrosion pathology would be represented.

Figure 1.7 – Visual inspection of corroded RC
source: `https://csengineermag.com/evaluation`

Electrochemical methods

Electrochemical methods are widely recognized as one of the most effective inspection and evaluation techniques for assessing rebar corrosion in concrete structures. These methods can provide rapid and reliable information about the likelihood of corrosion, the corrosion rate, and the resistivity of the concrete [96, 97]. Basically, the principle of electrochemical methods are associated with the interrelation between the chemical and electrical process. The electrical parameters of oxidation and reduction reactions *i.e.*, potential and current, could be measured by an electrochemical system, as indirect information of rebar statement [98, 99]. Like other NDT techniques in the inspection subcategory, this method provides indirect information that is measured during inspection as an ND observable. The collected data must be calibrated to provide a quantitative interpretation of variations in the durability indicator.
In this section, we will focus on two well-known electrochemical techniques associated with rebar corrosion, which include:

— Open Circuit Potential (OCP)
— Linear Polarization Resistance (LPR)

In the Open Circuit Potential (OCP) monitoring, the principle is measuring the potential difference (in [mV] or [V]) between a rebar and a reference electrode (*i.e.*, a copper/copper sulfate cell), in contact with the concrete surface (Figure 1.8a) [100, 101]. This technique is also called Half-cell potential and was first used by Stratful [87]. By using the OCP technique, the information related to the probability and potential level of corrosion in RC structures could be obtained [102, 103].

Table 1.2 – Interpretation of corrosion with potential level and resistivity (electrochemical techniques)

Corrosion level	Potential Level (mV)	Concrete resistivity (Ω.m)
Very high	-	-
High	$\leq$ -350	$\leq$ 100
Moderate	between -200 to -350	between 100-500
Low	$\geq$ -200	between 500-1000
Negligible	-	$\geq$ 1000

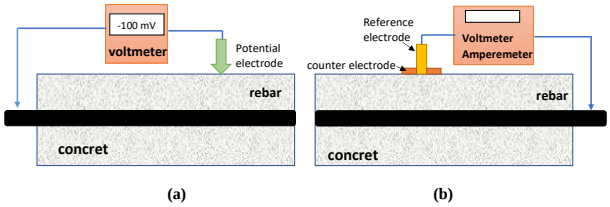

Figure 1.8 – Principle of open circuit methods methods for monitoring corrosion in RC: (a) open Circuit Potential (OCP) (reproduced and modified from [94]) (b) polarization resistance (Reproduced and modified from [98])

Table 1.2 gives the potential ranges for different corrosion conditions of steel inside the RC [15]. Interpretation of the half cell potential measurements involves comparing the measured potential values to a known scale of values, which allows for an assessment of the corrosion activity in the concrete. Generally, a more negative potential indicates a higher likelihood of corrosion, while a less negative or positive potential indicates a lower likelihood of corrosion. Thus, this method could assess the probability of rebar corrosion with draw a correlation among the measured potential and corrosion level.

Advantages of the this method include its simplicity and relatively low cost. It can be used to rapidly assess a large area, and the results can be easily interpreted by non-experts. Through this method, both the potential level of half cell and also the concrete resistivity could be provided, at the same time.

However, the measured data highly depends on the condition of the RC structures, in terms of cover concrete state. Hence, the interpretation of the results is often subjected to debate due to sensitivity to environmental factors, such as temperature and moisture content. To be more precise, studies in [94, 104] show that moisture levels and amount of chloride concentration can affect the potential readings and give erroneous results. Thereby, in marine environment which the RC structures are subjected to moisture and aggressive agents, the potential values become more negative value, according to [15, 94]) and thus, so difficult to interpret. Additionally, this method cannot provide precise information about the extent of corrosion or the area of rusting in the assessed zone.

Linear Polarization Resistance (LPR) is another electrochemical technique (also known as polarization resistance). It is usually suggested for measuring the corrosion rate in rebar. The principle of the LPR technique is based on making the rebar polarized with an electric current. Then, the rebar polarization effect on the reference electrode potential would be monitored (see at Figure 1.8b). It is carried out with a reference electrode (incorporating an auxiliary electrode) and a variable low voltage direct current (DC) power supply. The reference electrode potential is primary, measured and then a small current is passed from the auxiliary electrode to the reinforcement. The changes in the reference electrode potential Δv [V], is simply related to the corrosion current (i_{corr} [A]) [105]. Eventually, the polarized resistance R_p [Ω] could be calculated

by:

$$R_p = \frac{\Delta v}{i_{corr}} \tag{1.26}$$

This method offers the advantage of being a rapid technique and useful for short measurements, without significant variations in results due to minor perturbations. Moreover, the method is highly useful for uniform corrosion and can be used to evaluate the corrosion rate of rebars in concrete without requiring prior knowledge of the concrete's electrical properties.
Nevertheless, LPR measurements suffer from some limitations. LPR is a surface-based technique, so it can only assess the corrosion rate at the rebar concrete interface, and not the corrosion rate throughout the entire rebar. Although LPR can be used to evaluate uniform corrosion rate, it is not a common occurrence in practice. Additionally, in marine environments where pitting corrosion is highly likely, this method can produce misleading results [106, 107].
To summarize, electrochemical techniques take benefits from providing detailed information about the corrosion behavior of rebar in concrete structures, such as the corrosion rate, the potential of the steel, and the probability of corrosion. They are also quite fast to provide information about the internal condition of the concrete. However, there are some disadvantages, including the need for trained personnel, the requirement for access to the rebar surface, and the susceptibility to environmental conditions that may affect the accuracy and interpretation of the data. Moreover, electrochemical techniques are generally limited to the detection and measurement of corrosion on the rebar surface, and they can not be used as a preventive technique for rebar corrosion.
In the following, another NDT inspection method for rebar corrosion, referred as mechanical wave propagation will be reviewed.

Mechanical wave propagation

Mechanical wave propagation are based on the principle that mechanical waves, such as stress waves, can be used to probe the internal structure of materials. These waves propagate through a material and can be measured and analyzed to determine various properties of the material, including its mechanical properties and the presence of defects and damage such as cracks or micro-cracks caused by corrosion at very early stages [101]. When it comes to detecting rebar corrosion, these techniques have the ability to identify its presence without requiring direct contact or physical access to the rebar. This makes it a relatively simple and non-destructive technique. This section will review two of the most commonly used wave-based techniques for assessing rebar corrosion, including:

— Ultrasonic Pulse Velocity (UPV)
— Impact Echo (IE)

The Ultrasonic Pulse Velocity (UPV) test is based on an active method that measures the

velocity of mechanical waves propagating through concrete [25, 108]. Figure 1.9a illustrates the UPV method principle. The mechanical wave energy propagates through the concrete as a stress wave and then, the wave would convert into electrical energy via a surface transducer, illustrated in the Figure 1.9a. The UPV method operates in the frequency range of 20 kHz to 1 MHz, which is considered low. However, this frequency range allows the UPV method to propagate over long distances within the concrete and be sensitive to the interface conditions between steel reinforcement and concrete. Therefore, it is efficient in detecting structural defects, such as voids, cracks, and delaminations, making it a safe and effective method for evaluating the integrity of structures [109]. According to [26, 85], the available crack or void in the concrete lead to attenuation of ultrasonic waves. Focusing on rebar corrosion, measuring the amplitude attenuation of UPV in the area of concrete that is exposed to rusting (through possible internal cracks), it would be possible to detect corrosion through the associated mechanical damages in the concrete. By extending rebar rusting, the delimitation degree between rebar and the concrete would rise, due to corrosion product accumulation. Hence, the amount of UPV peak which is measured in primary value fluctuates by increasing and then decreasing, according to [110]. The studies conducted in [111, 112] have shown that in certain specific cases, there exists an empirical correlation between the amplitude attenuation of UPV and corrosion damage. However, this correlation is not a true physical one.

Advantages of Ultrasonic Pulse Velocity (UPV) in application of rebar corrosion include its non-destructive nature, ease of use, and ability to detect early stages of corrosion before it becomes visible on the surface of the structure. It is also a relatively quick and cost-effective method for assessing the mechanical properties of concrete.

Disadvantages of UPV include its inability to detect localized corrosion such as pitting corrosion and its sensitivity to other factors that can affect the velocity of sound waves through concrete, such as the presence of micro-cracks and voids. Additionally, the accuracy of the results can be affected by the distance between the transducers and the surface of the concrete, the orientation

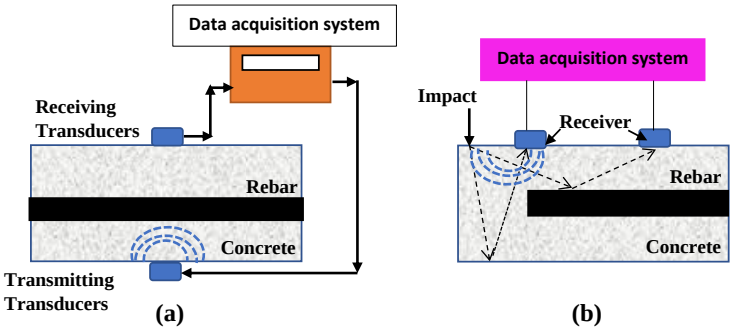

Figure 1.9 – The principle of mechanical wave propagation (a) UPV (reproduced and modified from [85]); (b) IE (reproduced and modified from [86])

of the transducers, and the type and quality of the concrete being tested. In addition, the UPV method can not precisely detect the rebar corrosion or the corrosion statements, compare to other methods.

Impact Echo (IE) is an active mechanical wave propagation that is widely used to detect certain defects in concrete such as micro-cracks cracks and also delimitation of the concrete structure. Figure 1.9b shows the principle of this method. The principle of IE technique in RC structure inspection is based on the propagation of stress waves in the structure due to the impact of a steel spheres (ball bearings) or small hammer on the surface, illustrated in Figure 1.10. The stress waves create a series of pulses that propagate through the structure and are reflected at various interfaces, including the bottom of the slab and any cracks or delaminations within the structure. The reflected waves are recorded and analyzed to determine the thickness of the slab and the presence of any defects, such as voids or cracks, that may be affecting the structure's integrity [27, 113]. Focusing on rebar corrosion, it is possible to detect corrosion by analyzing changes in signal characteristics such as frequency, attenuation, and amplitude of the reflected waves caused by corrosion products and associated damage in concrete structures, which can lead to cracks. [114, 115].

The advantages of impact echo in the application of rebar corrosion are that it is a non destructive method, capable of detecting detect micro-cracks caused by corrosion. It also provides relatively quick and easy method to carry out and can be used on large concrete structures.

However, the method has some disadvantages, including the fact that it requires a certain level of skill and expertise to perform and interpret the results accurately. The results can also be affected by external factors, such as temperature and humidity, and can be limited by the geometry of the structure being tested. Additionally, impact echo may not be effective in detecting early stages of corrosion or damage, as the changes in signal characteristics may not be significant enough to detect [15, 86].

In the following section, we will review methods that are sensitive to the contamination level of

(a) (b)

Figure 1.10 – Impact Echo method: (a) measuring IE with echo source and surface receiver (b) IE hammer to produce echo

concrete, which could ultimately result in corrosion.

Electromagnetic (EM) method

Electromagnetic (EM) methods are another main categories of NDT inspection. They use ND measurments to gather indirect information about the material being tested. These methods typically involve inducing an electromagnetic field into the material and then measuring the response of the field. By analyzing the properties of the field, such as its amplitude, phase, or frequency, it is possible to obtain indirect information about the material's electrical conductivity, magnetic permeability, or other characteristics. These methods are widely used in applications such as locating the rebars, voids, and concrete defects and *etc.*

The application of EM methods is highly dependent on the range of operational frequency. Studies in [116, 117] show that EM techniques are sensitive to the presence of water and chlorides in concrete even when the electrical resistance of the concrete is very low. Subsequently, the concrete's electrical parameters, such as electrical resistivity, are influenced by environmental conditions such as water content and chloride ion penetration, among others. EM methods can, therefore, be used to detect the ingress of water and aggressive agents in concrete. Since moisture and aggressive agents can result in rebar corrosion, evaluating their availability using EM methods could be used as preventive NDT methods in rebar corrosion, as well.

As mentioned before, EM methods are capable of operating at different frequency ranges, which enables a range of techniques to be employed. The primary factor that differentiates these methods is their operational frequency range, and accordingly, EM techniques can be divided into three categories: low frequency, relatively higher frequency, and high frequency.

Concerning low frequency operation, studies show that concrete resistivity is not sensitive enough to frequency ranges below 1000 Hz [118]. Hence, using alternating current is usually preferred over direct current to avoid electrode polarization. In this case, EM techniques that work with direct current, such as Electrical Resistivity Tomography Test (ERT), are suggested in [22, 44, 119]. Capacitive methods are typically used at relatively higher frequency of circuit and use the AC currents to measure the capacitance of the subsurface. Finally, at higher frequency ranges, such as 10-3000 MHz, other EM methods, such as Ground Penetrating Radar (GPR), could be used.

Resistivity method is another EM based technique used for predicting corrosion through evaluation of chloride ion penetration in reinforced concrete. This method operates at low frequencies, as previously stated. The principle of this method is based on the measurement of the electrical resistivity of a material, which is determined by the movement of free charges in response to an electric field. A direct current (DC) with a constant frequency below 1 Hz is applied to a media, and the resistance of the media's material can be obtained through an inverse approach [22]. As demonstrated, an ionic current needs to flow between the anode and cathode regions [120]. The resistivity of the concrete can be calculated by measuring the potential difference between

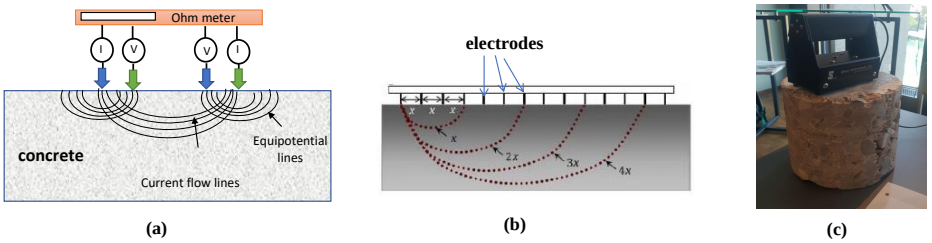

Figure 1.11 – (a) The principle of resistivity technique (reproduced and modified from [121]) (b) penetration depths in function with spacing between electrodes [122] (c) resistivity measurement instrument, on top surface of concrete sample

the two electrodes and the current passing through the concrete, illustrated in Figure 1.11. The resistivity is an indirect indication of active corrosion of the steel reinforcement [123]. The resistivity of concrete is related to its pore structure and composition, and can be influenced by various factors such as moisture content and chloride ion concentration. The lower the resistivity, the higher the chloride ion content in the concrete. Thus, by measuring the resistivity of the concrete, it is possible to indirectly estimate the chloride ion content and evaluate the likelihood of corrosion in the reinforcement [124].

Moreover, this method has capability to determine the aggressive agent's penetration depth. Typically, the resistivity is measured using an array of electrodes that are inserted into the concrete at different depths. The penetration depth is highly dependent on the distance between the surface electrodes and the measurement, according to the quadrupole principle [122]. The resulting resistivity data can be used to create a resistivity profile of the concrete, which provides information on the distribution of chloride ions and other aggressive agents in the material.

The resistivity method is a reliable indicator of the risk in concrete structures, particularly at low levels of resistivity caused by exposure to chloride. It can generate the chloride ion concentration profile, providing a better understanding of the corrosion's extent. The method is relatively simple and low-cost when compared to other techniques like GPR, and it can be used for both laboratory and field measurements.

Despite these advantages, this method's performance is highly dependent on concrete's homogeneity. It means that the results would change with the creation of any crack or embedded damage to concrete, size of aggregates which influence the shape of electrical lines in concrete, shown in Figure 1.11. Moreover, environment variations such as humidity or temperatures could influence the resistivity of concrete and subsequently, the results would be affected, as well [101, 125, 126].

The capacitive method is another EM technique that is usually suggested to use for the applications such as evaluations of concrete's moisture profile, water content, thickness assessment, chloride ingress and *etc.* [24, 83]. The capacitive methods operate on the principle of measuring permittivity variations, which are sensitive to the dielectric permittivity of the media and its

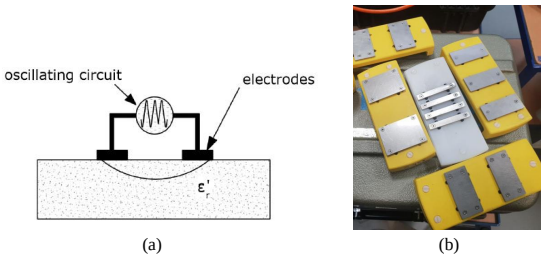

Figure 1.12 – (a) Schematic diagram of the capacitive probes applied on the surface of the material [127] (b) capacitive probes involving different electrode sizes for the University Gustave Eiffel (UGE) system

water/chloride content in the cover concrete [23]. This method operates at a relatively higher frequency of the circuit range compared to the resistivity method, as mentioned earlier. Figure 1.12a shows the schematic of capacitive electrodes and the related oscillating circuit, on the surface of concrete material. In order to measure the permittivity of the medium, they use capacitive probes, involving surface electrodes of different sizes (Figure 1.12b) that would be placed on the surface and allowed to investigate different depths of cover concrete. For each probe, the space between electrodes x, is equal for all. Similar to resistivity measurements in Figure 1.11b, the concrete depth could be determined as a function of spaces between electrodes and also the number of them, on the probe. Any change in the dielectric permittivity of the medium by water/chloride penetration would cause shifting in the resonant frequency, measured by the probe, in the frequency around 33 MHz. Through this data, it will be possible to find the medium's capacitance variation and eventually, the variation of permittivity in function concrete's depth, by precise calibration curve and inversion methods. Finally, the water or chloride ion's profile in concrete vs. depth could be obtained, as indirect ND observable [122].
Figure 1.12b shows capacitive electrode kite that has been designed by the University of Gustave Eiffel (UGE) and suggest in [122, 128], for estimation of gradient permittivity vs. concrete depth by developing an inverse signal processing method. By carrying out a calibration phase on the studied concrete, the relation between permittivity and the water/chloride ion contents, and the permittivity gradient at the depth of penetration would be obtained.
The capacitive method offers an advantage in evaluating the penetration of moisture, water, or aggressive agents in reinforced concrete structures. It provides highly sensitive results that can detect even small changes in the dielectric properties of concrete, making it highly effective for detecting the ingress of aggressive agents. Moreover, it can operate over a wide frequency range, allowing for a more comprehensive analysis of the concrete's electrical properties. Overall, this promising technique provides highly accurate results, is relatively quick and easy to perform, and has the potential to be a valuable tool in the field of non destructive testing.
The capacitive method, however, has some limitations. Firstly, it is unable to differentiate the presence of chloride ions from water on site with high accuracy. Secondly, it requires a flat

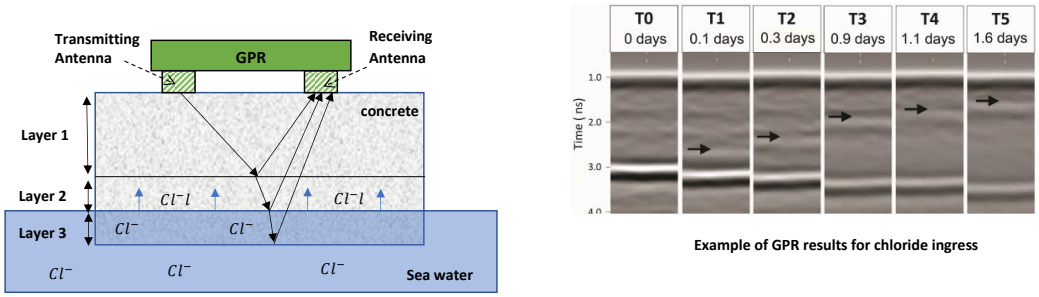

Figure 1.13 – The principle of GPR technique (reproduced and modified from [121]) and the corresponding results that indicate the reflected wave from ingress front in function of imbibition time [23]

concrete surface to ensure proper electrode contact. Finally, the presence of rebar in concrete affects the media's permittivity, making data analysis more challenging due to the conductive properties of rebar.

The GPR principle is based on propagating an electromagnetic wave into the concrete and then recording the strength and time delay of the reflected signal from the various layers within the concrete. By analyzing the reflected signals, information about the condition of the concrete, such as the presence of rebar and cracks, can be obtained. GPR can also provide indirect information on the ingress of moisture, chloride ions, and other aggressive agents.

Since the bulk permittivity of a concrete specimen is highly sensitive to the presence of water and dissolved ions, GPR technique could evaluate the moisture and aggressive agents penetration in the concrete through dielectric permittivity variations of concrete [20, 82]. GPR involves transmitting and receiving antennae, which are dragged along the ground surface. The transmitter antennas propagate EM waves into an RC structure, the corresponding reflected EM wave will be received by the antenna whenever they encounter the interface of two media with differing dielectric constants [129, 130]. Figure 1.13 shows the principle of GPR technique and the associated transmitter and receiver antennas. A GPR antenna receives direct and reflected waves, which are recorded as amplitude–time signals (A-scan) by the system. The propagation of EM waves depends on the corresponding dielectric permittivity of concrete layers, which is a quantity related to the ability of concrete to resist the flow of an electrical charge [82, 130, 131]. The concrete permittivity is dependent on the EM properties, which are also influenced by temperature, moisture content, chloride content, pore structure, and deterioration state of rebar [132]. The advantages of GPR measurement include its ability to provide high-resolution images of the internal structure of the concrete, including the location and depth of chloride ion penetration, without the need for physical access to the structure. GPR can also detect both surface and subsurface features, making it a versatile tool for concrete inspection. Additionally, GPR can inspect a large area pretty quickly, making it a time-efficient and cost-effective method for evaluating the presence of chloride ions in concrete.

However, as previously mentioned, GPR results suffer from drawbacks associated with the high level of uncertainty which can be hugely modified due to environmental variation. Therefore, it is very difficult to interpret quantitatively, the GPR results and distinguish the data. Moreover, the presence of moisture content such as chloride ions would change the GPR waves [133, 134], which modify the amplitude of the wave, as well as the average velocity of the reflected wave [135, 136] during the travel time of the wave [137, 138]. In addition, the GPR method can not determine precisely the aggressive agent types (*e.g.*, distinguish chloride ions among other water content effects) [139].
In the following, magnetic-based methods associated with rebar corrosion assessment would be reviewed.

Magnetic-based methods

The Magnetic-based technique is another NDT inspection method that can be used to assess rebar corrosion. There are various magnetic ND methods available for rebar corrosion inspection, which rely on the principle of magnetic-stress coupling. [140]. They are useful methods and are usually suggested for inspecting the ferromagnetic materials damages like pip lines or metallic ships that are subjected in an aggressive environment of sea [141]. Magnetic based techniques rely on the magnetization of ferromagnetic materials [142, 143]. When an external magnetic field is applied to these materials, they become magnetized and act as a magnet with a north/south pole in the same direction as the external source, due to the magnetic dipolar moments in their atomic structure. Rebar corrosion can result in cracks, cross-sectional loss (Figure 1.14), and pitting corrosion, which can change the magnetic properties of the rebar. By using an external magnetometer, it is possible to detect rebar damage through induced magnetic field quantitative variations. They take benefits from being not affected by environmental factors such as water level, temperature, and soil quality, making them a promising method for rebar inspection, compare to other NDT [140, 141, 144].
Magnetic based methods are divided into active or passive techniques, in terms of external magnetic field source. Concerning the active approaches, they usually need actuators and receivers such as the model illustrated in Figure 1.14. For the passive one, the magnetic field of the earth is used as their external source [145].
The Magnetic Flux Leakage (MFL) is a reputed active method in the application of rebar condition assessment [84]. Figure 1.14 shows the principle of the MFL technique. In this method, the magnetic source is generated by an electro-magnet coil, called a yoke, which is moving along with the rebar's length, illustrated in Figure 1.14a. The basic idea of MFL inspection is that the magnetic field emitted in rebar and would become distorted near the cross-section loss [147] (Figure 1.14b and c). The magnetic field distortion can be significant and detectable when the ferromagnetic materials are locally magnetized to full or near saturation. The amplitude of a flux

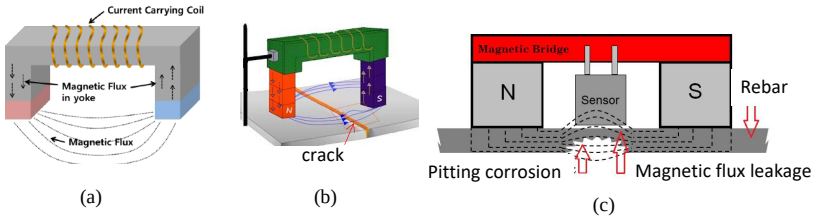

Figure 1.14 – The principle of MFL method (a) electromagnetic coil to produce magnetic field called as yoke [146] (b) schematic of magnetic field use to detect crack (c) schematic of magnetic field use to rebar pitting corrosion
(b): `https://www.marineengineersknowledge.com`
(c): `https://www.onestopndt.com/blogs`

leakage signal is generally proportional to the magnetization level and increases at cross-section losses, as demonstrated in [147, 148]. As mentioned, the magnetic source of the yoke is moved on the around rebar to detect any leakage emerging from cross-sectional loss through the magnetic sensor that is in the middle of the yoke.
The main advantage of MFL is its ability to detect and quantify the depth and extent of corrosion in rebar with high accuracy. It is a fast and non-destructive technique that can be used to scan a large area of concrete in a short amount of time [149, 150].
However, the application of MFL systems is mostly for pre-stressed concrete structures and for monitoring the rebar's state that is located near the surface. Thus, for inaccessible steel reinforcements and operations, non-homogeneous concrete structures are not usually recommended. Moreover, results can be significantly affected by the distance between the magnetic source, magnetic sensor, and rebar [140, 147]. Furthermore, this method focuses solely on detecting corrosion at the rebar level and does not provide any preventive solutions before it occurs.
The Residual Magnetic Field (RMF) is one example of the magnetic based passive method [151, 152]. The principle of RMF in rebar corrosion detection is based on the magnetic properties of ferromagnetic materials. When rebar is subjected to an external magnetic field, it is magnetized and will retain some degree of magnetization even after the external field is removed. This residual magnetization depends on the magnetic permeability of the rebar and its micro structure, and is affected by any changes or defects in the rebar, including corrosion [152]. By measuring the residual magnetic field of the rebar using a magnetic sensor, changes in the magnetic properties due to corrosion can be detected. The method is non destructive and can detect corrosion in the early stages before it becomes visible on the surface of the structure.
The RMF method has several advantages in the application of rebar corrosion detection. Firstly, it does not require physical access to the rebar or any damage to the structure during measurements. This makes it a cost-effective and convenient method for regular inspections of large structures such as bridges and buildings. Another advantage of the RMF method is that it is sensitive to localized corrosion and can detect corrosion at an early stage before it becomes

visible on the surface of the structure. The method can also be used to estimate the extent of corrosion damage by analyzing the strength and distribution of the magnetic field [151].
However, the RMF method also has some limitations. One disadvantage of the RMF method is that it requires the use of highly sensitive and specialized magnetometers to measure the small magnetic fields produced by the residual magnetism in the rebar. This can make the method expensive. Moreover, this method cannot serve as a preventative technique for corrosion as it can only detect the presence of corrosion after it has occurred. Additionally, to detect the rebar corrosion the presence of other sources of magnetic interference in the environment, such as nearby steel structures or electromagnetic perturbation, can complicate the interpretation of the RMF results, which can lead to false positives or false negatives in the detection of rebar corrosion.
In summary, magnetic-based methods have a significant advantage in their insensitivity to non-magnetic environmental factors like soil, water content, moisture level, and concrete mixing. This is due to the fact that these materials are non-magnetic. As a result, the proposed solution in this thesis can take advantage of these benefits.
Thus far, the most reputable ND inspection methods for evaluating the corrosion state of rebar and chloride ion ingress have been studied. However, none of these methods can provide a reliable, low-cost, accurate, insensitive to environmental factors and corrosion-sensitive technique for preventive ND assessment of rebar corrosion. In the following section, the use of NDT monitoring techniques (SHM category) will be reviewed.

1.6.4 Non Destructive Testings (NDT): Structural Health Monitoring (SHM) methods

The second category of NDT methods is SHM. The SHM is the process of collecting, interpreting, and analyzing data from structures in order to determine their health status and the remaining life span [153]. The SHM techniques typically involve monitoring systems that use sensors, interrogators, devices and *etc.* In some techniques, part of this devices can be embedded in the structure or placed near a high-risk area for direct exposure. In such cases, an external interrogator can be used to record the changing in the output signature of the embedded device, which enables the health monitoring to be carried out remotely [154]. Concerning the embedded devices geometry, they must meet particular requirements associated with the mechanical behavior of the concrete structure. Thus, developing SHM system require engineering design step, extensive investigation for the optimized location of embedded devices and their sufficient numbers, maintenance process, data communication between internal and external equipment, and *etc.*. These are the crucial steps that must be considered in order to develop an accurate and reliable SHM system [155, 156, 157].
In order to keep embedded devices working for a long time, one of the primary requirements

is providing a reliable power source and also a communication system between the embedded devices and the external analysis system. Concerning this challenge, SHM devices are divided into two main categories of wired and wireless methods. In the wired system, embedded tools are connected with external devices, through communication wires. Wireless systems would use wireless communication standards to interconnect external and embedded tools. Moreover, Wireless systems are also categorized into battery and battery-less technologies. The last group has become very popular in recent years [158] and the latest remarkable achievements in wireless communications engineering standards. Thus, the SHM embedded devices are capable of being distributed in various locations regardless of using long cables for a power source or connection to the main analysis system to transfer data. Moreover, it is possible to store acquired data in the cloud system through a wireless network in the continuous monitoring [159].
Focusing on rebar corrosion pathology, SHM devices could be embedded close to the reinforcements. It would allow the collection of more accurate information about the rebar corrosion status and continuously monitor the corrosion evolution. Thus, providing a continuous assessment of observables related to concrete health, highlighted SHM methods from the other inspection techniques.
Focusing on evaluation of aggressive agent penetration, the embedded devices could be placed in cover concrete, direct exposure to aggressive agent ingress. As reported in [158], SHM method can be employed as a preventive technique for rebar corrosion by determining the level of aggressive agents. This aspect is the main focus of this research study.
This section will review some of the current SHM methods for evaluating chloride ion penetration. Both wired and wireless methods will be discussed, along with some specific examples of each technique.

Wired system

In the traditional wired SHM for monitoring chloride ion penetration in concrete typically involve embedding wired sensors or electrodes within the concrete structure. These sensors can be designed to measure various parameters, including electrical resistivity and potential, which can be used to infer the chloride ion concentration within the concrete. The data collected from these sensors is typically transfer through cables to a central data acquisition system for storage, processing, and analysis. These wired SHM techniques allow for continuous monitoring of the concrete structure, providing real-time data on the extent and progression of chloride ion penetration.
The Ag/AgCl electrodes is one of the most well-known embedded SHM devices for monitoring chloride ion penetration in concrete, as mentioned in a study by [28]. Due to its high sensitivity to chloride ions, embedding the Ag/AgCl electrode into concrete or cement-based materials as a chloride ion selective electrode (ISE) shows great potential for application in this field [160, 161].

Figure 1.15 illustrates the Ag/AgCl electrode. In this method, the principle is measuring the potential of chloride ions through an ISE electrode (in the schematic of Figure 1.15b, it is a silver electrode). The reference electrode was prepared by electrolysis has a low amount of potential fluctuation rate in chloride solution with concentrations about 0.1 *mol/l* [163]. By increasing the concentration level of chloride ions, the different potential between two electrodes would be changed, depending on the activity of chloride ions that are used as an indicator of chloride level [164]. Through recording the differential potential of two electrodes, it could be possible to determine the critical concentration chloride rate in the concrete using a calibration curve obtained in the laboratory.

The Ag/AgCl electrode is highly sensitive to aggressive agents, which makes it a useful tool for accurate evaluating the their concentration in concrete or cement-based materials. The use of Ag/AgCl electrodes in concrete is a promising application in the field of non destructive testing, as it provides a cost effective and reliable method for evaluating the corrosion risk of rebar.

One disadvantage of Ag/AgCl electrodes in chloride ion evaluation is that they can be affected by the presence of other ions in the concrete, such as sulfates or hydroxides, which may interfere with the accuracy of the measurements. Additionally, the electrodes may corrode over time, requiring replacement or recalibration. Finally, the installation of the electrodes can be challenging and may require specialized equipment and expertise. Therefore, the method cannot provide a punctual assessment [165, 166].

Microwave resonance-based system is another example of wired SHM techniques. It operates on the principle of frequency resonance and is capable of detecting thickness loss caused by chloride ion-induced corrosion rather than directly detecting aggressive agents, as presented in [167]. The device is based on zinc wires of different widths, placed on the ceramic resonator's surface which is a resonator operating at 2.45 GHz. By increasing the chloride level in the materials and passing through their critical value, the zinc wires would be rusted. Consequently, it will result in modification of resonance frequency, measured by an external antenna. According to numerical modeling results in [167], by corrosion evolution on zinc wire, the coefficient transmission of the

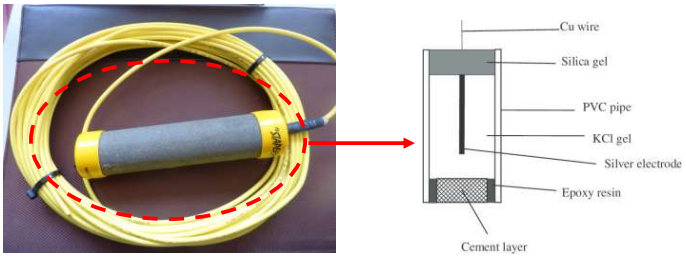

Figure 1.15 – (a) Ag/AgCl electrode device (b) structure of Ag/AgCl reference electrode [162]
Source (a): `https://www.tecnosealindustry.com/products/`

resonator would fall from -8 dB to less than -35 dB, and resonance frequency shift would occur. Eventually, the total breaking of the zinc wires due to corrosion, the operating frequency of the resonator would rise to 2.72 GHz [168] (equal to 275 MHz shift relative to the initial resonator operating at 2.45 GHz). Therefore, resonance frequency variation is introduced as observable to estimate the availability of chloride ions in materials.

This method is quite simple and provide a high sensitivity method for detecting the thickness loss of embedded device in concrete, as result of induced corrosion. It could provide a continuous monitoring of chloride ion ingress, as ND method.

However, the method suffers from all problems concerning the long cables and needs a power source for the EM resonator. Additionally, it may not be effective for detecting chloride ions in the deeper layers of concrete. Finally, it requires specialized equipment and expertise for the installation and interpretation of the results.

Multi Ring Electrode (MRE) sensors are another type of wired sensors that are specialized devices used primarily for monitoring moisture or humidity levels within concrete structures [169]. Their application is particularly important in the field of civil engineering and infrastructure management, where the durability and integrity of concrete are vital. The principle behind MRE sensors is same as resistivity method and lies in their ability to measure electrical resistivity, which is highly sensitive to the moisture content of concrete. As illustrated in Figure 1.16a, these sensors typically consist of multiple concentric rings or electrodes placed at various depths within the concrete (Figure 1.16b). As the humidity within the concrete changes, the electrical resistivity also changes, allowing MRE sensors to provide valuable data on moisture profiles over time. Figure 1.16c shows some embedded MRE devices in concrete. Then, using cables to connect the measuring probes, electrical resistivity changes of concrete, could be evaluated [171]. One of the key advantages of MRE sensors is their ND nature; they can be embedded within concrete at risky zone, making them suitable for long-term monitoring. They provide valuable insights into the moisture conditions of concrete structures and also the chloride ion profile,

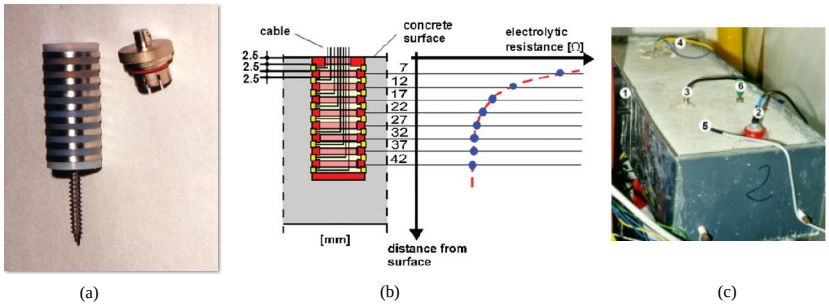

(a) (b) (c)

Figure 1.16 – (a) MRE sesnor [169] (b) MRE as monitoring sensor for the distribution of the water content of the concrete [169] (c) Locations of the 7 embedded MRE Systems on the connected probes to measure the electrical resitivity [170]

helping to assess the risk of corrosion and other deterioration processes. However, MRE sensors also have limitations, including the need for calibration with specific concrete types and environmental factors. Nevertheless, their ability to contribute to the preservation and maintenance of concrete infrastructure makes them indispensable tools in the field of civil engineering.
Furthermore, a diverse array of wired sensors is available for the measurement of moisture content within concrete, and their operational principles align with those based on resistivity or capacitive measurements, as previously elucidated in Section 1.6.3. Additionally, wired devices intended to monitor and measure corrosion rates, such as Reference cells ([172]), GPM-Sensors (Galvanic Pulse Method, explained in [173]), EIS-Sensors (Electrochemical Impedance Spectroscopy, discussed in [174]), operate in similar principles as explained upon earlier. These methods share common limitations, which have been previously outlined and can be explored further in the provided references [175, 176].
In addition, the common issue concerning the wired-based SHM devices is with respect to their installation and also the cables. In some cases, cabled systems show limited flexibility in terms of arrangement and also the geometry of embedded devices. The installation costs become uncritical, compared to operation and maintenance costs [177]. Nevertheless, wired SHM sensing methods are still used. Nevertheless, with advancement of technology in wireless devices, nowadays most infrastructure managers prefer to use wireless devices to save maintenance, installation, energy, and communication costs. In the next section, some advanced wireless techniques would be reviewed.

Wireless devices: battery-powered

The advancement of communication and information technologies has led to the introduction of wireless embedded equipment in SHM systems, eliminating the need for traditional cables, providing faster communication, saving energy, and reducing installation costs. Wireless devices can be categorized as either battery-powered or battery-less. Concerning wireless battery-powered SHM devices for rebar corrosion monitoring, these techniques generally involve corrosion sensors such as embedded corrosion sensors, half-cell corrosion sensors, or linear polarization resistance sensors, which are connected to a wireless transmitter [178]. The sensors monitor the corrosion

Figure 1.17 – A novel wireless data acquisition device with ability to connect through IoT and cloud computing for bridge inspection
Source: `https://www.tfb-diagnostic.ch/`

activity of the rebars, and the data is transmitted wireless to a remote monitoring system. The monitoring system then processes the data and provides information on the corrosion status of the rebars, such as the corrosion rate, corrosion potential, or corrosion risk. The wireless transmission allows for continuous, real-time monitoring of the rebars, enabling early detection of corrosion and preventing the need for costly repairs [179].
Focusing on chloride ion ingress evaluation, the wireless battery powered sensors could be embedded in concrete, exposure to chloride ions flow (at risky area). The sensor node then wirelessly transmits this data to a central data acquisition and management system, where it can be analyzed to determine the level of chloride ion ingress and the corrosion risk to the rebar in the structure [179, 180].
The Ion-Sensitive Field-Effect Transistors (ISFETs) is one example of a general principle for battery-powered wireless SHM devices for chloride ion ingress [181]. ISFETs are sensors that can detect changes in the ion concentration in concrete and convert them into electrical signals. These signals can then be wirelessly transmitted to a data acquisition unit for monitoring and analysis. The sensors can be embedded in the concrete and powered by batteries, eliminating the need for wires and allowing for remote and continuous monitoring of chloride ion ingress.
The advantage of these wireless devices is that they can be easily installed and provide real-time data on the corrosion status of the structure.
The most important issue related to battery-powered sensing devices is the lifetime of the battery. Basically, the replacement of batteries after an amount of time is essential for continuous monitoring. As far as the devices are embedded within concrete, only by destructive techniques such as drilling numerous holes into concrete, it would be possible to replace batteries [182]. Moreover, battery-powered wireless SHM devices typically have a larger geometry than their battery-less counterparts due to the need for additional space for the battery. This increased size can have a significant impact on the mechanical strength of the concrete structure. As a result, this section will only examine the battery-less type of wireless device.

Wireless devices: battery-less

Figure 1.17 illustrates a wireless data acquisition system that utilizes advanced technologies such as IoT and cloud computing for real-time monitoring. Wireless devices provide a low-cost solution for connecting embedded devices to the external monitoring system using wireless communication for data transmission (*e.g.*, antenna) and power supply, eliminating the need for cables. This significant cost reduction enables long-term structural monitoring [183].
RFID (Radio Frequency Identification) technology has become integral in various fields, offering diverse applications ranging from logistics and manufacturing to access control and security. Its growth is attributed to standardized communications, inter-operability (according to the local

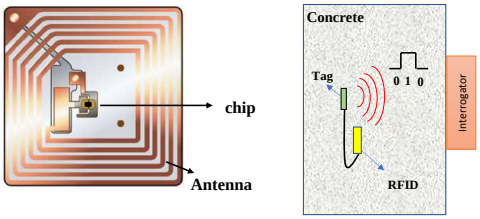

(a) (b)

Figure 1.18 – (a) RFID (b) schematic passive RFID Tag device in concrete Source (a): `http://www.technovelgy.com/ct`
Source (b): `https://www.taiheiyo-cement.co.jp/english`)

regulations either from ESTI in Europe or FCC in US, with well-defined protocols, mainly ISO and EPCglobal), low maintenance, and an almost unlimited operational lifespan [33, 184]. RFID operates on the principle of using readers to interact with "tags", also known as smart labels, attached to objects, animals, or individuals (Figure 1.18a). These tags contain identifiers and information that can be read or written by the reader [31, 32].
RFID tags come in various types, the most common being passive tags. These passive tags are cost-effective and efficient for applications like corrosion monitoring. Focusing on the application of chloride concentration evaluation, RFID devices involve stripped metal wire which can corrode in contact with concrete and chloride ions (Figure 1.18 b). When the corrosion condition reaches a critical stage, such as when the concentration of chloride ions and pH level of the environment pass through a specific threshold value, the metallic wire will be stripped and broken. Finally, the RFID device will emit an identification code to alert about the exceeding of corrosion thresholds [185].
Another category is active RFID tags use an onboard battery for power, enabling them to cover extensive communication distances independently. However, this autonomy comes at the cost of regular maintenance and higher expenses. They shine in scenarios that demand real-time data and long-range connectivity, like large-scale asset management and environmental monitoring.
Nowadays, the chipless RFID tags are represented that stand apart by lacking integrated electronics [186]. They rely on intricate reader signals and the tag's reflective properties. Though they face limitations in terms of range and coding capabilities due to propagation complexities, ongoing research holds potential for their growth. Chipless tags offer the unique advantage of being electronics-free, opening doors to innovative applications in the future.
Additionally, RFID technology is categorized based on the frequency of operation, each with distinct characteristics and applications. These classifications provide valuable insights into their main attributes [33]. They could be:

— LF (Low Frequency): Operating in the range of 125 kHz to 134.2 kHz, LF RFID tags have a maximum detection range of approximately 50 cm. They are known for their

reliability but come at a relatively higher cost, even in large volumes. LF tags are ideal for applications requiring close-range, contact-based reading, and are often used for access control and electronic passports. NFC (Near Field Communication) is a subset of LF RFID,

— HF (High Frequency): HF operates at 13.56 MHz, offering a maximum detection range of about 1 meter. These tags are more cost-effective than LF tags and are suitable for applications requiring proximity reading without a large number of tags. Access control and electronic passports also fall under this category,

— UHF (Ultra-High Frequency): With frequencies ranging from 864 to 928 MHz, UHF RFID tags have a detection range of 3 to 20 meters, depending on propagation conditions. They are cost-effective in large volumes and excel in applications requiring long-range and rapid reading of numerous tags. UHF tags are commonly used in logistics, item identification, traceability, and toll systems,

— SHF (Super-High Frequency): SHF RFID tags operate within the 2.45 to 5.8 GHz range, enabling detection at distances of about 100 meters. They offer performance similar to UHF but are highly sensitive to metal and liquid environments. SHF systems are notable for their directional tag detection. These frequency bands are globally unlicensed, allowing their use worldwide, but they can be susceptible to interference from devices like cordless phones and microwave ovens.

Ongoing research and development in chipless RFID technology, especially for applications like remote corrosion risk identification in reinforced concrete structures. Since, the chipless tags offer the advantage of being completely passive and devoid of electronics, making them cost-effective and ideal for real-time, non-destructive, and long-term monitoring of chloride ingress in hard-to-reach areas. Their small size allows for extensive deployment in high-risk zones within structures, opening up new possibilities for effective monitoring and maintenance.

In general, a great deal of work is currently being carried out on this technology, which has the immense advantage of using tags in various applications. There is no doubt that this technology will find its own applications in the near future [33].

1.6.5 Summary of ND method and the remain problems

Table 1.3 provides a summary of the discussed NDT techniques, including their principles, advantages, and disadvantages for both inspection and SHM methods. These techniques are associated with the evaluation of rebar corrosion pathology.

Here, various inspection methods for rebar corrosion evaluation, including visual inspection, electrochemical, mechanical wave, electromagnetic, and magnetic-based techniques, with examples, advantages, and disadvantages provided for each subcategory, have been discussed and compared. In general, while these methods are helpful in evaluating the condition of rebar cor-

rosion and providing early-stage detection solutions, their results are subject to uncertainty due to their high sensitivity to variations in environmental factors and require calibration. Electromagnetic methods, such as capacitive, resistive, and ground-penetrating radar (GPR), can be used to evaluate the presence and extent of chloride ions in concrete. However, the accuracy of these methods is often affected by various environmental factors, and they may not be able to distinguish chloride ions from other aggressive agents. Therefore, their results should be carefully interpreted and validated. In addition, none of these methods can propose a preventive solution to rebar corrosion pathology.

The second subcategory of NDT methods, namely SHM techniques, has been presented as a continuous monitoring solution for rebar corrosion assessment and chloride ion evaluation. SHM systems use integrated devices within the structure to monitor exposure to corrosion pathology. Two main families of SHM systems have been discussed: wired and wireless techniques, with examples of each provided. These techniques provide reliable real-time and continuous monitoring of rebar corrosion and chloride ion levels in concrete. However, wired systems can have issues with external power supply and the use of long cables in structures. Wireless SHM systems solve this problem by using wireless technology for data transfer, but there are still issues related to data transfer interference or geometry and maintenance of embedded devices that need to destruct the concrete.

In addition, further research is needed to address these challenges and develop effective and reliable corrosion monitoring solutions that are less sensitive to environmental factors, cost-effective, and accurate. Such solutions should be able to estimate the probability of rebar corrosion before it emerges, which can save maintenance costs and reduce the risk of structure collapse.

Table 1.3 – Summary of ND techniques

Inspection methods			
1-Visual inspection			
Methods name	Principle	Advantages	Disadvantages
Visual (or periodical) inspection	Identifying any visual signs of RC corrosion like rusting trace in periodical inspecting	Relatively low-cost simple and fast	Incapable to identify the corrosion rate active or passive or extend of corrosion Need experience inspector complementary inspection NDT techniques
2-Mechanical wave propagation			
Ultrasonic Pulse Velocity (UPV)	Measuring the variations of amplitude of electrical energy that is converted from stress wave by propagation of UPV mechanical wave Mostly use for characterization of concrete's mechanical damage like crack's size and shape	Quick, portable, large penetration depth, It is easy to use for estimating the size shape and nature of the concrete damage.	Results are very sensitive to method of data collecting Require high analysis techniques to interpret data
Impact Echo (IE)	measuring the wave velocity as indicator of corrosion Based on the analysis from reflection and impact-generated stress wave, propagated in concrete	Able to detect micro-cracks caused by corrosion	The reliability of the IE method decreases with an increase in thickness. Less suggests for corrosion monitoring in comparison to electrochemical methods
3-Electrochemical methods			

Table 1.3 continued from previous page

Methods name	Principle	Advantages	Disadvantages
Open Circuit Potential (OPC)	Measuring the potential level between rebar and reference electrode that is in contact to surface Mostly use in measuring corrosion probability	Simple, portable Only use single value of electrical potential (mv) as corrosion indicator	The results are effected by: wet/dry condition of concrete -level of moisture -level of chloride ions -etc. Time consuming
Linear Polarization Resistance (LPR)	Polarization of rebar through electrical current and monitor polarization effect on potential variation Mostly use to measure corrosion rate	Rapid Useful for uniform corrosion Less perturbation by applied noise	Results are sensitive to: -Distance between rebar and reference electrode -Temperature -Non-Homogeneous concrete
4-Magnetic based methods			
Residual Magnetic Field (RMF)	Detects rebar corrosion by measuring the residual magnetic field using a sensor to find variation in magnetic property of rebar	Can detect corrosion in early stages Sensitive to localized corrosion Able to estimate extent of corrosion damage Don't require physical access to the rebar Not sensitive to environmental factors variations	Need expensive magnetometers Magnetic interference can lead to incorrect results

Table 1.3 continued from previous page

Methods name	Principle	Advantages	Disadvantages
Magnetic Flux Leakage (MFL)	Detect rebars defects by piezomagnetic effect recording through magnetic flux density variation by external interrogator	Quite useful to detect pitting corrosion Insensitive to concrete media or environment variations as non-magnetic materials	Results can be significantly affected by the distance between the interrogator and rebar Difficult to carry out test due to coupling effect by other rebars
5-Electromagnetic (EM)			
Resistivity method	Measuring the resistivity variations of concrete as indicator of chloride ions Operating at very low frequency	Fast, cost effective Useful for regular monitoring	Results highly dependent on concrete's homogeneity or any damage or rebar cracks
Capacitive method	Measuring the capacity variations of concrete based on resonance frequency Evaluate the chloride ions or water content penetration depth Operating at low frequency (more than resistivity)	Low frequencies sensitive to chlorides Estimate the gradient of penetrations	Calibration required Decorrelation between aggressive agents and water or chloride is very difficult Sensitive to reinforcements useful in flat concrete surface

Table 1.3 continued from previous page

Methods name	Principle	Advantages	Disadvantages
Ground penetrating radar (GPR)	Transceiver of EM wave (frequency range 0.5 to 2GHz) through the concrete Durability indicator would be the difference of reflection caused by permittivity variations Mostly suggests for locate rebars, concrete voids or pavement inspection	Portable equipment Can be use to detect chloride and aggressive agents penetration	Complex results, Difficult to interpretations, results Can not distinguish between the source of variation and unable to diagnose pathology
Structural Health Monitoring (SHM) methods			
Wired devices			
Ag/AgCl electrodes	Embedded electrodes in concrete, measures chloride ion potential and determines chloride levels through differential potential	Highly sensitive to aggressive agents Cost-effective and reliable	Inaccuracy due to interference from other ions Require replacement of electrode or recalibration Difficult installation Needs long cable
Multi Ring Electrode (MRE)	Measuring the resistivity variations of concrete same principle as resistivity methods	Useful for long term ND monitoring Useful method for detect moisture penetration depth	The results are sensitive to temperature variations Need calibration

Table 1.3 continued from previous page

Methods name	Principle	Advantages	Disadvantages
Microwave resonance-based	Applies resonance frequency shift to detect chloride ions by placing zinc wires of different widths on a ceramic resonator's surface	Quite simple and sensitive Cost-effective Preventive method for rebar corrosion	The Requires long cables, reliable power source, specialized expertise Difficult for monitoring deeper concrete layer
Wireless devices			
Battery-power	-Example: Ion-Sensitive Field-Effect Transistors (ISFETs) -Principle: can detect changes in the ion concentration and convert them into electrical signals	Using wireless devices Fast data communication Easily installation (no cable) Provide real-time monitoring and preventive method.	Battery life limitation Difficult to replace the battery Device geometry limitation due to battery size
Battery-less	-Example: RFID family -Principle: electronic device operating at radio frequency/magnetic field for communication Involves a stripped metal wire can breaks when chloride concentration exceeds a certain threshold level and sending an RFID alarm	Provide remote continues monitoring of aggressive agents ingress without cable Low-cots SHM method Small geometry easy for extensive distribution in high-risk zones	Need to be more studied in future

1.7 Orientation of the thesis

As previously mentioned, there is still a need to develop methods that are reliable, low-power, autonomous, robust, and cost-effective for real-time and continuous monitoring to detect rebar corrosion before it emerges as preventive method. Since, the SHM methods are designed for long-term monitoring, a solution from this subcategory could useful to be proposed. Additionally, a magnetic-based method may be a favorable option regarding its significant advantage of insensitivity to non-magnetic materials such as concrete, water level, moisture content, *etc.*
As part of the ANR LabCom OHMIGOD project, this thesis aims to propose a magnetic based SHM solution as preventive methods to evaluate the availability of corrosive agents in cover concrete. To develop and investigate the feasibility of the proposed SHM device, a combination of numerical and experimental studies must be conducted to create a physical model, associated with the performance of this technological solution. Moreover, we would represent a proposed forward method,including an analytical model, to provide a physical explanation associated with the novel technological solution functionality. The orientation of this study will be outlined in the following sections.

1.7.1 Hypothesis

In the context of SHM techniques, we propose a technological solution in the form of a novel magnetic SHM device referred to as "Functional Magnetic Materials" or FMM. Figure 1.19 illustrates the principle of this device, which consists of two parts: the permanent and the reactive part, and can be embedded in cover concrete, exposed to aggressive agent ingress front. The permanent component of the FMM device is constructed from intrinsic magnetic materials, specifically rare earth magnets, and is protected from corrosive agents through the use of a

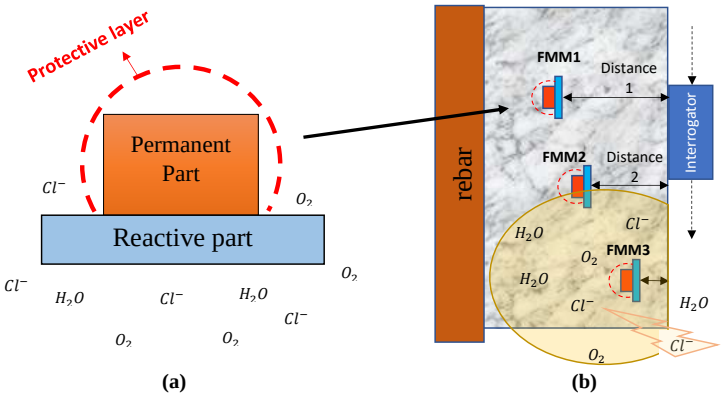

Figure 1.19 – Principe of method (a) Functional Magnetic Material (FMM) schematic (b) Embedding number of FMM devices in function of distance between to the surface of cover concrete, expose to aggressive agents penetration

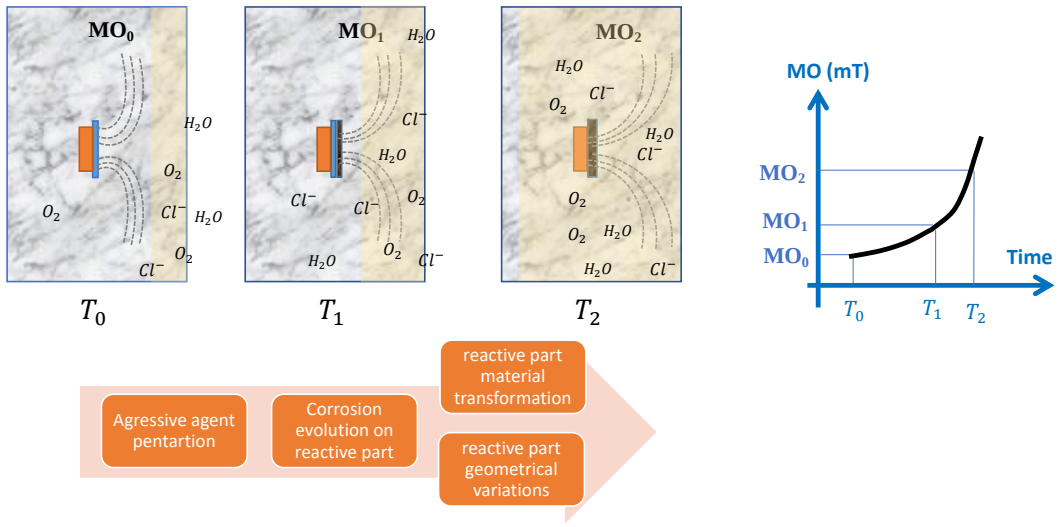

Figure 1.20 – Block diagram of MO variation with evolution of corrosion on FMM reactive part

coating. The reactive part, is composed of ferromagnetic materials, including pure iron. This particular type of iron is highly sensitive to corrosive agents and is prone to rusting quickly in aggressive environments. Since both the permanent and reactive parts contain magnetic and ferromagnetic materials, the FMM generates a magnetic flux density, referred as MO or Magnetic Observable (MO) that can be remotely measured using an external interrogator. The FMM device can be embedded in the cover concrete, situated between the primary rebar and surface, with the reactive portion being exposed to corrosion over time.

The hypothesis is that the evolution of corrosion on the reactive part may result in significant variations in the materials and geometrical properties. Therefore, the overall generated MO from the FMM device would change as the corrosion progresses. By using an external interrogator and punctual monitoring, it is possible to correlate the range of MO variation with the availability of aggressive agents in the medium and eventually assess the risk of rebar corrosion as a preventive ND method. Figure 1.20 illustrates a diagram of MO variations associated with corrosion evolution on the reactive part.

The advantages of this technique are that, firstly, the novel SHM method proposes an autonomous, low-cost, battery-less, and simple solution, which provides an environment-friendly monitoring technique. Secondly, the generated MO is not sensitive to environmental property variations such as concrete media properties or moisture level. Finally, it could provide real-time and continuous monitoring to regularly evaluate the aggressive agent front presence during the time. Thus, the device could act as an alert of rebar corrosion before it occurs.

In the next part, the important question related to the FMM performance and the thesis objective will be presented.

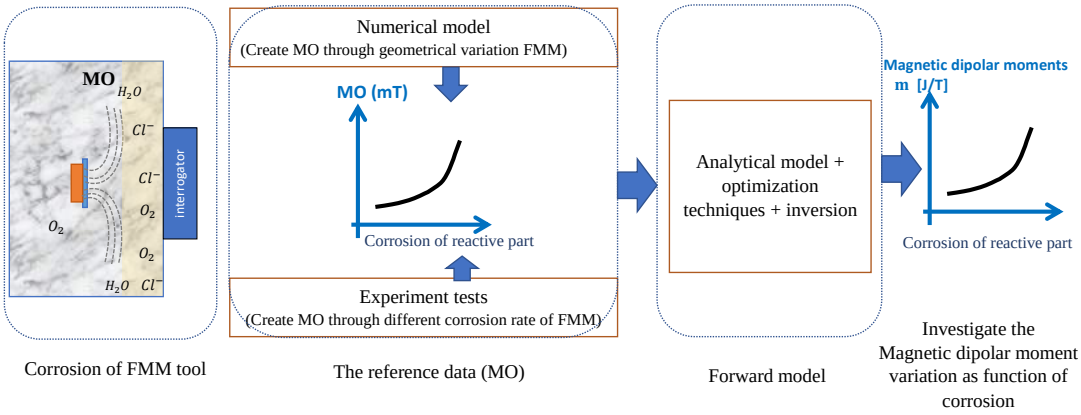

Figure 1.21 – Block diagram forward method to estimate the magnetic dipolar variation, as a function of corrosion on reactive part of FMM

1.7.2 Objectives

This research focuses on employing FMM, which by their self-corrosion due to exposure to aggressive agents front in concrete, could estimate the risk of rebar corrosion in RC structures. The study has two primary objectives: the characterization of the FMM device and the evaluation of its associated forward model.

Firstly, regarding the FMM, the research aims to evaluate key parameters, including FMM's geometry and materials, using numerical modeling via Ansys Maxwell software. Specific objectives include finding an optimal geometry that compromise the detachable MO variation range with concrete mechanical properties, determining efficient device placement to minimize coupling effects and interference with rebar, and assessing the sensitivity and effectiveness of the FMM device in monitoring corrosion-induced MO variations.

Secondly, the study concentrates on the feasibility of a proposed forward model and inversion method. This forward model establishes a relationship between MO variations generated by FMM devices and changes in the magnetic properties of FMM's reactive part, particularly the magnetic dipolar moments induced by aggressive agents. This approach ensures that observed changes are solely attributed to reactive part degradation due to corrosion, enhancing result reliability and validity.

As The block diagram illustrated in Figure 1.21, represents using the optimization technique and inversion method to estimate the extent of variation in the magnetic dipolar moment, providing valuable insights into the corrosion state of the reactive part. Consequently, this method facilitates the ND estimation of the corrosion level within the embedded device, using the unique magnetic dipolar moment.

Subsequently, the objectives related to the forward model and inversion method include identifying an appropriate analytical model and optimization algorithm, assessing the method's

accuracy in estimating magnetic dipolar moment vector variations in FMM, determining the required number of vectors to represent the FMM, evaluating its effectiveness in predicting magnetic dipolar moment tendencies concerning reactive part degradation, and validating results through numerical simulations and experiments.
The successful accomplishment of these objectives, associated with the FMM device's effectiveness in concrete, can validate the proposed forward and inversion method and highlight its significant implications for NDT techniques and structural maintenance. Hereinafter, the proposed method's results could potentially offer valuable insights into concrete contamination levels and consequently, rebar corrosion risk assessment. This information empowers engineers and maintenance professionals to make informed decisions on repairs, rehabilitation, or rebar replacement, potentially saving costs. Thus, the proposed method enhances NDT practices by providing a fast, reliable, simple, and cost-effective preventive solution for rebar corrosion.

1.7.3 Methodology

In order to achieve the mentioned objectives, a suitable methodology must be established for each objective. The first step is to study the physics of magnetic and ferromagnetic materials, as well as propose an engineering design and evaluate the device's performance, in Chapter 2. A parametric study using numerical modeling of the device is conducted to investigate the role of the reactive part in MO generation. Additionally, a materials study with numerical modeling is carried out to select the most effective material for the reactive part. This chapter also examines the impact of corrosion products on MO variations through numerical modeling. A separate experimental study is conducted to characterize the corrosion products of the reactive parts. The corrosion products are collected by performing an accelerating corrosion test in NaCl saline solution (30 g/L concentration of chloride), followed by specific laboratory techniques such as washing, filtering, and drying. The corrosion products are characterized using the XRD diffraction technique, and the relative permeability of the corrosion products is obtained using the reflection/transmission method. In Chapter 2, MO tendency is also investigated through various numerical modelings and corrosion products layers.
Subsequently, to find the effective geometry of the reactive part, in terms of MO variation range and tendency, associated with the device performance as well as an optimal location in concrete, a parametric study with a numerical model is represented in Chapter 3. Moreover, in this chapter, the coupling effect among FMMs (in the application of multi-devices arrays in concrete) and also the border effect to rebar, has been investigated.
To achieve the primary step, a series of numerical models for FMM were developed using Ansys Maxwell software as a reference model. A parametric study was conducted on the reactive part's geometry (surface and thickness) as well as the relative distance to the external interrogator to obtain MO variations. In this regard, a variety of FMM devices with different geometrical prop-

erties served as reference data. Secondly, using an analytical model, optimization, and inversion method, the magnetic dipolar moment variations as a function of the reduction in reactive part geometry were obtained, separately for each reference model. Consequently, the estimated magnetic dipolar moment variation curves for each FMM reference model were drawn to ensure the method's repeatability and eventually, validate the hypothesis. Further details on the analytical model, optimization techniques, and inversion method can be found in Chapter 4.
Chapter 5 presents the results of an experimental campaign carried out to validate the analytical model. The MO, generated by FMM would be evaluated in terms of its sensitivity to different concrete media characteristics, including different mixing, thickness and hyric state. The experimental campaign is performed at Cerema of Angers, where a series of tests are conducted on various concrete samples. These samples differed in concrete geometry (thickness of 30, 40, and 50 cm), concrete mixing (W/C = 0.38, 0.50, 0.78), and different concrete hydric states (dried, saturated with normal water, saturated with saline solutions of 30 g/L and 120 g/L). Additionally, the reactive part's thickness are varied (1 mm, 0.5 mm, 0.2 mm, and 0.1 mm) to investigate MO variations. The reactive parts are also subjected to different degree of corrosion, with percentages of 10%, 20%, 30%, 40%, and 50%, and the variation of MO as a function of corrosion degree was experimentally assessed. The results could validate the main method's advantage that the MO of FMM is independent of environmental variations. Finally, the proposed method would be evaluated, using experimental MO changing as reference model. Then, using the analytical model and inversion, the magnetic dipolar moments variations and range would be estimated as function of reactive part's different corrosion degrees. These results would be compared with the same results in Chapter 4, related to estimation of magnetic dipolar moments variations as function of degradation. Thus, the sustainability of result and reliability of proposed method could be justified at the end.

1.8 Conclusion

Chapter 1 provides an overview of RC concrete structure, including the concrete properties of its components as well as the durability in different environments. The focus then shifts to rebar corrosion, the main factor affecting the service life of civil engineering structures in marine environments. The mechanism of rebar corrosion is discussed, including the role of chloride ion penetration in the process. To improve maintenance planning and increase the lifespan of structures, it is important to have reliable methods for detecting and evaluating chloride ion ingress. A variety of the existing DT and NDT have been discussed through their advantages and limitations. As mentioned, there is still a lack of reliable, simple, autonomous, robust, and cost-effective monitoring techniques that could evaluate the aggressive agent of cover concrete which their results also less perturbed environment factor changing and could be used as a

preventive method of rebar corrosion.
In this context and under the French ANR project LabCom OHMIGOD framework, a novel embedded SHM device referred as the FMM, to monitor and evaluate the availability of chloride ion ingress front in the cover concrete has been proposed. This embedded device comprises two parts: a reactive part exposed to media, and a permanent part that would be intact from the environment. Due to using magnetic and ferromagnetic materials in both parts, it generates a magnetic field as Magnetic Observable (MO) to monitor. By corrosion evolution on the reactive part, magnetic properties would be influenced and lead to MO modifications, as well. Using an external interrogator, MO variation range allows to determine pathogens availability and subsequently evaluate the corrosion risk of RC structures. The advantages of this device are that the MO is independent of environmental elements variations and the embedded FMM is cheap and doesn't need a power supply, thus, it can be proposed for long-term monitoring in concrete structures.
Finally the thesis orientation has been discussed. Based on the proposal technological solution, a novel forward method based on functionality of FMM to generate MO variations as function of reactive part's degradation, would be represented. Thereby, the proposed method could be used as preventive technique to evaluate the amount of corrosion in embedded FMM device, cause by aggressive agents and eventually, estimate the risk of rebar corrosion. As explained, choosing the magnetic dipolar moment variations of ferromagnetic materials is due to the fact that they can provide quantitative representation about the magnetic property variation of magnetized reactive part, due to corrosion by aggressive agents. To assess the method, the methodology is firstly, using the numerical model of the FMM device as a reference model for proposed method. This numerical model enabled the generation of MO variations as function of the reactive part's geometrical changes. Secondly, experimental tests is conducted to validate the MO variations resulting from different corrosion states of the FMM device, in real case. Thus, the proposed method could estimate the tendency and variation range of magnetic dipolar moments, through both numerical model and experimental tests and the results could be justified. By combining numerical simulations and experimental validation, the method offers a robust approach for both corrosion detection and early warning of potential structural risks.

Chapter 2

Physics of magnetism and influence of corrosion

2.1 Introduction

As mentioned in Chapter 1, this research study proposes FMM device, as magnetic-based technological solution for SHM of RC structures which could be used as a preventive rebar corrosion method. In this chapter, firstly, the governing principles of magnetism, particularly the Biot-Savart law, emphasizing the magnetic dipolar moment's significance in the device's functionality, will be reviewed.
Next, the various materials, suitable for different parts of the FMM device, with a focus on ferromagnetic materials for the reactive part will be discussed. Moreover, the objective is to investigate how those ferromagnetic materials can redirect and attenuate magnetic flux induced by the permanent part, considering factors like material properties, geometry changes, and corrosion-induced shielding effects, all examined through numerical modeling.
Lastly, through some parametric studies, approximate MO variations and tendencies resulting from reactive part thickness changes and corrosion product evolution will be investigated. For this purpose, an experimental study characterizes corrosion products, in terms of their magnetic properties, providing realistic data for numerical modeling of corrosion evolution. The data, including material types in corrosion products and relative permeability assessments, informs our investigation into MO variations and tendencies as corrosion products grow on the reactive part, assessing feasibility.
Furthermore, these numerical models will help establish a preliminary understanding of the MO tendencies and an approximate range associated with the FMM device's performance in this chapter.

2.2 Maxwell equations

The equations governing the rules for the magnetic and electrical fields are the Maxwell's equations, as stated in [187]:

$$\nabla \cdot \mathbf{E}(\mathbf{r}, t) = \frac{\rho(\mathbf{r}, t)}{\epsilon_0} \tag{2.1}$$

$$\nabla \cdot \mathbf{B}(\mathbf{r}, t) = 0 \tag{2.2}$$

$$\nabla \times \mathbf{E}(\mathbf{r}, t) = -\frac{\partial \mathbf{B}(\mathbf{r}, t)}{\partial t} \tag{2.3}$$

$$\nabla \times \mathbf{B}(\mathbf{r}, t) = \frac{1}{\epsilon_0 c^2}\mathbf{J}(\mathbf{r}, t) + \frac{1}{c^2}\frac{\partial \mathbf{E}}{\partial t}(\mathbf{r}, t) \tag{2.4}$$

Table 2.1 summarizes the meaning of each symbol and the **SI** units of measurement. The Eq. 2.1 is referred as Gauss's law. Here, $\rho(\mathbf{r}, t)$ and ϵ_0 are the total charge divided by volume and the permittivity of free space, respectively. The divergence operator $\nabla\cdot$ operates on the electrical field vector $\mathbf{E}(\mathbf{r}, t)$, and this equation explains that the total outward flux of the electrical field over any closed surface in free space is equal to the total charge enclosed in the surface, divided by ϵ_0[187]. Similarly, the Eq. 2.2, referred as Gauss's law but in the magnetic domains, states that no monopole exists. Subsequently, the Eq. 2.3 is referred as the Maxwell-Faraday expression, and it implies that a time-varying magnetic field would result in an electric field in a closed loop. In this equation, $\nabla\times$ is a curl operator. Finally, the Eq. 2.4 is referred as the Ampere-Maxwell expression, and it states the relation between the electric current density $\mathbf{J}(\mathbf{r}, t)$, the time-varying electrical field $\mathbf{E}(\mathbf{r}, t)$, and the induced magnetic flux density of $\mathbf{B}(\mathbf{r}, t)$. Here, c is the velocity of wave propagation (speed of light) in free space. This value is calculated through $\frac{1}{\sqrt{\epsilon_0\mu_0}} \cong 3 \times 10^8$ [m/s]. There, μ_0 is also the permeability of free space, which equals $\mu_0 = 4\pi \times 10^{-7}$. The Eq. 2.3 and Eq. 2.4 are the EM constitutive equations, which establish the basis of the wave theory. In fact, the main focus is on the magnetic field measurements. In the stationary case, the terms $-\frac{\partial \mathbf{E}(\mathbf{r},t)}{\partial t}$ and $-\frac{\partial \mathbf{B}(\mathbf{r},t)}{\partial t}$ can be ignored. Then, the magnetic field will be governed by the magnetostatic equations.

$$\nabla \cdot \mathbf{B}(\mathbf{r}, t) = 0 \tag{2.5}$$

Table 2.1 – Definitions and units

Symbol	Meaning	**SI**
$\mathbf{B}(\mathbf{r}, t)$	Magnetic flux density	Tesla [T]
$\mathbf{E}(\mathbf{r}, t)$	Electrical Field	Volt per meter [V/m]
$\rho(\mathbf{r}, t)$	Charge density	Coulombs per cubic meter $[C/m^3]$
$\mathbf{J}(\mathbf{r}, t)$	Current density	Amperes per square meter $[A/m^2]$
ϵ_0	Permittivity of free space	Farads per meter [F/m]
μ_0	Permeability of free space	Henries per meter [H/m]

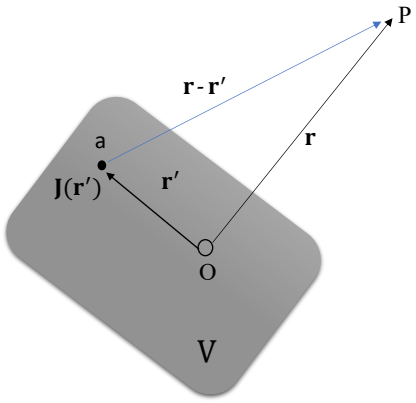

Figure 2.1 – Magnetic induction at point of P, induced by an electrical charge from localized current density $\mathbf{J}(\mathbf{r}')$, displacing from point O to the point a in a chosen mass with total volume of V

$$\nabla \times \mathbf{B}(\mathbf{r}, t) = \mu_0 \mathbf{J}(\mathbf{r}, t) \tag{2.6}$$

The source of magnetic field in Eq. 2.6 is the current density $\mathbf{J}(\mathbf{r}, t)$, which generates isotropic linear magnetic fields in free space. If the current density is time-dependent (magnetic flux density does not vary in time), the static assumption is no longer valid, and the complete Maxwell equations must be used. However, if the changes are small enough, a quasi-static approximation can be made, where the magnetostatic Eqs.2.5 and 2.6 still apply [188]. In the quasi-static approximation, Eq. 2.6 shows that a change in current density $\mathbf{J}(\mathbf{r})$ results in a magnetic field $\mathbf{B}(\mathbf{r})$, with infinite propagation velocity. This approximation is valid if the propagation delay is negligible compared to the time interval in which the currents undergo significant changes. In the following, we will calculate the induced magnetic field $\mathbf{B}(\mathbf{r})$ caused by localized current density $\mathbf{J}(\mathbf{r})$ in the static or quasi-static approximation case.

To calculate the induced $\mathbf{B}(\mathbf{r})$, it could be assumed that a current charged particle is confined within a specific region without any addition or removal of charge, as shown in Figure 2.1, the particle moves from the origin O to point a along the direction of travel vector $\mathbf{r}'$, inducing a magnetic field $\mathbf{B}(\mathbf{r})$ outside the region at point P as a function of distance $\mathbf{r}$, based on Eq. 2.6[189]. The divergence of $\mathbf{B}(\mathbf{r})$ is zero, as per Eq. 2.5, which implies that the magnetic field can also be expressed in terms of another vector field, such as the magnetic potential vector $\mathbf{A}(\mathbf{r})$. The curl of $\mathbf{A}(\mathbf{r})$ can result in $\mathbf{B}(\mathbf{r})$, given by:

$$\mathbf{B} = \nabla \times \mathbf{A}(\mathbf{r}) \tag{2.7}$$

Replacing the Eq. 2.7 with the Eq. 2.6, it gives:

$$\nabla \times (\nabla \times \mathbf{A}(\mathbf{r})) = \mu_0 \mathbf{J}(\mathbf{r}') \tag{2.8}$$

$$\nabla(\nabla \cdot \mathbf{A}(\mathbf{r})) - \nabla^2 \mathbf{A}(\mathbf{r}) = \mu_0 \mathbf{J}(\mathbf{r}') \tag{2.9}$$

To simplify, let us assume $\nabla \cdot \mathbf{A}(\mathbf{r})$=0, then the Eq. 2.9 would become:

$$\nabla^2 \mathbf{A}(\mathbf{r}) = -\mu_0 \mathbf{J}(\mathbf{r}') \tag{2.10}$$

The Laplacian operator of ∇^2, operates on the vector potential of $\mathbf{A}(\mathbf{r})$. A possible solution for the differential Eq. 2.10, is the Poisson equation that would be expressed as:

$$\mathbf{A}(\mathbf{r}) = \frac{\mu_0}{4\pi} \int_{\mathrm{V}} \frac{\mathbf{J}(\mathbf{r}')}{|\mathbf{r} - \mathbf{r}'|} dv' \tag{2.11}$$

The vector potential would be calculated through volume integral. Here, dv' is a differential volume element from selected mass of V, indicated in Figure 2.1. In the Eq. 2.7 the magnetic flux density $\mathbf{B}(\mathbf{r})$, can be obtained from curl of $\mathbf{A}(\mathbf{r})$. Thereby, $\mathbf{B}(\mathbf{r})$ would be expressed as:

$$\mathbf{B}(\mathbf{r}) = \nabla \times \frac{\mu_0}{4\pi} \int_{\mathrm{V}} \frac{\mathbf{J}(\mathbf{r}')}{|\mathbf{r} - \mathbf{r}'|} dv' \tag{2.12}$$

The volume integral is over primed coordinates (*i.e.*, $\mathbf{r}'$) and here, the curl operator derivations are over unprimed coordinates (*i.e.*, $\mathbf{r}$). Thereby, the curl operator can move into the integral and the Eq. 2.12 would be modified as:

$$\mathbf{B}(\mathbf{r}) = \frac{\mu_0}{4\pi} \int_{\mathrm{V}} \nabla \times \frac{\mathbf{J}(\mathbf{r}')}{|\mathbf{r} - \mathbf{r}'|} dv' \tag{2.13}$$

By using the vector identity rules, the curl of vector field $\mathbf{G}(\mathbf{r})f(\mathbf{r})$, where $\mathbf{G}(\mathbf{r})$ is a vector field and $f(\mathbf{r})$ is scalar field, can be expressed by:

$$\nabla \times (f(\mathbf{r})\mathbf{G}(\mathbf{r})) = f(\mathbf{r})\nabla \times \mathbf{G}(\mathbf{r}) + (\nabla f(\mathbf{r})) \otimes \mathbf{G}(\mathbf{r})) \tag{2.14}$$

$\otimes$ is the cross (vector product). Providing that the $\mathbf{G}(\mathbf{r}) = \mathbf{J}(\mathbf{r}')$ and $f(\mathbf{r}) = \frac{1}{|\mathbf{r}-\mathbf{r}'|}$, therefore, the curl operator in the Eq. 2.13 would be:

$$\nabla \times \left(\frac{\mathbf{J}(\mathbf{r}')}{|\mathbf{r} - \mathbf{r}'|} \right) = \frac{1}{|\mathbf{r} - \mathbf{r}'|} \nabla \times \mathbf{J}(\mathbf{r}') - \mathbf{J}(\mathbf{r}') \otimes \nabla \left(\frac{1}{|\mathbf{r} - \mathbf{r}'|} \right) \tag{2.15}$$

Knowing that the curl operator operates in unprimed coordinates, thereby, in the first term of the Eq. 2.15, $\nabla \times \mathbf{J}(\mathbf{r}') = 0$. Similarly, for the second term in primed coordinate system, we would have $\nabla \left(\frac{1}{|\mathbf{r}-\mathbf{r}'|} \right) = -\frac{(\mathbf{r}-\mathbf{r}')}{|\mathbf{r}-\mathbf{r}'|^3}$. Hence, the Eq. 2.15 becomes:

$$\nabla \times \left(\frac{\mathbf{J}(\mathbf{r}')}{|\mathbf{r}-\mathbf{r}'|} \right) = \frac{\mathbf{J}(\mathbf{r}') \otimes (\mathbf{r}-\mathbf{r}')}{|\mathbf{r}-\mathbf{r}'|^3} \tag{2.16}$$

Eventually, $\mathbf{B}(\mathbf{r})$ would be stated as:

$$\mathbf{B}(\mathbf{r}) = \frac{\mu_0}{4\pi} \int_{\mathrm{V}} \frac{\mathbf{J}(\mathbf{r}') \otimes (\mathbf{r}-\mathbf{r}')}{|\mathbf{r}-\mathbf{r}'|^3} dv' \tag{2.17}$$

The Eq. 2.17 is known as the **Biot-Savart law.**
In the next section, another representation of Biot-Savart equation, based on the magnetic dipolar moments would be represented.

2.3 Magnetic dipolar moment

In the previous section, we introduced the Biot-Savart law, which describes the magnetic field produced by a moving charge particle within a specific volume. This section will explore the different representations of the Biot-Savart law, using magnetic dipolar moments, which are important for expressing the magnetic properties of materials. As explained in [190], the circulation of current flow in a loop is equivalent to the orbiting of an electrical charge (*i.e.*, electron) in the current loop, in terms of magnetic field source (see Figure 2.2a). Based on the atomic Bohr model, electrons exhibit two types of motion: rotation or spin around their own axis and orbit around the nucleus of an atom. Both types of motion produce a moment vector, referred to as the magnetic dipolar moment $\mathbf{m}$. Thus, a single electron's spin can be considered as a magnetic dipole, similar to a tiny magnet, as illustrated in Figures 2.2b and 2.2c. The magnetic dipolar moment vector is perpendicular to the loop's surface and the north/south pole direction of that is determined by the right hand rule [192]. Moreover, the vector could be mathematically expressed by:

$$\mathbf{m}(\mathbf{r}) = \mathbf{I} \otimes \mathbf{a} \tag{2.18}$$

where $\mathbf{I}$ [A] is the current in the loop and $\mathbf{a}$ [m^2] is the loop's surface area. The magnetic dipolar moment $\mathbf{m}$ [$A.m^2$] is eventually, a vector. In Cartesian coordinate system it would have three components of $\mathbf{m}_x$, $\mathbf{m}_y$ and $\mathbf{m}_z$.
The definition of magnetic dipolar moment is closely related to the atomic structure of materials, such as the number of free electrons and their spin direction. This provides quantitative infor-

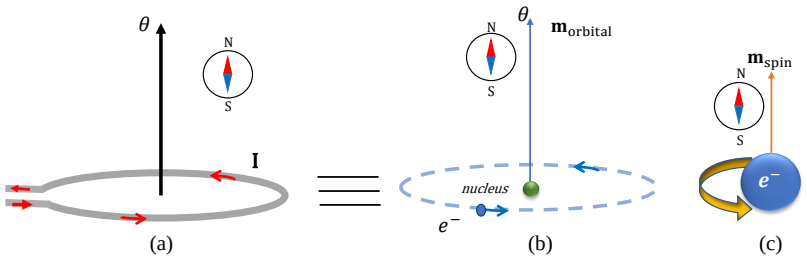

Figure 2.2 – Magnetic dipolar moment **m** in microscopic scale: (a) current flowing through a circular wire producing a magnetic field (b) the electron spins around nucleus and magnetic dipolar moment (c) magnetic dipolar moment that the direction is determined by the electron's orbit [191]

mation about the material's magnetic properties. For example, in materials like rare magnets, the magnetic dipolar moment vector can determine the amount of generated magnetic field. The Biot-Savart equation also relates the magnetic field generated to the magnetic dipolar moment. To establish this relation, we can start with Eq. 2.11, where the vector potential $\mathbf{A}(\mathbf{r})$ is obtained by integrating over the chosen volume of the medium. Referring to Figure 2.1, the magnetic flux density is induced at point **a**, which is a distance of **r** from the coordinate system center at O. Integrating Eq. 2.11 over the region of the localized current, the denominator is expanded by $\mathbf{r}'$ using the Taylor series, such that:

$$\frac{1}{|\mathbf{r}-\mathbf{r}'|} = \frac{1}{\mathbf{r}} + (-\mathbf{r}')^T\nabla(\frac{1}{\mathbf{r}}) + \frac{1}{2!} + (-\mathbf{r}')^T(\nabla\nabla(\frac{1}{\mathbf{r}}))(-\mathbf{r}') + ... \tag{2.19}$$

Here, $(\mathbf{r}')^T$ is the transpose of $\mathbf{r}'$.
Where, $\mathbf{r} = |\mathbf{r}|$. By using Taylor series in the Eq. 2.11 and the assumption of $\mathbf{r} >> \mathbf{r}'$, then vector potential would be:

$$\mathbf{A_i}(\mathbf{r}) = \frac{\mu_0}{4\pi}\left(\frac{1}{\mathbf{r}}\int_V \mathbf{J}(\mathbf{r}')dv' + \frac{\mathbf{r}}{\mathbf{r}^3}\cdot\int_V \mathbf{J}(\mathbf{r}')\mathbf{r}'dv' + ...\right) \tag{2.20}$$

Due to the fact that current density $\mathbf{J}(\mathbf{r})$ is localized and obeys to statistic continuity condition $\nabla\cdot\mathbf{J}(\mathbf{r}) = 0$, Gauss theorem make the first term in Eq. 2.20 equal to zero.
Then, it can be shown that:

$$\mathbf{r}\cdot\int_V \mathbf{r}'\mathbf{J}dv' = (\mathbf{m}\otimes\mathbf{r}) \tag{2.21}$$

Thereby, the magnetic dipolar moment would be:

$$\mathbf{m} = \frac{1}{2}\int_V \mathbf{r}'\otimes\mathbf{J}(\mathbf{r}')dv' \tag{2.22}$$

By truncation the equations of Eq. 2.20 and 2.22, we get:

$$\mathbf{A}(\mathbf{r}) = \frac{\mu_0}{4\pi} \frac{\mathbf{m} \otimes \mathbf{r}}{|\mathbf{r}|^3} \tag{2.23}$$

By performing curl on the vector potential $\mathbf{A}(\mathbf{r})$, the induced magnetic field at distance of $\mathbf{r}$ would be:

$$\mathbf{B}(\mathbf{r}) = \frac{\mu_0}{4\pi} \frac{3(\mathbf{r}.\mathbf{m})\mathbf{r} - |\mathbf{r}|^2 \mathbf{m}}{|\mathbf{r}|^5} \tag{2.24}$$

The Eq. 2.24 explains that the magnetic dipole in magnetic materials produces a magnetic field in the function of distance and magnetic dipolar moment vectors. This equation would be applied to any magnetic source that could generate a magnetic field at the distance of $\mathbf{r}$. In the next section, we will use the definition of a dipolar moment to explain the physics of materials, by inducing magnetic fields.

2.4 Magnetization

As discussed in Section 2.2, total material's volume can be divided into smaller regions. For each region, a localized current, which represents a unique magnetic dipolar moment, can be defined (Figure 2.1). If the region is further divided into smaller sub-regions, the localized current density can be considered for each sub-region as well. Therefore, for each sub-region, a magnetic dipolar moment can be determined using Eq. 2.22. The amount of magnetic dipolar moment can then be obtained by volume integration over each sub-region[188].

$$\mathbf{m}_i = \frac{1}{2} \int_{V_i} \mathbf{r}' \otimes \mathbf{J_i}(\mathbf{r}') dv' \tag{2.25}$$

Eventually, the magnetic dipolar moment of the whole region (assuming the number of sub-regions is i) would be the sum of the magnetic dipolar moments of each sub-region, as shown in Figure 2.3 and expressed as:

$$\mathbf{m}_{total} = \frac{1}{2} \int_{V} \mathbf{r}' \otimes \mathbf{J}(\mathbf{r}') dv' = \sum_i \frac{1}{2} \int_{V_i} \mathbf{r}' \otimes \mathbf{J_i}(\mathbf{r}') dv' = \sum_i \mathbf{m}_i \tag{2.26}$$

The total direction of the generated magnetic field is determined by the majority of magnetic dipolar moment vectors direction at the subregions.
Generally, for intrinsically magnetic materials such as rare earth magnets, most of the magnetic dipolar moment vectors are aligned in the same way and it would determine the north/south pole of that magnet. However, for other materials and in the absence of an external magnetic field, the magnetic dipolar moment vectors are randomly orbited, which results in no magnetic moment,

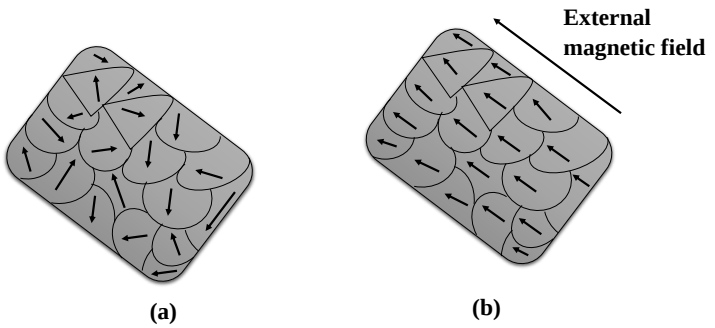

Figure 2.3 – Magnetic dipolar moment alignment (a) non-magnetized materials with independent dipoles for each sub-regions $\sum \mathbf{m_i} \approx 0$ (b) magnetized materials and dipoles are aligned with external magnetic field $\sum \mathbf{m_i} \neq 0$ [188]

as illustrated in Figure 2.3a ($\sum \mathbf{m}_i \approx 0$). The micro-structure of materials such as iron (like pure iron), steel, *etc.*, referred as ferromagnetic materials, can be divided into smaller sub-regions, each with an independent magnetic dipolar moment [193, 194]. Thus, the total magnetic dipolar moments vector are zero for that piece of material. For ferromagnetic materials, an external magnetic field causes most of their magnetic dipole moment vectors to align with the field's direction. The amount of vector's alignment is unique to each material and depends on the strength of the applied field (Figure 2.3b) ($\sum \mathbf{m_i} \neq 0$) [188].
This alignment is called Magnetization, or the magnetic moment density, which defines the coupling of the magnetic field.
Assuming that $\mathbf{m}_i$ is the magnetic dipolar moment of each atom, hence, for a certain volume of material with k atoms, we could determine magnetization ($\mathbf{M}$ [A/m]) by:

$$\mathbf{M} = \lim_{\Delta v \to 0} \frac{\sum_{i=1}^{k\Delta v} \mathbf{m}_i}{\Delta v} \tag{2.27}$$

Here, $\sum_{i=1}^{k\Delta v} \mathbf{m}_k$ is summarizing over all magnetic dipolar moments within the volume element of Δv. The magnetization vector of $\mathbf{M}$ associates with the current density $\mathbf{J}(\mathbf{r})$, referred as the magnetization current $\mathbf{J}_m(\mathbf{r})$ or bound current. By using Eqs. 2.11, 2.22, 2.23 and 2.27 and according to the calculations in [195, 196], the current would be defined by the curl of the magnetization, as:

$$\mathbf{J}_m(\mathbf{r}) = \nabla \times \mathbf{M} \tag{2.28}$$

Therefore in the magnetized materials, the total current density $\mathbf{J}(\mathbf{r})$ would be a combination of magnetization current $\mathbf{J}_m(\mathbf{r})$ (that is bounded to each atom like orbiting electrons) and also free current $\mathbf{J}_f(\mathbf{r})$ $[A/m^2]$ (which is not bounded to a single atom, like current in electrical wire), as:

$$\mathbf{J}(\mathbf{r}) = \mathbf{J}_m(\mathbf{r}) + \mathbf{J}_f(\mathbf{r}) \tag{2.29}$$

Using Eq. 2.6, it would be:

$$\frac{1}{\mu_0}\nabla \times \mathbf{B}(\mathbf{r}) = \mathbf{J}_m(\mathbf{r}) + \mathbf{J}_f(\mathbf{r}) = \mathbf{J}_f(\mathbf{r}) + \nabla \times \mathbf{M} \tag{2.30}$$

$$\nabla \times \Big(\frac{\mathbf{B}(\mathbf{r})}{\mu_0} - \mathbf{M}\Big) = \mathbf{J}_f(\mathbf{r}) \tag{2.31}$$

Here, the $\left(\frac{\mathbf{B}(\mathbf{r})}{\mu_0} - \mathbf{M}\right)$ leads to new quantity for magnetic field, known as Magnetic field intensity, $\mathbf{H}$ as:

$$\mathbf{H}(\mathbf{r}) = \frac{\mathbf{B}(\mathbf{r})}{\mu_0} - \mathbf{M} \tag{2.32}$$

By using $\mathbf{H}(\mathbf{r})$ [A/m] vector, there would be no need to deal with explicitly of magnetization vector $\mathbf{M}$ or equivalent current density $\mathbf{J}_m(\mathbf{r})$ to determine magnetic field. Thereby, the governing Eq. 2.6 for magnetostatic domain would be modified to:

$$\nabla \times \mathbf{H}(\mathbf{r}) = \mathbf{J}_f(\mathbf{r}) \tag{2.33}$$

Assuming that the magnetic properties of materials are linear and isotropic, the relation between $\mathbf{B}(\mathbf{r})$ and $\mathbf{H}(\mathbf{r})$ would be:

$$\mathbf{B}(\mathbf{r}) = \mu\mathbf{H}(\mathbf{r}) \tag{2.34}$$

For simplification, the definition of relative permeability of materials could be used, that is $\mu_r = \mu/\mu_0$.
Moreover, for linear and isotropic media, the relationship between magnetic field intensity and magnetization vector would be defined as:

$$\mathbf{M} = \chi_m\mathbf{H}(\mathbf{r}) \tag{2.35}$$

where χ_m is called Magnetic susceptibility and it has no dimension quantity. It referred to the degree of magnetism attitude of a material in response to an applied magnetic field.
From the Eq. 2.34, we would define relative permeability as follow:

$$\mu_r = 1 + \chi_m \tag{2.36}$$

Both χ_m and μ_r could be functions of space coordinates. For a simple linear, isotropic, and homogeneous medium, both χ_m and μ_r have a constant value.
Based on these definitions, for materials such as iron that can be easily attracted by the magnetic field, μ_r has a very large value around 150-5000 and even more for some special alloys. In the next section, we will categorize and study the magnetic behavior of materials and their response to the applied magnetic field.

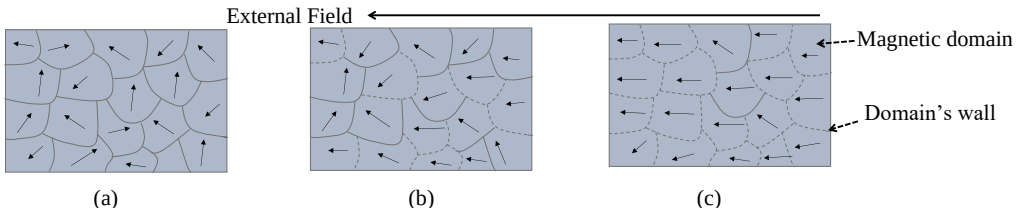

Figure 2.4 – Magnetic dipolar moments alignment in materials (a) randomly aligned (b) partially aligned with external field direction (c) magnetic domains are created and almost line up with an external magnetic field direction [187]

2.5 Magnetic behaviour of materials

According to [187], the materials, based on their magnetic response to the applied magnetic field, could be classified into three main categories: Diamagnetic, Paramagnetic and Ferromagnetic. Using the definition of χ_m in accordance with μ_r, a material could be:

— Diamagnetic if $\mu_r \leq 1$ (χ_m is a very small negative value)

— Paramagnetic if $\mu_r \geq 1$ (χ_m is a very small positive value)

— Ferromagnetic if $\mu_r >> 1$ (χ_m is a large positive value)

In the following, a qualitative explanation of various behaviour of magnetic materials, based on classic atomic model would be represented.

Diamagnetic materials

For Some materials, such as silver, diamond, germanium, bismuth, *etc.*, exhibit a net magnetic moment of zero due to the orbital and spinning motion of electrons, regardless of the presence or absence of an external magnetic field. However, applying an external magnetic field to these materials would induce a small magnetization in the opposite direction to the applied field, according to Lenz's law, resulting in an equivalent negative magnetization or negative susceptibility. Therefore, χ_m for such materials is typically weakly negative, and their relative permeability is also less than 1 ($\mu_r \leq 1$). Diamagnetic materials exhibit a weak magnetization in response to an applied field, but this induced magnetization disappears when the field is removed. Figure 2.4 shows the response of magnetic dipolar moments alignment to an external magnetic field for different materials. The randomly aligned magnetic dipoles in Figure 2.4a are representative of the response observed in diamagnetic materials.

Paramagnetic

The second The category of paramagnetic materials is similar to diamagnetic materials in terms of their reaction to external magnetic fields. However, more magnetic moment regions in paramagnetic materials align in parallel to the external field direction (Figure 2.4b). Upon withdrawal of the external magnetic field, they cannot maintain the induced magnetization.

The macroscopic effect is a positive magnetization, leading to positive susceptibility (χ_m) and a relative permeability value greater than 1 ($\mu_r \geq 1$). Materials such as aluminum, magnesium, titanium, and tungsten are examples of paramagnetic materials.

Ferromagnetic

The last main category corresponds to the materials that each of their atoms, has a relatively large dipolar moment value. It would be caused primarily by uncompensated electron spin moments. When an external magnetic field is applied to these materials, most of their magnetic moments align with the field direction, creating magnetized domains [197]. These domains are composed of magnetic dipoles that are strongly coupled and oriented parallel to the applied field direction. Between adjustment domains, there are transition regions called domain walls (Figure 2.4c).
The magnetization induced in ferromagnetic materials is highly dependent on the intensity of the applied field. For weak fields, the induced magnetic domain wall reorientation is reversible, but for strong fields, the wall movement is not reversible, resulting in residual or remanent magnetization. Ferromagnetic materials have a relative permeability $\mu_m \geq 1$ and a large and positive susceptibility χ_m. The hysteresis property of ferromagnetic materials is the relationship between B-H based on $\mathbf{B}(\mathbf{r}) = \mu\mathbf{H}(\mathbf{r})$ [198]. Other categories of magnetic materials such as Antiferromagnetic and Ferrimagnetic could also be studied at [199, 200].
The FMM device proposed in this research study operates based on magnetostatic principles and requires materials with magnetic properties, including permanent magnets and ferromagnetic materials. The efficiency of the FMM device in corrosion detection applications can be improved by selecting suitable materials for each component.
In the following section, we will explore potential materials for the FMM device by considering the physical principles of magnetism and magnetic coupling, which are integral to the device's performance and effectiveness in corrosion detection applications.

2.6 Materials for FMM device

As mentioned in Chapter 1, the FMM is composed of a permanent part (reference part that induces a magnetic field) and a reactive part (very sensitive to corrosion), which eventually generates a total magnetic flux density as MO.

Permanent part

Concerning the permanent part role, we use magnetic materials for it that could:
— Generate a relatively constant and homogenise static magnetic flux density at a given point,

— Have high amount of coercivity field (Hci) [201] to resist demagnetization for long time using,
— Relatively high operating temperature range (according to the curie temperature),
— Cost effective and available.

Here, we have focused on Rare Earth (RE) magnets (*e.g.*, Neodymium (Nd-Fe-B), Samarium Cobalt (SmCo) and *etc.*) which could generate pretty stable magnetic flux density and also have significantly higher performance than ferrite (ceramic) or alnico magnets [1]. According to [202, 203, 204], the magnets made of alloy Neodymium, iron, and boron (known as Neodymium magnets) are currently the most powerful permanent magnets that are commercially available [205]. Neodymium magnets offer a wide range of technological applications due to their excellent combination of high coercivity and maximum energy product $(B\text{-}H)_{max}$ in the room temperature [206]. Moreover, they are cheaper than Samarium Cobalt magnets, however, their working temperature range is relatively lower than Samarium Cobalt magnets.
In this thesis, we choose the neodymium disc magnets from the Supermagnet supplier [2], available in different sizes. The magnetic properties and data sheets of ordered magnets are mentioned in the Appendix A.
To protect the magnet (permanent part) from corrosion, various protective layers can be used such as plastic bags, waterproofing materials, or rust-proofing materials. Commercially available magnets usually use coating layers like nickel coating (*e.g.*, nickel-copper-nickel), gold-coating (*e.g.*, nickel-copper-nickel-aluminum), chrome coating (*e.g.*, nickel-copper-nickel-chrome), or epoxy resin (*e.g.*, nickel-copper-nickel-epoxy resin), depending on the manufacturing method and properties of the magnet. These layers have thicknesses around a few micrometers and provide sufficient protection against corrosion in outdoor situations. However, it is important to note that the protection of the magnet from corrosion is not the focus of this research study.

Reactive part

This part of the FMM device must use a material that could be coupled with a magnet, strongly. Therefore, the strong ferromagnetic materials are suitable for reactive part, due to:

— Considerable amount of relative permeability compare to permanent part, that could be properly coupled together,
— Extremely sensitive to aggressive agents like chloride that could be easily and quickly rusted,
— Cost effective, safe and available material.

In order to meet these requirements, we have chosen pure iron (purity 99.95% from NEYCO

1. The permanent magnets made primarily of an alloy of aluminum, nickel, and cobalt, hence the name "alnico"
2. www.supermagnete.fr

(a) (b)

Figure 2.5 – (a) FMM device with neodymium magnet as permanent part and pure iron plate as (b) FMM device placed on the top of a limestone core and its permanent part covered with protective plastic cover

company [3]). The advantages of using pure iron material for the reactive part are that:

- Offering a high magnetic permeability due to the ferromagnetic nature of iron,
- Pure iron is very sensitive to chloride ions. Therefore, it could be rusted easily with chloride ions ingress front,
- Iron is an abundant, safe use and the cost effective ferromagnetic material.

Figure 2.5 depicts a laboratory feasibility test of a FMM device that combines a permanent and reactive part, where the reactive part is exposed to the environment while the permanent part is covered. The geometry of the FMM device is a challenging issue as embedding devices could threaten the concrete integrity, making it important to carefully design and optimize their geometries for durability and safety of civil engineering constructions. Thus, in this research study, we would more focus on the efficient geometry of FMM, specifically, the reactive part. Since, the reactive part is made of iron that potentially has a high amount of relative permeability, it plays a magnetic shielding role in coupling with the permanent part, where the magnetic domains of the reactive part reorient the magnetic flux line of the permanent part, leading to attenuation in measurable magnetic field on top of the FMM. The range of MO and the performance of FMM are directly linked to the coupling between its permanent and reactive parts. Thus, further discussion on the shielding role of the reactive part and the parameters affecting the amount of magnetic shielding will be presented, supported by numerical modeling.

2.7 Magnetic shielding property of ferromagnetic materials

As previously mentioned, a ferromagnetic material can become magnetized by an external field, and this magnetization can induce the reorientation of magnetic domains, leading to a change in the spatial distribution of the magnetic field [207]. This effect is more pronounced in

3. https://www.neyco.fr

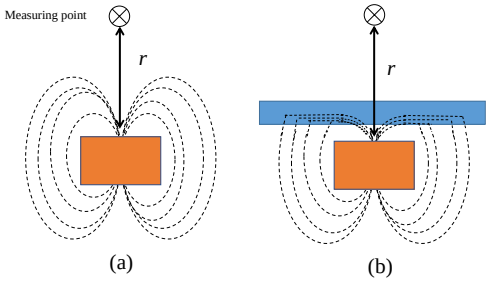

Figure 2.6 – (a) Magnetic flux density lines in free space area (b) magnetic flux density lines redirected into permeable matter of ferromagnetic substrate (shielding)

materials with higher permeability. The impact of this phenomenon on magnetic flux density can be seen in Figure 2.6, which shows the distributions of magnetic flux lines for a magnet alone (Figure 2.6a) and a magnet placed near a ferromagnetic substrate (Figure 2.6b). The redirection of flux lines into the ferromagnetic substrate results in a reduction of measurable MO at a certain distance, effectively acting as a "magnetic shield" [208]. Further discussion of the shielding role of ferromagnetic materials and the parameters that determine the amount of shielding will be presented through numerical modeling.

The magnetic shielding present in an FMM device using an iron plate as a reactive part determines its performance by attenuating the effective magnetic flux density generated by external sources. To investigate the shielding role of the reactive part and the parameters affecting magnetic attenuation, a 3D modeling of the magnetic shielding effect was performed using a cylindrical NdFeB magnet and a rectangular reactive part. Simulations were carried out using Ansys Maxwell software and the Finite Element Method (FEM) to solve Maxwell equations. The magnetic flux lines were visualized using uniform vectors with the option of limiting the distribution illustration size and mapping area.

Table 2.2 provides information on the numerical modeling configuration and material properties used in this model. The 3D model of an FMM device involves a cylindrical NdFeB magnet as a permanent part and a highly permeable ferromagnetic material like iron as a reactive part. To better understand the magnetic shielding and redirection of flux lines, the dimensions of the models used in the simulation are chosen arbitrarily and in relatively large proportions. Additionally, in the Ansys Maxwell software, the uniform vector plot is chosen as the representing configuration for field report, and the map size option is activated to limit the distribution illustration size and the area of mapping. This approach enables visualizing the magnetic flux line reorientation into the reactive part using uniform vectors. It's worth noting that the magnetic

Table 2.2 – Numerical modeling configurations and properties

	Materials	**Geometry**	**Relative permeability**	**Meshing size**
Permanent part	NdFeB35	Radius = 7.5 mm Thickness = 10 mm	1.04	1 mm
Reactive part	Pure iron	70 mm x 70 mm x 3 mm	4000	3 mm

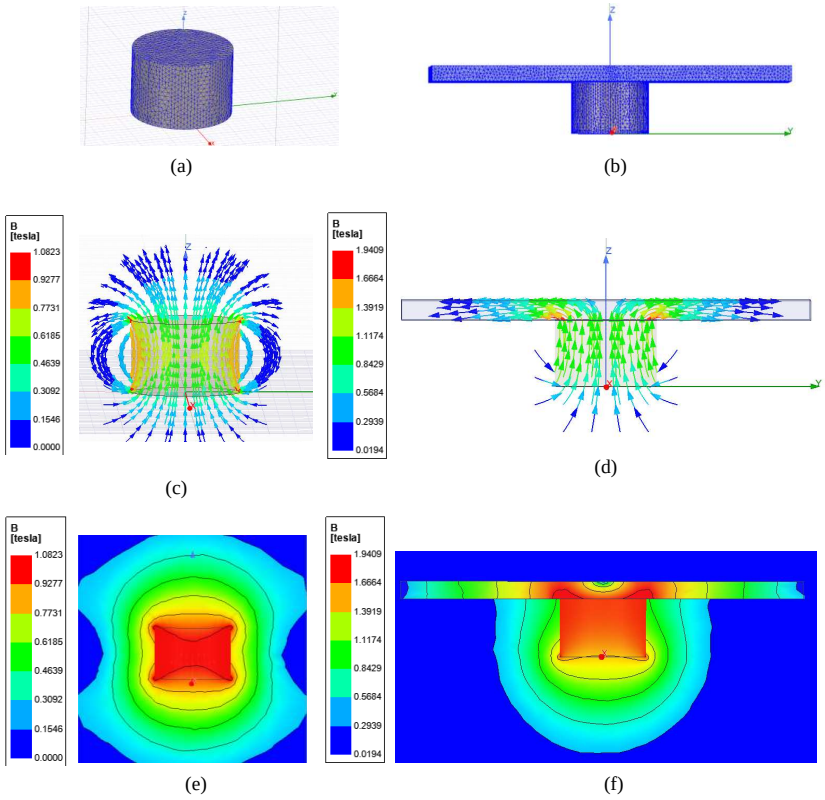

Figure 2.7 – 3D modeling of FMM device (a) meshing of a cylindrical permanent magnet with direction of north/south poles parallel to z-axis (meshing size = 1 mm) (b) meshing map of magnet coupled iron plate (meshing size = 3 mm) (c) homogeneous magnetic flux lines, generated by permanent magnet (d) magnetic flux lines, redirected by the iron plate (magnetic shielding) (e) magnetic flux density mapping of permanent part with iso-value field (f) magnetic field mapping of FMM device with iso-value image and attenuation magnetic field, just above of reactive part, due to shielding

flux line generated in all of the map are not displayed in the results.

Figures 2.7a and 2.7b show the meshing map for each component of the model. Figure 2.7c shows a static and uniform magnetic flux line generated by the permanent magnet, while Figure 2.7d shows the redirected flux lines towards the iron mass upon coupling the reactive part.

At the interface between the permanent and reactive parts, the flux lines are pulled nearly perpendicular to the magnet's north/south poles direction along the z-axis. From the ferromagnetic side, the lines are led along the plate, nearly tangential to the surface.

The reason for the redirection of magnetic flux lines can be explained by Gauss's laws, which state that there are no magnetic monopoles. Since the flux lines must lead continuously across materials and then be released back into the air and the opposite pole (south pole), the magnetic flux line will never be cut, interrupted, or removed. Instead, they are redirected to maintain con-

sistency and continuity. In this study, iron with a high relative permeability of $\mu = 4000$ was assigned for the reactive part from the Ansys Maxwell library. Thus, magnetic flux lines tend to be redirected more through materials with higher permeability than through air with a lower permeability value (for vacuum, the relative permeability is equal to 1).
Moreover, Figure 2.7e, shows a field mapping of the permanent magnet with iso-value, which is uniformly generated around the material. Similarly, Figure 2.7f, shows the shielding effect of the iron plate on the quasi-static magnetic field, generated by the magnet. These results illustrate that the presence of ferromagnetic materials coupled with a magnetic source, would attenuate the measurable generated magnetic field, above the reactive part, due to shielding. The notion of attenuation is associated with the amount of magnetic flux lines that would be redirected through shield and not necessarily means that magnetic flux lines would be totally blocked with iron shield. Thus, the some amount of magnetic flux lines could pass through the shield. The objective of the 3D modeling in Figure 2.7 is basically, to provide a general representing of magnetic shielding concept as main role of reactive part, when it coupled to the permanent part.
The extent to which quasi-static magnetic fields are attenuated by shielding depends largely on the physical characteristics of the shield, including its shape, geometry (thickness or length), and material properties, particularly relative permeability, as stated in [207]. To further explore the shielding properties of ferromagnetic materials, we propose two additional simulations in which we vary the following parameters of the reactive part:

— Geometry,
— Relative permeability,
— Material transformation to corrosion products.

2.7.1 Shielding property of reactive part *versus* geometrical variations

As a primary parameter, we investigate the role of geometrical variations (*i.e.*, surface and thickness) on the shielding property of the reactive part through numerical modeling. We use a similar cylindrical permanent magnet and iron plate presented in Table 2.2. For this batch of simulations, we choose a variety of reactive part geometries with different surfaces and thicknesses for a parametric study. Unlike the previous simulation setup, here, the results include the magnetic field distribution in the entire mapping area.
Figures 2.8 and 2.9 visualize the influence of reactive part surface and thickness, respectively, on the generated magnetic flux density around the FMM device. Figure 2.8 shows that increasing the surface of the reactive part from 30 × 30 [mm] to 60 × 60 [mm], while maintaining a constant thickness of 3 mm, results in greater magnetic shielding. Figure2.8a shows some magnetic flux lines escaping from the top center of the iron plate due to the smallest surface area. As the surface area is increased to 40 × 40 [mm] and 60 × 60 [mm], the number of escaped arrows is reduced (Figure2.8b and c). Therefore, it can be concluded that an increase in the surface area

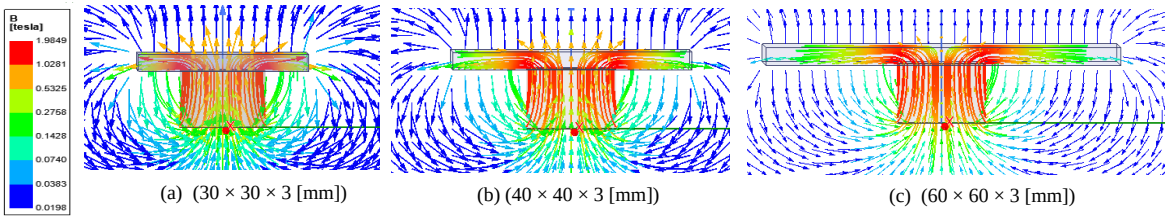

Figure 2.8 – Spatial distribution of the magnetic field, generated by magnet (radius= 7.5 mm and height=10 mm) coupled with iron shield through constant thickness 3 mm and variable surface 30 × 30, 40 × 40 and 60 × 60 [mm], respectively

of the iron plate leads to a reduction in the measurable magnetic field on the top of the reactive part.

Figure 2.9 depicts the shielding effect of the reactive part when the thickness is increased from 1 mm to 6 mm while maintaining a constant surface area of 30 × 30 [mm]. It is observed that the magnetic line leakage above the reactive part decreases significantly with an increase in thickness. As a result, the effective magnetic field density and magnetic flux lines are redirected through the iron shield more efficiently.

Both figures demonstrate the direct relationship between the geometry of the reactive part and its shielding property. A larger surface area and greater thickness of the reactive part result in lower magnetic field density on the top of the FMM.

Table 2.3 indicates that the amount of magnetic flux density has an inverse relationship with the geometry of the reactive part used as a shield. The magnetic field quantities were numerically calculated for each simulated device in Figures 2.8 and 2.9 at a relative distance of 20 mm from the magnet's bottom side. It can be concluded that the magnetic field is attenuated by coupling the magnet with the ferromagnetic reactive part. The degree of attenuation is dependent on the shield's geometry. Therefore, an increase in reactive part thickness would lead to a reduction in the measurable magnetic field. This attenuation is relatively more significant with an increase in reactive part surface. In the subsequent analysis, we will investigate the impact of variations in relative permeability on the shielding properties of the reactive part.

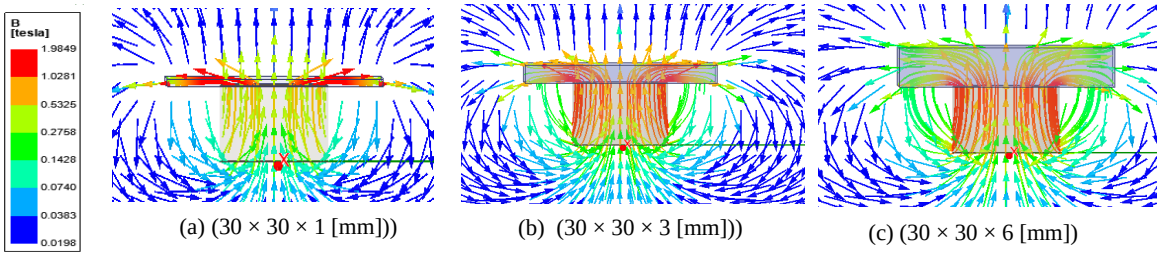

Figure 2.9 – Spatial distribution of the magnetic field, generated by magnet (radius= 7.5 mm and height=10 mm) coupled with iron shield through constant surface 30 × 30 [mm] and variable thickness 1, 3 and 6 [mm], respectively

Table 2.3 – Magnetic flux density [mT], calculated by numerical modeling associated with Figures 2.8 and 2.9, at the distance of 20 mm, respect to bottom of magnet

Reactive part with fixed surface = 30 mm × 30 mm					**Reactive part with fixed thickness= 3 mm**				
Reactive part thickness [mm]	**0**	**1**	**3**	**6**	**Reactive part length [mm]**	**0**	**30**	**40**	**60**
B [mT]	74	17	16	15	**B [mT]**	74	16	8	3

2.7.2 Shielding property of reactive part *versus* relative permeability variation

A new set of simulations is conducted using the same parameters presented in Table 2.2 for 3D model of FMM. The magnetic flux density (**B**) generated on the top surface of the reactive part was numerically calculated along a measurement line on the z-axis, at distances ranging from 2 cm to 6 cm from the coordinate origin, located at the bottom of the magnet (Figure 2.10a). The simulations also involved changing the material of the reactive part to different materials with varying relative permeabilities, in order of:

— iron (relative permeability = 50),
— cast iron (relative permeability = 60),
— cobalt (relative permeability = 250),
— ferrite (relative permeability = 1000),
— iron (relative permeability = 4000).

As noted, here we have used two different types of iron with a relative permeability of 50 and 4000. In fact, pure iron, with high purity levels typically around 99.95%, exhibits a permeability value of approximately 50. This characteristic defines pure iron as 'soft iron' in the context of magnetic materials, indicating its relatively weak magnetic properties. In contrast, iron alloys, particularly those subjected to specific additives or heat treatments, can display significantly higher permeabilities, often reaching values of approximately 4000 or even more. These materials are categorized as 'ferromagnetic' due to their distinctive ability to be easily magnetized

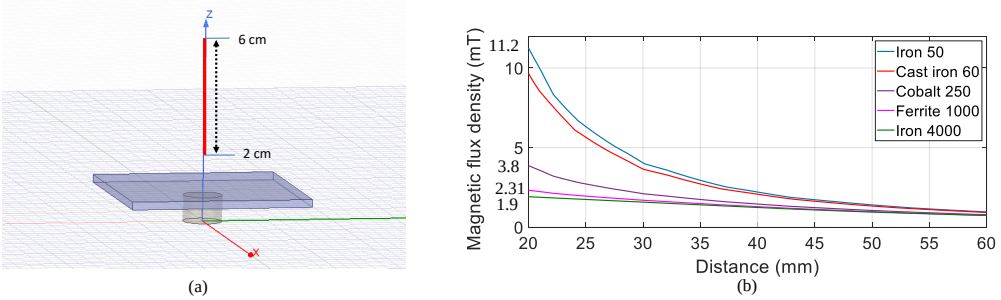

Figure 2.10 – Shielding effect of ferromagnetic material as function of the relative magnetic permeability (materials variation) (a) schematic representation of numerical modeling, magnet attached to ferromagnetic shield vs. observation points on the line from 2 cm to 6 cm on z-axis (b) magnetic flux density variations, as a function of distance and relative permeability of the materials used as shield

and to maintain their magnetization. This increased permeability in ferromagnetic materials is attributed to the alignment of magnetic domains within the material, a phenomenon that substantially enhances their magnetic properties [209].

A comparison of the shielding role of the reactive part using different materials with varying permeabilities is carried out. Iron-based materials such as cast iron with relative permeability 60 or ferrite with relatively higher permeability 1000 or iron with low permeability 50 or high permeability of 4000 were selected for comparison. The shielding properties is evaluated as a function of material permeability and also the relative distance between observer point and FMM top surface. Figure 2.10b illustrates the magnetic flux density along an observation line from 2 cm to 6 cm. It shows that the amount of magnetic shielding is dependent on the both relative permeability of the material and the distance. As the distance increases, the magnetic attenuation also increases. Beyond a distance of 6 cm, no significant variation in magnetic field attenuation was observed in this numerical model.
Considering the fact that the FMM device is designed to be embedded in cover concrete, and that in marine environments, the thickness of the cover concrete is typically less than 5 cm, according to [40]. Therefore, embedding the FMM at distances greater than 5 cm would be practically ineffective to study.
It was observed that using materials with higher relative permeability led to more significant attenuation of the magnetic flux density. For example, by using iron with a relative permeability of 4000 (which is 80 times greater than the value of 50), the generated magnetic flux density can be attenuated by 1.9 mT, which is 5.9 times less than when using iron with a relative permeability of 50. Therefore, it can be concluded that using materials with higher relative permeability results in higher attenuation of the magnetic flux density.
The results indicate that materials with lower relative permeability, such as iron (50) or cast iron (60), provide a greater magnetic attenuation range as a function of distance. For example, the calculated magnetic flux density variation ranges for iron with a relative permeability of 50 and cast iron with a relative permeability of 60 are 9.5 mT (from 11.2 to 1.7) and 7.3 mT (from 9 to 1.7), respectively. The variation ranges decrease to 2.1 mT (from 3.8 to 1.7), 0.6 mT (from 2.3 to 1.7), and 0.2 mT (from 1.9 to 1.7) for cobalt, ferrite, and iron with the highest relative permeability of 4000. Therefore, choosing iron with lower permeability as a ferromagnetic material for the reactive part is a suitable choice because it can provide a detectable and measurable magnetic flux density range that requires less use of expensive and sensitive magnetic interrogators for measurements at different distances.
In collaboration with the Laboratory of Materials and Chemistry at the University of Caen Normandy, France, we conducted a separate characterization study to determine the effective relative permeability of the chosen iron for the reactive part. The results showed that the effective permeability of the chosen pure iron is 50. This value of 50 aligns with the known magnetic

properties of 'soft iron,' which is characterized by relatively weak magnetic properties [209]. More details on the associated (B-H) curve of this chosen iron are mentioned in Appendix A. The following section will evaluate the shielding role of the reactive part as a function of its transformation into corrosion products. Considering the significance of corrosion products in this research and the extra parametric study that is conducted for a thorough analysis, an additional section is dedicated to this aspect

2.8 Shielding property of reactive part *versus* corrosion

In the previous section, the shielding properties of the reactive part were studied as a function of geometrical and relative permeability variations. In this section, the effects of corrosion on the reactive part's shielding ability will be examined. Pure iron is the chosen material for the reactive part, and thus, the study will focus on the different iron corrosion products, including oxides and hydroxides. These products can be distributed in the porous network of concrete media [210], but some of them may possess paramagnetic or ferromagnetic properties and attract to the FMM device's magnetic field, forming deposit layers of corrosion products. Therefore, the coupling phenomenon between the corrosion products layer and the FMM could affect the MO. Furthermore, if the corrosion products penetrate the porous network of concrete, a composite material (concrete mixed with corrosion products) would be formed, with an unknown relative permeability. It is necessary to evaluate the relative permeability of the corrosion products to estimate the composite's μ and ultimately study the MO variations as a function of corrosion products.
This section aims to investigate the potential impact of iron corrosion products on the magnetic flux density (MO) of the FMM device. To achieve this goal, the following steps will be taken:

— Firstly, a literature review will be conducted to identify the magnetic properties of different corrosion products that may be generated from iron materials.
— Secondly, numerical modeling will be used to assess the potential MO variation range and tendency of the FMM device considering the transformation of the reactive part into corrosion products.
— Thirdly, the corrosion products generated from the chosen material (pure iron with relative permeability of 50) will be characterized through a separate laboratory test. Using the results from this characterization, the effect of corrosion on MO will be evaluated through numerical modeling, by varying two parameters: the geometry and relative permeability of the reactive part.

2.8.1 The corrosion products of iron

According to [10, 211, 212], several iron corrosion products have been identified in the literature, including Hematite ($\alpha - Fe_2O_3$), Lepidocrocite ($\gamma - FeOOH$), Maghemite ($\gamma - Fe_2O_3$), Goethite ($\alpha - FeOOH$), Ferrihydrite ($Fe_5HO_8 \cdot 4\,H_2O$) or Feroxyhite ($\delta - FeOOH$) . Moreover, in the chloride containing media, the corrosion products like Akaganeite ($\beta - FeOOH$), Magnetite (Fe_3O_4), Ferrous ($Fe(OH)_2$), Ferric hydroxide ($Fe(OH)_3$) or Hydrated ferric oxide ($Fe(OH)_3 \cdot 3\,H_2O$) also frequently reported, as available corrosion products in marine environments. However, The identification of the precise type of corrosion products depends on various environmental factors such as temperature, aggressive agents types, oxygen level, moisture level, and *etc.* which determine the corrosion mechanism and chemical transformation types. However, studying the magnetic properties of each corrosion product type requires additional investigation beyond the scope of this research study.
In order to evaluate the MO variation and tendency through the transformation of all volumes of reactive part into the corrosion products deposit layers, we have chosen two common iron corrosion products, which their magnetic properties are also mentioned in the literature [213]. The first product is magnetite which has inherently magnetic properties and is known as a weak ferrimagnetic material, with relative permeability between 2.5 to 16 [213]. The second product is hematite with a relative permeability between 1.0004 to 1.001, and identified as antiferromagnetic material [213].
In the following, we will study the variations in MO due to the transformation of the reactive part materials into these corrosion products.

2.8.2 Investigate MO variation tendency through materials transformation to magnetite and hematite

In this section, our objective is to develop a numerical model of the FMM device that considers the transformation of the reactive part into corrosion products, and to evaluate the resulting MO variations. The initial objective is to determine the general tendency of MO due to the transformation of the reactive part into rusting products. Table 2.4 summarizes the materials, magnetic properties, and dimensions of each component of FMM. Using Ansys software's 3D modeling capabilities, we will first represent the magnetic flux density distribution through field mapping.
Secondly, we will evaluate the amount of MO as a function of the reactive part's material transformation and relative distance. We chose a relatively large plate as the reactive part to provide the possibility of representing a uniform and accurate vector field mapping report of FMM as a function of the reactive part's material transformation to hematite or magnetite and comparing it with iron. The mesh size applied to the magnet and reactive part is 1 mm and 0.5 mm, respec-

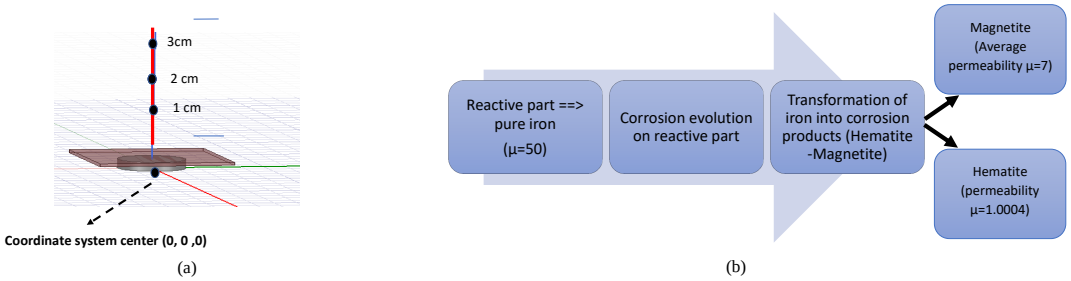

Figure 2.11 – (a) Schematic of numerical modeling of the FMM device with iron material (permeability =50) as reactive part. The observation points at 1 cm, 2 cm and 3 cm relative distance to coordinate origin (b) block diagram of numerical modeling order

tively. In order to investigate the effect of corrosion product evolution on the reactive part, we simplified the formation of the corrosion product layer as a transformation of the total volume of the reactive part into homogeneous layers of magnetite and hematite separately. As noted in [10], iron oxides have a greater volume than pure iron. To isolate the impact of corrosion products on MO, we fixed the geometry of the reactive part by considering its total volume as a constant parameter.

The reactive part is made of pure iron with a relative permeability of 50 and a total volume of 30 ×30×1 [mm]. It would be transformed into a layer of magnetite (average relative permeability of 7), and then a layer of hematite (relative permeability of 1.0004), each having the same geometry of 30×30× 1 [mm].

The Figure 2.11 represents a schematic diagram of this numerical modeling steps. Figure 2.12 displays a field mapping report on the variations in pure iron shielding caused by the transformation of materials into the two aforementioned corrosion products: magnetite and hematite. The figure shows that the magnetic shielding property of the reactive part is significantly altered by the transformation of iron, a strong ferromagnetic material, into magnetite, a weak ferrimagnetic material, and hematite, an antiferromagnetic material. These results are in line with the conclusion in Section 2.7.2, where it was explained that the amount of magnetic shielding attenuation has a direct relationship with the relative permeability.

In terms of corrosion products, magnetite with a relative permeability of 7 provides slightly more magnetic shielding compared to hematite with a relative permeability of 1.0004. As illustrated

Table 2.4 – Configurations of material's property in the numerical modeling

	Dimensions [mm]	**Materials**	μ [-]
Permanent part	Radius= 7.5 Height= 3	NdFeB35	1.04
Reactive part	30 × 30 × 1	Pure iron	50
	30 × 30 × 1	Magnetite	7
	30 × 30 × 1	Hematite	1.0004

Table 2.5 – The MO [mT] results of numerical modeling of FMM device, with different materials of reactive part and as a function of relative distance

	1 cm [mT]	**2 cm [mT]**	**3 cm [mT]**
Magnet alone	64	12	4
Iron	17.6	5	2.2
Magnetite	46.4	9.2	3.3
Hematite	62.2	11.1	3.5

in Figures 2.12c and 2.12e, the magnetic flux density deviation in the reactive part has been almost redirected through the air by the transformation of iron to hematite.

Additionally, the MO will be obtained through a vertical line on the z-axis for observation points at 1 cm, 2 cm, and 3 cm from the coordinate origin located at the bottom of the magnet, as shown in Figure 2.11a. The amount of magnetic flux density [mT] obtained for each observation point and material assigned to the reactive part is summarized in Table 2.5. As shown in Table 2.5, the MO exhibits an upward trend due to the transformation of the reactive part's iron material to hematite and magnetite. The magnitude of the variation is highly dependent on the observation point's relative distance. At a close distance of 1 cm, the MO would increase from 17.6 mT to 62.2 mT and 46.4 mT, respectively, with the transformation of iron to hematite and magnetite. However, for hematite and magnetite at a distance of 3 cm, the MO variation range would decrease to 1.1 mT (from 3.3 to 2.2) and 0.2 mT (from 3.5 to 3.3), respectively.

To evaluate the amount of relative variation range related to the shielding property of reactive part affected, the equation of *Relative attenuation* $\% = \frac{B_{Permanentpart} - B_{Reactivepart}}{B_{Permanentpart}} \times 100$ is applied to calculated percentage of MO changing due to corrosion. In fact, the shielding property

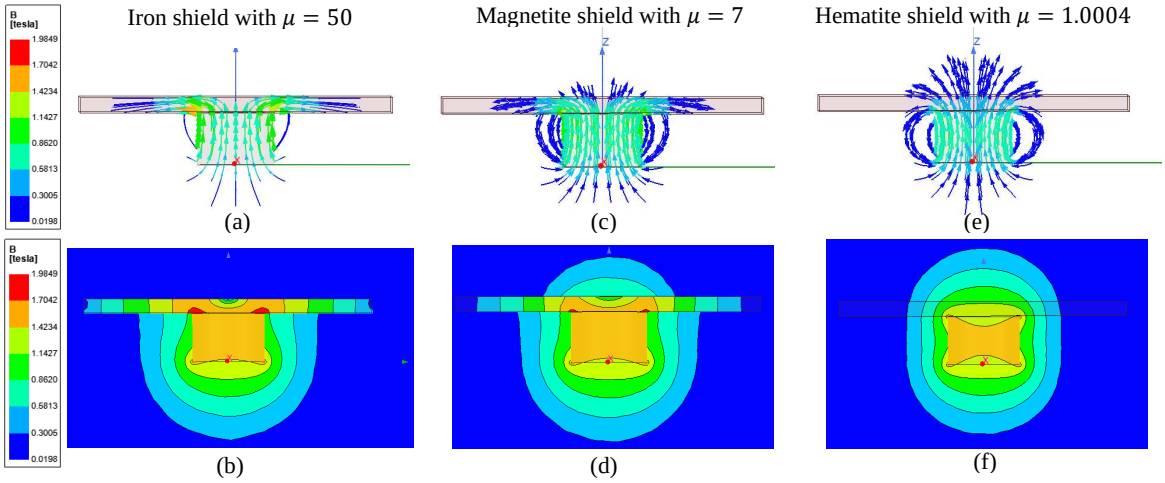

Figure 2.12 – Shielding effect of iron plate *versus* corrosion (a,b) magnetic flux lines and the field mapping report from magnet and reactive part with permeability = 50 (c,d) magnetic flux lines and the field mapping report from magnet and corroded reactive part, covered with magnetite layer with permeability = 7 (e,f) magnetic flux lines and the field mapping report from magnet and corroded reactive part, covered with hematite layer with permeability = 1.0004

of the reactive part is strongly weakened due to the transformation of iron to corrosion products. Additionally, amount of relative variation is also dependent on the distance to measuring point. The table indicate that the reactive part's shielding property are more significant for hematite. When iron is transformed to hematite at a distance of 1 cm, a 69% variation range (from 72% to 3%) is obtained. This value is reduced to 34% (from 72% to 38%) when iron is transformed to magnetite. Thus, it can be concluded that:

— MO has an upward tendency due to the transformation of the reactive part to corrosion products, regardless of the type of rust,
— The amount of MO variation is extremely dependent on the relative distance to the interrogator, indicated as an observation point,
— Concerning the shielding property of the reactive part, it would be weakened due to the transformation of iron material to corrosion products,
— The amount of reactive attenuation variations is dependent on the type of corrosion products and the amount of relative permeability.

These numerical study results could serve as a primary investigation into the FMM device's performance associated with corrosion evolution on the reactive part and the related consequences on MO tendency. However, in the real case, the corrosion is not linear in terms of geometrical variations. As mentioned before, the corrosion products do not have the same volume (geometry) as the original iron. Moreover, the amount of rusting products' relative permeability is not limited to one or two types of products only. In fact, this value would be defined as an average of the relative permeability for the mixing of possible rusting products.

2.8.3 Investigation MO variations due to both geometrical reduction of reactive part and corrosion product evolution

In this section, the objective is to present the primary feasibility parametric study on the evolution of corrosion products on the reactive part and changes in its volume to determine the MO tendency and amount of variations. To achieve this objective, an experimental study was conducted to identify the types of corrosion products generated by the chosen iron material and to determine the effective permeability of the corrosion product layer.

Characterization of corrosion products

To do this test, some iron plates have been selected from the chosen reactive materials. Pure iron plates were immersed in a 30 g/L NaCl solution, and an electrical current was applied to accelerate rusting. Two batches of corrosion products, named sample 1 and sample 2, were gathered and characterized through XRD analysis. Sample 1 was produced with an applied current density between 2 and 5 mA/cm^2, while sample 2 was produced with a current density between 1 and 2 mA/cm^2. The gathered materials were sent to Institut Lavasier for X-ray Diffraction

Table 2.6 – Volumetric content of iron oxide phases for each sample

	Hematite %	**Magnetite %**	**Goethite %**	**Lepidocrocite %**
Sample 1	61	18	10	1
Sample 2	66	17	5	2

Analysis (XRD) characterization.

The corrosion products of sample 1 and 2 were characterized through XRD in the range of 2θ from $10° - 80°$ using a $K\alpha - Cu$ source. The XRD patterns showed multiple phases and diffraction peaks corresponding to specific crystallographic planes. The same phases were detected in both samples, with slightly higher crystallinity in sample 2. The XRD patterns are shown in Figure 2.13. Table 2.6 presents the volumetric content of the identified compounds for corrosion products of two samples obtained through XRD. The table summarizes that both samples contain hematite and magnetite as their main components, with sample 2 having a slightly higher proportion of hematite. This indicates the formation of iron oxidized in Fe^{2+} and Fe^{3+} in accordance with previous studies on steel material corrosion in a marine environment [10, 211, 212].

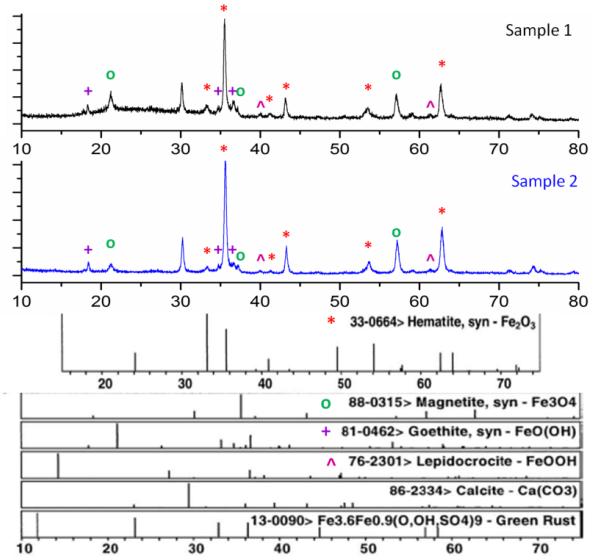

Figure 2.13 – XRD patterns for sample 1 and 2

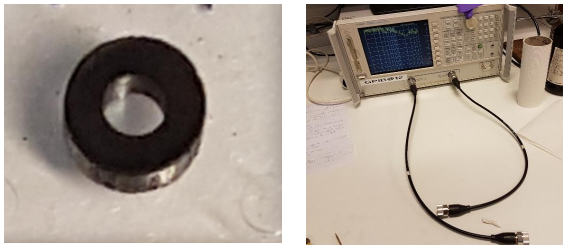

(a) (b)

Figure 2.14 – (a) Produced ring sample (pellet) (b) VNA with co-axial cables

Samples were sent to Lab-STICC in France for magneto-dielectric material characterization to determine the effective magnetic permeability of corrosion products. This technique involves shaping massive samples in APC7 format using a compressor device, followed by reflection/transmission measurements to calculate the real and imaginary parts of the complex magnetic permeability and dielectric permittivity of the material as a function of frequency [214, 215]. The study focuses on determining the effective value of relative permeability for massive form material. Composite samples were made by mixing corrosion products with epoxy resin and air, which were then compressed to form pellets (illustrated in Figure 2.14a). The pellets were inserted in a linear coaxial cell connected to an AGILENT 8753 ES type VNA (illustrated in Figure 2.14b), allowing measurement of the S parameters as a function of the impedance of the medium. The samples were prepared in different mixture percentages, with five pellets for each sample. The mass and apparent volume of the pellets were measured to determine the proportion of porosity in each pellet.
The complex magneto-dielectric spectrum obtained for a sample pellet were obtained at different frequencies for each pellet are listed in tables. Finally, Using Bruggemann model [216] and the Eq. 5.4, the effective value of μ' for the two batches of corrosion products was obtained as:

- Sample 1: $\mu' = 4.13 \pm 0.16$
- Sample 2: $\mu' = 5.52 \pm 0.29$

Thereby, the average value for these two samples would lead to an approximate amount of 5. This value is known as the relative permeability of the mixture of corrosion products, obtained for pure iron used in this study. The setup and details of this laboratory test results would be represented in Appendix B.

Numerical study of corrosion product evolution on reactive part

The obtained relative permeability from the characterization of corrosion products will be used to investigate the tendency and amount of MO variations caused by the formation of a deposited layer of corrosion products through numerical modeling in the following.
Basically, corrosion is a nonlinear phenomenon, and in real cases, the deposited layer of corrosion products does not have a homogeneous shape or uniform pattern, especially in the presence of chloride ions, which can cause pitting corrosion on the surface of steel. Moreover, determining

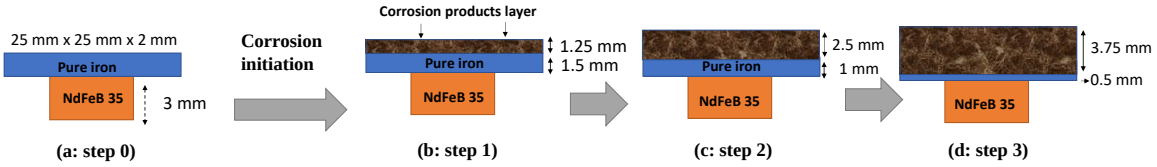

Figure 2.15 – Schematic representation of modeled FMM and the description of the corrosion modeling steps

Table 2.7 – Configurations of components in the numerical modeling

	Materials	Geometry	Relative permeability	Meshing size
permanent part	NdFeB35	Radius = 7.5 mm Thickness = 3 mm	1.04	1 mm
reactive part (iron layer)	pure iron	25 mm × 25 mm × 2 mm (thickness would be decreased)	50	adaptive with thickness variations
reactive part (corrosion products layer)	corrosion products mixture	25 mm × 25 mm (thickness would be raised in adequate proportion)	5	adaptive with thickness variations

the spatial distribution of the corrosion product layer in terms of growth thickness is a complex process that requires precise assessments through Scanning Electron Microscope (SEM) image techniques and measurements of volumes and estimated mass loss for each case. For modeling purposes, certain parameters are typically simplified. Experimental studies in [217] show that ferromagnetic plates with a rectangular shape lose their initial geometry, *i.e.*, surface and thickness, due to chloride-induced corrosion. Thus, here, we represent a numerical model of corrosion product evolution through a linear approximation of the reactive part's thickness loss (with a constant surface) as an index of corrosion. At the same time, a uniform layer of corrosion products would be formed on the reactive part's surface.

According to the studies in [10, 218, 219] the volume of the corrosion layers on iron is typically 2 to 3 times greater than the volume loss of the metal. Assuming an initial thickness of 2 mm for the iron reactive part, which is minimized to 0.5 mm due to corrosion, a rusting layer with a thickness of 3.75 mm would be formed on top of the reactive part plate. For numerical modeling purposes, a ratio of 2.5% is considered as the corrosion products thickness to reactive part thickness loss at each step. The surface area of the reactive part and corrosion layer is assumed to remain constant at 25 × 25 mm for simplification.

Figure 2.15 shows the schematic of the corrosion evolution model of the FMM device, which involves three steps. Additionally, table 2.7 summarizes the parameters used in the numerical modeling of the FMM device for this test. The meshing size of the reactive part is adaptively modified with respect to the thickness of the layers (pure iron or corrosion products) at each

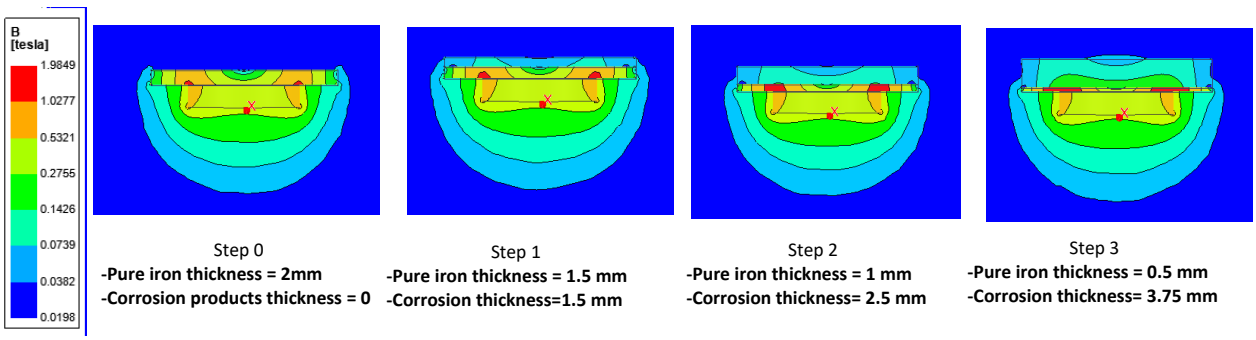

Figure 2.16 – Field mapping of iron shielding behaviour variations associated with its transformation to corrosion products layer

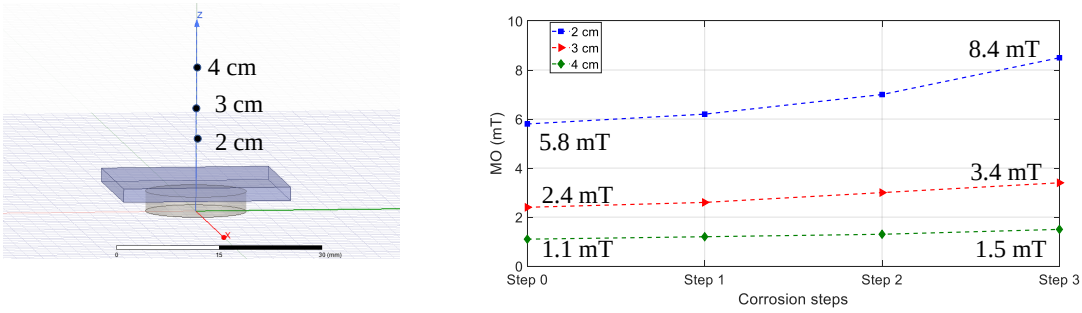

(a) (b)

Figure 2.17 – (a) Schematic of numerical modeling of sensor vs observation points at from 2 cm, to 4 cm from coordinate system origin (b) MO upward tendency curve obtained for 3 corrosion steps for observation points in 2 cm, 3 cm and 4 cm from coordinate origin

corrosion evolution step.

Figure 2.16 displays the iso-value images of the FMM device's numerical model, depicting the growth of the corrosion product layer. These simulation results are consistent with those presented in Section 2.8.2. The figure shows that variations in the geometry and material of the reactive part impact the spatial distribution of MO around the FMM. The total thickness of the reactive part has doubled (at step 3 in Figure 2.16) due to the formation of a relatively thick layer of rusting products with lower permeability than iron.However, the high amount of magnetic flux density is still present in the reduced iron layer with relatively high permeability (50). At the same time, the magnetic field is increasing within the deposit layer of corrosion products with lower relative permeability (5). In addition, the reduction in the thickness of the high permeability iron layer is compensated by the increase in the thickness of the corrosion product layer with lower permeability. As a result, even though the total thickness of the reactive part has increased due to the formation of the corrosion product layer, the net effect is still an increase in the amount of MO due to weak magnetized rusting layer.

To quantify the range and tendency of MO variations associated with the numerical modeling steps shown in Figure 2.15, Figure 2.17a illustrates a schematic of observation points located at distances of 2 cm, 3 cm, and 4 cm from the coordinate origin along the vertical z-axis line of the FMM. These observation points are used to calculate the MO amount at each corrosion step. The amount of MO variation associated with the corrosion evolution on the reactive part, as a function of distance, is shown in Figure 2.17b. The results indicate an upward tendency in MO obtained from all observation points at 2 cm, 3 cm, and 4 cm. This tendency is due to the reduction in iron layer thickness with a relatively high permeability (50) and the simultaneous increase in the deposit layer of corrosion products with lower relative permeability (5). Although the total thickness of the reactive part has doubled (from 2 mm to 4 mm) due to the material transformation and formation of a relatively thick layer of rusting products with lower perme-

ability than iron, the amount of MO is increasing. Thus, despite the increased total thickness of the reactive part from the corrosion product layer, the overall MO would be raised due to reducing the general magnetic permeability and shielding effect from corroded reactive part.
The results also indicate that the amount of MO variation is highly dependent on the distance of the observation points from the FMM device. At a distance of 2 cm, the MO increased from 5.8 mT to 8.4 mT, resulting in a total variation range of 2.6 mT (from step 0 to step 3). Although the MO is raised at distances of 3 cm and 4 cm, the total variation range is decreased to 1 mT (from 3.4 mT to 2.4 mT) and 0.4 mT (from 1.5 mT to 1.1 mT), respectively. Therefore, MO variations are more significant at near-distance.
In addition, the results showed that corrosion-induced reduction in iron layer thickness and formation of a corrosion product layer with lower permeability caused an upward tendency in the magnetic field. The amount of magnetic field variation was found to be dependent on the distance of observation points from the device, with significant variations observed at near-distance monitoring. However, this model has limitations as it does not consider the real case of corrosion products evolution where the reactive part would lose both thickness and surface, and pitting corrosion would occur. Further study is required to determine the precise amount of variations in the future.

2.9 Conclusion

In this chapter, we have reviewed the Biot-Savart equation, the dipolar moment definition, and magnetization related to ferromagnetic materials. As discussed, the magnetic dipole can provide quantitative information about the magnetic properties of materials. This model could be considered as analytical model for the proposed physical model related to this research study in chapter 4.
Furthermore, we performed a parametric study in this chapter to choose the proper material for the FMM. As mentioned, we chose a rare earth magnet of NdFeB for the permanent part and pure iron with 99.99% purity ratio for the reactive part, which is highly sensitive to corrosion and can rust quickly by aggressive agents. We described the magnetic shielding, which attenuates the MO generated by the permanent part, and studied the MO variation range and tendency through numerical models due to changing the geometrical and material characteristics (relative permeability) of the shield. It was numerically confirmed that reducing the geometrical dimensions of the reactive part would attenuate the shielding effect of the reactive part, increasing the MO. The obtained MO at near distances such as 1 cm, 2 cm, and 3 cm, respectively, could provide significant MO variations.
Eventually, through an experimental test, we characterized the corrosion products of the reactive part and calculated their relative permeability value to be equal to 5. Through a linear

numerical model of corrosion evolution on the reactive part, we evaluated the MO variation as a function of material transformation and relative distance. The results show that, although the thickness of the reactive part changes due to the formation of the corrosion product layer, the MO still provides an upward tendency because the permeability of the corrosion product layer is lower than iron. However, the amount of MO variation and the device's sensitivity are dependent on the relative distance to observation points. Environmental parameters such as the magnetic field of the earth, the sensitivity of the interrogators, the uncertainty of measurements, SNR, etc. were not taken into account in this study, and additional investigation is essential.
Additionally, since the geometry of the reactive part plays an important role in the amount of MO, it is essential to determine the effective dimensions of the reactive part and the relative distance. Therefore, in the next section, we will carry out a parametric study of the geometrical characteristics of the FMM device with numerical modeling to evaluate the FMM's performance. These results, along with Chapters 2 and 3, will serve as the basis for Chapter 4 to develop forward method and investigate the amount of magnetic dipolar moment's variation tendency as a function of corrosion.

Chapter 3

FMM principle: Numerical study validation

3.1 Introduction

As explained in Chapter 2, the technological solution of this research study is referred as the FMM, which is supposed to be embedded in RC cover concrete to evaluate its contamination, caused by aggressive agents. The FMM consists of magnetic and ferromagnetic materials in its permanent and reactive parts, respectively. The reactive part of the FMM is exposed to contamination and aggressive agents of concrete media and therefore, is subjected to corrosion. The evolution of corrosion on the reactive part can affect the generated MO of the FMM, which can be measured by an external interrogator. Through numerical models in Chapter 2, it was confirmed that the reactive part acts as magnetic shielding, and its magnetic property and geometry can be affected by corrosion which leads to variation in the amount of MO. In order to establish a relationship between the variation of MO and the contamination level of concrete, it is crucial to identify the key parameters that contribute to the evolution of MO. Therefore, by setting these parameters, it is possible to maximize the MO measurement range and enhance the reliability and accuracy measurements and generally, the FMM performance.
Therefore, Chapter 3 employs numerical modeling of FMM and conducts a series of parametric studies to investigate the MO variation range linked to various key parameters. Given the significant impact of the reactive part dimensions to determine the MO range due to its shielding role as well as the FMM relative distance to measuring points, on the MO variation, the objectives of this numerical study are:

- Determining the effective geometrical properties of the reactive part that could provide the fast and significant MO variation range,
- Evaluating the potential impact of the non magnetic medium with different properties (such as different hydric state, density, permittivity and *etc.*) that FMM coul be embedded there, on MO evolution,
- Investigating the impact of corrosion product evolution on MO variation range and compare the results with reactive part geometrical variation's influence on MO,

— Evaluating the possibility of using a multi-FMM configuration, which components embedding at different concrete depths,
— Verifying the influence of magnetic coupling between the FMMs and also to the rebar, as high permeable ferromagnetic object in reinforce concrete and also its impact on MO evolution.
— Giving an idea about the best location for the FMM in RC structures to minimize interaction with rebar.

In order to achieve these goals, three different numerical configurations are presented in this chapter.
The first configuration assesses the effective geometrical values of the reactive part as a single FMM device embedded in synthetic concrete, with a focus on how changing the reactive part's geometry could influence the range of MO variations. The aim is to determine the most efficient reactive part's geometrical range that can provide fast and considerable MO variations as function of relative distance between FMM and external interrogator. This information is crucial for designing the FMM device geometry. Moreover, configuration 1 would compare the MO variation range, caused by corrosion product evolution, with the variation MO from the reactive part thickness reduction as an index of corrosion evolution, explored experimentally in [217]. Furthermore, the sensitivity of MO to changes in media properties would be examined by embedding the FMM device in various media, such as concrete, mica, Teflon, and seawater. The objective is to determine whether altering the medium (which have very slight differences in magnetic properties) can affect MO or not.
Configuration 2 is examine the possibility of using multi-FMM devices in a synthetic concrete, rather than single device. Here, the objective is mainly to determine the minimum distance among the FMM components that could cause minimum magnetic coupling effect between the FMMs. Moreover, the performance of the multi-FMM configuration associated with reactive part's thickness reduction, would be examined, as well. In this configuration, all FMMs would be identical to avoid introducing additional parameters in the study.
Configuration 3 is similar to Configuration 2, but with the addition of rebar in the synthetic concrete medium. This configuration explores the magnetic coupling effect between rebar and the FMM devices. Moreover, the objective is to determine the possible distance between rebar and FMM that could cause less coupling. This configuration could be useful to give idea about possibility embedding device in RC rebar grids, at the end.
All of these numerical configurations are conducted in 3D module of Ansys Maxwell Software. The Finite Element Method (FEM) is used to solve the Maxwell equation in the modeling. These numerical study results are quite necessary because they provide a feasibility analysis of FMM devices behavior in concrete medium, which is essential for the development of such SHM systems. These numerical results could be helpful for engineers to give an idea to find the

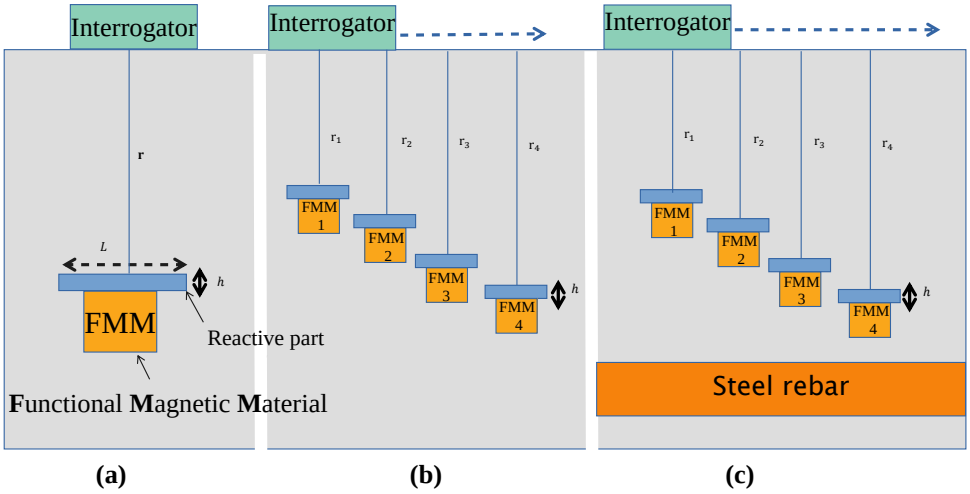

Figure 3.1 – Numerical modeling diagrams: (a) configuration 1 with a single FMM device, (b) configuration 2 with four FMM devices in synthetic concrete, and (c) configuration 3 with four FMM devices in synthetic concrete medium including a rebar

optimized location, where FMM devices could be embedded for monitoring applications and also about the geometry of such embedding components. In the following section, we will describe each configuration in more details.

3.2 The FMM device parametric study planning

In this section, we will provide a more detailed explanation about the methodology of the parametric study, specifically, three numerical modeling configurations. The associated schematic for each configuration is displayed at Figure 3.1. Thereby:

— Configuration 1: it consists of a single FMM device in a synthetic concrete medium, as schematized in Figure 3.1a. This device is be embedded in synthetic concrete at the relative distance **r** to an external interrogator. In the 3D modeling of FMM, the reactive part has a rectangular shape with three dimensions of length, width, and height. The width and length of reactive part are same (*i.e.*, square surface). Thus, the parametric study is focused on two geometrical properties thickness and length (h and L). In this configuration, we would investigate:

1. The effective range of reactive part's geometrical values, as a function of relative distance **r** between FMM and an external interrogator,
2. The MO variation due to reactive part's geometrical variations would be obtained. Then, the results would be compared with MO evolution, caused by corrosion products layer growth on reactive part surface. At this point the main idea is to evaluate

whether, the geometrical modification of reactive part could be used as a reliable indication of corrosion in some extend or not,

3. The possible MO variations due to non magnetic medium's properties changes, such as materials, hydric state, dielectric properties, *etc.* Thereby, the single FMM device would be embedded numerically, in different medium, including mica, concrete, sea-water, and Teflon, to evaluate MO variations, compared to other NDT methods, such as EM techniques, which suffer from high levels of uncertainty due to small variations in media. This analysis provides physical insight into the advantages of using FMM for SHM applications in concrete structures which are subjected to high variations of media's properties by environment.

— Configuration 2: it involves a model of a multi-FMM, embedded in different depths of a synthetic concrete, shown in Figure 3.1b. In fact, using multiple FMM devices can enhance the reliability of proposed SHM technique to detect contamination at various depths and locations in the concrete structure. For this numerical study, four FMM identical are chosen. The choice of using four FMM devices in this numerical study is arbitrary and based on the size of the synthetic concrete model. One effective reactive part geometrical dimensions, based on the results of Configuration 1, is used for FMMs. Then, the overall MO generated by the devices is obtained through an external interrogator which moves horizontally on the external surface. The study includes an investigation of the coupling effect between the FMM devices. It would allows to to determine the effective horizontal distance between FMMs that could result in minimum coupling. Additionally, an assessment of the FMM performance associated with parametric investigation on the reactive part geometry would be conducted. Here, only the parameter of thickness (h) would be changed, simultaneously for all of FMMs. Then, total MO variation range for all of FMMs, would be obtained, as function of reactive part's thickness loss,

— Configuration 3: This step is similar to the second one. The only difference is adding rebar (ferromagnetic material) within the synthetic concrete medium, (illustrated at Figure 3.1c). According to this configuration, beyond studying the effect of the reactive part's thickness variation on MO, the magnetic coupling effect between the rebar and FMM devices would be investigated, as well. Thus, it would be possible to determine the

Table 3.1 – General parametric setup for all objects involved in the 3D numerical configurations

Component's type and material	Shape	Dimensions [mm]	Relative permeability [-]	Meshing size (tetrahedral meshing) [mm]
Concrete	Cubic	half-infinite media	1	2
Permanent part of FMM device (Permanent magnet NdFeB35)	3D Disc	ϕ = 7.5, h = 2	1.099	1
Reactive part of FMM device (Pure iron)	3D Rectangular	variable	50	adaptive (0.1 to 1.0)
Rebar (Ferrite)	Cylindrical	Diameter:30 Length: 300	1000	10

optimal placement of FMM within an RC model through this configuration.
Table 3.1 compiles the general parametric setups of components involved in the three configurations for all the following simulation steps. Each configuration will be described separately in its associated section.
The parametric studies in this chapter focus solely on the reactive part's geometry of the FMM device, since this part is exposed to aggressive agents and corrosion which would results in induced MO variations. Therefore, it is necessary to investigate how reactive part's geometrical changes can affect the induced MO. Moreover, the permanent part of the FMM device is designed to generate the reference magnetic field and magnetize the reactive part. Therefore, It is assumed that by keeping the permanent part, unchanged throughout the study, the MO variations only due to reactive part's geometrical variation could be obtained. Thus, the permanent part serves as a reference value for the study, allowing to only focus on the effects of changes in the reactive part's geometry on generated MO from FMM.
In the next section, a numerical model of the permanent part alone is created to obtain the MO values as a function of distance, which would be used as a reference value for other parametric studies of this chapter.

3.3 Evaluation the MO, generated by FMM

3.3.1 The permanent part

Figure 3.2 shows a schematic of a disc NdFeB35 magnet, which serves as the permanent part and is embedded at the bottom of synthetic concrete. According to Table 3.1, the magnet has a radius of 7.5 mm and a thickness of 2 mm. We obtain the MO generated by the magnet as a function of distance $\mathbf{r}$ at 1 cm, 2 cm, 3 cm, and 4 cm from the center of the coordinate system of the half-infinite medium.
To achieve accurate calculations in numerical modeling, it is important to apply a small mesh size to provide enough details about the physic of each component model. Reducing the meshing size of the components would lead to increasing the simulation's accuracy, however it can significantly increase computational complexity and time of modeling. The reason is due to the fact that the Finite Element Method (FEM) analysis which is used in the numerical modeling, would divided each solid physical components into discrete smaller elements associated with their meshing size. Thus, using extremely small meshing sizes can also result in introducing huge number of element which the magnetic equations, must be solved at them. This may results in convergence issues if we apply a very small meshing size and make the modeling practically impossible.
In order to increase the numerical modeling accuracy without increasing the meshing size of all components, we could use proportional meshing size. For example, for a relatively big object,

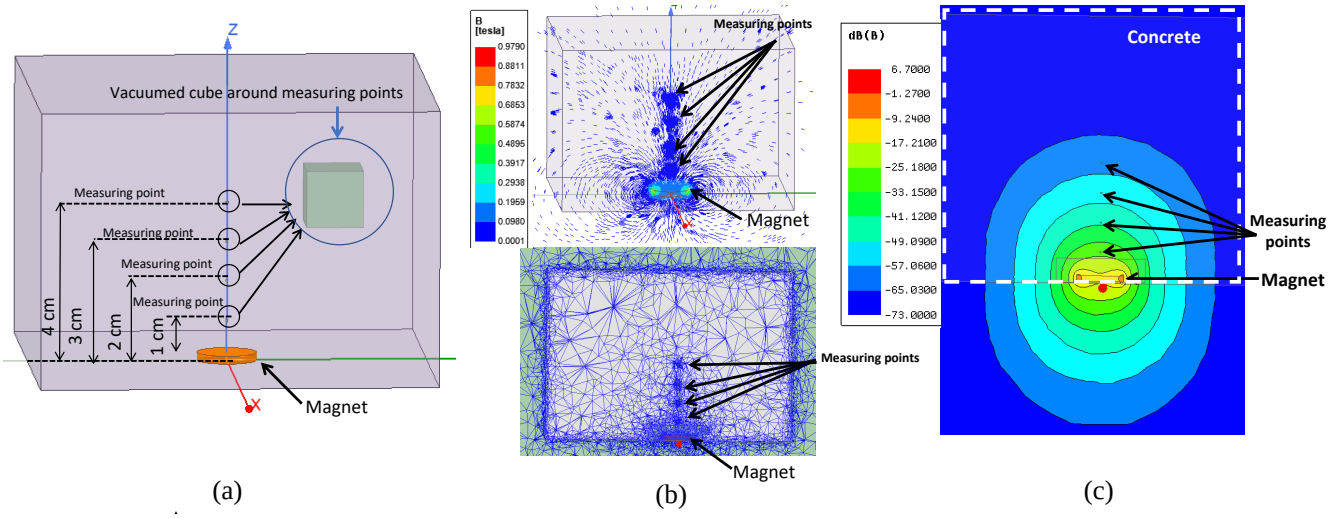

Figure 3.2 – (a) Schematic of the single disc shape magnet, as permanent part of the FMM device, placed at bottom of synthetic concrete. The generated MO are obtained from through four observation points are 1 cm to 4 cm. The measuring points are placing cubic vacuum with small 0.1 mm meshing size to increase the accuracy of modeling with FEM (b) top figure: magnetic flux density lines counter mapping around magnet which are more denser due to relatively small meshing of vacuum cubes around points and also for magnet, bottom figure: meshing plot of model that shows large amount of created elements by FEM, due to small size of meshing for magnet and vacuumed cubes to increase the modeling accuracy (c) MO through iso-value images

we can determine small mesh size in some specific zones of that component, which the calculation there, are important to study with high accuracy. This can be useful in the modeling such relatively big synthetic concrete geometry to obtain accurate calculations at those specific areas which are the interest of study. Therefore, in the model of embedded device in concrete, illustrated at Figure 3.2a, the measurement point are important areas that we need the magnetic calculation carry out there, with high accuracy. Therefore, we could apply some proportionate small meshing zone there.

To do that, a vacuum cube with small dimensions, around each measuring points is created. Knowing that, vacuum cubes do not have any magnetic properties, thus, their involvement in modeling could not affect the numerical results. Using small mesh size for these vacuum cubes ensures the accuracy of numerical modeling would be highly increased.

Eventually, each observation point is placed in a vacuum cube with dimensions of 0.5 mm $\times$ 0.5 mm $\times$ 0.5 mm (indicated in Figure 3.2a). The related meshing size of these vacuum cubes is equal to 0.1 mm (compare to meshing size of 2 mm for synthetic concrete component). Therefore, the FEM method would devided this vacuum cube volumes into large number of elements and the Maxwell calculation to find MO, would be accurately conducted, at measuring points. However, a trade-off between the enough mesh size to increase the accurately and also reducing

Table 3.2 – Amount of MO from permanent part (magnet)

Relative distance	**1 cm**	**2 cm**	**3 cm**	**4 cm**
MO [mT]	41.72	7.79	2.45	1.056

the excessive computational time exists that must be taken into account.
The upper part of Figure 3.2b shows the magnetic flux density generated around the magnet. Due to the small meshing of each of the vacuum cubes, the modeling would be conducted with high accuracy. Thus, magnetic flux lines are more concentrated around the observation points along the vertical line of the z-axis. Similarly, due to relatively small meshing of magnet, magnetic flux lines are denser around. The bottom part of Figure 3.2b shows the meshing plot associated with this modeling. Here, the finite elements have tetrahedra 3D shape. Therefore, the components of modeling such as the magnet and also vacuum cubes with small meshing size, divided into huge number of elements, represented as a denser meshing lines and displayed at Figure 3.2b, compare to synthetic concrete meshing map.
In Figure 3.2c, iso-value images is used to generate a homogeneous MO around the magnet. Usually, iso-value images represent the magnetic field modeling through the magnitude of the induced magnetic field in a given area in color bars. The figure shows that the magnetic field is strongest around the magnet and gradually decreases in a homogeneous tendency as the distance from the magnet increases. Additionally, there is no visible coupling in the distributed magnetic field is obtained, indicating that no magnetic material in the concrete model can alter the magnetic distribution. This suggests that the synthetic concrete medium of this model, being a non-magnetic material, does not significantly influence the MO.
Table 3.2 quantifies the amount of MO generated from only permanent part, as a function of relative distance. As previously explained in Chapter 2, the amount of MO decreases as the relative distance increases. This MO reduction is due to the Biot-Savart law that states an inverse square relationship of the magnetic field source (magnet) and its relative distance to each measuring point.

3.3.2 The MO generated by complete FMM device (permanent part attached to reactive part)

To quantify the MO, generated from a complete FMM (consists of the permanent part attached to the reactive part), a rectangular iron plate with dimensions of 25 mm $\times$ 25 mm $\times$ 1 mm (chosen arbitrarily) and a relative permeability of 50 is added to the reference magnet. Figure 3.3a display a schematic of the FMM component embedded in a synthetic concrete medium. The MO generated by the FMM, is then calculated at four observation points at relative distances of 1 cm, 2 cm, 3 cm, and 4 cm. Upper image at Figure 3.3b illustrates the distribution of magnetic flux density lines generated by the FMM. As explained before, due to placing the observation points in the vacuum cubes with small meshing sizes 0.1 mm, the number

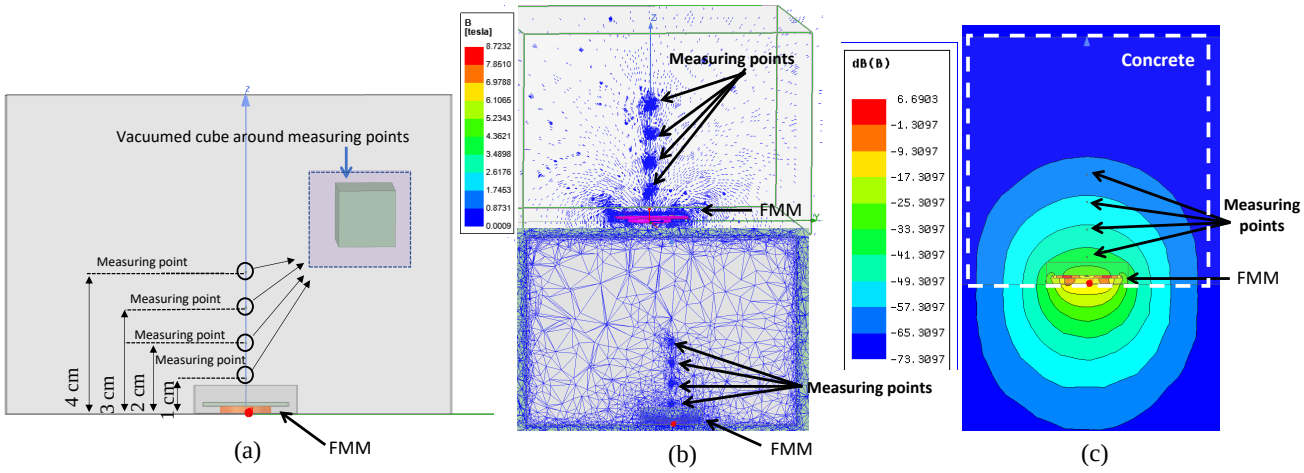

Figure 3.3 – (a) Schematic of the single FMM component, placed at bottom of concrete. The generated MO are obtained from through four observation points are 1 cm to 4 cm. The measuring points are placing cubic vacuum with small 0.1 mm meshing size to increase the accuracy of modeling with FEM (b) top figure: magnetic flux density lines counter mapping around FMM, more denser due to relatively small meshing of vacuum cubes and also for FMM, bottom figure: meshing plot of model that shows large amount of created elements by FEM, due to small size of meshing for FMM and vacuumed cubes to increase the modeling accuracy (c) MO through iso-value images

of modeling elements is higher in those areas, as indicated in the meshing plot at the bottom of Figure 3.3b. Consequently, as it shown in the upper image of Figure 3.3b, the magnetic field lines are denser, around observation points and therefore, the numerical modeling results would be more accurate and reliable on that those areas. Furthermore, Figure 3.3c displays the MO through an iso-value image. By comparing Figures 3.2c and 3.3c, it can be observed that the coupling of reactive part to permanent part, would attenuates the amount of generated MO at observation points, due to the reactive part's shielding property.

In order to quantify the amount of MO attenuation, Figure 3.4 compares the MO generated by the permanent part only and the complete FMM component. Figure 3.4 shows that the amount of MO initially generated by the permanent part of the FMM is 41.7 mT, but it reduces to 13.7 mT at a distance of 1 cm due to the shielding effect of the reactive part. This means that MO is attenuated about 28 mT (41.7 mT - 13.7 mT) by the reactive part. As the distance from the FMM increases, the amount of MO decreases significantly, as displayed in the figure. For instance, at a distance of 2 cm, the amount of MO generated by the magnet is 7.79 mT, but it would be attenuated to 5 mT due to the reactive part. The figure also shows that the amount of attenuation is highly dependent on the relative distance between the FMM and the measuring point. At farthest distance of 4 cm, the MO generated by the permanent part is 1.056 mT, but it is attenuated to 0.73 mT by the reactive part, which means that only 0.32 mT (1.056 mT - 0.73 mT) of MO is attenuated by the reactive part.

Moreover, the efficient MO variation range for the evaluation of cover concrete contamination, depends on other factors such as the type and concentration of contaminants, the depth of the contamination, the sensitivity and resolution of interrogator, and *etc.* Thus, it is crucial to accurately identify the source of any significant change in MO within a certain range, in order to differentiate MO caused by corrosion of the reactive part from other potential parameters. As previously mentioned, this numerical study aims to address some of these key parameters, in order to maximize the MO variation range related to the available contamination of concrete, as a feasibility study. In next section, the parametric study associated configurations 1 (single FMM) would be discussed.

3.4 Configuration 1: single FMM device

Figure 3.5 provides an overview of the first configuration. As previously mentioned, configuration 1 includes one FMM, placed at the bottom of a synthetic concrete. The configuration 1 involves three steps: firstly, to identify the effective geometry of the reactive part *i.e.*, its thickness (h) and the length (L). Due to square shape of reactive part, its surface parameter

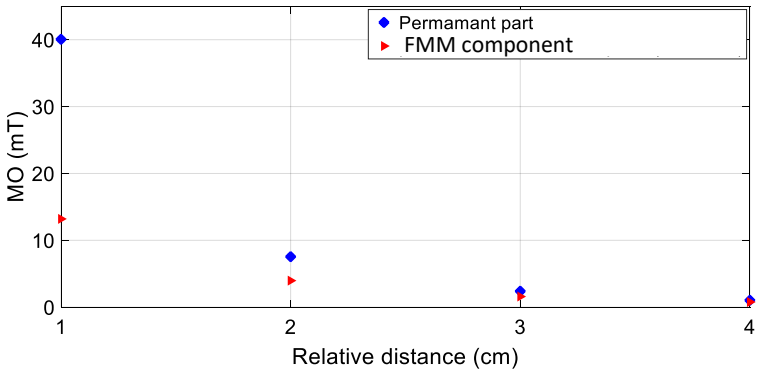

Figure 3.4 – Comparing MO generated from permanent part (reference value) and the FMM component

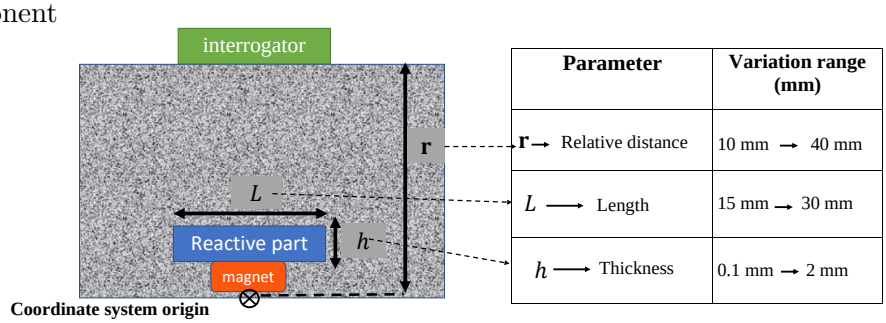

Figure 3.5 – Overview of the parametric study plan to find effective geometrical variables associated with FMM device's performance

is length. Then, the MO would be calculated through changing these two parameters and also as a function of relative distance to the external interrogator (**r**). To achieve the first objective, we will independently vary the thickness and length of the reactive part and calculate the MO changing for each parameter variation. This will enable us to determine the effective range of values of each parameter, which could provide fast and reasonable MO variation range.
Secondly, we will use the results from the experimental study in Appendix B about the characterization of corrosion products to evaluate the MO variation range, in terms of corrosion product evolution on the reactive part surface. The results would be compared with MO evolution due to reactive part's thickness loss. It would allow us to create a more reliable model that can provide a reliable assumption of the corrosion evolution, in some extend.
Finally, we will assess the impact of changing medium's properties (such as its hydric state, dielectric, material and *etc.*) on the MO generated from a single FMM to numerically evaluate that MO are not sensitivity to concrete medium's properties or not. AS previously mentioned, all of the numerical modelings will be conducted in 3D module of Ansys Maxwell software and the FEM is used to solve the Maxwell equations in magnetic domain.

3.4.1 Effective geometry of reactive part: thickness value

First, a fixed value of 25 mm was arbitrarily chosen for the length of the reactive part (L), which has a square-shaped surface of 25 mm × 25 mm. Then, we would examine the variations of MO as a function of thickness changes, ranging from 0.1 mm to 2 mm with a step size of 0.1 mm. Simultaneously, we would calculate the MO as a function of relative distance to interrogator (**r**), which is varied from 1 cm to 4 cm in increments of 1 cm. For each thickness value, MO variations is separately obtained at each relative distance.
Figure 3.6 illustrates the reduction in the amount of MO with an increase in reactive part

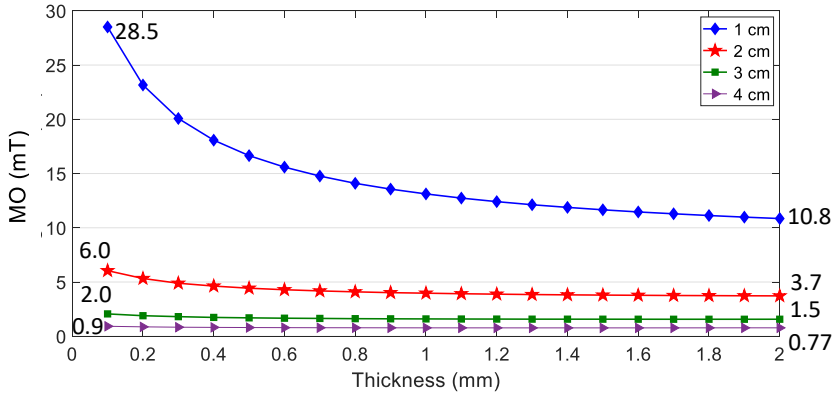

Figure 3.6 – Configuration 1: the amount of MO variation *versus* reactive part thickness increment and as function of different relative distances between FMM and interrogator, from 1 cm to 4 cm

thickness. The reduction in measured MO is a result of the shielding effect of the reactive part. As the size of the reactive part increases, the magnetic shielding effect becomes stronger, resulting in a decrease in the measurable MO above the reactive part. Figure 3.6 illustrates the amount of MO variations as function different relative distances, as well. It shows that the amount of MO reduction (range of MO changing) is also dependent on the relative distance between the FMM and the observation points, with a more significant at shorter distances. For instance, at a relative distance of 1 cm, the MO variation range was calculated by 17.7 mT (28.5 mT - 10.5 mT). However, for the observation points located at relative distances of 2 cm and 3 cm, the MO variation range dramatically dropped to 2.3 mT (6 mT - 3.7 mT) and 0.5 mT (2 mT - 1.5 mT), respectively.
Furthermore, based on the graphs tendency and slopes, shown in Figure 3.6, it can be concluded that the thickness of the reactive part has a significant impact on the performance of the FMM device. All of the graphs in Figure 3.6 exhibit a rapid changing in MO reduction with increasing thickness up to 1 mm. However, by raising reactive part's thickness more that 1 mm, the MO variation rate becomes slow down. The results suggest that selecting a thickness within the range of 0.4 mm to 1 mm can provide a rapid and sufficient MO variation range, which is essential for the FMM effective performance. While a thickness greater than 1 mm may result in a more significant MO variation range, it would be at the cost of slower changing and time. Therefore, it is recommended to choose a thickness within the range of 0.4 mm to 1 mm for the reactive part, could be a good compromise to achieve the most effective performance of the FMM device.

3.4.2 Effective geometry of reactive part: surface area

In the second step, with a slight modification, we investigate the MO variations of the FMM, due to parametric study on reactive part's surface area. The reactive part has a 3D rectangular

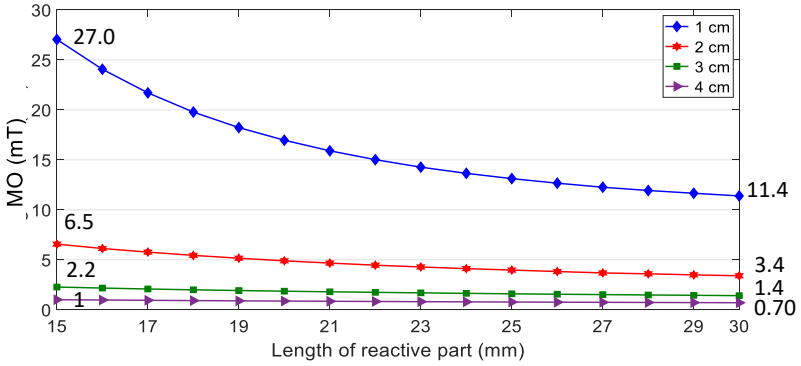

Figure 3.7 – Configuration 1: amount of MO variation *versus* reactive part surface increment and as function of different relative distances between FMM and interrogator, from 1 cm to 4 cm

shape with a square surface area of $L \times L$, where L represents the length of each side, and a thickness of h. To keep the other parameters constant, the thickness of the reactive part will be fixed at 1 mm. In order to conduct a parametric study on the surface area, the length (L) will be varied from 15 mm to 30 mm in increments of 1 mm.

The graph shown in Figure 3.7 displays the MO variation with increasing length of the reactive part. Increasing the surface of reactive part leads to higher magnetic shielding and a decrease in amount of MO. Additionally, the relative distance between the measurement point and the reactive part is a critical factor in amount of MO variations.

The effect of increasing the surface of the reactive part on MO variation range can be observed at different relative distances. At the nearest distance of 1 cm, the MO variation range is 15.6 mT (27 mT - 11.4 mT). However, as the relative distance increases to 2 cm and 3 cm, the MO variation range reduces to 3.01 mT (6.5 mT - 3.4 mT) and 0.8 mT (2.2 mT - 1.4 mT), respectively. At the farthest distance of 4 cm, the maximum MO variation range is only 0.37 mT (1 mT - 0.63 mT). The reduction in MO variation range is non-linear due to the inverse square relationship of the relative distance with the induced magnetic field, as mentioned in the Biot-Savart law. Therefore, the MO variation range is more significant at closer distances between 1 cm and 3 cm compared to farther distances beyond 4 cm.

Similar to the previous discussion, the rate of MO variation in the graphs shown in Figure 3.7 tends to slow down after a certain value of reactive part's length. The MO reduction is dramatic from a length of 15 mm to 26 mm, but the slope of the graphs slows down after 26 mm. On the contrary, increasing the length of the reactive part would result in a relatively bigger MO variation range due to the change in surface geometry, but at the cost of time. Therefore, for the application like corrosion which is a very slow processes, it is necessary to balance the trade-off between time and MO variation. Thus, selecting an effective length within the range of 18 mm to 26 mm can provide a good compromise between reasonable MO variation and relatively rapid MO changing. Below this range, the MO variation range is lower, and beyond it, the rate of MO variation slows down.

In addition, it should be noted that the selection of the initial surface size of 15 mm $\times$ 15 mm was based on the diameter of the magnet equal to 15 mm. Therefore, the provided geometrical range is with respect to the dimensions of the permanent part, as well. Of course, with using a smaller magnet, the compromise range, mainly for length parameter may be altered. Furthermore, additional experiments are required in future to determine the potential amount of volumetric loss of the reactive part that can occur in a real case scenario when it is attached to the magnet and FMM is embedded at concrete.

Based on the results of the previous two parametric studies, it can be concluded that for the ideal case where the geometry of the reactive part is significantly affected by corrosion, the effective range of the reactive part's geometry that can provide a good compromise between reasonable

MO range and fast variation are choosing:

— Thickness (h): between 0.4 mm and 1 mm,

— Length (L): between 18 mm and 26 mm.

In the previous two parametric studies, we focused only on geometric loss of the reactive part. However, in real cases, specifically the reactive part's thickness could be expended due to the growth of the corrosion product layer during the time (as discussed in Section 2.8, Chapter 2), which is not considered in the parametric study of this section. Therefore, in the next section, we will re-evaluate the MO variation range, by taking into account the evolution of the corrosion products layer on the reactive part.

3.4.3 The effect of corrosion products evolution *versus* thickness reduction

Section 2.8.3, from Chapter 2 discusses the impact of corrosion product evolution on the reactive part, in addition to its thickness reduction, through numerical modeling. While thickness reduction alone can lead to increased MO variations, the question remains as to what extent considering the evolution of rust along with the reduction in thickness can further affect MO changes. Additionally, it is important to determine whether thickness reduction alone can serve as a reasonable approximation for corrosion evolution on the reactive part without considering the presence of corrosion products.

To address these questions, a comparative study is conducted using numerical modeling to quantify and compare the MO variations obtained from the model that accounts only for thickness reduction (discussed in section 3.4.1) with the model that considers both thickness reduction and corrosion product evolution simultaneously on the reactive part.

As it discussed in Chapter 2, and also according to the studies in [10, 218, 219] the volume of corrosion layers on iron is typically 2-3 times larger than the volume loss of the metal. Therefore, similar to numerical modeling of corrosion products growth in Section 2.8.3, the ratio of 2.5% is considered for the corrosion products thickness evolution. In this study, a relative permeability of 5 is assumed for the corrosion products, as determined experimentally in Appendix B.

Table 3.3 presents a summary of the numerical modeling steps for thickness loss and rusting layer growth. The initial geometry of the reactive part is 25 mm × 25 mm × 2 mm to ensure a fair comparison with the results presented in section 3.4.1. The reactive part thickness is reduced from 2 mm to 0.1 mm, with the step of 0.5 mm. At the same time the corrosion products layer form on the surface of reactive part, with a rectangular deposit and constant surface area of 25 mm × 25 mm. As previously mentioned, the thickness of the corrosion products layer would be 2.5 times of reactive part's thickness loss at each step. Finally, four steps are indicated in the Table 3.3 which the thickness of corrosion products layer would be raised by 1.25 mm, 2.5 mm, 3.75 mm, and 4.75 mm, respectively.

Furthermore, the MO was measured at 2 cm, 3 cm, and 4 cm relative distances from the center

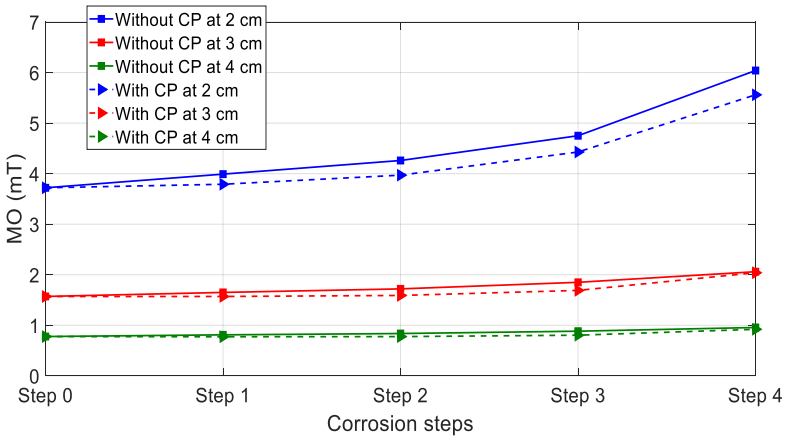

Figure 3.8 – (a) MO (mT) variations of four corrosion steps with Corrosion Products (CP) and without CP (b) the percentage of MO relative attenuation variation for corrosion evolution with and without CP different media types and their properties

of the coordinate system, likewise two previous parametric study on single FMM.

Figure 3.8 compares the MO variations with and without corrosion products as a function of different measurement points on the z-axis. The results presented in Figure 3.8 indicate that the evolution of corrosion products, would lead to a slight decrease in the amount of MO. This is expected, as the deposited layer of corrosion products has a relative permeability of 5 and exhibits weak paramagnetic properties. As discussed in section 2.8.3, this generates an additional weak shielding effect on the reactive part. Consequently, the reactive part attenuates the MO to a greater extent compared to the case where only the reactive part is present. Table 3.4 summarizes the MO variation ranges calculated for each observation point, taking into account the thickness loss of the reactive part with and without the presence of a corrosion product layer. The results indicate that at a relative distance of 2 cm, the MO variation range is 2.32 mT

Table 3.3 – The steps of modeling corrosion products

	Reactive part thickness [mm]	**Corrosion Products (CP) thickness [mm]**
Step 0	2	0
Step 1	1.5	1.25
Step 2	1	2.5
Step 3	0.5	3.75
Step 4	0.1	4.75

Table 3.4 – Comparing amount MO variation range (mT) caused by thickness reduction, with and without presence of corrosion products as function of relative distances

Measuring points [cm]	**MO variation from only thickness loss [mT]**	**MO variation from thickness loss and corrosion products evolution [mT]**
2 cm	6.04-3.72 = 2.32	5.56-3.72 = 1.84
3 cm	2.06-1.57 = 0.49	2.04-1.57 = 0.47
4 cm	0.95-0.77 = 0.18	0.92-0.77=0.15

when considering only the reactive part thickness loss. However, when the presence of corrosion products is taken into account, the MO variation range decreases to 1.84 mT, resulting in a difference of 0.48 mT. The same trend is observed at distances of 3 cm and 4 cm. However, the difference becomes smaller for farther distances. At the measuring points of 3 cm and 4 cm, the difference in MO variation range between with and without corrosion products is approximately 0.03 mT (30 μ). Given the uncertainty in numerical modeling due to meshing, it is possible that the differences in MO variations are a result of changing the meshing at each modeling step. As a result, the differences observed at farther distances could be considered negligible, but this requires further experimental tests to confirm.
Moreover, the presented results are limited to the effect of thickness reduction on MO variations, while in real case scenarios, the evolution of corrosion products is expected to be non-linear and non-homogeneous on the reactive part. Other factors such as pitting corrosion, stress corrosion cracking, and corrosion under insulation may not be reflected in the thickness reduction alone. Thus, thickness reduction can be used as an index of corrosion to some extent, but it is not a comprehensive assumption for all the cases. Thus, further experimental investigations are necessary to comprehensively assess the role of corrosion products in influencing MO variations to complete this study in the future.

3.4.4 Effect of medium properties on MO variations

The presented numerical model investigates the effect of changes in the medium properties, on the MO generated by single FMM. The model considers the device embedded in various types of medium, such as concrete, mica, Teflon, and seawater, which have different dielectric permittivity, hydric state, hardness, density, and other properties. However, all of these media have very weak and negligible magnetic properties and can be considered as non-magnetic materials. Figure 3.9a shows a schematic of the model, and the MO is calculated as a function of distance. The geometry of the reactive part of the FMM device is 25 mm $\times$ 25 mm $\times$ 1 mm, as obtained from the parametric study in the previous part. The properties of each medium, such as magnetic permeability, hydric state, density, and so on, are provided in Figure 3.9b, and are taken from the library of Ansys Maxwell.
Figure 3.10 shows the result of MO variations as a function of relative distances and varieties of the medium properties. The graph presented in the figure shows two main results. Firstly, it indicate the amount of MO decreases with increasing the relative distance (from 13.52 mT to 0.8 mT), which is consistent across all medium types tested, including concrete, mica, Teflon, and seawater. Secondly, it shows that the amount of MO is obtained identical for all medium types. It indicates that changing the properties of the medium, which the has not magnetic property, would have no impact on MO of FMM. These results could initially support the advantage of FMM, that the generated MO is independent of environmental variations and specifically, mod-

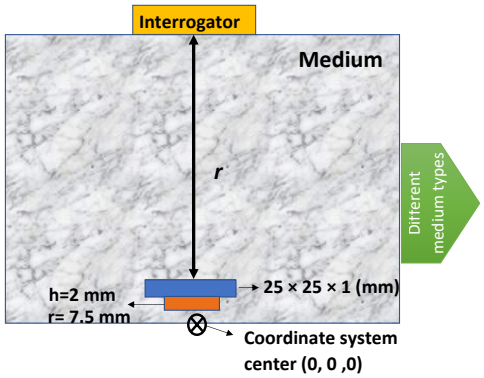

(a)

Medium types	Relative permeability	Bulk conductivity (siemens/m)	Magnetic coercivity	Hydric state	Density (gm/cm^3)
Concrete	1	0	0	dry	2.4
Mica	1	0	0	dry	2.6 - 3.2
Teflon	1	0	0	dry	2.2
Seawater	0.999	0.0002	0	wet	1

(b)

Figure 3.9 – (a) Schematic of FMM device and in the distance of r from surface of media (b) different media types and their properties

ification of medium properties.

Thus, the proposed FMM, could offer a more robust and reliable indicator for the penetration of aggressive agents in concrete. However, it is essential to validate these results through experimental tests with varying medium properties (different hydric states, porosity, thickness and *etc.*) in future.

The next section will present a complex FMM component model, consisting of four identical FMM components with the a chosen efficient reactive part geometry value (25 mm × 25 mm × 1 mm).

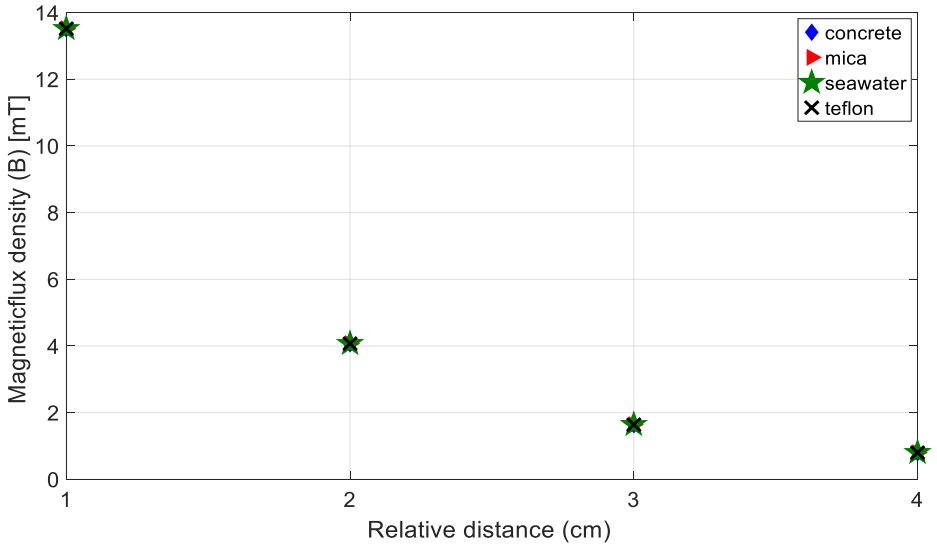

Figure 3.10 – MO (Magnetic flux density (B)) variations as function of relative distance and different media

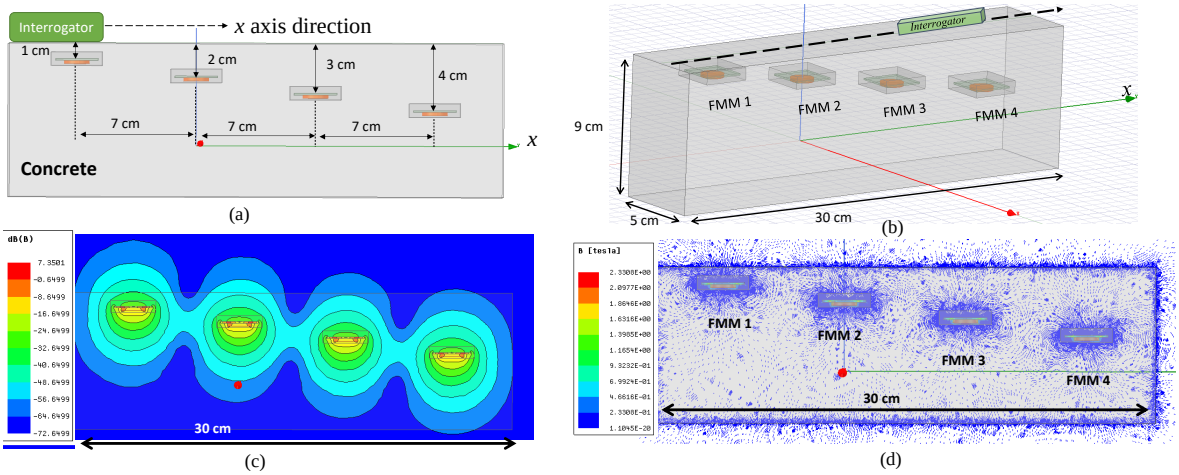

Figure 3.11 – (a) Four FMM components embedded in synthetic concrete with constant surface area of the reactive part equal to 25 mm × 25 mm (b) 3D view multi-FMM model (c) iso-value image of the system (d) MO contour lines

3.5 Configuration 2: multiple FMM components in concrete

The second configuration of the numerical study involves evaluating the performance of multi-FMM embedded components in synthetic concrete. The primary aim of utilizing multi-FMM at various depths within the concrete is to enhance the system's effectiveness in evaluating concrete contamination in various locations. Additionally, this configuration would allow to assess the performance of multi-FMM devices associated with MO variation range as function of reactive part thickness changing.

In order to determine the feasibility of using a multi-FMM component arrangement, it is crucial to evaluate the potential magnetic coupling between the components. To achieve this, four identical FMM components are positioned in the synthetic concrete at varying depths ranging from 1 cm to 4 cm, as depicted in Figure 3.11a. The dimensions of synthetic concrete model equals to 30 cm × 5 cm × 9 cm. The reactive parts of the FMM components have 25 mm length, and to minimize coupling between the FMMs, the horizontal distance has been chosen to be approximately three times larger than the length of the reactive parts (25 mm × 3 roughly equals to 7 cm). Basically, since two magnetic materials are placed at close distance, their induced magnetic field can interact with each other, causing deviations in the measured magnetic output. Therefore, by increasing the distance between the magnetic components, the possibility of such interactions and coupling can be minimized. Therefore, here, the idea is that whether the horizontal distance of 7 cm, sufficient to minimize the coupling between FMM or not.

To complete the setup, an external interrogator moves parallel to the components along a horizontal line on the top of the synthetic concrete, as shown in Figure 3.11b. As mentioned earlier, the simulation aims to achieve two objectives. Firstly, to determine the amount of possible cou-

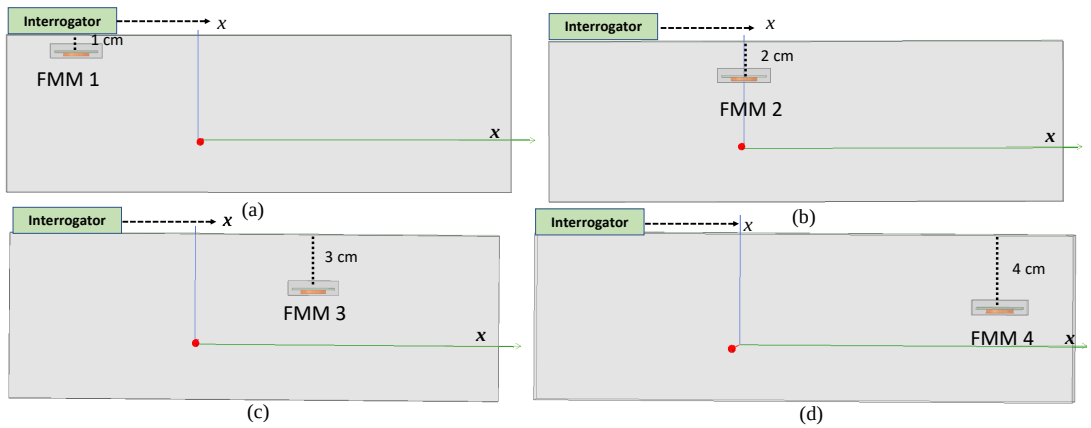

Figure 3.12 – Schematic of each FMM component alone without other components and the external interrogator that move parallel to x-axis

pling effect between the components, and secondly, to measure the amount of magnetic field variation (MO) in the multi-FMM component model, as an indicator of corrosion risk progression, with respect to changes in the reactive part's thickness.

To accomplish the first objective, the MO variations of each component are assessed individually. Then, by comparing them with the overall MO generated by all the components together, the coupling effect can be investigated. Regarding the second objective, we would model the MO variations as function of thickness increments of 0.2 mm, 0.5 mm, 0.8 mm, and 1 mm. For this model, the reactive part's geometry of the FMM components is initially set to the effective values obtained in the previous section (25 mm × 25 mm × 1 mm).

To address the first objective, Figure 3.11b illustrates a 3D schematic of the FMM component, embedded in a half-infinite synthetic concrete. Each component is placed in a vacuum box to prevent numerical modeling errors, caused by interaction between two different materials of concrete and FMM. Figure 3.11c presents the MO around each component through the iso-value image. It demonstrates the internal magnetic coupling between the components, which is quantitatively in the range of -49 dB to -50 dB.

Furthermore, in Figure 3.11d, the magnetic field contour lines around each component and in the medium are displayed. It reveals that the MO is more detectable for the FMM components closest to the concrete surfaces, at 1 cm and 2 cm distances, and less significant for the FMM components at 3 cm and 4 cm.

To quantify the magnetic coupling between the components, four separate MO graphs were obtained for each component. Figure 3.12 depicts a schematic of each FMM component in the concrete and the external interrogator that records the MO on its top surface.

Figure 3.13 compares the results of MO for each component independently (associated with each Figure 3.12) with the overall simulated MO simultaneously produced through the four FMM components. The maximum value of amount of MO generated by all of FMM components are

equal to 9.4 mT, 3.01 mT, 1.2 mT, and 0.65 mT. The comparison of the MO peaks of graphs associated with each FMM independently and the graph for the all four components together reveals that the maximum MO values are well adapted for components 1 and 2. However, for the furthest components, of FMM 3 and FMM 4, a very slight difference can be observed at the peak of graphs. These variations are less than 0.001 mT and could be be caused by changing the numerical modeling meshing and are possible to considered as negligible effect. Furthermore, the MO graphs in Figure 3.13 show slight overlaps at the valleys of MO curves. Although the horizontal distance 7 cm between the FMM components is chosen to minimize coupling and magnetic interaction, some degree of overlap is still observable. However, the amount of these overlaps are less than 0.1 mT. Comparing with the amount of MO at the peaks, the overlapping at the valleys of the MO graphs could be considered as insignificant value and can be ignored. In summary, the simulation confirms that the multi-FMM configuration can generate a reliable MO output without significant coupling between the FMM components, by the keeping 7 cm horizontal distance. This result is only applicable to FMMs with the mentioned geometry of 25 mm ×25 mm× 1 mm. Hence, if the size or geometry of FMMs differs from this efficient configuration, the minimum horizontal distance should be investigated accordingly.

To address the second objective of configuration 2, the variation of MO in the multi-FMM configuration is examined as a function of changes in the reactive part's thickness. Figure 3.14 compares the MO variations, calculated along the x-axis for each FMM component with respect to changes in reactive part thickness and the relative to the external interrogator. Actually, setting the reactive part thickness to 0 mm means that the MO value is only generated through the permanent part (magnets) and can be considered as the reference MO value. Thus, the MO generated from magnet shows the amount of MO at each peak are: 24 mT, 5.45 mT, 1.85 mT,

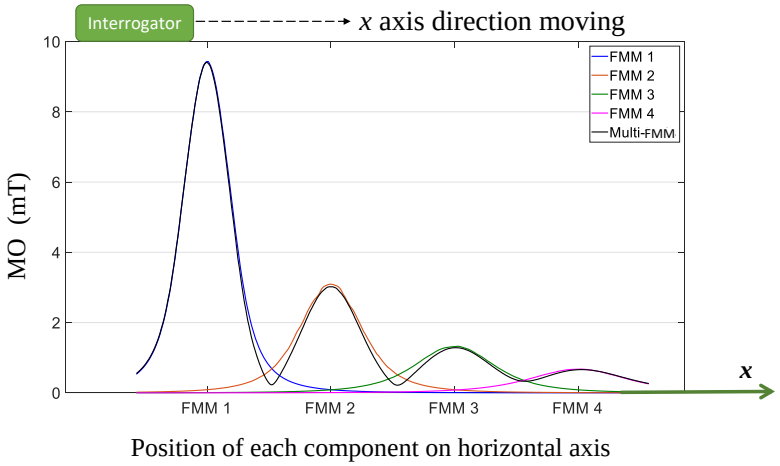

Figure 3.13 – Numerical model configuration 2: MO for each FMM components independently *vs.* MO from all four components with a reactive part dimension of 25 mm × 25 mm × 1 mm

and 0.84 mT, respectively, generated from FMM 1 to FMM 4.

The results shown in Figure 3.14 indicate that the MO variation is more significant for the component at the nearest surface, *i.e.*, FMM 1 (at a 1 cm distance in the synthetic concrete). The use of multi-FMM components can offer the advantage for the detection of local contamination level in concrete. Therefore, the FMM components can be strategically placed at different depths in the concrete (or several locations) with keeping minimum horizontal distance to avoid their internal coupling. Then, they detect the presence of aggressive agents at various depth and locations with the assumption of gradient penetration of aggressive agents from surface. Additionally, in practical situations, changes in the geometry of the reactive part due to corrosion, may not be occurred simultaneously for all FMM components. In fact, the FMM 1 is located near to concrete surface is more exposed to external factors such as moisture and other aggressive agents that can cause corrosion. Therefore, the deeper components could experience corrosion at a slower rate compared to FMM 1.

Additionally, the amount of MO variation for each component will be influenced by various factors, including the level of contamination concentration around the component, the aggressive agent's penetration depth, pH or porosity of medium, the component's location within the concrete, the interrogator's sensitivity to record variations in farther distances and *etc.* In these cases, calculating the relative MO variation would be a useful approach to detect and identify these variations, even the small changes.

In the next section, Configuration 2 will be extended by adding a rebar at within the synthetic concrete model.

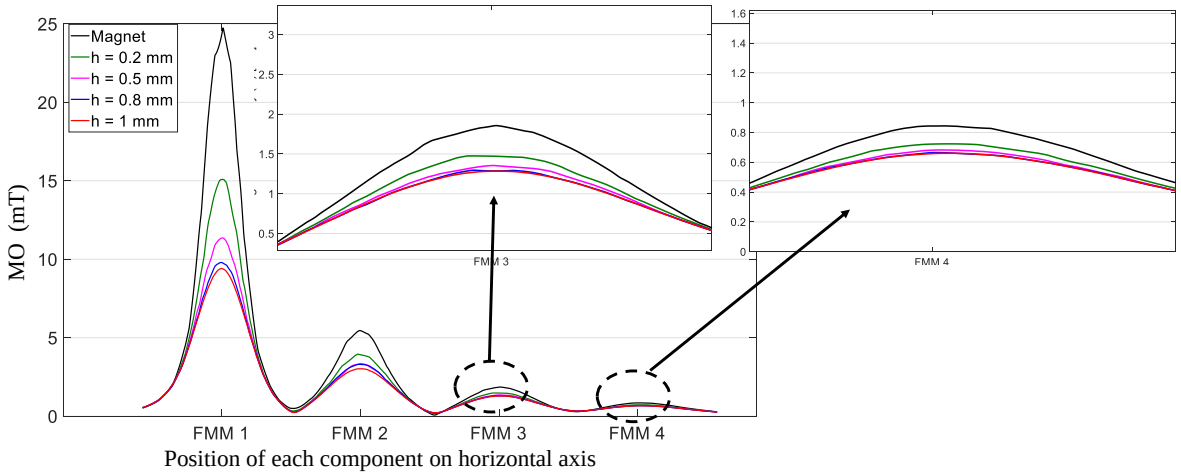

Figure 3.14 – Configuration 2: Variations in magnetic flux density (MO) relative to a changing of reactive part thickness with a constant reactive part surface area of 25 mm × 25 mm

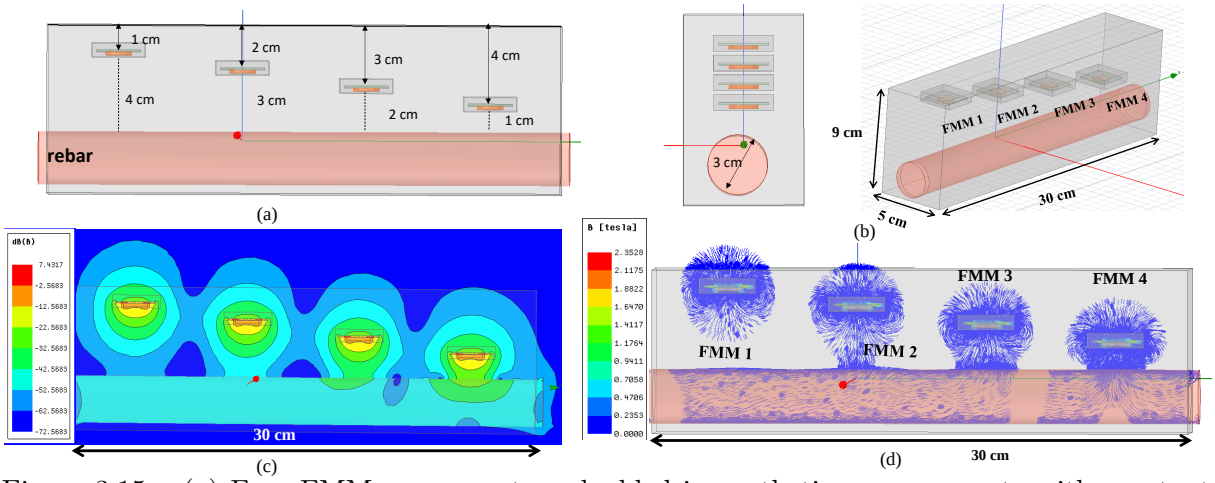

Figure 3.15 – (a) Four FMM components embedded in synthetic cover concrete with constant surface area of the reactive part equal to 25 mm × 25 mm and also a cylindrical ferrite rebar (b) side view and 3D view multi-FMM model with rebar (c) iso-value image of the system (d) MO contour lines

3.6 Configuration 3: multiple FMM components in concrete with rebar

Since the FMM is assumed to be embedded in RC structure as novel magnetic approach, there is a possibility that a magnetic coupling between the FMM magnetic materials and the nearest rebar, as highly permeable ferromagnetic object, would be occurred. This coupling could potentially cause variations in the MO values. To investigate the potential magnetic coupling with rebar, which also known as the border effect, the previous design of configuration 2 is modified by adding rebar. The dimensions of rebar as well as its location in a synthetic cover concrete model, have been taken from the French national standards for bridges and reinforced concrete structures in a marine environment [40]. However, only a longitude rebar is added to simplify the modeling. Thus, the chosen rebar has 30 mm diameter and placed in 5 cm relative distance from the top surface of the synthetic concrete, as shown in Figure 3.15a. Therefore, the FMM 1 to FMM 4, has the relative distances of 4 cm to 1 cm, from the rebar, respectively. Furthermore, Figures 3.15b show the 3D side views of this configuration. Regarding the information listed in Table 3.1, ferrite with a permeability of 1000 has been assigned as the rebar material and the deduced mesh size is equal to 10 mm. The dimensions of synthetic concrete is similar to configuration 2, equals to 30 cm × 5 cm × 9 cm. The main objectives of this numerical model are twofold: 1) investigating the couplin effect between FMMs and also from the rebar on MO, and 2) assessing the MO variation range with respect to the reactive part thickness variations. Considering the first objective, Figure 3.15c represents the MO, generated from FMMs in the medium, through iso-values. As it illustrated, by adding the rebar, all the magnetic FMM components would have some amount of coupling with the rebar. The amount of coupling is highly

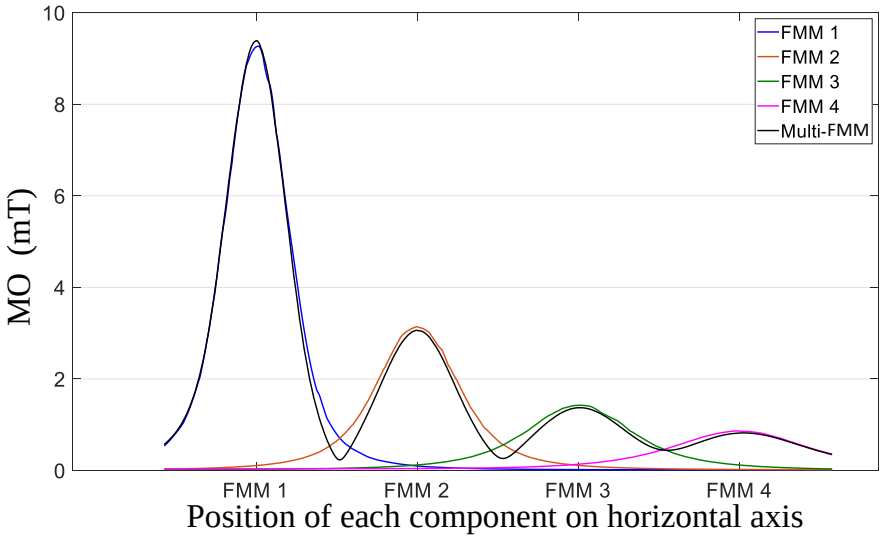

Figure 3.16 – Configuration 3: MO for each FMM components independently *vs.* MO from all four components with a reactive part dimension of 25 mm × 25 mm × 1 mm with the presence of rebar

dependent on the distance to the rebar. For instance, the last two nearest components to the rebar (FMM 3 and FMM 4) provide the more detectable coupling (between -22 dB to -32 dB), as it illustrated in Figure 3.15c. However, the amount of coupling is fewer for two other FMM components that are near the surface (*i.e.*, FMM 1 and FMM2). Similar results are provided in Figure 3.15d by magnetic flux line's contour map. As it displayed, magnetic flux lines at the FMM 3 and FMM 4 are clearly coupled with rebar and the rebar in those areas, become magnetized by FMMs and can redirect magnetic flux lines.

In order to investigate the effect of rebar coupling on MO graphs, Figure 3.16 compares the MO generated by the each of four components independently, and also through all four FMMs together, using a moving interrogator along the x-axis. The results indicate that the presence of rebar have not major impact on the peak values of the MO graphs, specifically for FMM 1 and FMM 2. However, for FMM 3 and FMM 4, the amount of MO peaks is very slightly increased, which is not lead to significant changes, as well. Therefore, the results suggest that the coupling effect between FMMs and rebar has negligible impact on amount of MO, by keeping the mentioned distance of minimum 1 cm, from rebar. While some overlap is visible in the valley of the graphs (similar to configuration 2), which the amount of these MO overlaps are less than 0.5 mT, and can be considered negligible, as well. Overall, the results suggest that the use of multi-FMM components in RC structures is feasible, with maintaining the minim distance from rebar.

In order to address the second objective, Figure 3.17 illustrates the results of MO variations, as a function of the reactive part's thickness reduction from 1 mm to 0 mm. The results indicate

that reducing the thickness of the reactive part leads to an increase in MO for all component's peak. The MO variation range is more significant for FMM 1 and FMM 2, which are closer to the interrogator. For FMM 1 and FMM 2, the MO variation range is obtained by 15.4 mT (24.7 mT - 9.3 mT) and 2.4 mT (5.4 mT - 3.0 mT). However, the MO variation range reduces to 0.5 mT and 0.05 mT for FMM 3 and FMM 4. Focusing on the MO variations for FMM 3 and FMM 4, reducing the thickness of the reactive part causes very slight fluctuations in their obtained peak MO (illustrated in Figure 3.17). The possible reason for this observed variations could be explained by the FMMs coupling with the rebar, as high permeable material. When the permanent part generates MO, it could magnetize both the reactive part and the rebar, as illustrated in Figure 3.15d. Thus, removing the reactive part could lead to more redirection of magnetic flux lines through the rebar, resulting in relatively stronger magnetic coupling. Although this could cause some extend of coupling, the amount observed fluctuations is still very small and not affected the overall tendency of the MO, even for FMM 4. Thus, for this configuration, the distance of 1 cm, is sufficient to minimize the coupling effect with rebar.

Based on the results from numerical configuration 3, the presence of rebar could cause some magnetic coupling with FMMs, mainly with the nearest FMM components. However, by keeping the minimum safe distance from rebar, it could be possible to decrease the border effect on performance of multi-FMM configuration. Therefore, it is very important to find the optimal position for FMM, in order to decrease potential interference between FMMs and rebar. It is important to note that these results are only applicable to this specific numerical modeling, with the given component dimensions. As previously mentioned, the amount of magnetic coupling to the rebar is highly dependent on various factors such as the geometry of the FMM device and rebar, the relative permeability of the rebar, power of permanent magnet and so on. Therefore, for each multi-FMM configuration with different geometries, it is necessary to re-evaluate the amount coupling effect and find the minimum safe distance from the rebar.

In the next section, the range of MO variations with and without presence of rebar, associated

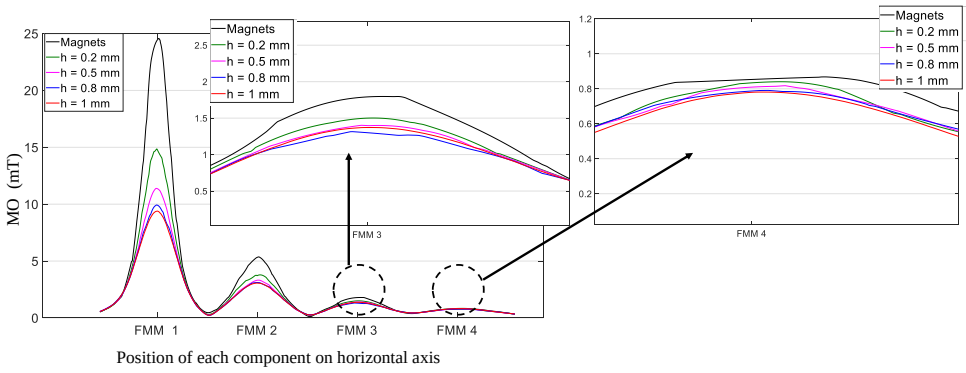

Figure 3.17 – Configuration 3: output signal with reactive part variations in the presence of rebar

with configuration 2 and 3, will be compared and discussed.

3.7 Coupling from rebar: results and discussions

To evaluate the multi-FMM configuration, with and without rebar, Figure 3.18 is used to compare the MO graphs, generated from multi-FMM in configurations 2 and 3, for reactive part with fixed dimensions of 25 mm × 25 mm × 1 mm. The graphs show that FMM1 and FMM2 have almost identical MO values in their peaks, regardless of the presence of rebar. However, for the nearest component to the rebar, FMM 3 and FMM 4, the MO peaks have slightly increased in the presence of rebar, compared to configuration 2. For instance the peak of MO in FMM 4, is increased from 0.65 mT to 0.77 mT due to adding the rebar.
In order to compare precisely the MO differences due to presence of the rebar, Table 3.5 provides a comparison between two configurations. Overall, the results indicate that the presence of rebar leads to slight raising in the amount of MO, for all FMMs. However, it is not the same results for MO variation range.
The table illustrates that the range of MO variations is very slightly higher with adding the rabar for far FMMs (FMM 1 and FMM 2), however for FMM 3 and FMM 4, the total MO variation range is lower by adding the rebar. As previously shown in Figure 3.17, some slight fluctuations were obtained in its related MO peak for FMM 3 and FMM 4, making it difficult to determine the exact MO peak value. Thus, the MO variation range decreases (or could fluctuate) in the FMM components that are affected with rebar coupling. This conclusion highlights the importance of maintaining a proper distance between FMMs and rebar.
Based on the insignificant differences in the range of MO variation for the other FMMs, it can be inferred that the presence of rebar has a negligible impact on the overall performance of multi-FMM configurations as long as they are positioned at the maximum possible distance from the rebar. However, as previously stated, the coupling would be existed and should be taken into

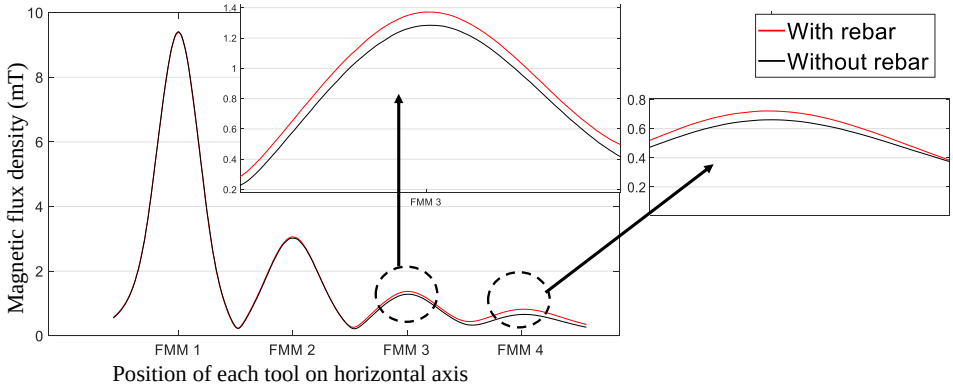

Figure 3.18 – Comparison of raw MO values for the multi-FMM components model in applying an identical components geometry value: 25 mm × 25 mm × 1 mm for configurations 2 and 3

Table 3.5 – Comparison of MO variation for multi-FMM configurations with and without presence of rebar as function of reactive part's thickness

Configuration 2: Without rebar				
MO [mT]				
FMM components	**FMM 1**	**FMM 2**	**FMM 3**	**FMM 4**
reactive part thickness = 0 mm (magnets or permanent part only)	24.5	5.38	1.7	0.80
Reactive part = 0.2 mm	14.7	3.7	1.47	0.72
Reactive part = 0.5 mm	11.3	3.5	1.35	0.68
Reactive part = 0.8 mm	9.7	3.1	1.26	0.66
Reactive part = 1 mm	9.2	3.02	1.25	0.65
Total variation range	15.3	2.36	0.45	0.15
Configuration 3: With rebar				
Reactive part thickness = 0 mm (Magnets or permanent part only)	24.7	5.4	1.8	0.83
Reactive part = 0.2 mm	14.8	3.77	1.49	0.81
Reactive part = 0.5 mm	11.39	3.3	1.39	0.79
Reactive part = 0.8 mm	9.9	3.1	1.28	0.77
Reactive part = 1 mm	9.3	3.04	1.37	0.78
Total variation range	15.4	2.36	0.43	0.05

the account.

The current numerical configuration only includes a single longitudinal rebar. However, in practical cases, concrete reinforcements consist of the mesh or grid of steel bars rather than a single rebar. Therefore, it is crucial to locate FMMs at a maximum distance from the grid of steel rebar to minimize magnetic coupling.

Based on the results of this section, one simple assumption is to place the FMM components at the center of the rebar mesh, which is the farthest point from the rebars and less susceptible to magnetic coupling. However, further investigations are essential, both numerically and experimentally, to validate this assumption.

Indeed, interpretation of the results would be more difficult, if other parameters from environment such as noise would be added and the results could be more precipitated. Therefore, such configurations should be re-examined by adding different possible parameters, while the others are keeping constant. Then, the experimental tests could validate the assumptions as well as the results.

3.8 Conclusion

In this chapter, a numerical parametric study was conducted using Ansys Maxwell software's 3D module and FEM method to investigate the range of MO variation associated with the FMM principle. It was assumed that the geometry of the reactive part would be affected due to cor-

rosion, caused by aggressive agents in the concrete medium. The study aimed to determine the effective geometrical properties of the reactive part to maximize the MO variation range measured by an external interrogator. In addition, other objectives included evaluating the potential impact of non-magnetic medium on MO, investigating the impact of corrosion product evolution on MO variation range, evaluating the possibility of using a multi-FMM component configuration, verifying the influence of magnetic coupling between FMMs and also to the rebar, and determining the best location to place FMM in reinforced concrete structures.
To address these objectives, three numerical configurations have been presented and their results was discussed.
Configuration 1 consists of a single FMM components embedded in synthetic concrete at different relative distance to an external interrogator. The study focused on the thickness and length as two key parameters related to geometry of reactive part. The objectives were to determine the effective range of the reactive part. The results of parametric studies have shown that the effective range of the reactive part's geometry that can provide a good compromise between reasonable MO range and fast variation is: a thickness range between 0.4 mm and 1 mm and a length range between 18 mm and 26 mm. This conclusion was drawn for the ideal case where the geometry of the reactive part is significantly affected by corrosion.
Moreover, the configuration 1 compare MO variations caused by corrosion product layer growth on the reactive part surface with only thickness reduction of reactive part. It was concluded that the reduction in the thickness of the reactive part of the FMM device led to a relatively greater range of MO variation compared to the growth of the corrosion products layer on the reactive part surface. However, the difference was very small. Thus, it concluded that taking geometrical modification of the reactive part could be used as a reliable assumption of corrosion.
Furthermore, in configuration 1 the possible impact non-magnetic medium properties changes on the MO have been evaluated. It was observed that the FMM had a relatively high immunity to the medium's changes in comparison to other NDT techniques. Therefore, the FMM could be a reliable option for SHM applications in concrete structures, which are subjected to high variations of media's properties by the environment.
Configuration 2 of the numerical study aimed to evaluate the performance of multi-FMM embedded components in synthetic concrete for the purpose of enhancing the system's effectiveness in evaluating concrete contamination in various locations. The configuration involved positioning four identical FMM components at varying depths ranging from 1 cm to 4 cm in the synthetic concrete and assessing the potential magnetic coupling between the FMMs. Additionally, the performance of multi-FMM devices associated with MO variation range as a function of reactive part thickness changing was evaluated. The results showed that the MO was more detectable for the FMM components closest to the concrete surfaces, and the magnetic coupling between the components was quantitatively in the range of -49 dB to -50 dB. It was also observed that for

this numerical model geometry, horizontal distance of 7 cm, could cause the minimum coupling effect, between FMMs. Overall, the use of multi-FMM components in synthetic concrete was found to be feasible for evaluating concrete contamination in different locations.

Configuration 3 involved investigating the potential magnetic coupling effect between FMMs and nearest rebar in a synthetic cover concrete model. A cylindrical ferrite rebar with a permeability of 1000, with a 30 mm diameter placed at 5 cm relative distance from the top surface of the synthetic concrete. The objectives of this model was to investigating the coupling effect between FMMs and rebar on MO, and assessing the MO variation range with respect to the reactive part thickness reduction. The results show that all the magnetic FMM components have some amount of coupling with the rebar, which is highly dependent on the distance to the rebar. The coupling effect has a slight impact on the MO, mainly obtained for nearest FMM to rebar at, distance of 1 cm. Finally, it concluded that the presence of rebar did not cause major impact the overall peak values of the MO graphs for FMMs. Thus, by maintaining the safe distance from rebar (for this model 1 cm), it could be possible to minimize coupling effect from rebar, on overall performance of FMMs.

Eventually, it could be concluded that in practical cases, concrete reinforcements consist of a mesh or grid of steel bars rather than a single longitudinal rebar, and it is crucial to locate FMMs at a maximum distance from the grid of steel rebar to minimize magnetic coupling. One simple assumption is to place the FMM components at the center of the rebar mesh, which is the farthest point from the rebars and less susceptible to magnetic coupling. However, further investigations are needed, both numerically and experimentally, to validate this assumption, especially when considering other environmental parameters.

Eventually, this study provide a feasibility analysis of FMM devices performance in concrete, which is essential for the development of SHM embedded systems. The study can be helpful for designers and engineers in providing insight into the optimized location for embedding multi FMM devices for monitoring applications in the risky zones of concrete. By knowing where to place the FMM components, engineers can optimize their SHM systems. This study can also serve as a basis for future investigations related to behavior of FMM devices in more complex environments with additional parameters such as noise.

Chapter 4

Forward model and Inversion

4.1 Introduction

In Chapter 2, we delved into the magnetization process in ferromagnetic materials, where external magnetic fields align their domains, creating magnetic dipole moments. This concept, governed by Maxwell's equations and the Biot-Savart law, permits the treatment of magnetic sources, like our FMM device, as magnetic dipoles. Chapter 3 introduced our FMM device, composed of magnetic components. We have assumed that if the reactive part of the FMM corrodes due to aggressive agents, its magnetic properties change, affecting its magnetic dipole moment. To test this hypothesis, a reliable forward model is essential to estimate the magnetization (quantify by magnetic dipolar moment) of the FMM's reactive part as it evolves due to corrosion. Drawing inspiration from [188], where magnetic dipolar moments were used to track vehicles, we propose a similar approach for estimating the FMM's magnetic dipolar moment. This forward and inversion method employs an analytical model to establish a relationship between the induced magnetic field (MO) of the FMM and its corresponding magnetic dipolar moment. By applying optimization techniques and inversion methods, we can quantify the magnetic dipolar moment. Evaluating the effectiveness of this proposed method in estimating magnetic dipolar moment variations, linked to the reactive part's corrosion evolution (including material changes and geometric deformations), is crucial as it introduces a new non-destructive technique.
To do that, we would investigate the proposed forward and inversion method in this chapter through several steps. The first step is to choose a proper analytical model. In this chapter, we evaluate and compare two existing analytical models for this purpose and finally, choose the best model. The second step of this study is applying and comparing two algorithms of Levenberg-Marquardt and the Nelder-Mead to solve the Nonlinear Least Squares (NLS) optimization problem. The NLS technique would be applied to estimate the magnetic dipolar moment as an unknown parameter. Finally, the results of optimization will be compared to choose the best-fitted algorithm for NLS optimization problem.
Furthermore, the proposed method requires a reference model which can provide the MO as a function of reactive part's corrosion evolution. In this chapter, we choose to use a numerical model of FMM to generate MO. The hypothesis is that corrosion can affect the geometrical properties of the reactive part. We have separately evaluated this hypothesis using multiple ex-

perimental tests and they results are published in [217]. The experimental study validated that the geometrical properties of the FMM's reactive part are subjected to changes due to corrosion, which, in turn, can alter the total amount of MO, generated by FMM. Using this result, in the numerical modeling of FMM, we would change the reactive part's thickness to obtain MO variations. For the numerical modeling, we will use the ANSYS Maxwell software and Finite Element Method (FEM). Various sources, including [220, 221], and the official ANSYS website [222], recommend ANSYS Maxwell as a powerful software tool for modeling and analyzing the behavior of devices in the electromagnetic, electrostatic, or magnetostatic domains, using FEM and FE Analysis (FEA) to solve Maxwell's equations. Therefore, we have decided to use ANSYS Maxwell to represent the numerical model of the FMM device and assume that it will offer accurate modeling of FMM.
To ensure the repeatability of the numerical modeling and the proposed method's results, we will create series of numerical configurations of FMM with different geometries as reference models. This will enable us to determine the range and tendency of magnetic dipolar moment variations as a function of the changes in reactive part geometry, for each FMM configuration.
In addition, through analysis and comparing the results of this chapter, we would be able to evaluate and validate the proposed method that correlates the variations in magnetic dipolar moment of the embedded SHM device with, corrosion level of reactive part and eventually, assess the risk of rebar corrosion, as a new magnetic ND approach. As previously discussed, this approach offers some advantages, such as being less sensitive to environmental variations and only highlighting the MO variations of FMM caused by corrosion through aggressive agents of the cover concrete. Once successfully validated, this new method could serve as a reliable means to monitor the aggressive agents level of cover concrete, and send an on time alarm for the risk of rebar corrosion to infrastructure managers as a preventive measure, compare to other traditional methods.

4.2 Analytical models

4.2.1 Single magnetic dipolar moments

As mentioned in the introduction, at the first step, we would study the existing analytical model that could relate the MO of any magnetic source to the amount of magnetic dipolar moment. One of the most commonly used analytical expressions for this purpose, as discussed in Section 2.2, is the Biot-Savart law. This equation is generally applicable to any material that can be magnetized by an external magnetic field. The induced magnetic field $\mathbf{B}(\mathbf{r})$ is calculated as a function of the relative distance between the measuring point and the magnetic dipolar moment of the FMM, as magnetic source. This equation would be labeled as analytical model

1:

$$\mathbf{B}(\mathbf{r}) = \frac{\mu_0}{4\pi} \frac{3(\mathbf{r}.\mathbf{m})\mathbf{r} - |\mathbf{r}|^2 \mathbf{m}}{|\mathbf{r}|^5} \tag{4.1}$$

The Biot-Savart law is indeed a general equation that can be used to calculate the magnetic field induced by any current carrying element in magnetized material (or magnet), including a magnetic dipole. It has advantage to calculate the magnetic dipolar moment of any magnetic source, regardless of its shape, provided that the distance between the measuring point and the source is greater than the magnetic source's geometry. This is required due to the use of the first-order Taylor series approximation in solving the Maxwell equations, mentioned in [189, 187].

Besides the Biot-Savart law, alternative existing analytical expressions for rare earth magnets can calculate the induced magnetic field at a distance **r** This model is highly dependent of the shape and geometry of magnet and can be found in [223, 224]. We would use the equations for cylindrical magnet shape here. As illustrating in the Figure 4.1, the cylindrical magnet has the length of L, radius α and total volume of V. It has a permanent magnetization of **M** which is uniform for inside, outside, and parallel to the z-axis. As displayed in Figure 4.1b, the direction of the magnetization vector is determined through the north/south pole as $\mathbf{M}_z$ (equivalent to surface charges of σ_m on both hypothetical monopoles). The objective is to measure the $\mathbf{B}(z)$ at the point of P, which is assumed to induced by a volume element of dv at the distance of **r**, as illustrated in Figure 4.1c.

Since, the magnetization for the inside of magnet is existed, the magnetization vector could be alternatively, stated as: $\mathbf{M}_z = \mathrm{M}_0\hat{z}$.

Using the magnetization vector and by solving the Maxwell equations in magnetostatic domain [224], the total uniform magnetic flux density for outside the cylindrical magnet would be

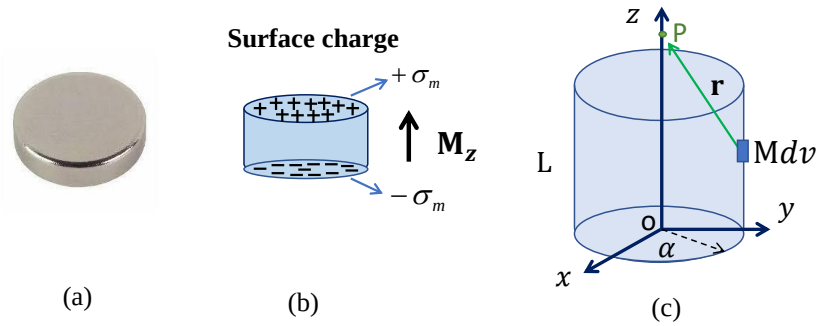

Figure 4.1 – (a) Real image of NdFeB magnet (b) distribution of surface charges on the north/south poles of a magnet and the generated magnetization vector (c) schematic of a cylindrical magnet with a thickness of L and radius of α and total volume of V that induced magnetic field by a volume element of dv at the point of P

calculated and labelled as analytical model 2:

$$\mathbf{B}(z) = -\frac{\mu_0 \mathrm{M}_0}{2}\left[\frac{z-\mathrm{L}/2}{\sqrt{\alpha^2+(z-\mathrm{L}/2)^2}} - \frac{z+\mathrm{L}/2}{\sqrt{\alpha^2+(z+\mathrm{L}/2)^2}}\right]\hat{z} \tag{4.2}$$

Reminding from Chapter 2, the amount of magnetization $\mathbf{M}$ could be also stated with the definition of magnetic dipolar moments per unit volume. Thus:

$$\mathbf{M} = \lim_{\Delta v \to 0} \frac{\sum_{i=1}^{k\Delta v} \mathbf{m}_i}{\Delta v} \tag{4.3}$$

Here, k is the number of dipoles which in case of considering single dipole, it would be equal to 1. Eventually, the Eq. 4.2 can be re-expressed MO in terms of the magnetic dipolar moment, as well.

As explained earlier, any variations in the magnetic properties of the FMM device can result in the overall magnetic dipolar moments variation. As discussed in Chapter 2, Section 2.4, the ferromagnetic substrate of the FMM's reactive part consists of a magnetic domains that are oriented in the same direction as the north/pole direction of the magnet, as permanent part. Thus, it could be assume that each domain could be considered as a magnetic dipole which determine the magnetic property of each material. When corrosion affects a specific part of reactive part's volume, the initial orientations and magnetite of the corresponding magnetic dipolar moments within that area, would be altered while for the rest of the material's volume, the magnetic properties may be remain unaffected. Therefore, in such cases, it is useful to divide the total volume of reactive part into smaller sub-regions and study the corresponding magnetic dipoles of each region separately. This approach provides a more comprehensive understanding of reactive part's magnetic property changing by corrosion, even small variations and have more advantageous than concentrating solely on a single dipole for representing its whole volume.

In the next section, both proposed analytical expressions of Eq. 4.1 and Eq. 4.2 will be represented based on multi-magnetic dipolar moment's model.

4.3 Multi-magnetic dipolar moments

As explained, magnetic properties variations in FMM due to corrosion, result in changes in amount of overall magnetic dipolar moments. Studying the behaviour of material, considering multiple magnetic dipolar moment model instead of a single dipole provides a more comprehensive understanding of the material's magnetic properties, even in the presence of small or partial variations. Thus, the hypothesis is that by dividing the reactive part's total volume into smaller sub-regions and analyzing the corresponding magnetic dipoles of each area separately, it can be possible identify any variations in magnetic properties that may not be detectable when

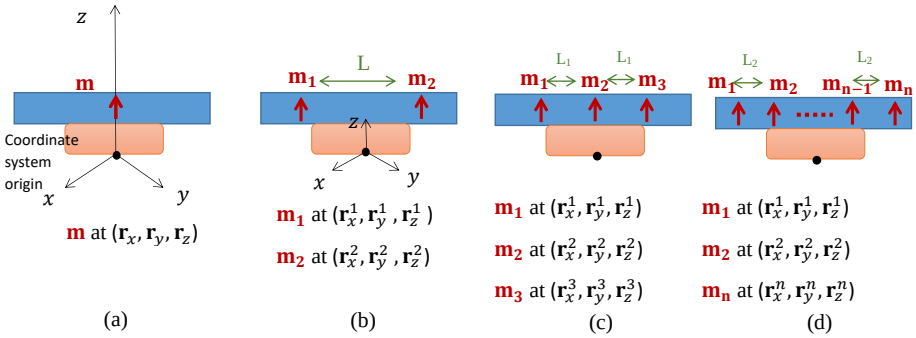

Figure 4.2 – Schematic representation of FMM with row of dipoles (a) one dipole (b) two dipoles (c) three dipoles (d) n dipoles

analyzing the material as a whole and through a single dipole.

To evaluate the hypothesis, Figure 4.2 illustrates a schematic representation of the FMM device, which consists of multiple magnetic dipolar moments on its reactive part. Each magnetic dipolar moment is a vector in the Cartesian coordinate system with components ($\mathbf{m}_x$, $\mathbf{m}_y$, $\mathbf{m}_z$), representing the values of the vector along the x, y, and z-axis, respectively. In this figure, the resultant of magnetic dipolar moment vectors is shown. Additionally, the relative distance vector $\mathbf{r}$ ($\mathbf{r}_x$, $\mathbf{r}_y$, $\mathbf{r}_z$) between each dipole and observation point is separately indicated. Figure 4.2b shows a configuration of two magnetic dipolar moments model. The dipoles are placed in a row, with internal distance of L from each other. Figure 4.2c and d display an arrangement of three dipoles and four dipoles with the same interval distance of L_1, respectively. Figure 4.3 illustrates a row of q dipoles. The magnetic flux density is calculated at an observation point P_n, located at a distance of d_n from the coordinate system origin. Therefore, the relative distance between each dipole and the observation point is denoted by $\mathbf{r}^1$ to $\mathbf{r}^q$, respectively, for each dipole. For instance, the relative distance between the i^{th} dipole and the observation point is calculated as $\mathbf{r}_i = |\mathrm{d}_i - \mathbf{r}^i|$. The interval distance between dipoles is also assumed to be equal for all.

To simplify the modeling, we have made the assumption, following [188], that the magnetic dipoles are arranged horizontally along a single axis. This means that the dipoles are positioned along either the x or y-axis, with similar values for z. The analytical model presented in [188], which is based on this row dipolar configuration, modifies the analytical model 1 as given by

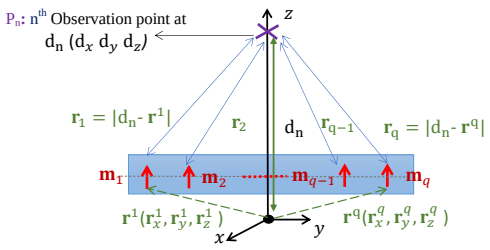

Figure 4.3 – Representing of FMM through q number of magnetic dipoles, placed in a row within the reactive part's volume and at relative distance of $\mathbf{r}_q$ from the observation point of P_n

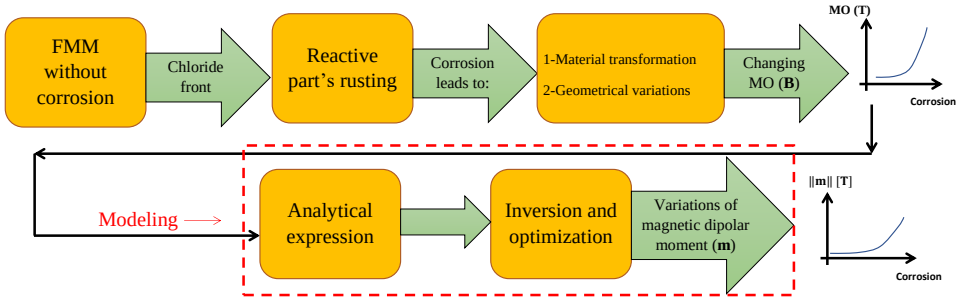

Figure 4.4 – Block diagram of proposed forward and inversion method

Eq. 4.1, as:

$$\mathbf{B}(\mathbf{r}) = \frac{\mu_0}{4\pi} \sum_{i=1}^{q} \frac{3(\mathbf{r}_i.\mathbf{m}_i)\mathbf{r}_i - |\mathbf{r}_i|^2 \mathbf{m}_i}{|\mathbf{r}_i|^5} \tag{4.4}$$

Subsequently, the analytical model 2, presented in Eq. 4.2 would be also changed with consideration of the Eq. 4.3, into the:

$$\mathbf{B}(z) = -\frac{\mu_0}{2\mathrm{V}} \sum_{i=1}^{q} \left[\frac{z_i - \mathrm{L}/2}{\sqrt{\alpha^2 + (z_i - \mathrm{L}/2)^2}} - \frac{z_i + \mathrm{L}/2}{\sqrt{\alpha^2 + (z_i + \mathrm{L}/2)^2}} \right] \mathbf{m}_i \hat{z} \tag{4.5}$$

In both of equations, **B** is magnetic flux density [mT] which is initially, introduced as MO. In Eq. 4.5, the parameter such as V, α and L are previously explained at Figure 4.1.
To sum up, in this section, we introduced the concept of magnetic dipolar moment and its relation to the magnetization of the FMM device and generation of MO. We also presented two analytical expressions for modeling FMM as the magnetic dipolar moment, both through one or multi-dipoles. In the next section, we will discuss the proposed forward and inversion method and the related essential steps to eventually, estimate the amount of magnetic dipolar moment of the FMM's reactive part.

4.4 Proposed forward and inversion method

As explained in previous sections, the objective of the proposed forward and inversion method is to estimate the amount of magnetic dipolar moment of the FMM's reactive part. The block diagram presented in Figure 4.4 outlines the steps of the forward and inversion method. As illustrated, the MO variations of FMM device due to reactive part's corrosion would be considered as reference data. Then, an analytical model would be applied to estimate the amount of magnetic dipolar moments. To carryout the estimation, a NLS optimization technique could be applied. Finlay, through inversion technique and by minimizing the error between MO of numerical model and analytical model, the amount of magnetic dipolar moments will be estimated as function of reactive part's corrosion. Cornering the modeling step (indicated in Figure 4.4) and in general framework for the estimation problems, the input parameters denoted by x_k and output param-

eters represented by $\mathbf{y}_k$, which are considered as multi-dimensional stochastic variables. These variables are related through a function of $\mathbf{h}$ as:

$$\mathbf{y}_k = \mathbf{h}(x_k) + \mathbf{e}_k \tag{4.6}$$

k is an integer value which is regarded as dimensions of input and output parameters $\mathbf{h}$ is actually, the forward model that relates the unknown parameter x_k to the measured data, and $\mathbf{e}_k$ is the error or any noise that could be measured from different sources and will be added to the system [225].
Concerning the reference model, the MO variations could be provided through either numerical modelings of FMM (MO as function of reactive part thickness reduction) or experimental tests (measuring MO variations as function of reactive part's corrosion state). As previously explained, in this chapter, numerical configurations will be used as reference models. These reference models can serve as a benchmark for evaluating the accuracy of the proposed forward and inversion method and its effectiveness to estimate the magnetic dipolar moment associated with degradation of reactive part. More information associated with the chosen numerical configurations, will be explained in the associated Section 4.4.1.
Regarding the analytical model 1, the Eq. 4.6 would be:

$$\mathbf{y}_k = \mathbf{h}(\mathbf{r}_k, \mathbf{m}_k, \mathbf{B}_0) + \mathbf{e}_k \tag{4.7}$$

In fact, magnetic dipolar moment is a vector quantity that represents the magnetic properties of the reactive part of the FMM, which is related to its physical characteristics such as geometry or material. The magnetic dipolar moment can be used to quantify the amount of magnetization caused by the permanent part of the FMM or its ability to shield the magnetic field generated by a magnet. Therefore, the amount of dipolar moment is a fixed value for each FMM, and totally independent from the parameters such as relative distance to measuring point [226]. Analyzing the behavior of FMM through variations in a single magnetic dipole vector can significantly simplify the modeling process, providing a significant advantage. The modeling for one single dipole, using analytical model 1 would be:

$$\mathbf{y}_k = \mathbf{B}_0(\mathbf{r}_k) + \frac{\mu_0}{4\pi}\frac{3(\mathbf{r}_k.\mathbf{m})\mathbf{r}_k - |\mathbf{r_k}|^2\mathbf{m}}{|\mathbf{r_k}|^5} + \mathbf{e}_k \tag{4.8}$$

Similar to [188], here we consider the $\mathbf{B}_0(\mathbf{r}_k)$ is the stationary magnetic field of the earth and a time-variant vector. $\mathbf{B}_0(\mathbf{r}_k)$ could be usually measured through experimental tests. Assuming that the magnetic field of earth is uniform throughout the region of study, the $\mathbf{B}_0(\mathbf{r}_k)$ could be simply considered as $\mathbf{B}_0$.

Eventually, the E.q. 4.8 for for multi-dipoles modeling will be:

$$\mathbf{y}_k = \mathbf{B}_0 + \frac{\mu_0}{4\pi} \sum_{i=1}^{q} \frac{3(\mathbf{r}_{k,i}.\mathbf{m}_i)\mathbf{r}_{k,i} - |\mathbf{r}_{k,i}|^2 \mathbf{m}_i}{|\mathbf{r}_{k,i}|^5} + \mathbf{e}_k \tag{4.9}$$

Here, q is the number of dipoles. Subsequently, for i^{th} dipole, the relative distance to observation point, would be $\mathbf{r}_{k,i}$. Eventually, using the superposition principle for magnetic dipoles, the magnetic dipolar moment resultant (total) would be calculated from:

$$\mathbf{m}_{total} = \sum_{i=1}^{q} \mathbf{m}_i \tag{4.10}$$

Therefore, $\mathbf{m}_{total}$ would be considered as final result which is the net amount of magnetic dipolar moments in reactive part.
Similarly, for analytical model 2, the modeling equation for row of dipoles (based on magnetic dipolar moment vector component on z-axis ($\mathbf{m}_{i,z}$), instead of magnetization $\mathrm{M}_i\hat{z}$, respect to Eq. 4.3) would be:

$$\mathbf{y}_k = \mathbf{B}_0 + \frac{-\mu_0}{2\mathrm{V}} \sum_{i=1}^{q} \left[\frac{\mathrm{z}_{k,i} - \mathrm{L}/2}{\sqrt{\alpha^2 + (\mathrm{z}_{k,i} - \mathrm{L}/2)^2}} - \frac{\mathrm{z}_{k,i} + \mathrm{L}/2}{\sqrt{\alpha^2 + (\mathrm{z}_{k,i} + \mathrm{L}/2)^2}} \right] \mathbf{m}_{i,z} + \mathbf{e}_k \tag{4.11}$$

By setting $q = 1$, this model will be used as single dipole. The analytical model 2 is fundamentally used for rare earth magnets. Thus, the related magnetic dipolar moments are initially represented based on the magnetization vector (M). Moreover, this model only expresses the magnetic dipolar vector component in the z direction. Thus, the relative distance is also identified as $\mathrm{z}_{k,i}$.
Finally, for both analytical models 1 and 2, the objective minimizing the cost function error between $\mathbf{B}_{reference}$ (obtained by numerical modeling or measured by experimental data) and $\mathbf{B}_{analytical}$ as:

$$\mathbf{e}_k = \sum_{k=1}^{n} |\mathbf{B}^k_{analytical} - \mathbf{B}^k_{reference}| \tag{4.12}$$

The n is the number of iterations, need to find global minimum of cost function error and eventually, determine the optimal value of $\mathbf{m}$, as output. As previously explained, the both proposed analytical models could relate the magnetic dipolar moment of the reactive part to the amount of MO generated by FMM.
To complete the discussion about the proposed method's steps, the next two sections will review the numerical configurations used as reference models, as well as provide a brief overview of the optimization techniques and relevant algorithms.

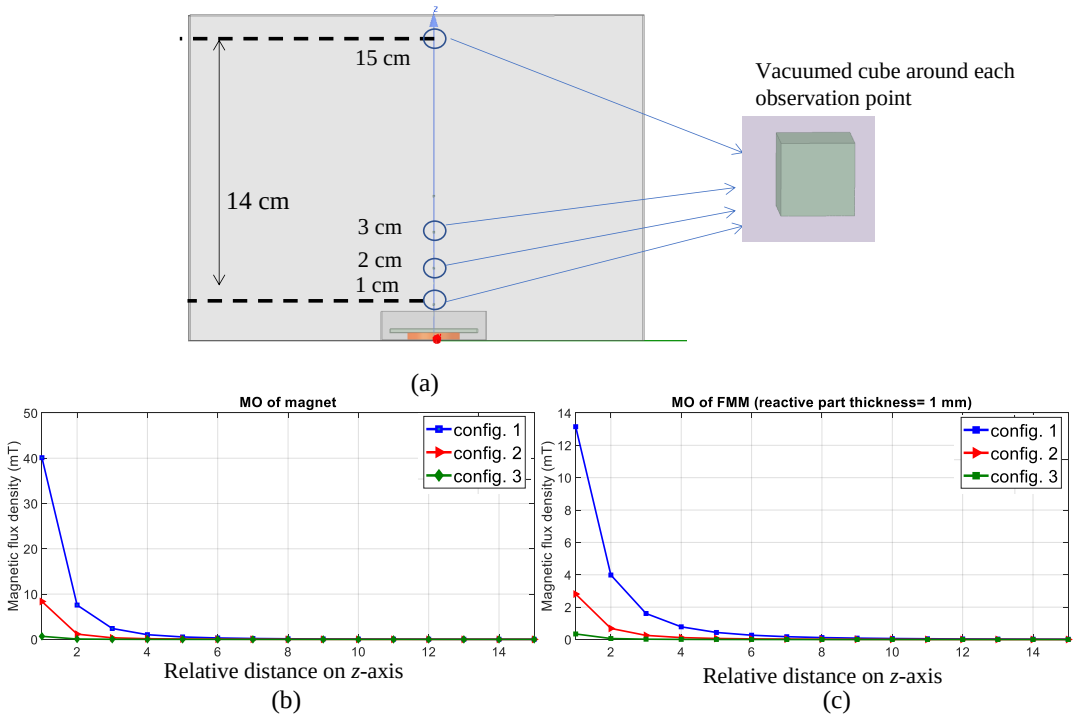

Figure 4.5 – (a) A FMM model, embedded at synthetic concrete and MO calculated through 15 measuring point, placed in cubic vacuumed box to increase accuracy of results (b) MO of only permanent parts (b) MO of three configurations, induced from FMM (magnet coupled with reactive part)

4.4.1 Numerical modeling step

As previously mentioned, we would use numerical model of FMM to generate MO, using as reference data for proposed method. Figure 4.5 illustrates a model of FMM, embedded at the bottom of synthetic concrete is schematically shown. To offer a variety of FMM geometries, we have proposed three different configurations in which the dimensions of both the permanent and reactive parts are varied. As summarized in Table 4.1, configuration 1 has the largest geometry, while configuration 2 and configuration 3 have smaller sizes, respectively. The approach of choosing different dimensions can be useful to provide significant insights into the impact of FMM geometry on ND inspection results, specifically the estimated magnetic properties such as the range of magnetic dipolar moments using the proposed method, as well as the detectable MO through an external interrogator. Furthermore, by utilizing numerical modeling to generate

Table 4.1 – Reference numerical configuration details

	Geometry of magnet (mm)	**Geometry of reactive part (mm)**	**Meshing size (mm)**	**Materials**
Configuration 1	$\phi = 7.5$ h $= 2$	25×25 x1	0.5	-Permanent part: Magnet NdFeB35 - Reactive part: Iron with μ=50
Configuration 2	$\phi = 4$ h $= 1$	18×18×1		
Configuration 3	$\phi = 1$ h$= 1$	10×10×1		

MO, we can initially evaluate the effects of FMM geometry on results of proposed method and analysis the physics of FMM in a controlled way, which may be challenging to achieve through experimental tests alone. This information can be highly valuable in designing such small embedded devices and optimizing their results, as well.

To improve the accuracy of numerical calculations, it is crucial to use a small mesh size to provide sufficient details about the physics of each component model. In this numerical modelings the meshing size of 0.5 mm is chosen. Reducing the mesh size of the components can enhance the simulation's accuracy, but it can also significantly increase the computational complexity and modeling time, as discussed in Chapter 3, Section 3.3. Furthermore, to increase the accuracy of numerical modeling, a vacuum cube with small dimensions is created around each measuring point, similar to Section 3.3 in Chapter 3. As previously discussed, using dense meshing around the measuring points would enable us to obtain more accurate results even for minor variations in the geometry of FMM components and its related effect on MO. Thus, each observation point is placed in a vacuum cube with dimensions of 0.5 mm $\times$ 0.5 mm $\times$ 0.5 mm, as shown in Figure 4.5a. These vacuum cubes don't have any magnetic properties, and their involvement in modeling will not affect the numerical results, in terms of materials. Thus, it is assumed that by applying the small mesh size is used for these vacuum cubes, the MO calculations around observations would be carried out with more precision.

To enhance the precision of the optimization technique in estimate unknown parameters, 15 observation points are chosen, arranged in a line from 1 cm to 15 cm. This allows for the characterization of the MO profile along the vertical direction of the z-axis. In this case, by selecting 15 observation points, the optimization technique has access to more data points, which allows it to better approximate the behavior of the MO over a wider range of distances [225]. This can help estimator to obtain more optimal values of the magnetic dipole moments. The choice of monitoring the MO in the z direction was also motivated by the fact that MO is a function of the relative distance between the FMM and the observation point (external interrogator). Thus, by using more distance, it could be possible to consider the FMM could be embedded at different concrete depths, as well.

Nonetheless, it is important to note that monitoring the surface in the perpendicular direction from 1 cm to 15 cm could be challenging in practical applications. Additionally, a 15 cm distance in concrete cover is not practical due to its thickness (usually less than 5 cm for marine environment structures). Therefore, the decision to choose 15 observation points arranged in a line from 1 cm to 15 cm is just an assumption made to enhance the estimation results, while acknowledging its limitations in real case scenarios. The MO from numerical modeling results associated with each configuration are presented in Figure 4.5b and c. Figure 4.5b shows the MO values obtained for the permanent part only (from magnets). Figure 4.5c illustrates the MO of each configuration of a complete FMM device (permanent part and reactive part with

a thickness of 1 mm). It can be observed from Figure 4.5c that the inclusion of the reactive part significantly affects the MO values compared to the permanent part only (Figure 4.5b). This is expected since the reactive part plays a crucial role in shielding the MO generated by the magnet. These MO of numerical modeling results would be used as a reference data for the proposed method to estimate the amount of magnetic dipolar moment associated with each FMM at numerical configuration.
In the next section, we will review optimization problem and the related algorithms which can used to solve it.

4.4.2 Optimization step

The optimization step is a crucial aspect of the proposed forward and inversion method, as it is closely integrated with analytical model to estimate amount of magnetic dipolar moments through inversion approach. In this study, our aim is to minimize the error between the MO values obtained from the numerical models and those generated by the analytical model. Thus, the role of the estimator is to find the optimal amount of magnetic dipolar moments that allows the analytical model to calculate MO with the least difference compared to those of numerical model. As shown in Figure 4.5b and c, the MO, generated by numerical configurations, have a nonlinear relationship with relative distance. According to Biot-Savart law, the amount of MO would have the inverse-square relationship with the magnetic dipolar moment as source of magnetic field. Therefore, an appropriate nonlinear optimization method needs to be chosen for estimating the unknown parameters.
Since, the proposed forward and inversion method of this study is inspiration from magnetic dipolar modeling of ferromagnetic vehicles [188], we would similarly employ the Nonlinear Least Square (NLS) optimization problem. NLS involves minimizing the sum of the squares of the difference between the predicted values and the actual data [227]. It is an unconstrained minimization method from:

$$\min_x \mathbf{f}(\mathbf{x}) = \sum_{i=1}^{m} \mathbf{f}_i(\mathbf{x})^2 \tag{4.13}$$

Here, the objective function is the $\mathbf{f}$ which minimizes the sum of squares of residuals. In this context, the auxiliary functions of $\mathbf{f}_i$ are residuals of the differences between MO of numerical and analytical models. The x are the series of the unknown parameter that the method is searching for optimal answers. Here, unknown parameter is magnetic dipolar moment vector.
Considering the reference input data as $\hat{\mathbf{y}}_i$ (MO of numerical configurations) and the analytical model as $\tilde{\mathbf{y}}_i(\mathbf{x})$, then, the objective function would be:

$$\min_x \mathbf{f}(\mathbf{x}) = \sum_{i=1}^{m} (\tilde{\mathbf{y}}_i(\mathbf{x}) - \hat{\mathbf{y}}_i)^2 \tag{4.14}$$

The solutions of NLS are distinctive. This is due to using the Hessian matrix in the least square objective function. The Hessian matrix in this case is the sum of two terms. The first only involves the gradients of $\mathbf{f}_i$ and the second one involves the second derivatives (however, it is zero if the errors are all zero). The related information and equations of NLS are extensively mentioned in [227].
Several algorithms have been proposed to solve NLS problems, such as the Gradient descent algorithm [228], Steepest descent [229], or Gauss-Newton method [230, 231]. As previously mentioned, we need to choose an efficient and robust algorithm to solve NLS problem. We have selected two algorithms; the first one is Levenberg-Marquardt algorithm [232, 233] due to its advantages over other algorithms, such as being much faster and more efficient for solving NLS problems. Secondly, in order to justify this choice, we have also compare the estimation results with the Nelder-Mead algorithm [234] as an alternative method. The Nelder-Mead algorithm is a derivative-free optimization method that does not require the computation of gradients, making it suitable for non-smooth or non-differentiable objective functions. For this algorithm, we would use the Fminsearch function of Matlab 2022 optimization toolbox. Thereby, We will compare the results of both algorithms to find the best solution to be adopted with the proposed forward and inversion method.
In the upcoming section, we will evaluate the effectiveness of the proposed forward and inversion method by implementing two analytical models and two optimization algorithms that were previously discussed. Thereby, we can determine the optimal solution for each step of the proposed method.

4.5 Calculating the MO with proposed method, using analytical models 1 and 2

In this section, we would calculate the MO using, two analytical models 1 and 2 and compare the results with the MO, generated by the numerical model. To obtain the MO by analytical model, the proposed method must be used to estimate the amount of magnetic dipolar moments associated with each FMM numerical configuration. Then, each analytical model would use the estimated magnetic dipolar moments to calculates the MO as a function of relative distance. To do this, we would use:

- Three numerical configurations, described in Table 4.1 and their associated MO curves shown in Figure 4.5c, as reference data,
- The Levenberg-Marquardt algorithm to solve optimization problem to estimate magnetic dipolar moment,
- FMM would be modeled with single magnetic dipole. The position of this dipole set at the center of the reactive part, as illustrated in the Figure 4.6.

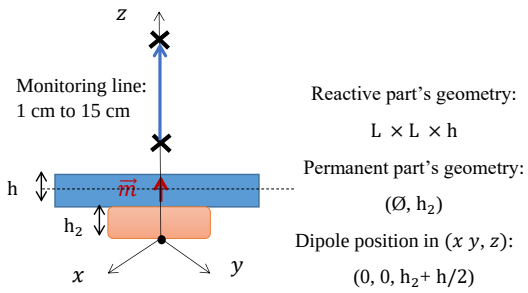

Figure 4.6 – Position of one dipole at the center of reactive part

As previously discussed, the magnetic dipole moment represents the magnetic property of reactive part and it is related to the distribution of magnetic charges or current in that object. For a uniformly magnetized object like the reactive part, the single magnetic dipole could be located at the center of mass of the object to represent the magnetic property of whole reactive part's volume (as illustrated in the Figure 4.6). This simplification is useful for modeling and interpreting the results of the proposed method, as it provides a clear physical explanation for any variations in the magnetic properties of the reactive part.

Figure 4.7, the results of the MO calculated by two analytical expressions and compare with the MO of reference numerical configurations 1-3. The results shows that the MO curves calculated by the analytical models closely similar to those generated by the numerical configurations. However, for numerical configurations 1 and 2 (Figures 4.7a and 4.7b), analytical model 1 provides slightly better results than analytical model 2. However, for reference configuration 3, which has a relatively smaller permanent part geometry (Figure 4.7c), both analytical models show good results.

This results suggests that the FMM geometry plays role in the results. Thus, FMM with relatively smaller geometry, generates a lower amount of MO compared to larger FMM geometries. Eventually, for smaller MO values, the error also would be relatively lower. It is the reason the FMM with lower geometry, represents lower difference in the MO at Figures 4.7c.

To quantify the difference between the MO calculated by the two analytical models and numerical model, we have calculated the Root Mean Square Error (RMSE). According to [225], RMSE is a commonly used metric to evaluate the accuracy of a model's predictions or estimate the difference between two sets of data. Additionally, to ensure the accuracy and reliability of the results, each modeling was repeated 5 time. The standard deviation of the results obtained from the repeated calculations are presented in Table 4.2. Also to compare a value for MO, for each configuration, the amount of average MO [dB] over 15 calculations (for 15 observation points), are calculated and indicated in table. Based on the results presented in Table 4.2 and the graphs shown in Figure 4.7, it can be concluded that both analytical models are capable of calculating MO that are similar to the reference MO, generated by the numerical model. However, compar-

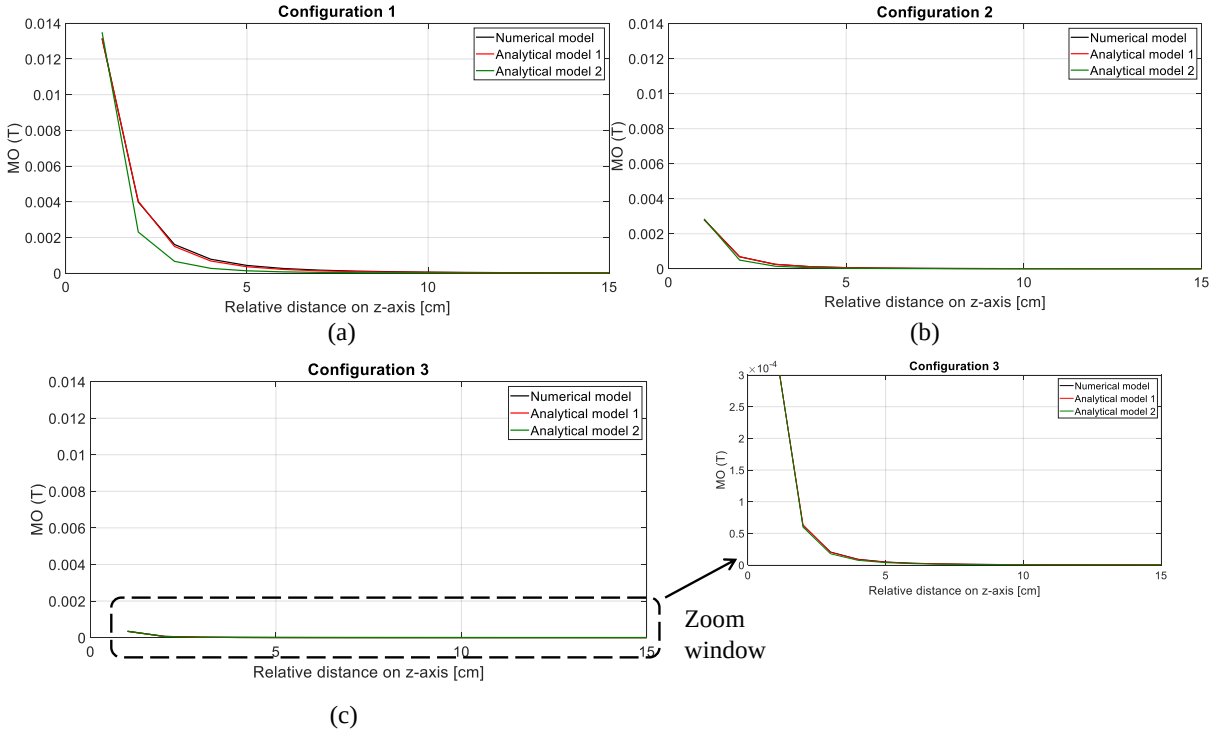

Figure 4.7 – Comparing the inversion results for analytical model 1 and 2 with one magnetic dipolar moment (a) configuration 1 (b) configuration 2 (c) configuration 3

ing the MO averages and the RMSE errors, it appears that analytical model 1 has a slightly better performance than analytical model 2.

This obtained difference in performance of analytical models could be attributed to the fact that analytical model 2 is designed specifically for cylindrical magnetic source shapes and is only able to calculate MO on the z-axis, whereas analytical model 1 can calculate MO for all magnetic source shapes and in any direction, such as x and y. Thus, analytical model 1 could be more suitable choice for applications where the magnetic source consists of two shapes (*e.g.,* the FMM which includes a cylindrical permanent part and a cubic reactive part).

In the next section, we will conduct a similar study as the previous section, but with the imple-

Table 4.2 – Comparing amount of RMS errors [dB] between MO of numerical model and analytical model 1 and 2, for each numerical configuration

	Analytical model 1 (Biot-Savart)			**Analytical model 2 (Geometrical model)**			**Numerical model**	
	MO Average [mT]	**MO Standard deviation [mT]**	**RMSE [dB]**	**MO Average [mT]**	**MO Standard deviation [mT]**	**RMSE [dB]**	**MO Average [mT]**	**MO Standard deviation [mT]**
Configuration 1	1.4	10^{-4}	-43	1.2	10^{-4}	-33	1.4	10^{-4}
Configuration 2	0.27	10^{-5}	-63	0.22	10^{-5}	-43	0.25	10^{-5}
Configuration 3	0.030	10^{-7}	-75	0.031	10^{-7}	-62	0.029	10^{-7}

mentation of two different optimization algorithms: Levenberg-Marquardt and Nelder-Mead.

4.6 Calculating the MO with proposed method, using two optimization algorithms

In the second step of our study, we will compare the calculated MO using the analytical model with two different optimization algorithms: Levenberg-Marquardt and Nelder-Mead. The comparison will be made to evaluate the estimation accuracy of the proposed method.

— The analytical model used will be Biot-Savart (analytical model 1) which was determined to be the best choice in the previous step,

— The reference model will be the MO generated from the numerical model presented in Table 4.1,

— A single magnetic dipole, similar to Figure 4.6, placed at the center of the reactive part will be used as the source of the magnetic field in the modeling.

Figures 4.8a and b compares the amount of MO calculated by forward model using the Nelder-Mead and Levenberg-Marquardt algorithms, respectively, and MO generated by three numerical configurations. Based on the comparison between the results obtained from the two optimization algorithms, it can be concluded that both algorithms show similar performance in estimating the magnetic dipoles and calculate similar MO. Therefore, both algorithms can be used in the proposed method for estimating magnetic dipoles.

To complete this section, the analytical model 1 (Biot-Savart equation) and the Levenberg-Marquardt algorithm are suitable choices for the proposed forward and inversion method steps,

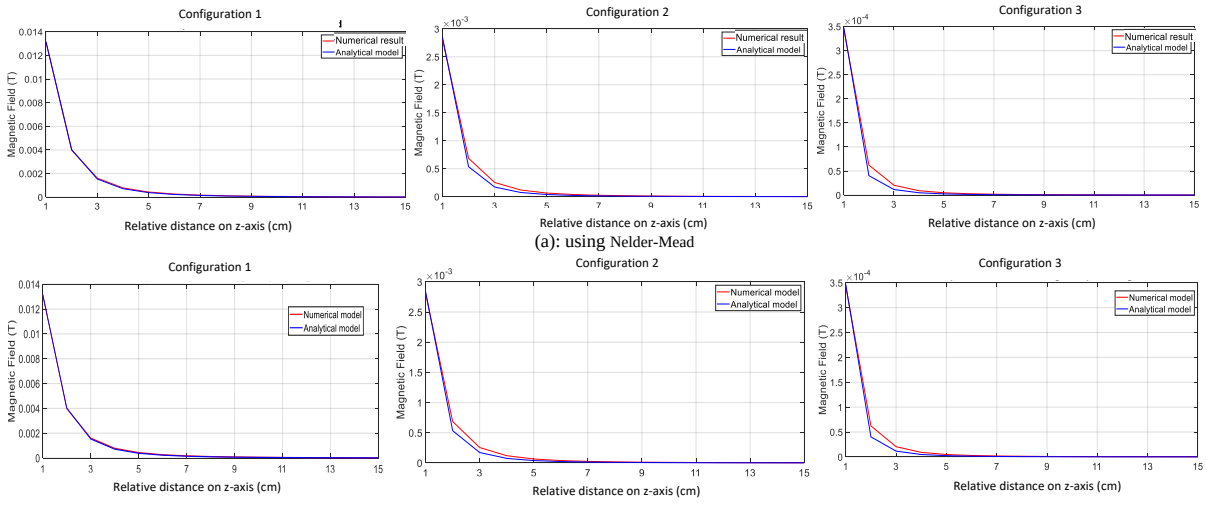

(a): using Nelder-Mead

(b): using Levenberg-Marquardt

Figure 4.8 – Comparing MO from numerical configurations 1-3 with MO analytical model with estimated magnetic dipolar moments (a) using Nelder-Mead algorithm (b) using Levenberg-Marquardt algorithm

and will be used, afterwards in the subsequent modeling. The next section will focus on using the proposed forward and inversion method to determine the variation of the estimated magnetic dipolar moment as a function of changes in the geometry of the reactive part.

4.7 Evaluating the magnetic dipolar moment's variations, as function of reactive part's geometrical changing

As previously discussed, the proposed method aims to establish a correlation between variations in the magnetic properties of FMM (*i.e.,* magnetic dipolar moment) and any degradation in the reactive part, such as material changes or geometrical deformation, due to aggressive agent's induced corrosion. It is assumed that the forward and inversion method is capable to estimate the amount of magnetic dipolar moment of the reactive part, based on MO variations, and indirectly, providing valuable information about the potential risk of rebar corrosion, cause by aggressive agents, as new ND method. Therefore, in this section, we will evaluate the proposed method and provide a primary assessment of the novel ND method.
Here, we aim to answer the following questions:

- Is the magnetic dipolar moment vector capable to represent magnetic behavior of the FMM, particularly in response to geometrical changes? Are the results reliable and repeatable and could be used as new magnetic ND method?
- Is it possible to assume that changes in the geometry of the FMM's reactive part result in its related magnetic dipolar moment variations?
- If so, what is the tendency of the magnetic dipolar moment changes as a function of reactive part's geometrical variations?
- How many dipoles are sufficient to represent the FMM device magnetic behavior? Concerning small geometry of FMM, could we assume that one dipole is sufficient?

To address these questions, we would investigate the performance of proposed method, using numerical modeling of FMM as reference model.
The numerical parametric study plan is presented in Figure 4.9. In this numerical modeling, three configurations are used and labelled as FMM 1 to FMM 3. The geometry of FMM 1-3 are similar as what presented in Table 4.1. To examine whether alterations in reactive part's geometry can impact FMM's magnetic properties, the thickness of the reactive part is reduced from 1 mm to 0.1 mm for each FMM. Thus, the numerical model would calculate MO variations of each FMM ($\mathbf{MO}_{\mathrm{FMM}_x}$) as a function of reactive part's thickness reduction ($f_{Num}(a)$), as reference data. The relative distance between dipole and interrogator is $\mathbf{r}$. Block diagram in Figure 4.10 presents the steps of the proposed method for estimating the magnetic dipolar moment as a function of changes in the reactive part for each FMM, as follow:

- First, the analytical model takes $\mathbf{MO}_{\mathrm{FMM}_x}$ and $\mathbf{r}$ as inputs, where $\mathbf{r}$ is a constant input

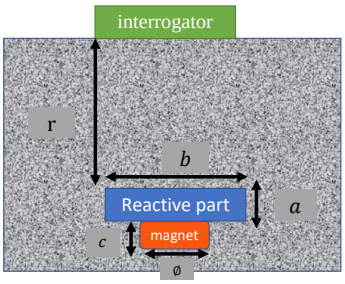

Numerical configurations	Magnet's geometry (mm)	Reactive part's geometry	
		Surface area $b \times b$ (mm)	Thickness a (mm)
FMM 1	$\emptyset = 7.5,\ c = 2$	25×25	**Variable:** 1 mm, 0.5 mm, 0.2 mm, 0.1 mm
FMM 1	$\emptyset = 4,\ c = 1$	18×18	
FMM 3	$\emptyset = 1,\ c = 1$	10×10	

$\mathbf{MO}_{\mathbf{FMM_x}} = \boldsymbol{f(a)}$

Figure 4.9 – Parametric study with numerical configurations 1-3 to obtain MO as function of reactive part's thickness changing

vector for both the numerical and analytical models,

— Second, the analytical model calculates the MO as a function of the magnetic dipolar moment ($f_{Ana}(\mathbf{m})$) and $\mathbf{r}$. At first iteration, we would use the initial values for magnetic dipolar moments,

— Third, optimization is then used to estimate the amount of magnetic dipolar moment through comparing the MO of the analytical and numerical models. The objective function of RMSE would be used to minimize the difference between two MO,

— This process will be repeated, untill estimator could find the optimal amount of magnetic dipolar moments for each reactive part's thickness, separately,

— Finally, the magnetic dipolar moments, as function of reactive part's thickness ($\mathbf{m}_{\mathrm{FMM}_x} = f(a)$) would be evaluated.

In the next section, we will initially use a single magnetic dipole, to evaluate the proposed method. Subsequently, we will increase the number of dipoles to compare the results and eventually, evaluate the sufficient number of dipoles that can represent magnetic behaviour of FMM.

4.7.1 Modeling with one dipole

As explained, the proposed method aims to evaluate the magnetic dipolar moment of each FMM configuration. Here, we would start to study the method with one dipole. The dipole's position is considered the center of the reactive part's volume, as illustrated in Figure 4.6. The results of the inversion and the estimated amount of magnetic dipolar moment in the Cartesian

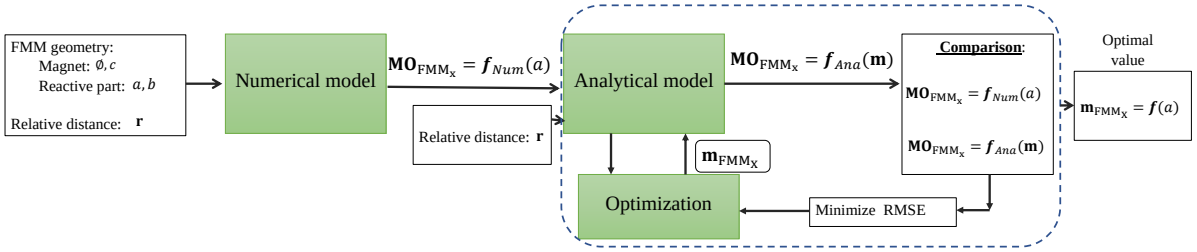

Figure 4.10 – Block diagram of the proposed method's step, including inversion to estimate the optimum amount of magnetic for each FMM ($\mathbf{m}_{\mathrm{FMM}_x}$) as function of a

coordinate system for each configuration are summarized in Table 4.3. The norm of $\mathbf{m}$ (*i.e.,* $||\mathbf{m}||$) is separately calculated for each configuration as a function of the reactive part's thickness reduction. To simplify the analysis, we will focus on the norm of $\mathbf{m}$ instead of studying each vector component individually. Considering the results in Table 4.3, it can be concluded that, firstly, for all three numerical configurations, the norm of the magnetic dipolar moment increases as the thickness of the reactive part is reduced. As discussed before, the permanent part of the FMM acts as an external magnetic field, causing magnetization in the reactive part. This magnetization can be modeled and quantified as a net amount of magnetic dipolar moment vector, which arises from the alignment of the magnetic dipolar moments vector within the material, at the same in the direction of the permanent part (magnet) north/pole. In the case of a shielding part (reactive part), the generated MO by the magnet is partially blocked by the shield, resulting in incomplete alignment of magnetic dipolar moment's vector and their lower net amount. However, removing the shield allows for a larger amount of measurable MO

Table 4.3 – Results of inversion for modelling with one dipole: the variations of estimates $\mathbf{m}$ [J/T] with reactive part thickness reduction

	Configuration 1			
Reactive part thickness [mm]	$\mathbf{m}_x$ **[J/T]**	$\mathbf{m}_y$ **[J/T]**	$\mathbf{m}_z$ **[J/T]**	$\|\|\mathbf{m}\|\|$ **[J/T]**
1 mm (Step 0)	0.012	0.0122	-0.025	0.030
0.5 mm (Step 1)	0.020	0.0203	-0.0273	0.039
0.2 mm (Step 2)	0.035	0.0468	-0.0227	0.062
0.1 mm (Step 3)	0.042	0.0510	-0.0136	0.067
0 mm (Step 4)	0.031	0.0373	-0.0214	0.075
Standard deviation	± 0.00001	± 0.00001	± 0.0001	± 0.0001
$\Delta_{\mathbf{m}}=\|\mathbf{m}_{Max}\text{-}\mathbf{m}_{Min}\|$	0.034	0.044	0.006	0.045
Configuration 2				
1 mm (Step 0)	0.0013	0.0013	-0.0023	0.0030
0.5 mm (Step 1)	0.0015	0.0016	-0.0027	0.0035
0.2 mm (Step 2)	0.0025	0.0025	-0.0035	0.0050
0.1 mm (Step 3)	0.0052	0.0020	-0.0028	0.0063
0 mm (Step 4)	0.0017	0.0086	-0.0015	0.0090
Standard deviation	± 0.000001	± 0.000001	± 0.00001	± 0.00001
$\Delta_{\mathbf{m}}=\|\mathbf{m}_{Max}\text{-}\mathbf{m}_{Min}\|$	0.004	0.007	0.001	0.006
Configuration 3				
1 mm (Step 0)	0.00012	0.00012	-0.00011	0.0002
0.5 mm (Step 1)	0.00013	0.00013	-0.00012	0.00022
0.2 mm (Step 2)	0.00015	0.00015	-0.00014	0.00025
0.1 mm (Step 3)	0.00017	0.00017	-0.00016	0.00029
0 mm (Step 4)	0.00025	0.00025	0.00023	0.00042
Standard deviation	± 0.0000001	± 0.0000001	± 0.000001	± 0.000001
$\Delta_{\mathbf{m}}=\|\mathbf{m}_{Max}\text{-}\mathbf{m}_{Min}\|$	0.00013	0.00013	0.00012	0.00022

(as obtained before in Section 2), resulting in a more magnetic flux lines to pass through permeable zones of reactive part, more alignment of magnetic dipolar moment vectors and eventually, more measurable MO at observation points. Thus, it could be concluded that the degradation of reactive part (loosing its magnetic properties) led to an increase in the amount of net magnetic dipolar moment, for each FMM., due to removing this shield.
Secondly, it should be noted that each modeling was repeated five times to ensure the accuracy of the results. The estimated magnetic dipolar moments for each component are reported as the mean value of these five repetitions, and the corresponding standard deviation is also included to represent the accuracy of the results. The analysis indicates that the overall geometry of the FMM has a significant impact on the net magnetic dipolar moment. Specifically, Configuration 1, which has the largest overall geometry, exhibits the highest total magnetic dipolar, compare to configurations 2 and 3.
Moreover, graphs in Figure 4.11 shows that the amount of $||\mathbf{m}||$ is highly dependent on the geometry of the FMM. The variation range of $||\mathbf{m}||$, represented by $\Delta_{\mathbf{m}}$, is significantly higher for FMM with a bigger permanent part's geometry (configuration 1). As mentioned, one possible explanation for the observed result is that the larger permanent part of FMM generates a stronger external magnetic field, resulting in more complete alignment of magnetic moments, particularly within the reactive part. Conversely, a smaller permanent part generates a weaker magnetic field, leading to a weaker magnetization vector and subsequently, a lower amount of magnetic moments within the reactive part.
Furthermore, as the reactive part starts to degrade (loss its thickness), the magnetic flux lines can more easily pass through the magnetic shield of the reactive part, resulting in a stronger MO at the observation points, and consequently, a greater alignment of magnetic dipolar moment vectors within the reactive part. Consequently, the net magnetic dipolar moment would increase,

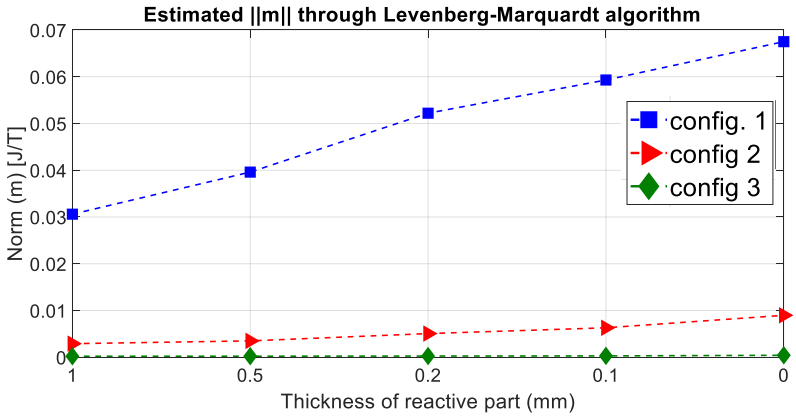

Figure 4.11 – The variations of estimated magnetic dipolar moment value ($||\mathbf{m}||$), as function of reactive part thickness reduction in configurations 1-3

as function of reactive part's degradation. Therefore, the graph of magnetic dipolar moments exhibits an upward tendency with the reduction in thickness of the reactive part.
The results of this study suggest that the proposed method has the potential to assess changes in the magnetic shielding properties of the reactive part and quantify its variations, through the magnetic dipolar moment vector. Additionally, the method could be also a simple technique for studying material and magnetic behavior changes of a magnetized object (like reactive part), through one single magnetic dipolar moment's vector. Thus, the proposed method has the potential to be a fast and simple approach in assessing the risk of rebar corrosion in cover concrete caused by aggressive agents through analysing the changes in the magnetic dipolar vector of embedded SHM devices, as a preventive ND technique.
In the following section, we will extend the model by using two dipoles to further evaluate the proposed method.

4.7.2 Modeling with two dipoles

In the previous section, we evaluated the proposed method to estimate the amount of magnetic dipolar moment as a function of reactive part's thickness loss and its degradation. However, in real cases, degradation is not always uniform, particularly in cases of corrosion. Corrosion can start from one side or the edges of materials and slowly extend to the whole side. Therefore, for FMM's reactive part which is subject to corrosion, and it could be partially deteriorated by aggressive agents. Hence, instead of solely studying the variation of a single dipole located at the center of the reactive part, it would be more beneficial to divide the entire volume of the reactive part into multiple subregions and analyze the magnetic dipolar moment in each region. This approach provides a more comprehensive understanding of the FMM's magnetic properties behavior under different corrosion scenarios (*e.g.,* material degradation or geometrical changes). By quantifying the magnetic dipolar moment in each subregion, the method can quantify any small defects or changes in the reactive part's geometry, through the amount of corresponding magnetic dipolar moment of that area and eventually, changing the net magnetic dipolar moment of FMM. To evalute this assumption, as illustrated in Figure 4.12, we have divided the reactive part's entire volume into two parts: left and right. Then, the idea is to estimate the

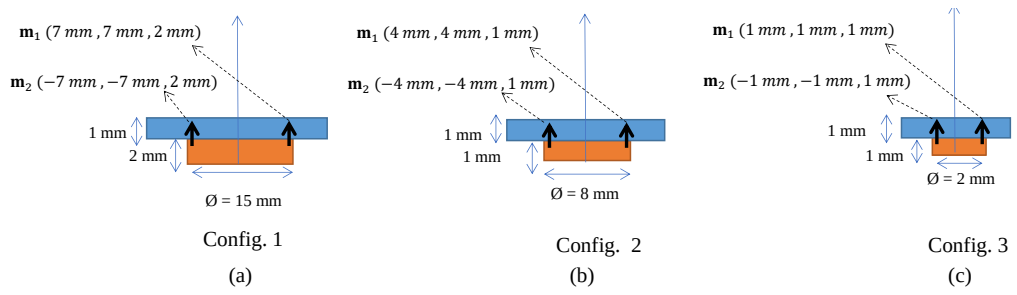

Figure 4.12 – Positions of dipoles at each reference numerical configuration

magnetic dipolar moment associated with each area, individually and eventually, determine the total amount of magnetic dipolar moment of FMM, through: $\mathbf{m} = \sum_{i=1}^{2} ||\mathbf{m}||_i$.
Figure 4.12 illustrates the dipole positions in each numerical configuration. The dipoles are located at the interface between the magnet and reactive part, sharing the same vertical position on the *z*-axis. However, their spatial position on the (*x*-*y*) plane is on opposite planes, (+*x*, +*y*) and (-*x*, -*y*), respectively. As a result, the dipoles are placed in a row, at the same *z* value, and in symmetrical positions on the (*x*-*y*) plane. Using the proposed method, amount of magnetic dipolar moment for each side, is estimated separately and mentioned in Table 4.4.
The table indicates that the estimated amount of the magnetic dipole moment at left and right sides, for all the components of $\mathbf{m}_x$, $\mathbf{m}_y$, and $\mathbf{m}_z$, are equal. This result can be attributed to the numerical modeling of FMM, which takes into account the materials and meshing of reactive part consistent and uniform. Due to this material's uniformity, the estimated symmetric dipoles at both sides, have similar values and directions.
Secondly, the study shows that the magnetic dipolar components' direction varies across different configurations. The sign (+/-) of the vector component represents the direction of the magnetic dipole moment vector and also the magnetization vector, caused by permanent part. The FMM's different geometries exhibit different patterns in generation of magnetic flux density lines due to various permanent part's dimensions. Moreover, using different shielding properties, the magnetic dipolar moment vectors would have different direction to be align with their

Table 4.4 – Results of inversion for two dipoles: the variations of estimated $\mathbf{m}$ [J/T] with reactive part's thickness reduction

	Configuration 1						
Reactive part thickness [mm]	$\mathbf{m}_{x,1}$ **[J/T]**	$\mathbf{m}_{y,1}$ **[J/T]**	$\mathbf{m}_{z,1}$ **[J/T]**	$\mathbf{m}_{x,2}$ **[J/T]**	$\mathbf{m}_{y,1}$ **[J/T]**	$\mathbf{m}_{z,1}$ **[J/T]**	$\sum_{i=1}^{2} ||\mathbf{m}||_i$ **[J/T]**
1 mm (Step 0)	0.005	-0.011	0.005	0.005	-0.011	0.005	0.026
0.5 mm (Step 1)	0.008	-0.012	0.008	0.008	-0.012	0.008	0.034
0.2 mm (Step 2)	0.018	-0.012	0.005	0.018	-0.012	0.018	0.044
0.1 mm (Step 3)	0.024	-0.011	0.002	0.024	-0.011	0.024	0.052
0 mm (Step 4)	0.009	-0.008	0.029	0.009	-0.008	0.009	0.062
Standard deviation	± 0.0001	± 0.00001	± 0.0001	± 0.0001	± 0.00001	± 0.0001	± 0.0001
$\Delta_{\mathbf{m}}=\lvert\mathbf{m}_{Max}\text{-}\mathbf{m}_{Min}\rvert$	0.019	0.003	0.024	0.019	0.003	0.024	0.036
Configuration 2							
1 mm (Step 0)	-0.0007	-0.0007	0.0012	-0.0007	-0.0007	0.0012	0.003
0.5 mm (Step 1)	-0.0008	-0.0008	0.0014	-0.0008	-0.0008	0.0014	0.004
0.2 mm (Step 2)	-0.0013	-0.0013	0.0018	-0.0013	-0.0013	0.0018	0.005
0.1 mm (Step 3)	0.0001	-0.0030	0.0015	0.0001	-0.0030	0.0015	0.006
0 mm (Step 4)	0.0002	0.0044	-0.0004	0.0002	0.0044	-0.0004	0.009
Standard deviation	± 0.00001	± 0.00001	± 0.00001	± 0.00001	± 0.00001	± 0.00001	± 0.00001
$\Delta_{\mathbf{m}}=\lvert\mathbf{m}_{Max}\text{-}\mathbf{m}_{Min}\rvert$	0.0006	0.0011	0.0006	0.0006	0.0011	0.0006	0.006
Configuration 3							
1 mm (Step 0)	0.000063	0.000063	-0.000058	0.000063	0.000063	-0.000058	0.00021
0.5 mm (Step 1)	0.000066	0.000066	-0.000061	0.000066	0.000066	-0.000061	0.00022
0.2 mm (Step 2)	0.000075	0.000075	-0.000069	0.000075	0.000075	-0.000069	0.00025
0.1 mm (Step 3)	0.000086	0.000086	-0.000079	0.000086	0.000086	-0.000079	0.00029
0 mm (Step 4)	0.000124	0.000124	-0.000114	0.000124	0.000124	-0.000114	0.00042
Standard deviation	± 0.000001	± 0.000001	± 0.000001	± 0.000001	± 0.000001	± 0.000001	± 0.000001
$\Delta_{\mathbf{m}}=\lvert\mathbf{m}_{Max}\text{-}\mathbf{m}_{Min}\rvert$	0.00006	0.00006	0.00005	0.00006	0.00006	0.00005	0.00020

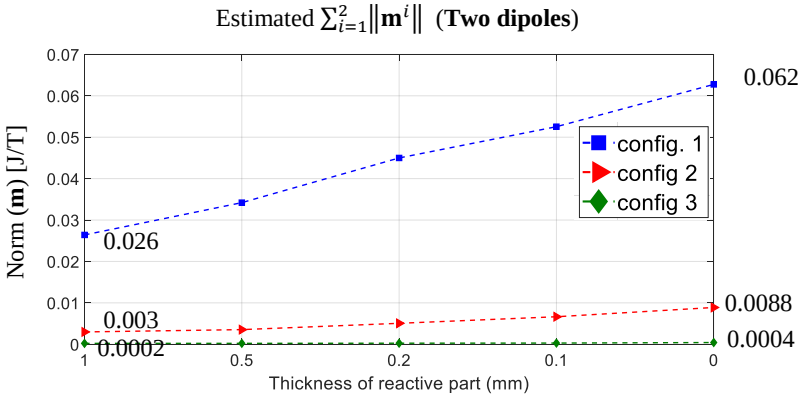

Figure 4.13 – Variation of sum of norm ($\mathbf{m}$), estimated from inversion with two dipoles, as a function of reactive part's thickness loss

the corresponding magnetization vector. Therefore, once we estimate the amount of each area's magnetic dipolar vector, the related direction would be more different from other areas. This direction determines only based on the MO, generated by permanent part on that area, density of magnetic flux lines, and magnetization vector. As mentioned, these factors are determine by the mostly, the permanent part's geometry and the reactive part's physical properties (dimensions and materials) which could reorient the flux lines into its permeable substrate of shield. As obtained in Table 4.4, for configuration 2, the magnetic dipolar vector direction is entirely oriented towards the $\mathbf{m}_z$ direction when the shield's thickness becomes zero (fully removed), showing that the shielding role of the reactive part in determining the magnetic dipolar moment vector's magnitude and direction, as well.

Thirdly, similar to modeling with a single dipole, the focus of our analysis is on the calculated $||\mathbf{m}||$. Here, the total value of $||\mathbf{m}||$ for all configurations shows an upward tendency as the thickness of the reactive part decreases. These results are consistent with those obtained for a single dipole. The range of $\Delta_{\mathbf{m}}$ decreases as the geometry of the FMM, particularly the permanent part, is reduced, as shown in Figure 4.13. Configuration 1, which has a relatively larger geometry of the permanent part, has a higher range of variation in the total magnetic dipolar moment $||\mathbf{m}||$ compared to configurations 2 and 3. This results again confirm the role of permanent part's, as source of magnetization, to determine the amount of magnetic dipolar moment.

Comparing the estimated $||\mathbf{m}||$ values for one dipole and two dipoles in Table 4.3 and 4.4, respectively, the mean values of $||\mathbf{m}||$ are approximately similar for both models. However, the total variation ranges ($\Delta_{\mathbf{m}}$) obtained for the modeling with one dipole are slightly higher compared to those for the modeling with two dipoles. The results indicate that the addition of a second dipole has a negligible effect on the estimated magnetic dipolar moment values and their range of variation. This is likely due to the uniformity of the FMM numerical modeling in terms of materials and meshing for all configurations. As a result, the thickness reduction of the reactive

part is also uniform for all sides, leading to similar net magnetic dipolar moment values and variation ranges as those obtained for one dipole.
In conclusion, it can be inferred that both one and two dipole are equally capable of representing the behavior of FMM under geometrical variations of the reactive part. However, due to the fewer computational complexity and simplifications involved, the one dipole model could be more preferable. However, the approach of modeling with two dipoles could be particularly show better results in real-world scenarios where the reactive part material and geometry encounter irregular and non uniformly impacts by aggressive agents and corrosion progress.
In the next section, we will extend the model to three dipoles to complete this study.

4.7.3 Modeling with three dipole

To extend the model to three dipoles, a new dipole is introduced in the middle volume of the reactive part, as shown in Figure 4.14. The goal of incorporating multiple dipoles is to create a more accurate representation of the FMM through magnetic dipolar moment vectors. By dividing the total volume of the reactive part into three regions (left, right, and middle), any changes in the magnetic properties of the reactive part due to degradation on any side can be quantified by estimating the corresponding magnetic dipole moment. The overall value, which is the sum of the magnetic dipolar moments, can then be used to establish a relationship between the reactive part's degradation state by corrosion (either material transformation or geometrical deformations) and the net amount of magnetic dipolar moment variation.
In order to determine the effective positions of the three dipoles on the reactive part, series of initial trial and error were conducted to calculate the minimum RMSE. The dipoles were arranged in a row along the top surface of the reactive part, symmetrically on the (x-y) plane, similar to the previous configuration for two dipoles. Finally, one dipole was added at the center of the row.
Table 4.5 presents the detailed results of estimated magnetic dipolar moments for numerical configurations 1 and 2. In fact, the estimation results for configuration 3 shows a significant RMSE error, which suggests that the results are not representative in the table. This could

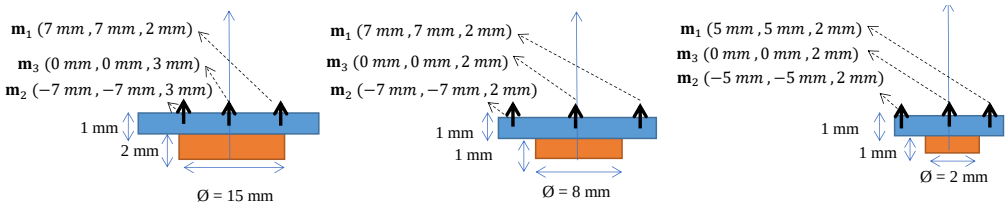

Figure 4.14 – Results of inversion for three dipoles and the amount of estimated magnetic dipolar moment at Cartesian coordinate system (x, y, z)

be attributed to the fact that FMM 3 has the smallest geometry and adding three dipoles located close to each other increases the complexity of the optimization problem. Basically, addition of more dipoles raises the number of parameters to be optimized and can also influence the optimization results. Therefore, the optimization algorithm may struggle to converge to a solution that accurately represents the behavior of the FMM, leading to an increase in the RMSE error in FMM 3. Thus, for such small FMM geometry cases, adding new dipoles will not be useful and it is reasonable to assume for such small geometries, modeling with one or two dipoles is sufficient.

Likewise the results of two dipoles, the amount of magnetic dipolar moments for symmetrical dipole pairs (left and right) are estimated exactly equal in the Cartesian coordinate system. It could be attributed to the assumption of assigning uniform and consistent material properties in the numerical modeling of FMM's reactive part, leading to similar magnetic properties and directions. As with the case of two dipoles, the signs (+/-) next to each component indicate the direction of the magnetic dipole moment vector. This direction is determined by the permanent magnet and the amount of magnetization vector in the reactive part. Consequently, the direction of the dipole vector for each FMM, can be different from other FMM geometries and depends on the direction and density of the magnetic flux lines in that area, as observed in the table.

The amount of magnetic dipolar moment at the center is slightly lower compared to the other two dipoles. This may be due to the fact that the reactive part acts as a shield, redirecting the magnetic flux lines horizontally through the permeable materials. As illustrated in Chapter 2, Section 2.7, fewer magnetic flux lines are concentrated at the center of the reactive part. Therefore, it can lead to lower magnetic properties and subsequently magnetic dipolar moment in the center of the reactive part.

Table 4.5 – Results of inversion for three dipoles: the variations of estimated **m**s [J/T] with reactive part's thickness reduction

	Configuration 1						
Reactive part thickness [mm]	$\mathbf{m}_{x,1,2}$ **[J/T]**	$\mathbf{m}_{y,1,2}$ **[J/T]**	$\mathbf{m}_{z,1,2}$ **[J/T]**	$\mathbf{m}_{x,3}$ **[J/T]**	$\mathbf{m}_{y,3}$ **[J/T]**	$\mathbf{m}_{z,3}$ **[J/T]**	$\sum_{i=1}^{3} \|\|\mathbf{m}\|\|_i$ **[J/T]**
1 mm (Step 0)	0.013	0.013	-0.009	-0.0016	-0.0016	-0.005	0.046
0.5 mm (Step 1)	0.015	0.015	-0.008	-0.0012	-0.0012	-0.005	0.052
0.2 mm (Step 2)	0.016	0.016	-0.009	-0.0017	-0.0017	-0.004	0.055
0.1 mm (Step 3)	0.020	0.020	-0.004	-0.0006	-0.0006	-0.008	0.066
0 mm (Step 4)	0.023	0.023	-0.002	-0.0015	-0.0015	-0.008	0.074
$\Delta_{\mathbf{m}}=\|\mathbf{m}_{Max}\text{-}\mathbf{m}_{Min}\|$	0.01	0.01	0.006	0.0005	0.0005	0.004	0.028
Configuration 2							
1 mm (Step 0)	0.0027	0.0027	-0.0011	-0.0003	-0.0003	-0.0009	0.0088
0.5 mm (Step 1)	0.0028	0.0028	-0.0010	-0.0004	-0.0004	-0.0009	0.0093
0.2 mm (Step 2)	0.0032	0.0032	-0.0005	-0.0005	-0.0005	-0.0012	0.0106
0.1 mm (Step 3)	0.0035	0.0035	-0.0002	-0.0006	-0.0006	-0.0014	0.0116
0 mm (Step 4)	0.0040	0.0040	0.0003	-0.0012	-0.0012	-0.0018	0.0139
$\Delta_{\mathbf{m}}=\|\mathbf{m}_{Max}\text{-}\mathbf{m}_{Min}\|$	0.0013	0.0013	0.0014	0.0009	0.0009	0.0009	0.0051

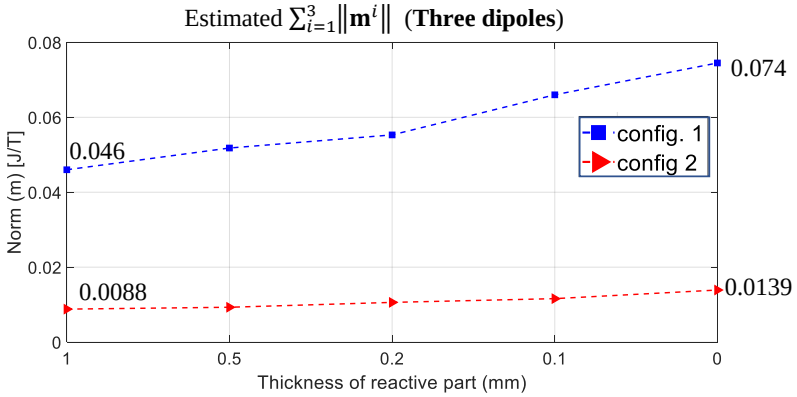

Figure 4.15 – Variation of sum of norm ($\mathbf{m}$), estimated from inversion with three dipoles, as a function of reactive part's thickness loss

As Similar to the modeling with one or two dipoles, the focus here is on the overall amount of $||\mathbf{m}||$ for analyzing the results. Based on the results of Table 4.5 and Figure 4.15, it can be concluded that the size of the FMM has a significant impact on the total amount of net $||\mathbf{m}||$. Thus, the a relatively bigger FMM geometry can provide stronger magnetization at the reactive part, more alignment of magnetic dipoles vectors orientation, resulting in higher values of net $||\mathbf{m}||$. Moreover, Figure 4.15 illustrates the variations of $||\mathbf{m}||$, which tend to increase as the thickness of the reactive part decreases, similar to modeling with one and two dipoles. The estimated values of $||\mathbf{m}||$ are slightly higher in the modeling with three dipoles compared to two dipoles. However, the variation ranges of $\Delta_{\mathbf{m}}$ are approximately similar (slightly more in two dipoles). This suggests that adding one more dipole may not be necessary in terms of range, and modeling with one or two dipoles could be sufficient for numerical modeling. Furthermore, considering the added complexity of estimating three more parameters for each additional dipole compare to simplification of modeling FMM with only one single vector, it can be concluded that for this purpose, modeling with two or even one dipole is more preferable to represent the FMM behavior in terms of changes in magnetic properties of reactive part due to geometrical degradation. However, in real case scenario of corrosion evolution and non uniform rusting impacts, probably three dipoles could provide more accurate information.
Finally, Figure 4.16 compares the results of the proposed method for one, two, and three dipoles associated with numerical configurations 1-3 and as a function of reactive part's thickness loss. As it illustrated, we can concluded that:

— Firstly, the amount of estimated magnetic dipolar moment for FMM 1 is higher compared to configurations 2 and 3 due to the use of a relatively large permanent part geometry. As discussed, this is due to the fact that the bigger magnet could cause higher magnetization that leads to more alignment of magnetization and significant amount of net magnetic dipolar moment,

— Secondly, concerning the sufficient number of dipoles, since the FMM has small geometry, one single magnetic dipolar moment vector is sufficient to represent FMM behaviour as function of reactive part's degradation,

— Thirdly, it was assumed that the magnetic dipolar moment vector could represent the magnetic property behavior of FMM due to reactive part degradation. The results of this study justify this assumption and show that the magnetic dipolar moment vector is sensitive to changes in the reactive part's geometry. The results confirm that by altering the reactive part's dimensions and removing the shielding, the generated MO can pass more strongly through the attenuated reactive part's shield. Consequently, the net amount of estimated magnetic dipolar moment for FMM, would be also increased. These results were obtained for all three numerical FMM geometries and as well as, modeling with one, two, or three dipoles.

— Finally, modeling FMM with multiple dipoles may provide valuable insights into changes in magnetic properties of reactive parts due to corrosion in real scenarios. However, this study was based on uniform numerical modeling of FMM and showed similar net magnetic dipolar moment values for both two and three dipole models. It may be beneficial to consider multi magnetic dipole model, when using experimental data as a reference model in real-world scenarios. This would allow for independent estimation of magnetic property variations in each region, resulting in more accurate information about the degradation of FMM and evaluate the potential corrosion risk of rebar.

As mentioned earlier, the primary goal of FMM technology is to use an embedded SHM device in concrete to rapidly corrode and change its magnetic properties. By measuring the variations in MO with an external interrogator and using the proposed method, we can evaluate the amount of FMM rusting in a ND way, through monitoring the variations in one or two single magnetic dipolar moment vectors. The results of this section show that the proposed method is capable of

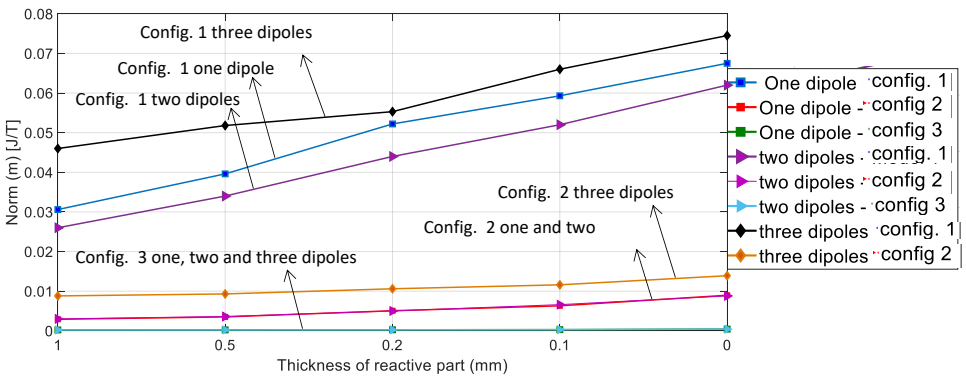

Figure 4.16 – Variation the net amount of $||\mathbf{m}||$, estimated from inversion for one, two and three dipoles, as a function of reactive part's thickness loss

correlating the reactive part's degradation with magnetic dipolar moment variations. This can eventually help evaluate concrete contamination and assess the risk of rebar corrosion.
However, based on these results, we found that there is a trade-off between the magnetic dipolar moment's variation range and the time required for corrosion. A relatively larger FMM can provide a wider range of variations in MO or magnetic dipolar moment, but it would take longer to corrode in practical applications. Therefore, it is crucial to use an FMM with a reactive part size that is relatively large to rust quickly and provide a considerable variation range. Among the proposed configurations in this section, FMM 2 can be selected as the most efficient geometry as it offers a sufficient variation range of $\mathbf{m}$, rusts faster, and has a lower RMSE compared to the other configurations.

4.8 Conclusion

In this chapter, we represented and evaluated the propose forward and inversion method of this research study, as novel preventive ND method to assess the risk of rebar corrosion caused by aggressive agents on reinforced concrete structures. The proposed method involves studying the magnetic dipolar moment variations of the reactive part of embedded FMM device, which is subjected to corrosion by aggressive agents in cover concrete. The chapter aimed to assess a suggested proposed forward and inversion method for estimating the magnetic dipolar moment of the FMM based on the degradation of FMM's reactive components. The proposed method consists of several steps, including an analytical model that relates variations in MO (generated by FMM) to the estimated amount of magnetic dipolar moment vector. The forward and inversion method employs NLS optimization techniques and inversion to perform the estimation.
As explained, the proposed method requires a reference model that can provide the MO as a function of the reactive part's corrosion evolution. In this chapter, we choose numerical model of FMM device, using ANSYS Maxwell software and FEM to develop it. Since the magnetic properties of the reactive part can be altered by the geometrical variations, we assumed to model the degradation of the FMM's reactive part and generate the related MO as reference data, by reactive part's thickness reduction. To ensure the repeatability of the numerical modeling and the proposed method's results, three different numerical configurations of FMM with various geometries are used in this study.
To justify the effectiveness of the proposed method, we first evaluated it, with two existed analytical models of Biot-Savart (analytical model 1) and a geometrical dependent model (analytical model 2). After comparing the MO generated by the analytical models with the reference MO from the numerical model of FMM, we chose the Biot-Savart equation due to its lower amount of difference between MO and eventually, lower RMSE value. Secondly, for the estimation part, we applied two algorithms of Levenberg-Marquardt and Nelder-Mead, to solve the NLS op-

timization problem and estimate the magnetic dipolar moment. Comparing the results, both algorithms showed similar results, but we eventually, chose the Levenberg-Marquardt algorithm for the proposed method.
In the next step, the study evaluated the effect of changes in the reactive part's geometry on the FMM's magnetic properties, specifically on the magnetic dipolar moments changes. The investigation also aimed to determine the minimum number of dipoles required to represent the device's magnetic behavior in associated with the reactive part degradation. Additionally, the study aimed to identify the range and tendency of magnetic dipolar moment variations related to the reactive part's geometrical degradation. To achieve this, three numerical FMM models were used, and the MO was obtained as a function of reactive part thickness reduction for each FMM. We investigated the method, using one, two and three dipoles.
The results of the study indicated that:

— The size of the FMM geometry has a significant impact on the total amount of magnetic dipolar moment for each FMM. It was concluded that the FMM with relatively bigger geometry could provide more magnetic dipolar moment value and subsequently, more variation range,
— Additionally, the results show that the proposed method is capable to represent the magnetic property behavior of FMM through one single magnetic dipolar vector. Specifically, for FMM with smaller geometries, one or two dipole modeling is sufficient to represent the behavior of the FMM, under reactive part's degradation. However, in real-case scenarios of non uniform corrosion evolution on reactive part, more number of dipoles may be required to provide accurate information in this context,
— Moreover, the results confirmed that the magnetic dipolar moment vector is sensitive to changes in the reactive part's geometry. The results of this study justify the initial related assumption about and show that the magnetic dipolar moment vector are capable to represent the magnetic property changes of FMMs due to reactive part degradation,
— The results also confirm that by altering the reactive part's dimensions and removing the shielding, the generated MO can pass more strongly through the attenuated reactive part's shield. Consequently, the net amount of estimated magnetic dipolar moment for FMM would also increase. Therefore, the magnetic dipolar vector would have raising tendency with reactive part's degradation.

To sum up, the findings of this chapter confirm that the proposed method is an effective and straightforward approach for monitoring alterations in the magnetic properties of FMM's reactive part. The proposed method is capable of analyzing the behavior of FMM, in response to corrosion, using only a single magnetic dipolar moment vector, making it a valuable and simple ND technique for remotely assessing the rusting status of FMM's reactive part. Eventually, it can be used to evaluate the risk of rebar corrosion in cover concrete due to aggressive agents, as

well. Therefore, this method can be used as a preventive ND technique and a novel RC monitoring technique, which has the advantage that its MO measurements are only sensitive to changes in magnetic properties of FMM and not to environmental factors such as media properties. Overall, the proposed method is simple, fast, and has the potential to be utilized in the health monitoring of RC structures.

Chapter 5

Experimental Investigation

5.1 Introduction

In Chapter 4, we investigated the feasibility of the forward and inversion method, which focuses on estimating variations in the magnetization of the FMM, caused by thickness loss, through some numerical modeling. The approach involves using an analytical model to establish a relationship between the measured MO variations, the magnetic dipolar moment vector, and the thickness loss of the FMM's reactive part. The results of the inversion method reveal an upward trend in magnetic dipolar moments with reactive part geometrical loss, attributed to the removal of the reactive part's shielding.

In order to validate those numerical findings of Chapter 4, in this chapter, we use some experimental test on variety of FMM samples with different with different geometries, specifically in the reactive part. Using accelerating corrosion, the reactive parts would be rusted at different states. Eventually, the MO variations for each FMM sample as a function of the reactive part's degradation level, would be measured, using an interrogator. This allows us to provide the MO variations as function of reactive part's corrosion states, through practical tests. Similar to Chapter 4, we would use the analytical model and estimation to investigate the magnetic dipolar moment's tendencies and variation range for each FMM samples, as function of corrosion state of the reactive part.

Moreover, in this experimental study, we would also evaluate, practically:

- The potential stability and approximate sensitivity of MO measurements, due to magnetic field of Earth variations (due to Earth rotation) that can affect the results as a available magnetic bias as well as other available magnetic noises,
- The sensitivity of MO generated by FMM's permanent part to concrete media properties such as hydric state, concrete mixing, water content or chloride ion concentration. Here, the objective is to evaluate the uncertainty of MO measurements due to changes the media properties,
- As previously mentioned, the MO variation range and tendency as function of different reactive part's corrosion states to use as reference data for forward and inversion method,
- Finally, the amount of magnetic dipolar moment will be estimated, function of reactive part's corrosion state for single and multi dipoles models.

To reach these objectives, the methodology would be:

— In the first step, the bias magnetic field environment in the experimental area, including any available noise and the Earth's magnetic field, will be measured for some certain duration before and after the main MO measurements. At this level, we will control of the experimental environment and ensures the absence of any magnetic objects that could alter the measurements as magnetic source. Then, in the second step, the MO generated by the permanent magnet will be measured as a reference magnetic field, for the same duration. These two separate measurements would allow us to determine the approximate Signal to Noise Ratio (SNR) of measurements as well as the uncertainty level of the MO, due to available noise,

— Considering to second objective, a wide range of concrete slabs with different mixing ratios, thickness, and hydric states would be used to investigate the uncertainty level of MO measurements to media's characteristics changing. The slabs are manufactured concrete that can be found in sea areas. As mentioned, the would have different characteristics, such as different mixing with Water to Cement (W/C) ratios of 0.38, 0.5, and 0.78. Additionally, the slabs are designed to have three different thicknesses of 3 cm, 4 cm, and 5 cm and are either dried or saturated. To ensure the reliability and repeatability of measurements, a total of 27 slabs are manufactured, with three identical slabs for each concrete mixing and thickness. The slabs would be used to fill gap between the reference magnet (as source of MO generation) and the external interrogator. Then, it is possible to practically evaluate whether the MO is sensitive to concrete media conditions or not. Moreover, the stability of MO measurements would be assessed and the amount of uncertainty level for each test, would be separately evaluated,

— Considering the third objective, a varieties of reactive parts with thicknesses of 1 mm, 0.5 mm, 0.3 mm, and 0.1 mm will be used. Each of these reactive parts are separately corroded at different states (*i.e.*, 10%, 20%, 30%, 40%, and 50%) through an electrolysis accelerated corrosion technique in a 30 g/L NaCl solution as the electrolyte. Additionally, the MO variation tendency and range for each reactive part's thickness as function of corrosion state and different relative distances between FMM and the interrogator, would be obtained. These MO would be serve as reference data, for the forth mentioned objective.

In this experimental study, the Morphosense technology's interrogator serves as the magnetometer for MO measurements. The specific features and characteristics of this magnetometer are described in detail in the relevant section of this chapter.

As explained before, in this chapter, aims to validate the feasibility of proposed forward and inversion method to use magnetic dipolar moment vector changes due to aggressive agents induced corrosion, through experimental approach. We would evaluate the model of FMM, using

one magnetic magnetic dipole vector and also multi-dipoles vectors. Through the comparison of the findings from Chapter 4 with the outcomes of the experimental tests conducted in this chapter, the reliability and feasibility of the results can be assessed. This comparative analysis serves to evaluate the efficacy of the proposed method as an innovative SHM technique for assessing the contamination of the cover concrete, which leads to the different state of FMM's corrosion and subsequently, alterations in its magnetic properties. Finlay, the findings from this study will contribute to evaluating the potential applications of the proposed method, for RC monitoring, as fast and simple preventive ND technique.

5.2 Experimental campaign: material and device

5.2.1 The concrete slabs

The concrete slabs selected for this experimental campaign have properties similar to those typically used in infrastructures, particularly in sea areas. To evaluate the possible influence of concrete mixing on MO, three slabs with different W/C ratios of: 0.38, 0.5, and 0.78, have been selected. The W/C ratio of 0.38, which is mainly used in sea area structures, considered as high performance concrete. The ratio of 0.5, which is close to the standard concrete used in civil engineering structures, considered as a medium concrete. Finally, the W/C of 0.78, considered as mortar concrete and usually allows for rapid moisture penetration which eventually, has a much higher water content than typical concrete. These choices allow for investigation of the W/C ratio's influence on MO measurements for realistic cases.
The components, used for the manufacture of these slabs are:

— Aggregate and sand from the Nouveau quarry (department 79)
— "EXTREMAT CEM I 52.5 N-SR3" cement (used for sea area structures).

The dimensions of the slabs are consistent, with a surface area of 30 cm × 30 cm for each one.

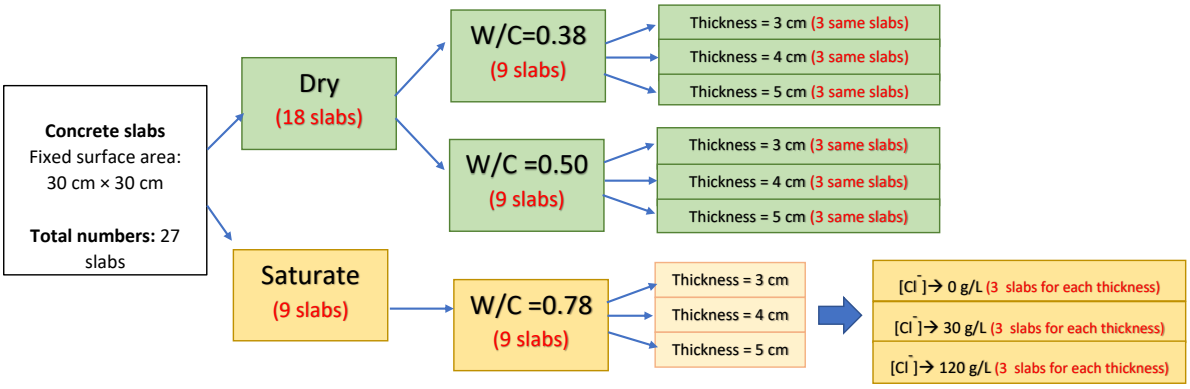

Figure 5.1 – The number of concrete sample and the associated liquid conditions, used in the experimental campaign

(a) (b)

Figure 5.2 – Concrete samples (a) example of wet slab with W/C=0.78 (b) example of dried slab from side view, with W/C=0.50

The slabs were designed with three different thicknesses: 3 cm, 4 cm, and 5 cm. By positioning the slabs between the FMM samples and the interrogator, we can assess the impact of the slab's thickness and saturated state on MO measurements.

A total number of 27 concrete slabs were manufactured for this experimental campaign and more information related to their manufacturing process can be found in [235]. To ensure the repeatability of the measurements, three identical slabs were manufactured for each concrete mixing and thickness. Figure 5.1 illustrates all 27 concrete slabs used in this experiment categorized by mixing and saturation states.

As summarized in this diagram, for the dried concrete slabs, two W/C ratios (0.38 and 0.50) were chosen, and for each mixture, slabs with thicknesses of 3 cm, 4 cm, and 5 cm were prepared,

(a) (b) (c)

Figure 5.3 – Concrete slabs placed in liquid pool to be saturated (a) three concrete slabs with W/C= 0.78 in liquid solution with 0 g/L chloride concentration (b) three concrete slabs with W/C= 0.78 and labels of 3-2 and 5-2 and 4-2 in liquid solution with 30 g/L chloride concentration (c) three concrete slabs with W/C= 0.78 and labels of 3-3 and 4-3 and 5-3 in liquid solution with 120 g/L chloride concentration

Table 5.1 – Concrete slabs, used in the experimental campaign

Concrete	Dimensions	thickness	state of chloride concentration (water condition)	label
W/C=0.38	30 cm × 30 cm	3 cm	dried	3-1
	30 cm × 30 cm	3 cm	dried	3-2
	30 cm × 30 cm	3 cm	dried	3-3
	30 cm × 30 cm	4 cm	dried	4-1
	30 cm × 30 cm	4 cm	dried	4-2
	30 cm × 30 cm	4 cm	dried	4-3
	30 cm × 30 cm	5 cm	dried	5-1
	30 cm × 30 cm	5 cm	dried	5-2
	30 cm × 30 cm	5 cm	dried	5-3
intermediate concrete W/C= 0.50	30 cm × 30 cm	3 cm	dried	3-1
	30 cm × 30 cm	3 cm	dried	3-2
	30 cm × 30 cm	3 cm	dried	3-3
	30 cm × 30 cm	4 cm	dried	4-1
	30 cm × 30 cm	4 cm	dried	4-2
	30 cm × 30 cm	4 cm	dried	4-3
	30 cm × 30 cm	5 cm	dried	5-1
	30 cm × 30 cm	5 cm	dried	5-2
	30 cm × 30 cm	5 cm	dried	5-3
Mortar W/C=0.78	30 cm × 30 cm	3 cm	0 g/L - sat.	3-1
	30 cm × 30 cm	3 cm	30 g/L - sat.	3-2
	30 cm × 30 cm	3 cm	120 g/L - sat.	3-3
	30 cm × 30 cm	4 cm	0 g/L - sat.	4-1
	30 cm × 30 cm	4 cm	30 g/L - sat.	4-2
	30 cm × 30 cm	4 cm	120 g/L - sat.	4-3
	30 cm × 30 cm	5 cm	0 g/L - sat.	5-1
	30 cm × 30 cm	5 cm	30 g/L - sat.	5-2
	30 cm × 30 cm	5 cm	120 g/L - sat.	5-3

each in three specimens. A total of 18 dried concrete samples were prepared: nine slabs with a W/C ratio of 0.38 and nine slabs with a W/C ratio of 0.50.

The saturated concretes chosen for this study have a W/C ratio of 0.78, which due to their high porosity (15% according to [235]) would allow for easier and faster moisture penetration process. The Figure 5.2a shows a saturated slab. Moreover, Figure 5.2b shows a side view of the concrete dried slab with a W/C ratio of 0.50, showing the porosity present in the sample.
Three thicknesses of 3 cm, 4 cm, and 5 cm were manufactured for each saturated concrete mixture. For each thickness, the concrete slabs were immersed in separate pools containing three different chloride contents: 0 g/L (representing water without chloride), 30 g/L (typical of sea water), and 120 g/L (corresponding to de-icing water). Figure 5.3 illustrates the concrete slabs being placed separately in the pools with the corresponding chloride ion concentrations. The pools were covered to avoid water evaporation, and the slabs were left for more than two years to become fully saturated with their respective chloride concentrations.
The dried slabs are stored for two years in an oven at a temperature of 60 degrees Celsius. At the time of the experimental study, the oven was turned off and after a sufficient cooling, the slabs were taken out of oven. Moreover, to avoid carbonation or penetration of any ambient moisture or pollution in the porous network of concrete, the slabs were kept in some plastic bags.

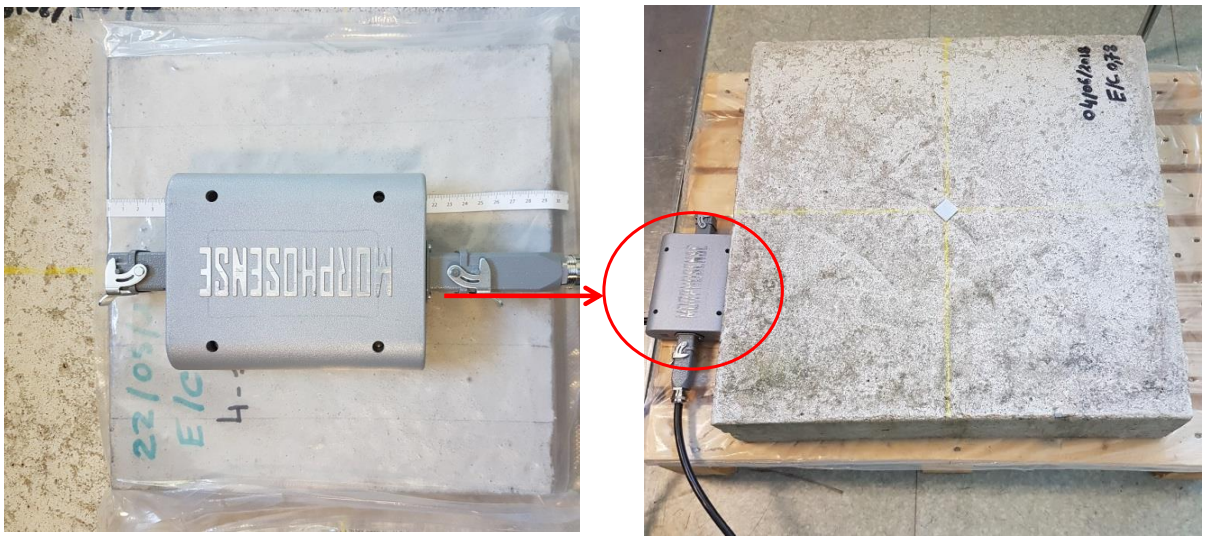

Figure 5.4 – Interrogator used in the experimental campaign for Morphosense neuron system

Eventually, Table 5.1 summarizes the details of all 27 slabs used in this experimental study. In the next section, the properties of magnetic interrogator would be explained.

5.2.2 Magnetic interrogators

In this experimental study, the instruments for monitoring come from Morphosene company. Morphosense is NEURON, plug-and-play low-maintenance system for setting up Micro-Electro-Mechanical System (MEMS) sensor networks, as illustrated indicated in Figure 5.4. The measurement node combines a 3-axis accelerometer, a 3-axis magnetometer, and a temperature sensor. In fact, the 3-axis magnetometer, used in this system is from ST-microelectronics which offers ultra-low-power high performance sensor used for continuous monitoring with possibility of connection to the cloud servers to store data. Table 5.2 reports the practical features of this product.

More practical characteristics of this device (such as SNR), is practically measured during the tests and the results are included at each section, separately. In next section, the descriptions, protocol and results of each test, associated with mentioned objectives, will be presented.

Table 5.2 – Magnetometer's features

Parameters	Min	Unite
measurement range	-16	Gauss
Sensitivity	1711	LSB/Gauss
Operating temperature	-40/+85	C°
Weight	1.034	Kg
standard deviation	$3.2 \times 10^{-}4$	Gauss
RMS noise	3.2	mgauss
Non-linearity	$\pm$ 0.12	
Magnetic disturbance field	Maximum 50	Gauss

5.3 Influence of concrete slab's characteristics on measurements of MO

In this section, we follows two objectives:

1. Wee would evaluate the approximate SNR of MO measurements. Assessing the SNR provides valuable information about the sensitivity of the MO measurements to the presence of environmental magnetic fields and background noise. By quantifying the SNR, the study aims to determine the level of signal strength in relation to the available noise, which is essential for accurate and reliable MO measurements,
2. Secondly, we will investigate the influence concrete slab's different characteristics on MO measurements.

Considering these objectives, the measurement's steps are:

— Firstly, the amount of available magnetic field in the experimental testing area, including the Earth's magnetic field ($\mathbf{B}_0$) and background noise would be randomly measured. This value is highly dependent on the location of the interrogator. Therefore, during all of these measurements, the magnetometer will not move and the data recording will be in free space. Finally, the average of MO measured data, would be considered as minimum available magnetic field of free space (minimum noise level),

— Secondly, a disc NdFeB magnet with a diameter of 15 mm and height of 2 mm is used as a permanent part. The magnet will be attached to an aluminum support at a relative distance of 7.5 cm from the surface of the interrogator (knowing that aluminum is a very weak paramagnetic material, thus it cannot perturb the test). Then, the magnetic field of environment with the presence of reference magnet, would be measure, as reference MO. This configuration allows the interrogator to measure any influence of the concrete media as well. Finally, the amount of SNR could be evaluated from average of measurements, obtained at first and second steps. Moreover, the measured MO value serves as a reference data for the next steps,

— Thirdly, the variation of the MO will be measured by positioning different concrete slabs (*i.e.*, having different thicknesses, moisture conditions, and W/C), between the interrogator and FMM. The obtained MO variations would be compared to the reference MO value, obtained at second step. Thus, it would allow the identify any influence of the concrete slabs characteristics on the MO measurement results.

In the following section, we will present the MO measurement results, related to each step.

5.3.1 Free space investigations: measuring the minimum MO of environment

Figure 5.5 depicts the experimental setup used to measure the MO of the environment. The interrogator is positioned on a concrete block with a geometry of 60 cm × 60 cm × 16 cm and

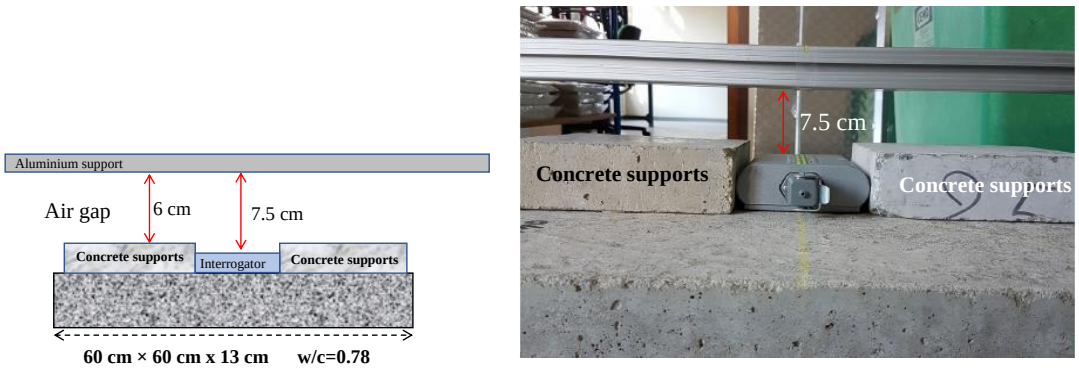

(a) (b)

Figure 5.5 – (a) Schematic representation of the experimental setup, used to measure the minimum magnetic field of the environment (b) experimental setup, with the interrogator placed between the concrete supports, placed on the top of relatively big concrete block size to measure the environmental magnetic field

is supported by two concrete supports with dimensions of 30 cm × 30 cm × 6 cm. The magnetometer can measure the amplitudes of the three components of the **B** vector (MO) in the Cartesian coordinate system: $B_x\hat{x}$, $B_y\hat{y}$, and $B_z\hat{z}$. The primary objective of this experiment is to evaluate the minimum magnetic field available in the environment (including the Earth's magnetic field or any induced magnetic fields in the vicinity of the measurement benchtop). During this step, data acquisition would be initiated without the presence of any magnetic source, for approximately 6 to 7 minutes on two different days.

The minimum measurable MO of environment will be labelled as $\mathbf{B}_{environment}$. It will be served as the bias available magnetic field that can be recorded. The amount measurement's norm (*i.e.*, $||\mathbf{B}_{environment}||$) will be calculated from $||\mathbf{B}_{environment}|| = \sqrt{B_x^2 + B_y^2 + B_z^2}$, for each measurement. The experimental setup was not moved or adjusted during the two days of measurement, ensuring that the MO measurements are obtained under similar locations. As explained, the

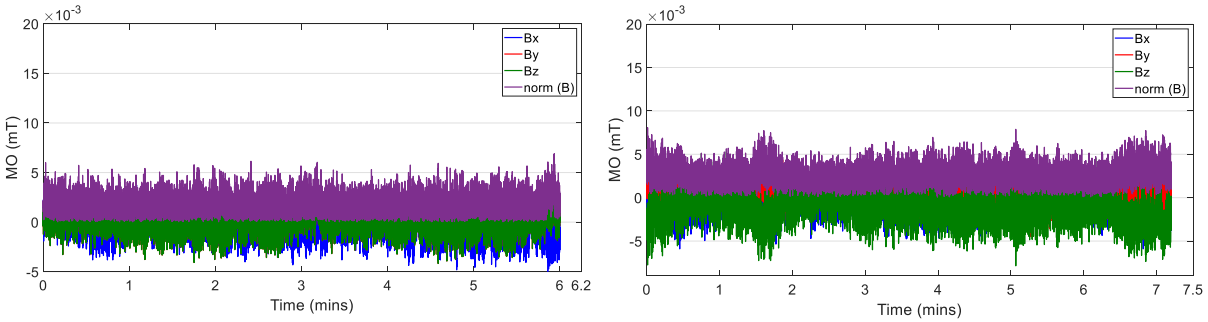

(a) (b)

Figure 5.6 – Comparison of $||\mathbf{B}_0||$ measured at different days (a) measured values of B_x, B_y and B_z day 1 - date: 21/09/2021 (b) measured B_x, B_y and B_z day 2 - date: 23/09/2021

measurements were carried out at different times of two days (morning and evening for 7 minutes) to evaluate the minimum measurable MO. Figure 5.6 shows the measured MO for each direction of x, y and z at two days. The measurements exhibited some variations in recorded data. In fact, these observed variation are associated with standard deviation of interrogator during continues monitoring. We would labelled them with Δ, afterwards. Furthermore, the average MO measurements at each x, y, z and also for $||\mathbf{B}_{environment}||$ is calculated and indicated at Table 5.3. Additionally, the calculated standard deviation of the measurements is included in the results.

The results show some minor deviations in MO measurement during the four repetitions of recording. This difference (between the maximum and minimum MO measured values) is calculated and labeled as $\Delta^{'}$ and indicated in Table 5.3. This difference could be attributed to the natural changes in the Earth's magnetic field ($\mathbf{B}_0$) caused by its rotation.

Upon comparing the results, the average available MO of environment (bias value) during the days of measurement, in each direction of x, y, and z, as well as the $||\mathbf{B}_{environment}||$, are approximately equal to:

— $B_x = 4.8 \times 10^{-4} \pm 1.2 \times 10^{-6}$ [mT]
— $B_y = 5.17 \times 10^{-4} \pm 1.5 \times 10^{-6}$ [mT]
— B_z = -0.0013 $\pm$ 2.9 $\times 10^{-6}$ [mT]
— $||\mathbf{B}_{environment}|| = 0.0014 \pm 1.2 \times 10^{-6}$ [mT]

As mentioned, the difference between the maximum and minimum measured values, labeled as $\Delta^{'}$ is also calculated during four repeated measurements, separately for each components and norm value. The value of $\Delta^{'}||\mathbf{B}_{environment}||$ was found to be 0.0002 [mT], which should be considered as an order of magnitude for the uncertainty of $||\mathbf{B}_{environment}||$.

The measurements in free space provide a baseline for the available MO in the experimental area,

Table 5.3 – Measurements of MO in free space, for each components of B_x, B_y, B_z in Cartesian coordinate system and the related $||\mathbf{B}_{environment}||$ [mT], obtained through continuous monitoring for 6-7 minutes in the morning on two different days

	B_x [mT]	B_y [mT]	B_z [mT]	$||\mathbf{B}_{environment}||$ [mT]
Day 1 morning	-5 $\times 10^{-4}$	5.7 $\times 10^{-4}$	-0.0012	0.0014
Day 1 evening	-4.7 $\times 10^{-4}$	5 $\times 10^{-4}$	- 0.0015	0.0016
Day 2 morning	-4.9 $\times 10^{-4}$	5.2 $\times 10^{-4}$	-0.0013	0.0014
Day 2 evening	-4.9 $\times 10^{-4}$	5.2 $\times 10^{-4}$	-0.0013	0.0014
Δ (standard deviation of interrogator)	$\pm$ 1.2 $\times 10^{-6}$	$\pm$ 1.5 $\times 10^{-6}$	$\pm$ 2.9 $\times 10^{-6}$	$\pm$ 1.2 $\times 10^{-6}$
$\Delta^{'} = \lvert B_{max} - B_{min} \rvert$	0.3 $\times 10^{-6}$	$\pm$ 0.7 $\times 10^{-6}$	0.0003	0.0002

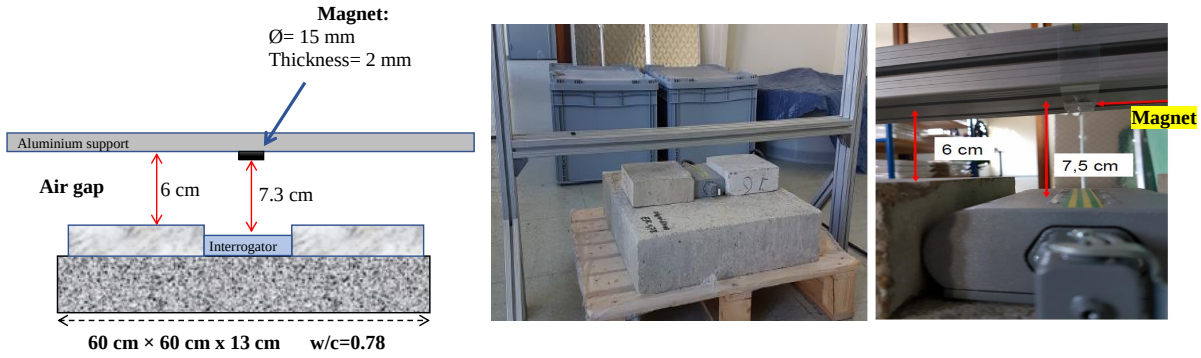

(a) (b) (c)

Figure 5.7 – Schematic representation of measuring MO generated by reference magnet at the distance of 7.3 cm from interrogator (b), (c) the photos from experimental setup with a magnet, attached to aluminum support

where we plan to carry out the main MO measurements from FMM. By measuring the MO in free space, any potential interference or noise from external sources can be identified and accounted for during subsequent measurements. Furthermore, the repeatability of the measurements also provides information on the stability of the experimental setup and protocol during two days. These measurements are very important to calculate the SNR of the these measurements. By quantifying the approximate SNR, it is possible to roughly assess the sensitivity and quality of the subsequent MO measurements of FMM. In the following section, we would measure the MO, at the presence of reference permanent magnetic.

5.3.2 Free space investigations: measuring MO at the presence of reference magnet

At this step, we have attached a reference magnet with a radius of 7.5 mm and a height of 2 mm to the aluminum support, as shown in Figure 5.7a. As mentioned, at this level, we would measure the MO of free space, at the presence of reference magnetic source. The north pole of the disc magnet is on its upper face, and subsequently, the south pole is on its bottom face, and the measurement is taken in the z-axis direction. The distance between the interrogator and the lower face of the magnet (south pole) is 7.3 cm, accounting for the 2 mm thickness of the magnet. The distance between the top surface of the concrete support slabs and the aluminum support remains at 6 cm, as in the previous step, and the medium between the magnet and interrogator is air.

The amplitudes of MO, at each B_x, B_y, and B_z components from the reference magnet are measured for approximately 5 minutes. Similar to the previous section, the measurements are repeated in two days, in the morning and afternoon, to evaluate the repeatability and uncertainty of the results. The raw MO measurements at each component of x, y, z, and $||\mathbf{B}||$ are shown

Table 5.4 – Averaged measurements of MO [mT] of the reference magnet ($\mathbf{B}_{magnet}$) at distance 7.3 cm

	B_x [mT]	B_y [mT]	B_z [mT]	$\|\|\mathbf{B}\|\|$ [mT]
Day 1 morning	0.021	-0.003	0.290	0.291
Day 1 evening	0.022	-0.003	0.281	0.281
Day 2 morning	0.022	-0.002	0.292	0.288
Day 2 evening	0.023	-0.002	0.292	0.290
Δ (standard deviation of interrogator)	$\pm$ 0.0011	$\pm$ 0.0011	$\pm$ 0.0017	$\pm$ 0.0017
$\Delta^{'} = \|B_{max} - B_{min}\|$	0.002	0.001	0.011	0.010

in Figures 5.8. Since the measurements are carried out at z direction (due to north/south pole direction of magnet), the amount of B_z is relatively dominant component, compare to others and determine the amount of norm MO.

These four times measurements are conducted immediately after measuring the $\mathbf{B}_{environment}$, discussed in Section 5.3.1. Table 5.4 presents the average values of MO measurements, at this section. Additionally, the standard deviation of interrogator and the standard deviation of MO measurements ($\Delta^{'}$), due to repeating the recording, are calculated for each measurement and indicated at the table.

The average values of MO measurements for each component and $||\mathbf{B}_{magnet}||$ are:

- $B_x = 0.022 \pm 0.0011$ [mT]
- B_y = -0.0026 $\pm$ 0.0011 [mT]
- $B_z = 0.28 \pm 0.0017$ [mT]
- $||\mathbf{B}_{magnet}|| = 0.287 \pm 0.0017$ [mT]

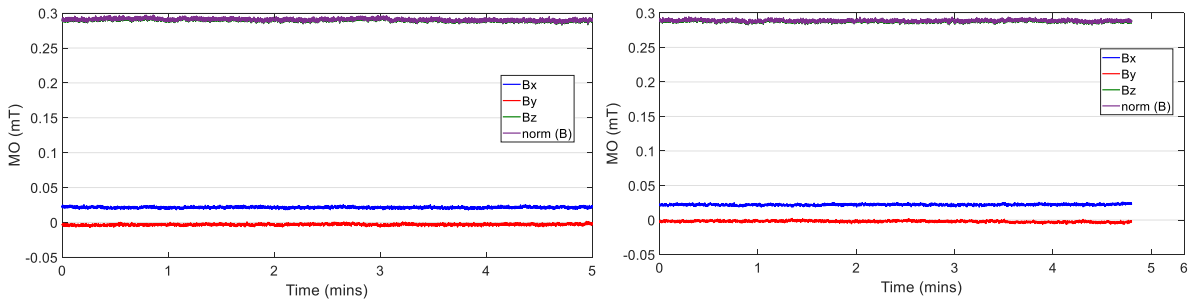

Figure 5.8 – The variations of MO [mT] with presence of magnet at 7.5 cm of interrogator, at two different days (a) day 1: 21/09/2021 (b) day 2: 23/09/2021

Comparing the results of MO measurements with and without a magnet, as shown in Tables 5.4 and 5.3 respectively, reveals a notable increase in the total average of MO measurements when a magnet is present at a distance of 7.3 cm. The results indicate that the MO generated by the magnet is stronger than the bias magnetic field of environment. This suggests that the magnet has a more substantial influence on the measured MO values compared to the background noise. Thereby, the MO of permanent magnetic as reference source of following tests, even at distance like 7.5 cm, is the primary factor, contributed in amount of measured MO, while the background noise has a fewer effect.
Additionally, the amount of $\Delta^{'}$ in measurements of with and without magnet, showed a slight increase in the order of uncertainty. The reasons for this change could be related to various factors such as the heating process of electronic kits in the interrogator, interrogator error, or changes in the magnetic field of Earth. However, finding the precise reason that causes such standard deviations is very difficult and requires further measurements.
Finally, to calculate the approximate SNR of these measurement, the reference MO permanent magnet ($||\mathbf{B}_{magnet}||$) is considered as the desired signal and the measured MO of environment ($\mathbf{B}_{environment}$), considered as noise signal. Thus, the SNR ratio is calculated using the following equation:

$$\mathbf{SNR}[dB] = 20 \log \frac{||\mathbf{B}_{magnet}||}{||\mathbf{B}_{environment}||} \tag{5.1}$$

The calculated SNR is about 42 dB, for these measurements. This value indicates that the desired signal is approximately 42 dB stronger than the background available bias magnetic field of environment. This value would be served as important quantitative information, related to stability of MO measurements from FMM device as well.
In the following, we will add concrete slab in the gap between reference magnet and interrogator. As mentioned, we aim to evaluate the effect of concrete slab's different conditions, a the MO measurements.

5.3.3 The influence of concrete thickness on MO measurements from magnet

In the previous section, we assessed the amount of MO generated from a reference magnet. In this section, we will investigate the impact of concrete different characteristic such as: its thickness, its different mixing and its hyrdic state, respectively, on MO measurements. To explore the impact of concrete different thickness, we have placed various concrete slabs between the magnet and Morphosense interrogator. Figure 5.9a illustrates a schematic representation of this experimental setup. The reference magnet (which is a disk NdFeB magnet with a diameter of 15 mm and a height of 2 mm), positioned at a relative distance of 7.3 cm from the interrogator. The gap between the magnet and interrogator would be filled through concrete slabs with a fixed surface area of 30 cm $\times$ 30 cm and varying thicknesses of 3 cm, 4 cm, and 5 cm are utilized.

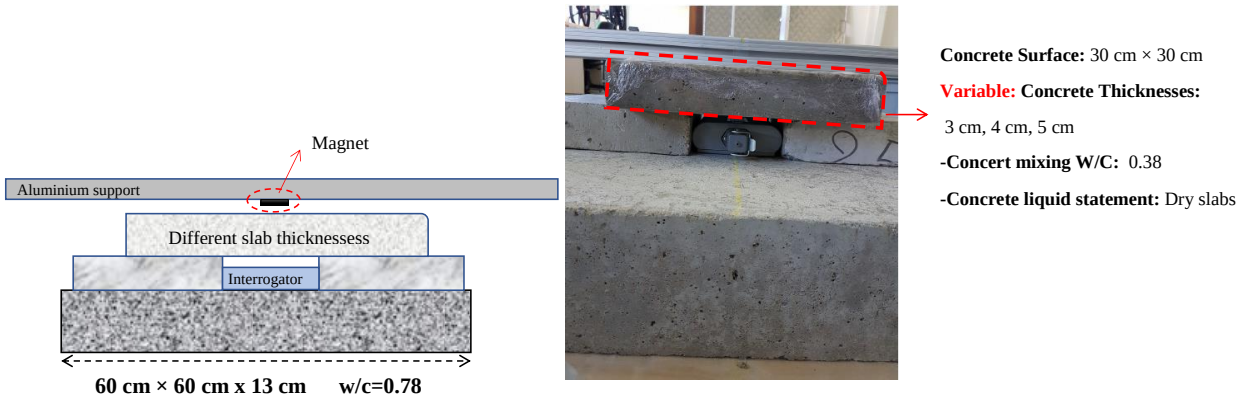

(a) (b)

Figure 5.9 – (a) General schematic representation of the test, magnet in distance of 7.5 cm from interrogator, surrounding with concretes (b) measurement of MO, generated by magnet in 7.3 cm of interrogator and the gap filled by concrete slabs (with fixed W/C=0.38 and dry samples) and different thickness of 3 cm, 4 cm and 5 cm

All nine dry slabs with W/C=0.38 are used in this experiment. Figure 5.9b shows a photo of a concrete sample filling the mentioned gap between the interrogator and magnet. The relative position of the magnet or interrogator is fixed for all of these measurements.
The results of MO measurement, in the Cartesian coordinate system for the three components of B_x, B_y, and B_z as a function of concrete thickness with 3 cm, 4 cm, and 5 cm are shown in Figure 5.10a. Figure 5.10b illustrates the calculated amount of norm MO ($||\mathbf{B}||$) for each concrete slab. As depicted in this graphs, using concrete slabs with different thickness have no significant impact, not measured MO components or norm value of MO. The obtained signal variation in Figure 5.10b is due to the standard deviation of the interrogator, labelled as $\Delta\mathbf{B}$ in this figure. For more quantitative comparison, Table 5.5 summarizes the average of recorded MO for each nine slab, in the directions of x, y, and z. The calculated standard deviation $\Delta\mathbf{B}$, is

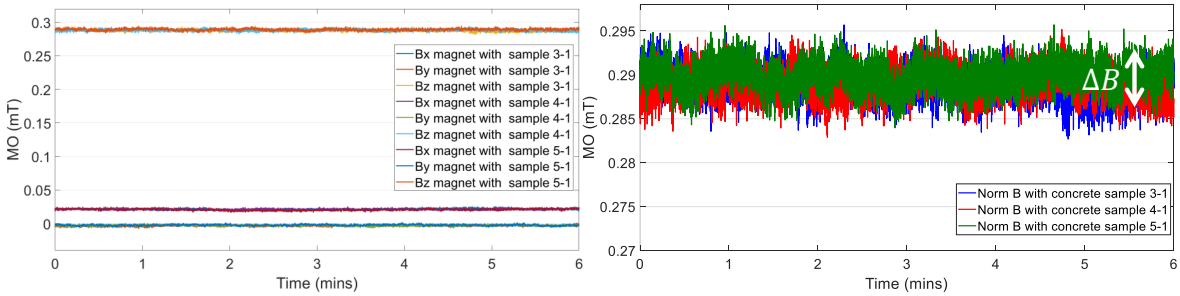

(a) (b)

Figure 5.10 – (a) Measurement of MO, generated by magnet in 7.3 cm of interrogator and the gap filled by different concrete slabs with variety of parameters (b) $||\mathbf{B}||$, measured for three concrete slabs (the signal variation of $\Delta\mathbf{B}$ represented the interrogator standard deviation)

Table 5.5 – Mean values and standard deviations of B_x, B_y and B_z measured from the magnet at 7.3 cm from the surface of the node and with the presence of all dry slabs formulated with the ratio W/C=0.38.

Slab's thickness	**Slab's labels**	$B_x \pm \Delta B_x$ [mT]	$B_y \pm \Delta B_y$ [mT]	$B_z \pm \Delta B_z$ [mT]
3 cm	**3-1**	0.0215 ± 0.0012	-0.00319 ± 0.0012	0.288 ± 0.0017
	3-2	0.0210 ± 0.0012	-0.00237 ± 0.0012	0.287 ± 0.0016
	3-3	0.0221 ± 0.0011	-0.00272 ± 0.0012	0.287 ± 0.0017
4 cm	**4-1**	0.0214 ± 0.0012	-0.00267 ± 0.0012	0.288 ± 0.0017
	4-2	0.0208 ± 0.0012	-0.00375 ± 0.0012	0.288 ± 0.0017
	4-3	0.0206 ± 0.0012	-0.00307 ± 0.0012	0.288 ± 0.0016
5 cm	**5-1**	0.0207 ± 0.0012	-0.00219 ± 0.0012	0.289 ± 0.0017
	5-2	0.0211 ± 0.0012	-0.00348 ± 0.0011	0.289 ± 0.0017
	5-3	0.0202 ± 0.0012	-0.00298 ± 0.0012	0.2887 ± 0.0017
B magnet without slabs		0.0214 ± 0.0011	-0.00284 ± 0.0011	0.2889 ± 0.0018

also added to the measurements. Calculating the average value of norm MO, for each thickness, Figure 5.11 compare the measured MO as function of changing the concrete thickness. At this figure, the amount of standard deviation of MO due to interrogator ($\Delta\mathbf{B}$) represented as error bars.

comparing the results of Table 5.5 and Figure 5.11, the variation range of MO at each thickness, indicated as $\Delta^{'}||\mathbf{B}||$= max ($||\mathbf{B}||$) - min ($||\mathbf{B}||$), are calculated as:

- Concrete with 3 cm thickness: $\Delta^{'}||\mathbf{B}|| = 0.0009$ mT.
- Concrete with 4 cm thickness: $\Delta^{'}||\mathbf{B}|| = 0.0007$ mT
- Concrete with 5 cm thickness: $\Delta^{'}||\mathbf{B}|| = 0.0004$ mT

Considering this results, it can be concluded that by changing the concrete thickness, the MO measurements would be affected roughly around 0.0002 mT. Considering the uncertainty level of measurements, due to the interrogator standard deviation (about 0.0017 mT), the obtained

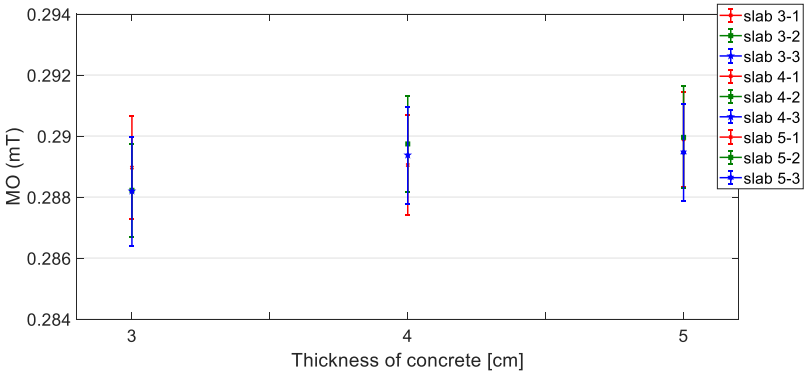

Figure 5.11 – Comparing the mean of $||\mathbf{B}||$ and the associated standard deviation of measurement, recorded form magnet at distance of 7.3 cm, with and without presence of dried concretes (W/C=0.38), as function of concrete thickness 3 cm, 4 cm and 5 cm

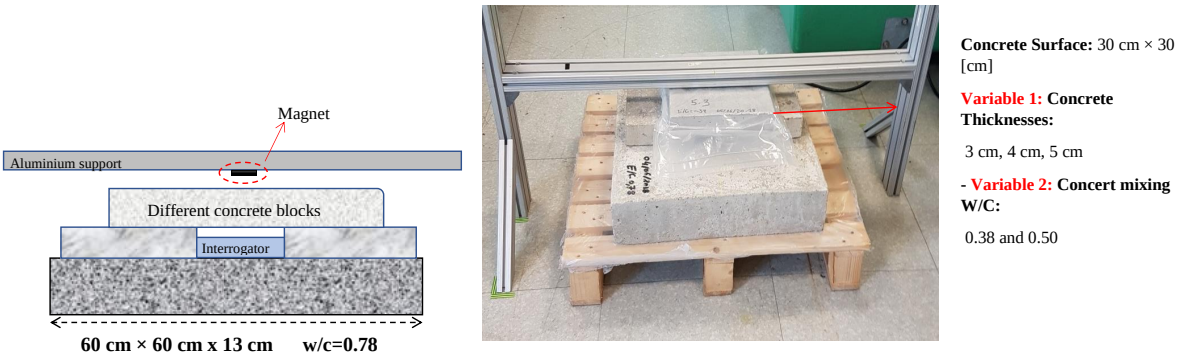

Figure 5.12 – (a) General schematic representation of the test, magnet in distance of 7.3 cm from interrogator, surrounding with concretes (b) measurement of MO, generated by magnet in 7.3 cm of interrogator and the dried concrete slabs with different concrete mixing W/C=0.38 and 0.50 as well as different thickness of 3 cm, 4 cm and 5 cm, are filled the gap

variations due to changing concrete thickness is lower than standard deviation of interrogator. Thus, it can be concluded that altering the slabs and concrete thickness would have a negligible effect on MO. Therefore, the aforementioned assumption that MO are insensitive to concrete thickness, could be justified, through these results.

Moreover, since the test involved the use of nine concrete slabs, each slab undergoing 5 minutes of MO measurements, a total time duration of 45 minutes was spent to record data. Therefore, it is possible to assume that the obtained variations, could be caused by the data interrogator's shifting due to hot processing of its electrical board and not for changes in concrete thickness.

In the next section, the effect of concrete mixing on MO measurements will be experimentally evaluated.

5.3.4 The influence of concrete mixing on MO measurements from magnet

To assess the impact of concrete mixing on MO measurements, various parameters such as water to cement ratio, aggregate size, and porosity level could be taken into consideration. In this section, we specifically aim investigates the impact of the W/C ratio on the experimental MO measurements. To achieve this, three different concrete mixing are selected, each with a specific W/C ratio of 0.38, 0.50, and 0.78, and would be used to fill the gap between magnet and interrogator. The study also includes the the concrete slab with different thicknesses, 3 cm, 4 cm, and 5 cm. Thus, the amount MO is evaluated as a function of both the concrete mixing and thickness? as well. Figure 5.12 shows a schematic representation of this step. Here, a total of 18 slabs with W/C ratios of 0.38 and 0.50, listed in Table 5.1, are used. The MO measurements takes about 5 minutes for each slab, resulting in a total test duration of 90 minutes. As previously mentioned, to evaluate the repeatability of results, three identical concrete slabs are used for each thickness. In order to prevent any variations in MO measurements that may be caused

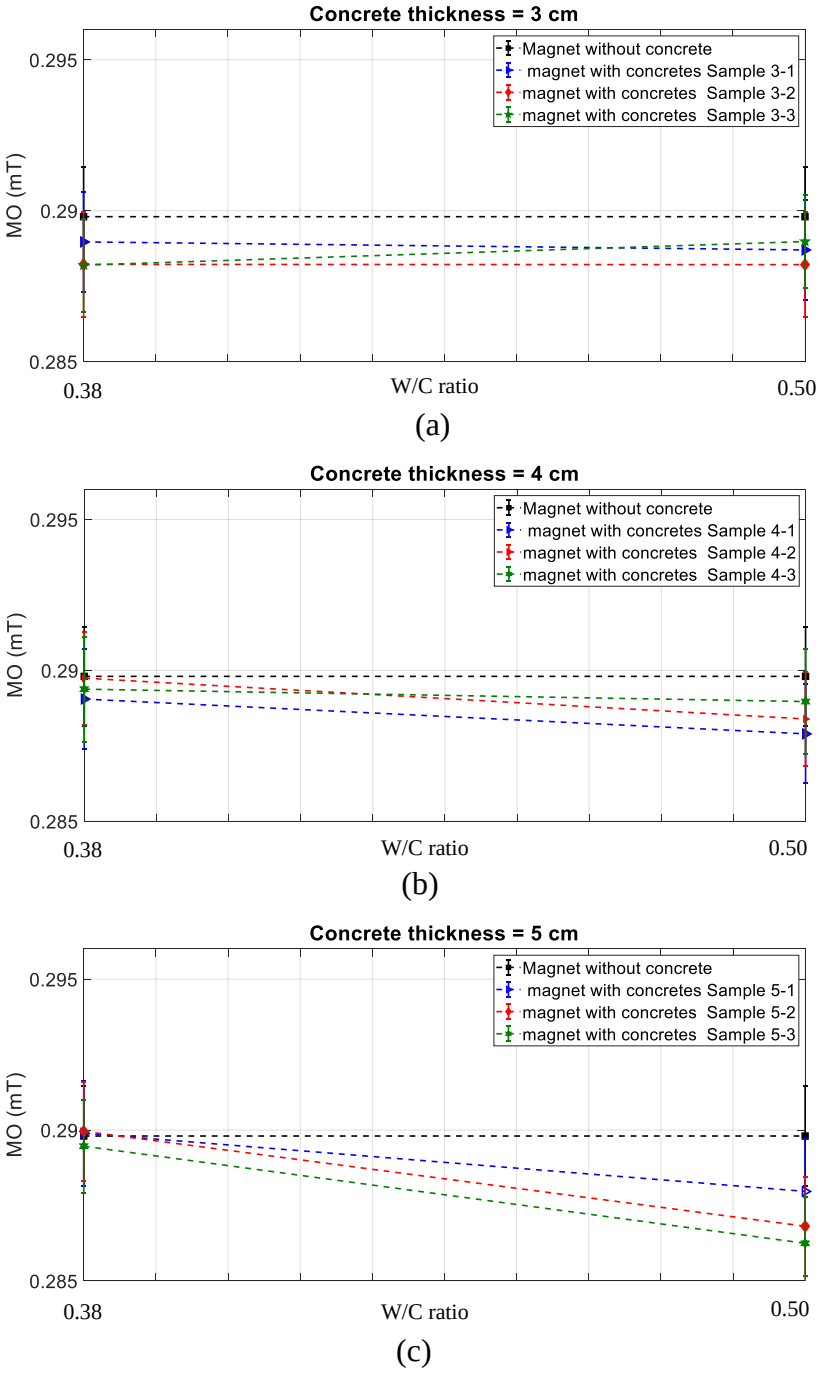

Figure 5.13 – Comparing the average amount of MO, and the associated standard deviation of measurements, recorded form magnet at distance of 7.3 cm, as a function of concrete mixing with 0.38 and 0.50 and also thickness 3 cm, 4 cm and 5 cm

by human error, the experimental setup (specifically relative position of magnet and interrogator) is kept fixed throughout the measurements. Thus, the only modification made during the

experiment is the replacement of the concrete slabs in the middle.
The results of MO variation due to the use of different concrete mixing and thickness are presented in graphs at Figure 5.13. To avoid redundancy, only the results of average amount of norm MO, are illustrated in graphs. We have assumed that the norm value is considered as a representative quantity in these 3-axis measurements, instead of focusing on each measured components at x, y and z direction. Additionally, the standard deviation of the repeated measurements for each concrete mix, has been added into the graphs presented in Figure 5.13. By including the standard deviation, we can assess the precision and consistency of the measurements, highlighting the level of uncertainty associated with the MO measurements.
As illustrated in Figure 5.13, the amount of MO altering is slightly higher for concrete slab with W/C=0.50 compared to W/C=0.38. When taking into account the uncertainty level caused by the interrogator's standard deviation ($\Delta||\mathbf{B}|| = 0.0017$ mT), it can be observed that the majority of the MO variations resulting from changes in the concrete mixing are below this standard deviation. However, for the concrete sample with a thickness of 5 cm (slab 5-3), the calculated uncertainty level due to changes in the mixing is found to be 0.0017, which is equivalent to the uncertainty level of the interrogator. This indicates that the obtained variations in MO measurements are comparable to the level of uncertainty associated with the interrogator's measurements. The long duration of the test (90 minutes) could have potentially impacted the interrogator's electrical board, leading to some deviations in the measurements. However, determining the exact cause of these deviations is challenging.
In addition, based on the experimental results, it can be concluded that the concrete mixing does not have a significant effect on MO measurements. This implies that the initial assumption regarding the insensitivity of MO to concrete mixing is justified. The experimental data supports the notion that concrete mixing can be considered a non-magnetic parameter in the context of MO measurements.
In the following section, we will examine the impact of varying hydric states of concrete, specifically the water content such as chloride ion concentration, on MO measurements.

5.3.5 The influence of concrete hydric state on MO measurements from magnet

In the previous sections, we have concluded that concrete properties such as thickness and mixing have minimal influence on MO measurements. In this section, we will investigate the impact of the hydric state of concrete, specifically the water content, on MO measurements. To conduct this evaluation, we will focus on concrete slabs with a W/C ratio of 0.78. These slabs were fully saturated by immersing in the solution pools for two years. The content of the solutions was different, in terms of chloride ions. Thereby:

— The first group of slabs, with thicknesses of 3 cm, 4 cm, and 5 cm, are immersed and

saturated in a pool containing city water and 0 g/L additional chloride ion concentration.

— The second group of slabs, with thicknesses of 3 cm, 4 cm, and 5 cm, are immersed and saturated in a pool containing NaCl saline solution with 30 g/L chloride ion concentration.

— The third group of slabs, with thicknesses of 3 cm, 4 cm, and 5 cm, are immersed and saturated in a pool containing NaCl saline solution with 120 g/L chloride ion concentration.

Totally, 9 slabs were used to slid between interrogator and reference magnet, as illustrated in Figure 5.14a. As previous steps, the MO measurements last for 5 minutes for each slabs. The concrete slabs were moved carefully to make sure that the experimental setup is not altering. Figure 5.15 illustrates the results of MO measurements, as function of chloride ion concentration level.

The results indicate that there are some changes in MO due to variations in the chloride ion concentration of the concrete. However, the observed MO variation ranges in this experiment are lower than the standard deviation of the interrogator ($\Delta||\mathbf{B}|| = 0.0017$ mT). Additionally, the observed variations are smaller than the uncertainty level resulting from environmental fluctuations (0.0002 mT), as discussed in Section 5.3.1. However, for a concrete slab with a thickness of 3 cm and a chloride ion concentration of 30 g/L, there is a more noticeable deviation in Figure 5.15, with a value of 0.0016 mT, which is close to the standard deviation of the interrogator (0.0017 mT).

Based on the results obtained, it can be assumed that the observed MO variations are more likely to be caused by the standard deviation of the interrogator rather than changes in the hydric state of the concrete. The fact that the tests for all slabs lasted 45 minutes suggests that the hot processing of the interrogator could be the most possible reason contributing to this deviation. Therefore, overall, it can be concluded that the hydric state of concrete, specifically

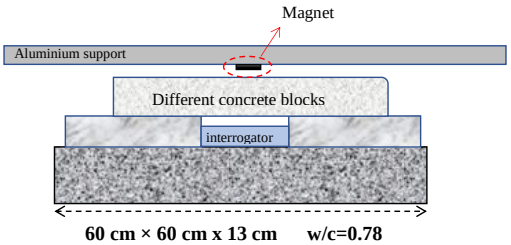

(a)

(b)

Concrete Surface: 30 cm × 30 cm
Concert mixing W/C: 0.78
Variable 1: Concrete Thicknesses:
3 cm, 4 cm, 5 cm
- Variable 2: Concrete hydric state:
-Saturated slabs
-[Cl^-] ions concentrations:
0 g/L, 30 g/L and 120 g/L

Figure 5.14 – (a) General schematic representation of the test, magnet in distance of 7.3 cm from interrogator, surrounding with concretes (b) with different saturated concrete slabs (0 gL, 30 g/L and 120 g/L chloride ions concentrations) and as function thickness changing from 3 cm to 5 cm

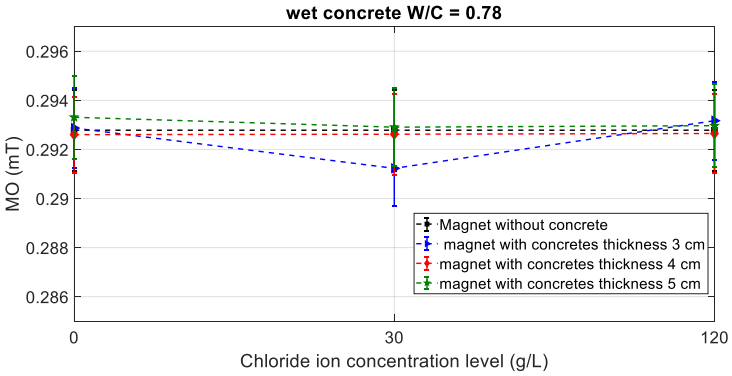

Figure 5.15 – MO variations, as function of different chloride ion concentration level

the level of chloride ions, have no significant effect on MO.

Based on the various experimental tests conducted in this section and the two previous sections, it has been observed that different concrete characteristics, such as the thickness, mixing, and hydric state, have negligible effects on the measured MO induced by the reference magnet. According to [236], concrete may exhibit exceedingly weak paramagnetic or diamagnetic behavior when exposed to intense external magnetic sources, that could give a raise to its magnetic dipolar moments. Based on the experimental findings of this study and considering the relatively small geometry of the FMM device used, it can be concluded that the MO generated by the FMM is unable to alter the magnetic dipolar moments of concrete in the same direction or magnetize the material. Therefore, it further confirms that, for the purposes of this study, concrete can be regarded as a non magnetic medium.

The results further emphasize the potential advantage of using MO measurements as magnetic ND techniques for RC inspection, compare to other techniques such as EM waves, which are sensitive to media's condition. This characteristic makes FMM's MO as a promising solution for SHM applications in terms of the stability and reliability of results.

The next section will focus on quantifying the impact of reactive part corrosion on MO through further experimentation.

5.4 MO variations range by corrosion evolution on FMM's reactive part

In the previous section, the initial assumption that concrete could be considered as non magnetic medium was evaluated by some experimental test. In this section, the main focus is to investigate the MO variation range and tendency, generated by FMM's, as a function of reactive part corrosion evolution. It would allow to assess, experimentally the performance of FMM on a concrete media, as well. As obtained in Chapter 4, the MO would have upward tendency with reactive part's thickness loss, which it was assumed that geometrical variations

could alter the magnetic properties of FMM, specifically, its net magnetic dipolar moment value. To evaluate that hypothesis and also justify experimentally, the results of Chapter 4, we have chosen some reactive part samples with different thicknesses for this experimental test. The chosen reactive parts would be separately, subjected to accelerated corrosion in NaCl saline solution to induce different corrosion states. Afterwards, they would be attached to the reference magnet and eventually, prepared FMM samples with different reactive part's thicknesses and corrosion states. Finally, each of these FMM samples would be placed individually on top of a concrete slab, and the MO variations would be experimentally measured through an external interrogator.

A schematic representation of the experimental setup, where the FMMs are placed at the top center of the concrete slab is presented in Figure 5.16. The MO are measured in z-axis direction. To do that, similar to previous sections, the north/south pole direction of reference magnet is adjusted with trial and error roughly at z-axis direction. As already explained, the concrete properties and condition, have no affect on MO measurement. Therefore, to avoid repeating measurements for all 27 concrete slabs, three dried concrete slabs with different thicknesses of 3, 4 and 5 cm are used to fill the gap between the FMM and interrogator. The remaining characteristics of the concrete slabs will be maintained constant throughout the experiment.

The interrogator is placed on a large concrete support with dimensions of 60 cm × 60 cm × 13 cm, and PVC sheets are used to move the interrogator closer to the concrete slab, as depicted in Figure 5.17. Similar to the experimental setup described in the previous section, two concrete supports are placed on the left and right sides of the interrogator to position the chosen slabs above it. Red PVC supports are added on top of the concrete supports to prevent the slabs from crushing the interrogator. To ensure accurate positioning of the FMM samples on top of the chosen concrete slab (maintain the relative distance between all FMMs and interrogator),

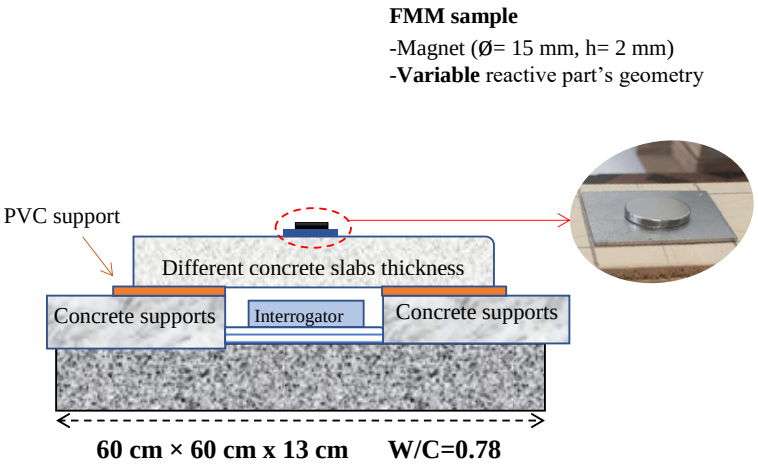

Figure 5.16 – Schematic representation of experimental setup

(a) (b)

Figure 5.17 – Experimental setup photos (a) interrogator placed on top of PVC sheets on a concrete block and among two concrete supports (b) concrete slab is placed on the top for interrogator and a grid line page used to find the place of FMM sample for punctual monitoring

a grid-line paper and other markers are used, as shown in Figure 5.17b. This allows for precise determination of the FMM sample's position for punctual monitoring purposes. The dry concrete slabs are kept in sealed plastic bags to prevent carbonation and moisture penetration during the tests. In the following section, we describe the materials used in this test.

5.4.1 Concrete slabs and FMM samples

As previously explained, only three concrete slabs are chosen for this section. Their concrete mixing (W/C) is equal to 0.38 and all are dried slabs with thickness of 3 cm, 4 cm and 5 cm. Thus, the chosen concretes are:

— Dry slab W/C=0.38- geometry = 30 cm × 30 cm × 3 cm- label: 3-2,
— Dry slab W/C=0.38- geometry = 30 cm × 30 cm × 4 cm- label: 4-1,
— Dry slab W/C=0.38- geometry = 30 cm × 30 cm × 5 cm- label: 5-1.

Additionally, four different FMM samples with varying reactive part thicknesses are prepared for this test. Their permanent part geometry remains The NdFeB disc shaped magnet with a diameter of 15 mm and a thickness of 2 mm is used as permanent part for all of the FMM samples. The four reactive part's geometries that would result in providing four FMMs are:

— 25 mm × 30 mm × 1 mm, labelled as FMM 1,
— 25 mm × 30 mm × 0.5 mm labelled as FMM 2,
— 25 mm × 30 mm × 0.3 mm labelled as FMM 3,
— 25 mm × 30 mm × 0.1 mm labelled as FMM 4.

To assess the impact of corrosion evolution on the MO of each FMM sample, we corroded the corresponding reactive parts using electrolysis technique to achieve corrosion states ranging from 10% to 50%. Consequently, for each FMM sample, we prepared 6 reactive parts with corrosion

states of 0% (without corrosion), 10%, 20%, 30%, 40%, and 50%. In the following, we will provide a further explanation of the accelerating corrosion information associated with each reactive part's sample.

5.4.2 Corrosion of the reactive parts

Figure 5.18a illustrates the setup used for accelerated corrosion to rust the reactive parts. A NaCl solution with a chloride ion concentration of 30 g/L is used as electrolyte. The corrosion state of reactive parts are evaluated using Relative Mass Loss (RML) as the index. Hereinafter, we would use the term of iron patch for those of reactive part's samples, to simplify the writing. The preparation steps of experiment are:

— The initial mass and geometrical values of each iron patch are carefully measured,
— Each iron patch is immersed in a beaker containing 30 g/L NaCl solution separately. As shown in the schematic representation of the Figure 5.18a, the iron patch is connected to the positive terminal (which serves as the cathode) and a platinum-coated titanium electrode is connected to the negative terminal (as the anode) of a DC generator,
— A current intensity of 10 mA is specifically applied during a given duration for each patch, in order to achieve precise RML,
— For the 1.0 mm thick patch, a current intensity of 20 mA is applied for 25 hours and 15

(a)

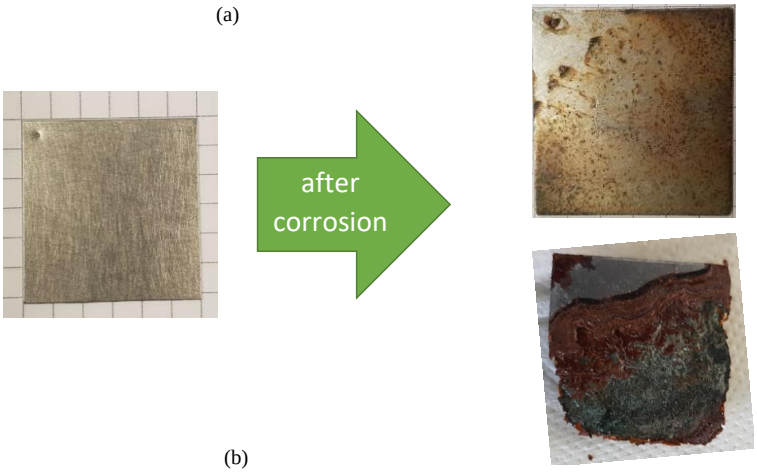

(b)

Figure 5.18 – Acceleration corrosion experimental setup to rust the reactive part

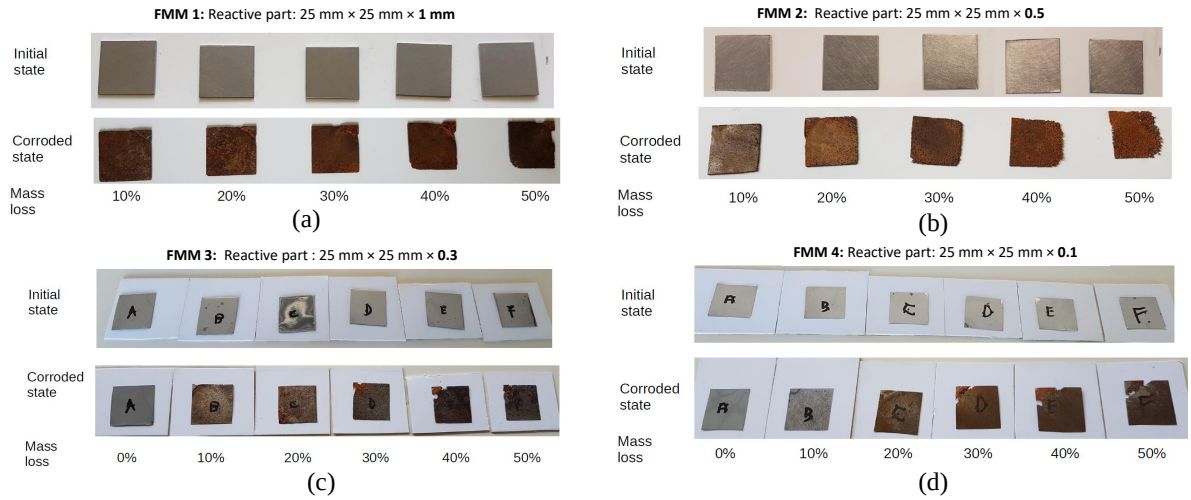

Figure 5.19 – Patches before and after accelerated corrosion (a) FMM 1: six samples with 1.0 mm thickness (b) FMM 2: six samples with 0.5 mm thickness (c) FMM 3: six samples with 0.3 mm thickness (d) FMM 4: six samples with 0.1 mm thickness

minutes to reach 10% RML. This time is halved for the 0.5 mm thick patch (12 hours and 15 minutes for corrosion till 10%),

— By weighing the patches and determining the mass loss, the amount RML is calculated for each patch,

— Once the corroded patches reach 10%, 20%, 30%, 40%, and 50% RML, they are ready to use as reactive parts.

Figure 5.18b shows a patch, before and after corrosion. Pitting corrosion is formed on the surface of the patch due to the presence of NaCl agents.

Moreover, Figure 5.19 illustrates all of four reactive parts with thicknesses of 1 mm, 0.5 mm, 0.3 mm, and 0.1 mm, before and after corrosion, at each related corrosion state. As it illustrated, the patches are degraded and their geometry are affected, mainly after 50% of corrosion. The most loss is observable at the edges of reactive parts.

Regarding the corrosion products generated during the accelerated corrosion process, they were removed before weighing from the patches. Therefore, the effect of corrosion products layers on the MO was not evaluated in this experiment. The corrosion process of the patches is expected to follow the Tuutti diagram [22], which describes the exponential degradation of RC structures due to corrosion. Specifically, the corrosion of iron materials in RC structures typically has three main phases, as shown in Figure 5.20. The first phase is the initiation of corrosion, during this phase, no noticeable deterioration may be occurred. In the propagation phase, iron materials would be relatively quicker rusted, and the mass loss would follow relatively linear pattern. Finally, in the alerting stage, the corrosion progress would raise exponentially and causes significant damage to the RC [22]. Table 5.6 presents information on the applied current intensity, measured geometrical value, and weight of each patch at each corrosion state. Considering the corrosion

Table 5.6 – Related information of accelerated corrosion process for each patch

Corrosion rate (%)	Initial mass (g)	Initial length 1 (mm)	Initial length 2 (mm)	Initial thickness (mm)	Final mass (g)	Final length 1 (mm)	Final length 2 (mm)	Final thickness (mm)	current intensity (mA)	RML (%)	Corrosion time (hours. mins)
Patch thickness = 1 mm											
patch 0 %	5.296	25.16	25.48	1.06	5.296	25.16	25.48	1.06	20		
Patch 10 %	5.275	25.25	25.38	1.05	4.743	25.16	25.37	1.03		10.09	25.25
Patch 20 %	5.194	25.22	25.12	1.07	4.158	24.98	24.77	1.02		19.95	50
Patch 30 %	5.184	25.06	24.97	1.09	3.634	24.66	24.76	0.9		29.90	71.67
Patch 40 %	5.167	25.16	24.99	1.05	3.096	24.42	24.51	0.95		40.08	98.42
Patch 50 %	5.205	25.19	24.92	1.05	2.608	24.3	24.45	0.95		49.89	122.92
Patch thickness = 0.5 mm											
patch 0 %	2.498	25.25	25.03	0.52	2.498	25.25	25.03	0.52	20		
Patch 10 %	2.481	25.23	24.75	0.55	2.241	25.21	24.72	0.49		9.67	12
Patch 20 %	2.513	25.31	25.18	0.51	2.029	25.2	25.06	0.495		19.26	24.28
Patch 30 %	2.446	24.64	25.03	0.52	1.692	24.64	25.03	0.52		30.83	35.45
Patch 40 %	2.462	24.8	24.97	0.52	1.484	24.31	24.57	0.5		39.72	47.57
Patch 50 %	2.462	25.13	24.94	0.51	1.222	24.47	23.32	0.5		50.37	59.46
Patch thickness = 0.3 mm											
patch 0 %	1.574	25.73	25.24	0.32	1.574	25.73	25.24	0.32	10		
Patch 10 %	1.565	26.05	25	0.31	1.411	26.01	24.98	0.33		9.84	15.07
Patch 20 %	1.558	25.33	25.19	0.31	1.251	25.03	25.01	0.3		19.70	30
Patch 30 %	1.55	25.5	25.08	0.34	1.086	25.34	24.85	0.3		29.94	44.77
Patch 40 %	1.53	25.32	25.08	0.32	0.918	25	24.88	0.3		40.00	58.92
Patch 50 %	1.499	25	25.04	0.33	0.75	24.51	24.42	0.25		49.97	72.17
Patch thickness = 0.1 mm											
patch 0 %	0.546	25.36	25.18	0.1	0.546	25.36	25.18	0.1	10		
Patch 10 %	0.545	25.6	25.05	0.09	0.489	25.46	25.04	0.09		10.28	5.25
Patch 20 %	0.533	25.18	25.08	0.09	0.426	25.08	24.99	0.09		20.08	10.27
Patch 30 %	0.531	25.14	25.01	0.1	0.37	25.12	24.85	0.1		30.32	35.33
Patch 40 %	0.529	25.04	24.96	0.09	0.318	24.93	24.89	0.1		39.89	27.37
Patch 50 %	0.528	25.09	25.19	0.09	0.264	24.99	25.01	0.1		50.00	25.42

environment involving an electrolyte of NaCl, the likelihood of pitting corrosion occurrence is notably high. In the context of our iron plates with varying thicknesses (ranging from 1 mm to 0.1 mm), the detection of significant changes in thickness following limited pitting events can be exceptionally challenging. Pitting corrosion often results in the removal of iron atoms from localized areas, potentially leading to mass loss. However, the complex nature of corrosion processes, especially in the presence of chloride ions, may result in the formation of corrosion products that occupy and replace the empty pit cavities. Consequently, while pitting corrosion may occur and contribute to mass loss, the overall thickness of the iron plates may not exhibit substantial alterations, thus requiring highly sensitive measurement techniques to discern such subtle changes accurately .

Upon comparing the linear mass loss of patches during the accelerated corrosion states from

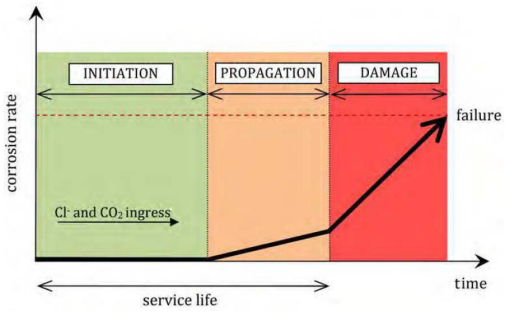

Figure 5.20 – A conceptual model of the phases of corrosion in reinforced concrete [22]

10% to 50% (as presented in Table 5.6), it is confirmed that the corrosion of the patches up to 50% follows the second phase of the Tuutti diagram (linear part). Therefore, the corrosion pattern obtained linear, for this study, from 10% to 50%.
Eventually, to provide FMM samples of this experiment (labelled as FMM 1-4), the magnet (permanent part) and reactive parts are coupled together. Subsequently, MO was measured as a function of the corrosion state of the reactive part and also for different concrete thicknesses (3 cm, 4 cm, and 5 cm), separately. The obtained MO variations would be used as reference data for the forward and inversion method.
In the next section, the Mo measurement results would be represented.

5.5 MO measurement as function of reactive part's corrosion evolution

To measure the range of MO variations for each FMM sample in terms of corrosion evolution from 0% to 50% on their related reactive parts and also as a function of the relative distance between the interrogator and FMM, the following protocol is implemented:

- Step 1: placing the concrete slab with 3 cm thickness (labelled 3-2) at the gap between the interrogator and FMM sample,
- Step 2: placing the reference magnet alone and measuring the MO for 5 minutes,
- Step 3: coupling magnet with reactive part of 1 mm, without corrosion, and measuring the MO for 5 minutes,
- Step 4: use the 5 corroded patches (10% to 50%). Separately, coupled to the reference magnet and measure MO for each of them, for 5 minutes,
- Step 5: repeat steps 3 and 4 for FMM 2-4 separately.
- Step 6: replacing the concrete slab with 4 cm and 5 cm thicknesses (labelled as 4-1 and 5-1, respectively) and repeat the measurements

The graphs in Figure 5.21a to c display the MO variation range and tendency as a function of corrosion state and also at different relative distances of 3, 4, and 5 cm, respectively, to the interrogator. The MO generated solely by the magnet is also represented in all figures. The error bars for each point represent the uncertainty level in the results due to interrogator standard deviation ($\Delta\mathbf{B}$), which is measured during each test and added to the results.
Similar to Section 5.3, the 3D interrogator measures the magnitudes of B_x, B_y, and B_z. As in the previous section, the mean of $||\mathbf{B}||$ is calculated from B_x, B_y, and B_z components. The measurement takes approximately 5 minutes. The MO variation range ($\Delta^{''}||\mathbf{MO}|| = \max(||\mathbf{MO}||)$-$\min(||\mathbf{MO}||)$) for each of FMM 1-4 is calculated for reactive part's corrosion from 0% to 50%, as function of relative distance between interrogator and FMM device, indicated at Table 5.7. The results indicate that:

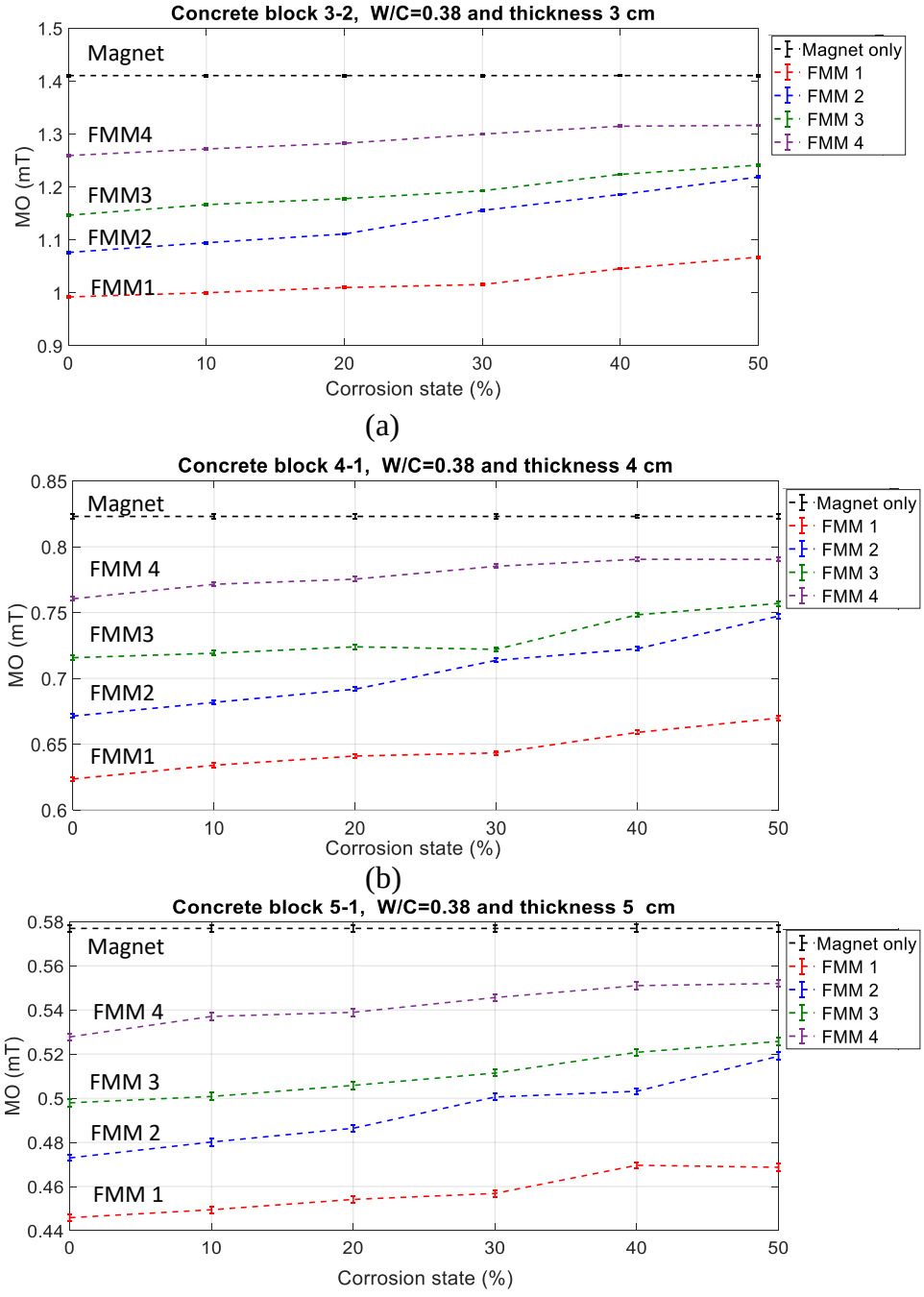

Figure 5.21 – MO changing of FMM 1-4 as function of corrosion state at distance of 3 cm, 4 cm and 5 cm

— Firstly, the range of MO variation is strongly influenced by the relative distance between the interrogator and the FMM samples. In general, as the relative distance increases,

Table 5.7 – The MO variation range ($\Delta^{''}||\mathbf{MO}||$) due to the reactive part corrosion from 0% to 50%, for each FMM at the distances of 3, 4 and 5 cm

	$\Delta^{''}||\mathbf{MO}||$ [mT]		
Relative distance	**3 cm**	**4 cm**	**5 cm**
FMM 1	0.075 ± 0.001	0.046 ± 0.001	0.026 ± 0.0001
FMM 2	0.141 ± 0.001	0.074 ± 0.001	0.047 ± 0.0001
FMM 3	0.061 ± 0.001	0.031 ± 0.001	0.024 ± 0.0001
FMM 4	0.041 ± 0.001	0.028 ± 0.001	0.022 ± 0.0001

the range of MO variation decreases. This suggests that the accuracy and efficiency of FMM measurements related to MO variations are relatively higher at shorter distances, compared to embedding the device in deeper concrete depths. These findings are consistent with the numerical simulations conducted in Chapter 3, where a parametric study revealed that the MO measurements taken at closer distances could result in higher variation ranges,

— Secondly, the MO variation results due to corrosion are significantly more than the uncertainty level MO for the magnet alone, measured in free space ($\Delta^{'}\mathbf{B}$ = 0.0002 mT) and the uncertainty level due to interrogator standard deviation (shown as error bars). Therefore, it can be concluded that the obtained MO upward tendency caused by corrosion of reactive part and it is not occurred due to environmental factors changing like Earth's magnetic field rotations or the hot processing of the interrogator and *etc.*,

— Thirdly, the experimental results indicate that the measured MO for each FMM have an upward tendency as the corrosion progresses in the reactive part. This finding are consistent with the results presented Chapter 2, where it was assumed that the reactive part's thickness reduction could lead to an increase in MO. This assumption was further examined through numerical simulations of altering reactive part's shielding properties in Section 2.8.2. Thus, the obtained experimental results strongly support those numerical results as well as the aforementioned assumptions to consider geometric changes in the reactive part as an indicator of corrosion. In addition, from both numerical and experimental results, it could be justified the MO would be raised by reactive part's corrosion evolution and geometrical changing (as consequence of rusting),

— Finally, the results indicate that FMM 2, with a 0.5 mm thickness, exhibits a notably wider range of MO variation compared to the other FMM samples. This aligns with the findings from the parametric study in Chapter 3, suggesting that a reactive part measuring 25 mm × 25 mm× 0.5 mm strikes an effective balance for achieving rapid and detectable MO variation.

These experimental results will serve as a benchmark for the forward and inversion method to estimate the changes in magnetic dipolar moments as a function of the reactive part corrosion states. In the upcoming section, we will initially evaluate the model using a single dipole, and

in the following sections, we will expand the model to multiple dipoles.

5.6 Evaluation of forward and inversion method through experimental tests

In this section, our objective is to assess the feasibility of the proposed forward and inversion method to correlate the variations of estimated magnetic dipolar moments of FMM with the corrosion state of the reactive part, obtained by the experimental tests. As described in Section 4.7 of Chapter 4, the forward and inversion method involves an analytical model and optimization techniques to estimate the associated magnetic dipolar moment of the FMM, since it acts as the magnetic source. In Chapter 4, various numerical configurations were used to calculate the MO variations as a function of geometrical changes in the reactive part, assuming that geometrical changes potentially can alter the magnetic properties of the FMM, mainly due to attenuation the shielding properties of reactive part.
The results obtained in Chapter 4 illustrates that the estimated magnetic dipolar moment increases with the thickness loss of the reactive part, due to removing the shield and leads to more measurable magnetic flux line density and subsequently, relatively more alignments of magnetic dipolar moment vectors. In this chapter, we assumes that corrosion causes changes in the magnetic properties of the reactive part. These changes are attributed to various factors such as material transformations, the shape deformation, and overall degradation of iron materials in the reactive part. Consequently, we assume that it could change the amount of magnetic properties of reactive part, *e.g.,* its magnetization vector and net magnetic dipolar momnet vector.
Thus, the following key points would be addressed, in this section:

- Experimentally, the assumption that the corrosion evolution of the iron patch could lead to changes in its estimated magnetic dipolar moment would be evaluated,
- If so, what is the variation tendency and range of the magnetic dipolar moment, as function of corrosion,
- Then, we will evaluate how many magnetic dipolar moment vectors are necessary to represent the FMM magnetic behaviour, under the degradation process,
- Investigate whether changes in MO caused by corrosion, reaching up to 50%, can provide consistent and reliable results from forward and inversion method for the rapid detection of the corrosion evolution of embedded FMM device, as ND approach.

These evaluations will provide valuable insights into the potential of the proposed method of this study as an effective ND approach for monitoring the evolution of aggressive agents in cover concrete, that could lead to corrosion of FMM embedded device and ultimately, rebars.
Figure 5.22 shows the schematic representation of forward and inversion method, with consideration of one dipole at the center of reactive part. The measured MO from experimental tests

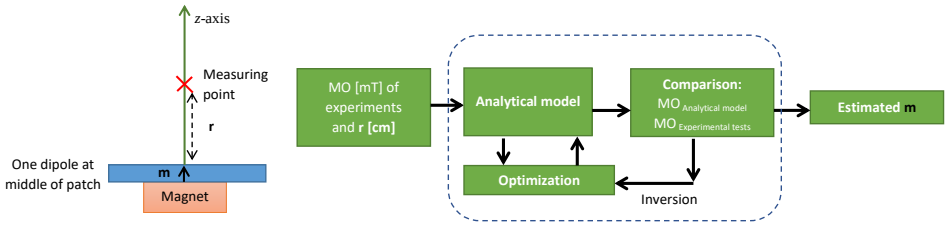

Figure 5.22 – Configuration of one dipole and forward and inversion method to find the value of magnetic dipolar moment **m** with experimental data

would be given to the analytical model for calculating the MO through an initial values of **m**. The relative distance parameter (**r**) between the dipole and measuring point, considered as known parameter would be same for both of analytical model and experimental tests.
Using inversion approach, the magnetic dipolar moment of the FMM can be estimated by comparing the calculated MO of analytical model and the measured MO from experimental tests. This comparison would continue to minimize the cost function error between the calculated and measured MO through an optimization technique which adjusts the amount of **m**, at each iteration. Once the cost function error reaches its minimum, the optimal value of **m** would be estimated and served as the output of proposed method, as illustrated in Figure 5.22.
Similar to Chapter 4, it is important to remind the amount $||\mathbf{m}||$ assumes to be calculated and used for analysing the results, instead of focusing on each vector's components at x, y and z directions, separately.
In the following, the forward and inversion method will be evaluated through modeling with one magnetic dipolar moment vector.

5.6.1 Modeling with one dipole

As explained, in this section we would represent the FMM with one dipole, as illustrated in schematic representation of Figure 5.22. It is hypothesized that placing the single dipole at the center of the reactive part would effectively represent the behavior of the magnetic property of its entire volume. This assumption is made to simplify the modeling approach and streamline the analysis of the reactive part's magnetic properties, which use only one vector norm value to study. Using forward and inversion method, the amount of magnetic dipolar moment changes for each of FMM 1-4 sample would be estimated, using the measured MO variations in Figure 5.21, as input to the analytical model. To more investigation, the amount of magnetic dipolar moment of single magnet (permanent part only), is separately estimated, using forward and inversion method.
The results of estimation illustrated at Figure 5.23 that represent an raising tendency in the $||\mathbf{m}||$ by corrosion evolution of the reactive parts. As it hypothesised, this raising tendency can be attributed to the fact that, the rusting of the iron material in the reactive part (includes

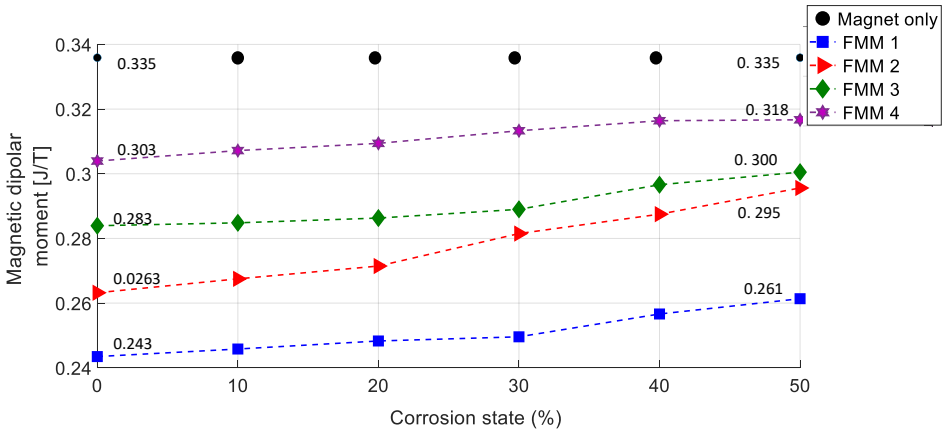

Figure 5.23 – Amount of $||\mathbf{m}||$ associated with each FMM device, as function of corrosion evolution on reactive part

both shape deformation and material transformation as indicated in real images of reactive parts as Figure 5.19), could alter gradually, its strong initial shielding capabilities. Thereby, it affects the amount of magnetization within the reactive part, caused by permanent part. It is important to remind that the permanent part of the FMM remains unaffected during corrosion, as source of magnetization. Thus, the only reason to change the magnetization would be corrosion impact. Eventually, by evolution of corrosion and altering the magnetization vector, the alignment of the magnetic domains as well as the magnetic dipolar moment vectors would be changed. Considering the estimated net magnetic field of the FMM as one dipole vector, the results justify this hypothesis that $||\mathbf{m}||$ changes in correlation with the corrosion progress at the reactive part, as result.

Considering the results for modeling FMM with one dipole, the following conclusion are also obtained:

— The results confirm that corrosion leads to variations in the magnetic dipolar moment of the FMM, regardless of the FMM's relative distance between the interrogator and the device. Hence, the magnetic dipolar moment, particularly its norm value, can serve as a unique vector to represent the corrosion state of the FMM and any degradation affecting its magnetic properties,

— Using the forward and inversion method, even when the corrosion level reactive part is lower than 10%, leads to significant changes in the estimated magnetic dipolar moments. This result justify that the proposed method is capable, sensitive and quick enough to detect even small changes in the reactive part, enabling the estimation of corrosion progress of en embedded device, in a ND way,

— The results confirm that a single dipole vector, is enable to effectively represent the behavior of the FMM device in relation to corrosion. This suggests that the proposed method can serve as a simplified approach for detecting corrosion in FMM embedded

devices, requiring only a single vector value (norm value in this study),

Furthermore, the variation ranges of $||\mathbf{m}||$ due to the corrosion of the reactive part from 10% to 50%, for each FMM are:

— FMM 1: $\Delta||\mathbf{m}|| = 0.018 \pm 0.0001$ [J/T]
— FMM 2: $\Delta||\mathbf{m}|| = 0.032 \pm 0.0001$ [J/T]
— FMM 3: $\Delta||\mathbf{m}|| = 0.017 \pm 0.0001$ [J/T]
— FMM 4: $\Delta||\mathbf{m}|| = 0.015 \pm 0.0001$ [J/T]

The results suggest a clear relationship between the geometry of the reactive part of the FMM device and the obtained magnetic dipolar moment variation range. In this experimental study, all FMM devices have the same geometry for their permanent part, with the only difference being the dimensions of the reactive part (unlike to Chapter 4, that used different permanent part's geometries). The results suggest that FMM devices with larger reactive part geometry exhibit relatively larger variation ranges. This is attributed due to the fact that larger reactive part's volume includes more magnetic domains and magnetic dipolar moment vectors that could be aligned due to magnetization with permanent part. Thus, the corrosion evolution and changes in reactive part's magnetization, the variation range of magnetic dipolar moment would be more significant for larger reactive part samples.

However, it is important to note that FMM devices with larger reactive parts also take longer to corrode. Therefore, there is a trade-off between the effective geometry of the reactive part for fast detection and the desired variation range of the magnetic dipolar moments that must be taken into account. Similarly, the FMM 2 which has the effective geometry (investigated in Chapter 3), exhibits the most significant variation magnetic dipolar range compared to other FMM devices. Thus, it justify that using the FMM with effective geometry, could provide both fast and sufficient changes in amount of magnetic dipolar moments and could be a good choice for designing of FMM device.

Furthermore, comparing the variation range of the magnetic dipolar moment for a single dipole, with the results obtained in Section 4.7.1 of Chapter 4, it is observed that the variation range is relatively lower in the experimental study compared to the numerical modeling in Chapter 4. This difference can be attributed to the assumption made in the numerical modeling, where the total thickness of the reactive part is considered to be lost completely. However, in the experimental study, corrosion was limited to a maximum of 50%. Moreover, the experimental study takes into account environmental noise and measurement uncertainties, which were not considered in the numerical study and can affect the MO measurements. Therefore, they could be a reason for greater variation range in the numerical modeling results of Chapter 4, compare to experimental study.

Despite this difference, the results obtained in both the numerical study in Chapter 4 and the current experimental study are consistent in overall point of view. This consistency suggests

a single dipole vector can potentially represent the behavior of FMM devices in response to the corrosion of their reactive part. Therefore, employing the forward and inversion method is capable to estimate the degree of corrosion reactive part's corrosion, as embedded device, in ND way.
In the next section, we will increase the number of dipoles from one to two in order to investigate the sufficient number of dipoles in this purpose. Thus, we would be able to investigate the assumption that by dividing the reactive part entire volume into multiple areas and evaluating the related magnetic dipolar moment vector variations of each area separately, the reliability of proposed method results could be improved.

5.6.2 Modeling with two dipoles

In this section, we aim to evaluate the proposed forward and inversion method, using configuration of two magnetic dipoles. As previously discussed, the corrosion evolution usually follows some non linear patterns. Thus, in case like a reactive part with square shape, it could be possible that rusting follows asymmetrically pattern, affecting only one side of the reactive part while the other side remained unaffected (such as what is shown in Figure 5.19). Considering this characteristic, dividing the total volume of the reactive part into multiple area, and study the associated magnetic dipolar variation of each area separately, can provide a more precise analysis of the total magnetic property variation of reactive part, due to rusting. Furthermore, this approach allows us to determine the minimum number of dipoles, required to effectively model the FMM embedded device and estimate the magnetic property variation of that due to corrosion evolution, without destructive tests.
Figure 5.24 illustrates the schematic representation of FMM, which includes two dipoles. It is important to remind that the surface area of all reactive parts is equal to 25 mm × 25 mm (for all of the FMM samples). Thus for all of FMM samples, the two dipoles are symmetrically considered at the right and left sides of the reactive part, with a horizontal distance of 7.5 mm from its center. For each dipole ($\mathbf{m}_1$ and $\mathbf{m}_2$) the relative distance to the measuring point are denoted as $\mathbf{r}_1$ and $\mathbf{r}_2$, as depicted in Figure 5.24.
Similar to the modeling with a single dipole, the $||\mathbf{m}||$ is calculated for each dipole. As described

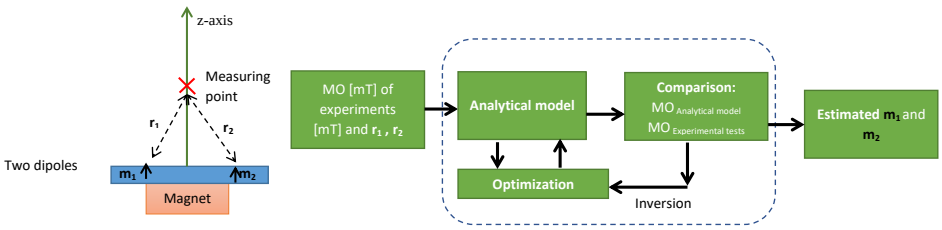

Figure 5.24 – Configuration of two dipoles and inversion method to find the value of magnetic dipolar moment $\mathbf{m}_1$ and $\mathbf{m}_2$ through experimental data

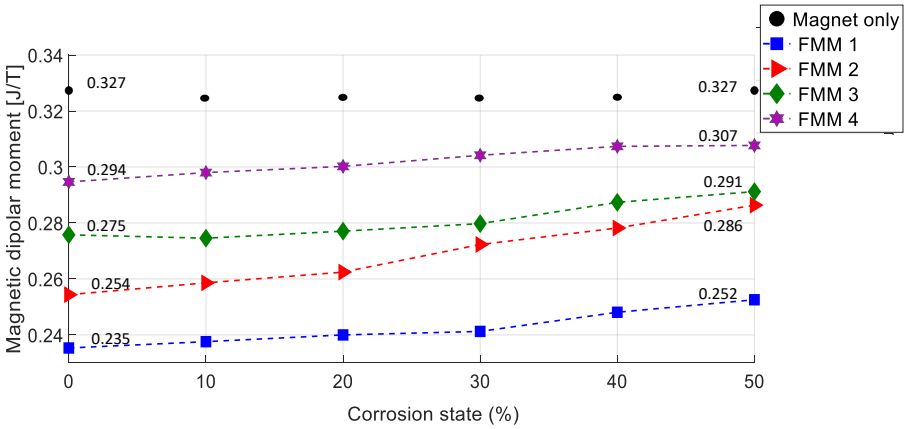

Figure 5.25 – Total amount of $||\mathbf{m}_t||$ associated with each FMM device, as function of corrosion evolution on reactive part

in Section 4.7.2 and in accordance with Eq. 4.10, the total amount $||\mathbf{m}_t||$ is calculated by summing the $\mathbf{m}_1$ and $\mathbf{m}_2$ which would be referred as net magnetic dipolar moment of FMM.
Figure 5.25 presents the results of estimated $||\mathbf{m}_t||$, for each FMM and as function of reactive part's corrosion evolution from 10% to 50%.
The graphs shows that $||\mathbf{m}_t||$ has upward tendency, with corrosion evolution. The results are inline with those obtained for one dipole configuration and also numerical modeling in Chapter 4. Upon comparing the results depicted in Figures 5.23 (for one dipole) and Figure 5.25 (for two dipoles), it suggests that the inclusion of an additional magnetic dipolar moment does not have a significant impact on the net amount of magnetic dipolar moment. To be more precise, there is a very slight decrease in the magnitude of the overall magnetic dipolar moment, using two dipoles modeling, however, in general, the total estimated values and tendency remain consistent for the one dipole and two dipole cases.
This observation suggests that adding another dipole to the model may not always provide an improvement in representing the magnetic property variation of the FMM device due to corrosion. This could be attributed to the fact that, for this specific study, the corrosion of the reactive part followed a linear pattern, as discussed in Section 5.4.2, in terms of both mass loss and geometrical loss. Therefore, it could be concluded that since the corrosion exhibited an approximately linear pattern, the behavior of the reactive part in terms of changing in magnetic properties may remain consistent whether analyzing carry out with one or more dipoles. Therefore, it can be concluded that for this controlled accelerating corrosion test, where corrosion reaches up to 50%, using a single magnetic dipolar moment vector is sufficient to accurately represent the behavior of the FMM device in terms of corrosion process.
Additionally, the variation ranges of $||\mathbf{m}_t||$ are also calculated, according to Figure 5.25, as:

— FMM 1: $\Delta||\mathbf{m}_t|| = 0.017 \pm 0.0001$ [J/T]
— FMM 2: $\Delta||\mathbf{m}_t|| = 0.032 \pm 0.0001$ [J/T]

— FMM 3: $\Delta||\mathbf{m}_t|| = 0.016 \pm 0.0001$ [J/T]
— FMM 4: $\Delta||\mathbf{m}_t|| = 0.013 \pm 0.0001$ [J/T]

Similarly, the obtained variation ranges of total $||\mathbf{m}_t||$ for two dipoles and $||\mathbf{m}||$ with one dipole, have approximately similar values. As explained, it can be attributed to the linear pattern of the corrosion process and the behavior of the reactive part in this experimental study.
It can be concluded that due to symmetrical shape of reactive part, two dipole have the similar values. Through the linear progression of corrosion, it each dipole in the model would have the similar variations, as function of degradation. Additionally, when using two magnetic dipolar moment vectors, the total magnetic properties of the reactive part are equally divided into two smaller values. As a result, the combined magnetic dipolar moment of the two dipoles would have a similar magnitude as that of a single dipole. This results again suggests that the inclusion of an additional dipole does not provide significant additional information monitoring the magnetic dipolar moment's variation range, due to corrosion.
Moreover, similar to one dipole, it's important to note that FMM 2, which has the effective geometry, shows a higher variation range. This suggests that the geometry of the reactive part plays a significant role in determining the amount of magnetic property variation due to corrosion (to provide quick and significant changes). FMM 2, with its optimal dimension rage, allows for a more significant change in the magnetic dipolar moment compared to the other FMM devices. The results highlight the importance of optimizing the geometry of the reactive part in FMM devices designing to achieve desired sensitivity and range of variation.
In conclusion, the experimental results strongly support the feasibility of the using the proposed forward and inversion method, to estimate the variation of magnetic dipolar moments of FMM due to corrosion, for ND method. Thus, monitoring the estimated magnetic dipolar moment variation due self-corrosion of FMM embedded device, would provide insight for the risk of rebar as well, that could accrue by aggressive agents. The results suggest that the estimated magnetic dipolar moment vector is highly sensitive to even minor changes in magnetic properties of FMM, making it suitable for early-stage corrosion detection and send on time alarm of raising the risk of rebar corrosion due to raising the contamination level in concrete. It offers cost-effective, fast and feasible advantages compared to traditional ND methods that mostly suffer from huge uncertainty of their results, due to environmental elements changing, compare to magnetic ND methods. The experimental results align with the numerical models, validating the forward and inversion methods as fast and simple technique, which can use only one magnetic dipolar moment vector value to determine the early corrosion state of an embedded SHM device. The method holds promise for health monitoring in marine environments RC structures and can provide real-time monitoring as well. Overall, the experimental results strongly support the proposed method's reliability and effectiveness, making it a promising preventive ND technique for RC structures, particularly in sea areas.

5.7 Conclusion

In this chapter, we conducted experimental campaign on a variety of FMM samples with different reactive part geometries to assess the effectiveness and reliability of proposed forward and inversion method to estimate magnetic dipolar moment variation of embedded FMM device, due to corrosion, in ND way. Moreover, the performance of FMM device, on concrete media, in terms of its MO sensitivity to medium, has been evaluate. For this campaign, the concrete slabs with properties similar to those used in sea areas were selected. The manufactured concrete slabs have different characteristics such as the concrete mixing with W/C ratios of 0.38, 0.5, and 0.78. The slabs were designed with three different thicknesses (3 cm, 4 cm, and 5 cm) and also in types of dried or saturated one. A total of 27 slabs were manufactured, with three identical slabs for each concrete mixing and thickness used to ensure reliability and repeatability of measurements. A total of 18 dried concrete samples were prepared. The saturated concretes chosen for the study had a W/C ratio of 0.78 and were immersed in pools containing three different chloride contents for each thickness. The dried slabs were stored for two years in an oven at a temperature of 60 degrees Celsius to avoid any moisture penetration in their porous network. To prevent carbonation or penetration of ambient moisture or pollution, the slabs were kept in plastic bags.
The MO measurements were conducted, using 3-axis magnetometer, embedded in the a NEURON system, designed by Morphosense instruments, as interrogator.
In this experimental study, we have assessed the following aspects:

1. The potential stability and approximate sensitivity of MO measurements to the variations in the Earth's magnetic field (caused by Earth rotation) and other environmental noise. The significance of such study variations is due to measure the bias available magnetic field that may affect the MO measurement results. Secondly, we aimed to evaluate the approximate SNR of measurements, by measuring the random noise.
   To do that, measurements of the minimum available magnetic field in the environment, includes the magnetic field of the Earth ($\mathbf{B}_0$) and background noise, were conducted through various free space measurements, that were randomly taken over two days. The results showed that the average measured $||\mathbf{MO}_{\text{environment}}||$ was $0.0014 \pm 1.2\times 10^{-6}$ [mT], with the value of $\pm\ 1.2\times 10^{-6}$ associated with the interrogator's standard deviation level. The obtained $||\mathbf{MO}_{\text{environment}}||$ is labeled as the random measurement's noise.

2. To calculate the SNR and stability of MO generated by magnet, the initial measurements were repeated with the presence of a reference magnet at a distance of 7.3 cm from the interrogator. The results showed that $||\mathbf{MO}_{magnet}||$ was 0.287 ± 0.0017 [mT], where 0.0017 [mT] was similarly associated with the standard deviation of the interrogator. Finally, the approximate SNR of the measurements was assessed to be 42 dB, indicating

that the magnetic field strength of the reference magnet was 42 dB stronger than the ambient magnetic field and noise.

3. Furthermore, the sensitivity of MO, generated by reference magnet due to changing the concrete medium's characteristics had been conducted.
   To do that, a series of MO measurements were conducted using different concrete slabs, fill in the gap between the magnetometer and the reference magnet. The aim was to evaluate the range of MO variation as a function of concrete slab properties changes, including its thickness, mixing, hydric state, *i.e.,* chloride ion concentration level. The experimental results confirmed that the variations in the concrete media's characteristics have no significant influence on the MO measurements. This finding supports the initial advantage of the method, which is that the MO of the FMM is not sensitive to the concrete characteristics. Additionally, the results indicated that the relatively small geometry of the FMM as a magnetic source, can not give a raise to the magnetic dipolar moment in the concrete media or generate measurable magnetization. Therefore, the concrete can be considered as a non magnetic medium for the MO measurements of the FMM.

4. The MO variation range and tendency measurements, as result of reactive part corrosion evolution was evaluated.
   To do that, some reactive part samples with similar surface area of 25 mm × 25 mm and different thickness (from 0.1 mm to 1 mm) were chosen. Then, they became rusted from 10% to 50% with an accelerating corrosion technique. By coupling the reactive parts to one fixed reference magnet, four FMM samples (FMM 1-4) were prepared which different reactive part's thickness that were corroded with different states. Then, the MO was measured for different concrete thicknesses (3 cm, 4 cm, and 5 cm) and as a function of the corrosion states.
   The results justify experimentally that firstly, the range of MO variation is strongly influenced by the relative distance between FMM and interrogator. As the distance increases, the range of variation decreases, indicating that shorter distances yield higher variation ranges. This results are justify, experimentally, the related numerical modeling results in Chapters 2, 3, about the role of relative distance in determination the MO variation range.
   Secondly, the measured MO variations due to corrosion were significantly higher than the uncertainty level associated with the interrogator's standard deviation and background noise. This indicates that the observed MO variations are not caused by external factors like changes in the Earth's magnetic field or the interrogator's processing, but rather by the corrosion of the reactive part.
   Thirdly, the experimental results consistently illustrate an upward tendency in the measured MO as the corrosion progresses in the reactive part. This aligns with the assump-

tions made in Chapter 2, which proposed that a reduction in the reactive part's thickness leads to an increase in MO, due to shielding attenuation of reactive part.
Lastly, among the tested FMM samples, FMM 2 with a thickness of 0.5 mm exhibited a significant range of MO variation compared to the others. This finding corroborates the outcomes of the parametric study in Chapter 3, which highlighted that a reactive part with dimensions of 25 mm × 25 mm × 0.5 mm provide a good compromise in achieving rapid and detectable MO variations.

5. The last objective was concerning the evaluation the proposed forward and inversion method to estimate the mount of norm magnetic dipolar moments ($||\mathbf{m}||$), using MO variation of the experimental results. Both one dipole and multi dipole configurations were evaluated.
   The results obtained for both the one-dipole and two-dipole cases exhibit similar tendency and variation range. The experimental results justify the hypothesis that corrosion induces changes in the magnetic dipolar moment of FMM devices, due to material's transformation and its geometrical degradation. Thus, the strong shielding property of reactive part would be affetced by corrosion. It would lead to changes in its magnetization, magnetic domains reorientation and finally, more alignment of net magnetic dipolar moment of FMM, with magnetic field direction of permanent magnet. The results show that, magnetic dipolar moment would be alter even with small amount of degradation (around 10%). This suggests that the magnetic dipolar moment can serve as an effective indicator of the device's corrosion state or any degradation affecting its magnetic properties. The results shows that proposed method demonstrates high sensitivity, capable of detecting even minor changes in the reactive part, enabling non-destructive detection of corrosion. Moreover, the results suggest that using only single dipole vector is sufficient to represent the FMM device's behavior in relation to corrosion, that provide a simple ND method.
   Furthermore, the experimental results highlight the relationship between the geometry of the reactive part in FMM devices and the variation of magnetic dipolar moments. Larger reactive part geometries result in relatively more variation ranges of magnetic dipolar moment . This is because a larger reactive part volume includes more magnetic domains, allows for alignment of more magnetic dipolar moments vector numbers with the permanent part's direction. However, it is important to consider that larger reactive part geometries also exhibit slower corrosion rates. As previously mentioned, there is a trade-off between the desired variation range of magnetic dipolar moments and the reactive part geometry to achieve faster variations. In this case, the FMM with the optimal geometrical range, demonstrates the most significant magnetic dipolar moment variation range among the tested device would be highly recommended.

In summary, the experimental results provide strong support for the practical application of the proposed forward and inversion method in estimating the variation of magnetic dipolar moments in FMM devices due to corrosion. This method offers the capability to detect corrosion state of FMM devices, serves as a novel ND indicator of cover concrete contamination level that could emerge corrosion in FMM as well as rebar. The results justify that the estimated magnetic dipolar moment vector is highly sensitive to even minor changes in the magnetic properties of the FMM, making it suitable for early-stage corrosion detection and timely alarm of increasing rebar corrosion risk associated with rising contamination levels in concrete. The proposed method offers cost-effective, rapid, and feasible advantages over traditional ND methods, which are often subject to high uncertainty due to environmental factors. The experimental results align well with the results of numerical modeling in Chapter 4, validating the effectiveness and simplicity of the forward and inversion method, which only requires a single magnetic dipolar moment vector value to estimate the early corrosion state of an embedded structural health monitoring device. This method shows promise for health monitoring in marine environments RC structures and has the potential to provide real-time monitoring , as well. Overall, the experimental results strongly support the reliability and sustainability of the proposed method, positioning it as a promising novel preventive ND technique for RC structures, especially in RC structures of sea areas.

CONCLUSIONS AND PERSPECTIVES

Conclusion general

Concrete is a key material in building the civil engineering structures and infrastructures, but it faces challenges from environmental factors like freeze-thaw loads, temperature gradients, and erosion. One of the most significant threats to reinforced concrete (RC) structures is corrosion, which occurs when aggressive agents penetrate the concrete and degrade the steel rebars. Moisture, oxygen, chloride ions, and other chemicals initiate corrosion reactions, leading to the formation of corrosion products and structural damage. Factors like carbonation and chloride ion ingress can weaken the protective film around the rebar, making it more susceptible to corrosion. Swelling of the concrete due to corrosion further accelerates the process and allows more aggressive agents to penetrate the structure. Therefore, regular health inspection of concrete is quite necessary to timely detection of corrosion, especially in coastal areas like France, to ensure the safety of residents and prevent catastrophic failures. Early detection allows for cost-effective maintenance strategies, minimizing the extent of repairs.

To address this problem, different inspection techniques have been developed over the decades. At the primary level, regular concrete inspection is typically necessary for detecting rebar corrosion early, through some visual traces such as corrosion products orange or red color around surface cracks. These regular inspections are usually visual techniques and use for periodic inspections to assess the overall health of structures, but they need complementary tests to precisely diagnosis the observed pathology. The complementary inspection methods could be divided into both Destructive Testing (DT) and Non Destructive Testing NDT.

DT involves extracting concrete cores for laboratory analysis, but it can damage the structure and may not provide precise results about the extend of corrosion. NDT methods use electromagnetic or mechanical waves to evaluate internal conditions or geometry without damaging the structure. NDT are divided into two main categories of inspection and Structure Health Monitoring (SHM) techniques. The inspection techniques such as resistivity measurements, Ground Penetrating Radar (GPR), ultrasonic pulse velocity, and impact echo, offer quick and inexpensive information over a large area. Although, these methods show successful results in detection of corrosion, their results suffer from uncertainties due to factors like environmental conditions and also they are mostly useful to evaluate the rebar corrosion degree. Thus, they can not estimate the rebar corrosion risk, before it emerges. Furthermore, SHM technique are second category of NDT and design to provide punctual and long-term monitoring of concrete properties and

structural behavior. They are using monitoring equipment such as interrogators, data acquisition systems and sometime embedded devices that located within the specific area of concrete that is interested to be monitored. The connection between the embedded device and external interrogators, and embedded devices can be established through both wired and wireless standards. Wired connections involve the use of physical cables. Wireless connections usually use some communication standards such as WiFi and propose for remote monitoring of SHM embedded device. The SHM methods allow for distributed monitoring at various locations and continuous data acquisition. Wired methods have limitations due to presence of cable which could damage the RC structure, while wireless methods face different challenges in providing the power supply and data transmission interference. Nowadays and thanks to advancement of technology, the battery-less wireless devices like RFID systems show promise monitoring techniques. Generally, further research is needed to improve these technologies for practical application in SHM.
Despite the availability of NDT inspection and monitoring techniques, there remains a need for autonomous, reliable, cost-effective, battery-less and accurate methods that are insensitive to environmental condition. These techniques should enable punctual monitoring, have low power requirements, and be compact in size. Ultimately, there is a need for advanced approaches that can offer accurate preventive technique and effectively address the issue of rebar corrosion.
To address this problem and under frame work of the French national research project (ANR) LabCom OHMIGOD, this research study aimed to propose a novel NDT method that could detect the availability of aggressive agents in the cover concrete, which can potentially lead to rebar corrosion, as preventive method. The method, includes a technological solution that could detect availability of aggressive agents by self-corrosion. It made of magnetic and ferromagnetic materials and referred as Functional Magnetic Material (FMM). Thus, it produces Magnetic Observable (MO), as its output signature. Benefiting from SHM techniques, the FMM device would be embedded in the cover concrete, expose to aggressive agents at risky zones. The reactive part of the FMM, made of iron material, is highly sensitive to the aggressive agents, leading to be rusted, during the time. The corrosion would gradually, alters the MO of the FMM, which can be measured using an external interrogator. Additionally, the proposed method of this study, incorporates an analytical model based on the Biot-Savart equation, which establishes a relationship between the MO variations and the magnetic properties of the FMM, specifically the magnetic dipolar moment. By employing Nonlinear Least Squares (NLS) optimization and inversion techniques, the proposed forward method can estimate the extent of variation in the magnetic dipolar moment, corresponding to the corrosion state of the reactive part. Ultimately, this method enables the ND estimation of the corrosion level of the embedded device, utilizing the unique magnetic dipolar moment vector and autonomous and cost effective technology such as FMM device. Thus, it offers a fast, simple, and relatively cheap NDT solution.
Thus, the objectives of this research study were as follows:

— The first objective was to characterize the FMM device through a comprehensive numerical study. This involved determining the optimal geometrical design of the embedded device, investigating its efficient location within the concrete structure, and evaluating the range and tendency of MO variations in relation to corrosion on the reactive part,
— The second objective was to assess the feasibility and effectiveness of the forward method. This included selecting the appropriate analytical model and optimization algorithm to solve NLS problem, evaluating the method's accuracy in estimating magnetic dipolar moment vector variations, determining the required number of magnetic dipolar moment vectors, assessing the method's reliability and repeatability in determining variation range and tendency, and validating the obtained results through numerical simulations and experimental tests.

Based on these objectives, in Chapter 1, the focus was on bibliographic studies about the concrete, corrosion phenomena and the impact on their service life, particularly in marine environments. Thus, the mechanism of rebar corrosion, with emphasis on the role of chloride ion penetration, was explained. Moreover, a bibliographic study has been carried out to review and compare the most famous Destructive Testing (DT) and NDT techniques, considering their strengths and limitations, associated with rebar corrosion.
In Chapter 2, several key topics were covered. The Biot-Savart equation, magnetization and raising the dipolar moment vectors in relation to ferromagnetic materials were reviewed through a bibliographic study, highlighting the ability of the magnetic dipole to represent a quantitative information about a material's magnetic properties. Moreover, a parametric study was conducted, using numerical model of FMM, to select appropriate materials for the FMM device. The rare earth magnet NdFeB was chosen for the permanent part, while pure iron with permeability of 50, due to its high sensitivity to corrosion was selected for the reactive part. The magnetic shielding role of reactive part associated with the MO generated by the permanent part, was introduced. Numerical models were employed to study the variation range and tendency of MO using the geometrical variation of the reactive part as shield. The results indicated that reducing the dimensions of the reactive part weakened the shielding effect, leading to increased MO. Significant MO variations were observed at close distances.
Additionally, an experimental test was conducted to characterize the corrosion products of the reactive part and determine their relative permeability value, which was found to be 5. A linear numerical model was developed to assess the MO variation based on material transformation and relative distance. The findings illustrate an upward tendency in MO despite changes in the reactive part's thickness caused by the formation of a corrosion product layer. This was attributed to the lower permeability of the corrosion product (5) layer compared to iron (50). However, the study acknowledged the need for further investigation into environmental parameters and measurement uncertainties.

In Chapter 3, we have more focused on the development and implementation of a numerical model to characterize the FMM device. Several parametric study with numerical configurations were performed to investigate the MO variation in FMM, due to geometrical changes of FMM. In the first numerical configuration, a single FMM component was placed at different distances from an external interrogator in synthetic concrete. The parametric study focused on determining the effective range of the reactive part's geometry by considering the thickness and length of the FMM. The results indicated that a reactive part thickness of 0.4 mm to 1 mm and a length of 18 mm to 26 mm provided a suitable balance between MO range and variation rate.
In numerical configuration 2, multiple FMM components were embedded at varying depths in synthetic concrete to assess their performance in evaluating concrete contamination. The magnetic coupling between the FMM components and the MO variation range were evaluated. It was found that FMM components closest to the concrete surface had higher detectability, and the use of multiple FMM components was feasible for assessing concrete contamination in different locations.
In numerical configuration 3, the potential magnetic coupling effect between FMMs and the nearest rebar in a synthetic concrete model was investigated. The impact of rebar proximity on MO variation range with respect to the reactive part's thickness reduction were examined. It was concluded that all magnetic FMM components showed some degree of coupling with the rebar, but maintaining a safe distance minimized the impact on overall FMM performance. Locating FMM components away from the grid of steel rebar (at center of concrete mesh) found to be crucial in reducing the magnetic coupling.
Chapter 4 focused on the proposed forward method to estimate the magnetic dipolar moment variations FMM's reactive part, due to its geometrical variations devices. The chapter aimed to evaluate the robustness of the proposed method, develop a reference model using numerical simulations. The study compared different analytical models and optimization algorithms to refine the proposed method. Additionally, the effect of changes in the reactive part's geometry on magnetic properties was investigated. Finally the magnetic dipolar moments were estimated for configuration of one dipole and multi dipoles.
The results study illustrate that the magnetic dipolar moment vector was sensitive to changes in the reactive part's geometry, supporting the initial assumption. By altering the dimensions of the reactive part and removing the shielding, the generated magnetic output could pass more strongly through the attenuated shield, resulting in an increased net estimated magnetic dipolar moment. Moreover, the results revealed other important findings. Firstly, the size of the FMM geometry had a significant impact on the amount of estimated magnetic dipolar moment, with larger FMM geometries generating higher magnetic dipolar moment values and a wider range of variation. Secondly, the proposed method proved successful in representing the magnetic behavior of the FMM using a single magnetic dipolar moment vector. Moreover, the results show

that for FMM device due to its small geometry, one or two dipoles were sufficient for accurate representation.

Overall, the results suggest that proposed method is sustainable and reliable to estimate the changes in the magnetic properties of the FMM's reactive part, due to corrosion. With its simplicity and insensitivity to environmental factors, the method holds promise for the health monitoring of such structures.

Chapter 5 of the study involved an experimental campaign to evaluate the the proposed forward method, as well. The objectives was similar as Chapter 4. The campaign also aimed to assess the sensitivity of MO, generated by FMM devices to the different concrete medium with variety of characteristics such as hydric states, concrete mixing and thickness. The experimental results indicated that variations in the concrete medium did not have a significant influence on the MO measurements. This finding supports the initial advantage of the method, which is that the MO of the FMM is not sensitive to the concrete characteristics. The relatively small geometry of the FMM as a magnetic source was unable to generate measurable magnetization or raise the magnetic dipolar moment in the concrete medium.

The second part of the experimental study evaluated the range and tendency of MO variations caused by reactive part corrosion in FMM devices. The results showed that shorter distances between the FMM device and interrogator led to higher MO variation ranges, while longer distances decreased the range of variation. Furthermore, the results related to MO as function of FMM's corrosion justified that MO have upward tendency, supporting the similar numerical results obtained in Chapter 2 and 3 related to MO.

In the last part of Chapter 5, the proposed forward method for estimating magnetic dipolar moments of FMM devices using MO variation data was evaluated. The results showed that corrosion led to changes in the magnetic dipolar moment, indicating the effect of material transformation and geometric degradation. The method exhibited high sensitivity in detecting even minor corrosion level and provided a robust ND way to assess corrosion. Similar to Chapter 4, the results show that using a single dipole vector was sufficient for representing the device's behavior, larger reactive part geometries resulted in larger variation ranges, albeit with slower corrosion rates. The findings emphasized the trade-off between desired variation range and reactive part geometry. The obtained results validated the results of Chapter 4, related to model. Thus, the model is reliable to estimate the corrosion state of FMM embedded device, using magnetic dipolar moment's vector variations.

In conclusion, the experimental and numerical results validate the novel ND method (both its analytical part and FMM technology), to using the estimated magnetic dipolar moment variations in FMM embedded devices as novel indicator for monitoring the corrosion in embedded magnetic device. This method shows high sensitivity and can effectively detect even minor changes in the magnetic properties of FMM devices, making it suitable for early stage corrosion detection

and monitoring. The method offers advantages such as cost-effectiveness, rapidity, and feasibility compared to traditional ND methods. This method has the potential to provide real-time monitoring. Overall, the research study results provide strong support for the reliability and sustainability of novel magnetic ND technique, positioning it as a promising monitoring method for preventive maintenance of reinforced cover concrete structures, particularly in marine areas.

Perspectives

Following this thesis that validating the concept of a new SHM-embedded device and the signal processing method in relation with magnetic dipolar moments, several studies could be proposed to carry out in the future to improve the work:

— The performance of multi-FMM devices in fresh concrete media must be evaluated. Since in real concrete media and due to the alkaline environment of concrete, the reactive part would be corroded gradually, thus, it is necessary to find the MO variations as a function of natural corrosion to check the FMM performance accuracy to provide fast MO variations before rebar corrosion.

— The velocity of chloride ion front ingress could be obtained through a time delay between the performance of FMM devices in different concrete depths. Therefore, by embedding different FMM in variety of concrete depths, it would be possible to evaluate the chloride ion front velocity through FMM devices.

— In the numerical modeling configuration of FMM device corrosion, the reactive part rusting is modeled with thickness reduction and rusting products layer rising, through a linear approximation. However, in practice, the corrosion of iron material, specifically with the presence of chloride ions, is not homogeneous or linear. In fact, it includes the evolution of pitting corrosion as well as non homogeneous rusting layers formation. In the future, we suggest improving the FMM device corrosion modeling with consideration of pits. To do that, some complementary experimental tests will be suggested to follow the pits' geometrical variations through Scanning Electron Microscope (SEM) photography techniques from different reactive part. Therefore, the corrosion of the reactive part would be more realistic and the results of the numerical model will be more accurate and representative.

— The other remaining problems that could be answered in the future are concerning the practical point of view. In this thesis, the influence of corrosion products on MO assessed only through numerical models. However, in the future, complementary experimental studies could be suggested to find the amount of MO with and without the presence of rusting products to find the related influence of FMM rusts on MO variations.

— The accurate amount of uncertainty level of measurements, in terms of repeating the

punctual measurements, must be also investigated in future.

— Additional environmental noise measurements is also required to precise the amount of SNR, in order to determine the sensitivity of the FMM device to the reactive part's corrosion.
— It also could be assumed that by using the embedded device for a long time (more than years), the important challenge is to precisely determine the location of the device in concrete. In this case, using some techniques such as GPR radars are useful to find the FMM accurate location.
— The performance of FMM in the presence of rebar, must be evaluated through experimental tests to find the amount of coupling, as a border effect.
— At last but not least, in practice, it should find a solution to fix the location of embedded devices and avoid any FMM displacement or bending, for in-service structures under mechanical loads since, the relative distance plays important role on MO variation range.

The above list shows many complementary experimental studies to improve the essential remaining questions of this thesis to improve the functionality of the proposed method. different techniques and optimization methods could be performed to improve the estimation error and optimize the proposed method.

LIST OF PUBLICATIONS

[1] S. Kadkhodazadeh, A. Ihamouten, D. Souriou, X. Dérobert, and D. Guilbert, "Parametric study to evaluate the geometry and coupling effect on the efficiency of a novel fmm tool embedded in cover concrete for corrosion monitoring," *Remote Sensing*, vol. 14, no. 21, p. 5593, 2022.

[2] S. Kadkhodazadeh, D. Souriou, A. Ihamouten, X. Dérobert, and J.-M. Simonin, "Numerical study to evaluate characteristics of an embedded shm tool to prevent rebar corrosion in concrete using magnetic flux density," *International conference and Symposium on Nondestructive Testing in Civil Engineering (NDTCE 2022)*, Zurich, Switzerland, August 2022.

[3] S. Kadkhodazadeh, D. Souriou, A. Ihamouten, and X. Dérobert, "Numerical and experimental study to investigate the performance of a novel embedded shm tool to evaluate chloride front probability of reinforced concrete structures in maritime zone," *International conference and Symposium on Nondestructive Testing in Civil Engineering (NDTCE 2022)*, Zurich, Switzerland, August 2022.

[4] D. Souriou, S. Kadkhodazadeh, X. Dérobert, D. Guilbert, and A. Ihamouten, "Experimental parametric study of a functional-magnetic material designed for the monitoring of corrosion in reinforced concrete structures," *Remote Sensing*, vol. 14, no. 15, p. 3623, 2022.

[5] D. Souriou, S. Kadkhodazadeh, A. Ihamouten, X. Dérobert, and G. Vilan, "Experimental study to investigate the correlation between magnetic flux density and chloride-induced corrosion of a structural health monitoring sensor for reinforced concrete structures," Poster-*International conference and Symposium on Nondestructive Testing in Civil Engineering (NDTCE 2022)*, Zurich, Switzerland, August 2022.

[6] D. Souriou, A. Ihamouten, S. Kadkhodazadeh, B. Fan, and D. Guilbert, "Experimental study to characterize a magneto-functional technology vs. corrosion in reinforced concrete structures," in *NSG2021 2nd Conference on Geophysics for Infrastructure Planning, Monitoring and BIM*, vol. 2021, no. 1. European Association of Geoscientists & Engineers, 2021, pp. 1–5.

[7] B. Fan, D. Souriou, F. Bosc, D. Guilbert, S. Kadkhodazadeh, A. Ihamouten, C. Fauchard, and X. Dérobert, "Dielectric relaxation of iron corrosion products in limestone under saline

environment," in *NSG2021 2nd Conference on Geophysics for Infrastructure Planning, Monitoring and BIM*, vol. 2021, no. 1. European Association of Geoscientists & Engineers, 2021, pp. 1–5.

APPENDIX A

To characterize the magnetic properties of the NdFeB magnets, as permanent part and also iron plate, as material of reactive part, the collaboration work were carried out at laboratory CRISMAT from ENSICAEN, Caen University, Normandy, France.
Table 5.8 shows the properties of NdfeB magnet that were ordered from www.supermagnete.fr, supplier. To perform magnetic characterization, a SQUID magnetometer were used to draw the hysteresis loop and determine material's magnetic permeability through the first magnetization curve. The hysteresis loop (or **B**-**H** loop) is obtained by exciting the magnetic material of the sample with a controlled, and varied, external magnetic field and simultaneously recording the resulting magnetization induced in the sample. The hysteresis loop represents sample's magnetization **M** as a function of applied field **H** or internal field $\mathbf{H}_i$. Through these information, it is possible to draw the intrinsic hysteresis loop that corresponds to the properties that would have the material if it had infinite dimensions.
The internal field $\mathbf{H}_i$ can be deduced from applied field H and magnetization M from the relation:

$$\mathbf{H}_i = \mathbf{H} - \mathbf{N} \cdot \mathbf{M} \tag{5.2}$$

Here, **N** is demagnetizing factor calculated from sample's geometry according to (Oharoni, 1998).
The slope of the first magnetization curve extracted from the intrinsic hysteresis loop allows to calculate the value of the magnetic susceptibility χ_m, so to deduce the relative magnetic permeability μ_r through relation:

$$\mu_r = \chi_m + 1 \tag{5.3}$$

Firstly, concerning to magnet, Table 5.9 shows the physical property of the materials that sent for analysis. By applying the external magnetic field, the hysteresis curve corresponding to the magnet is obtained and illustrated in Figure 5.26. Induction, **B**, is displayed on the vertical axis and applied magnetizing force **H**, is on the horizontal axis. Positive and negative values of both parameters are utilized. One variation of the **B**-**H** loop is the demagnetization curve commonly used to display the properties of permanent magnet materials. The demagnetization curve only

Table 5.8 – Material data sheet NdFeB magnet

Shape	**Geometry tolerance**	**Coating**	**Magnetization**	**Adhesive strength (approximately)**	**Shear force (approximately)**	**Max operational temperature**
Disc	+/- 0.1mm	Nickel-plated (Ni-Cu-Ni)	N45	2.4 kg (approx. 23.5 N)	490g (approx. 4.76N)	80°C

Table 5.9 – The physical property of magnet NdFeB sample, sent for laboratory test

Materials	**Magnet type**	**Weight**$[g]$	**Density** $[Kg/m^3]$	**Radius**$[mm]$	**Height**$[mm]$	$\mathbf{C}_{ferrite}$ $[\%]$
Fe 99.95	NdFeB	0.06	100	7.5	2	1

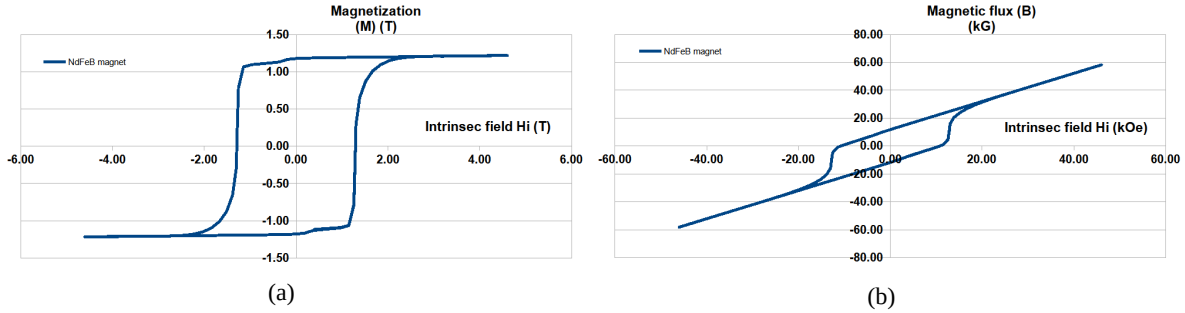

(a) (b)

Figure 5.26 – (a) Hysteresis loop of magnet after laboratory test [T-T] (b) Hysteresis loop of magnet after laboratory test [KG-KOe]

represents the second quadrant of the full **B-H** loop. The material has been magnetized and then a gradual demagnetizing field is applied in an attempt to demagnetize the sample, thus the term demagnetization curve. Considering this curve, the magnet properties are calculated and mentioned in Table 5.10.

In the second part of this laboratory test, a sample of reactive part's iron materials were magnetized to assess the value of relative permeability. In this order, Table 5.11 shows the physical parameters of sample, used in this test. By using applied field **H**, the hysteresis intrinsic and extrinsic loop of iron sample is obtained and illustrated in Figure 5.27 Table 5.12 summarized the results of characterization, obtained from hysteresis loops. The amount of relative permeability is calculated hysteresis intrinsic loop at Figure 5.27a.

In fact, it is the slope of hysteresis intrinsic loop curve. To observe the slope, Figure 5.28 represented a focused window on the initial magnetization area of this sample. As mentioned in Table 5.12, the amount of relative permeability of the iron reactive part would be 50.84.

Table 5.10 – The measured properties of magnet NdFeB, after characterization with laboratory test

$\mathbf{M}_s$ [T]	$\mathbf{M}_r$ [T]	$\mathbf{H}_{ci}$ [T]	$\mathbf{H}_{ci}$ [kOe]	$\mathbf{BH}_{max}$ [T]	$\mathbf{BH}_{max}$ [kOe]	$\mathbf{M}_r/\mathbf{M}_s$	**Permeability**$[-]$
1.218	1.178	1.292	10.773	1.04	26.13	0.967	1.0773425323

Table 5.11 – The physical parameters of iron sample for magnetic characterization test

Materials	**Weight [g]**	**Density**$[Kg/m^3]$	$\mathbf{C}_{ferrite}$ [%]	**geometry**$[mm]$
Fe 99.95	0.06	7.874	1	2.73 × 1.98 × 1.94

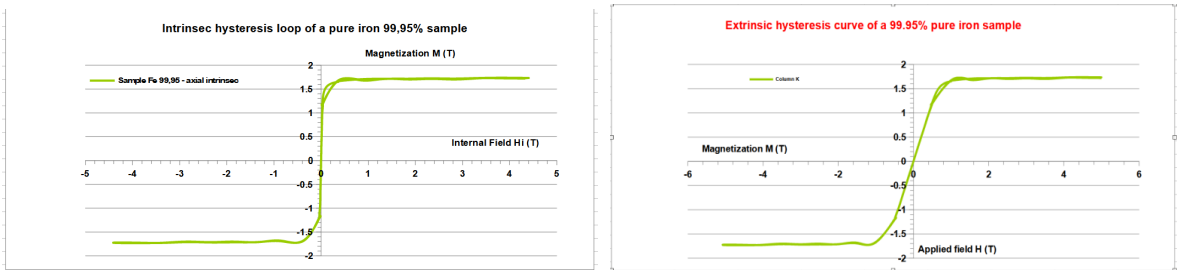

(a) (b)

Figure 5.27 – (a) Intrinsic hysteresis loop of iron sample (b) Extrinsic hysteresis loop of iron sample

Table 5.12 – Results of iron plate characterization

Intrinsic				**extrinsic**				
$\mathbf{M}_s$ [T]	$\mathbf{M}_r$ [T]	$\mathbf{H}_c$ [T]	$\mathbf{M}_r/\mathbf{M}_s$ [-]	$\mathbf{M}_s$ [T]	$\mathbf{M}_r$ [T]	$\mathbf{H}_c$ [T]	$\mathbf{M}_r/\mathbf{M}_s$	**Relative Permeability [-]**
1.734	-0.025	0.001	-0.015	0.244	1.683	5.00	0.971	50.466

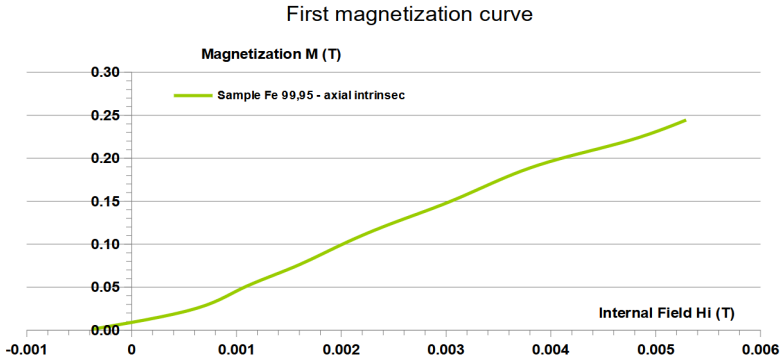

Figure 5.28 – Relative permeability of iron plate in the first quadratic area of hysteresis loop

Appendix B

Corrosion products characterization

The study was a collaboration between three French laboratories: the Cerema laboratory in Angers, the Institut Lavasier of Versailles University, and Lab-STICC in the Faculty of Sciences in Brest. Its main goal was to determine the effective permeability of the corrosion product layer that may result from the pure iron 99.99%, the chosen material of the reactive part, encompassing all possible types of corrosion products. Specifically, the study aimed to achieve two objectives: to identify the typical corrosion products generated in a saline solution with 30 g/L chloride concentration, similar to seawater properties, and to determine the relative permeability of the resulting mixture of corrosion products, to improve numerical modeling accuracy.
In Figure 5.29, the experimental setup is shown where pure iron plates with a purity of 99.95% from NEYCO were immersed in a 30 g/L NaCl solution contained in a Pyrex Becker. The plates were connected to the positive terminal of an electric generator as anode, while titanium coated with platinum was used as cathode. An electrical current was applied to accelerate corrosion, resulting in the formation of dark/brownish particles at the bottom of the Becker. Two batches

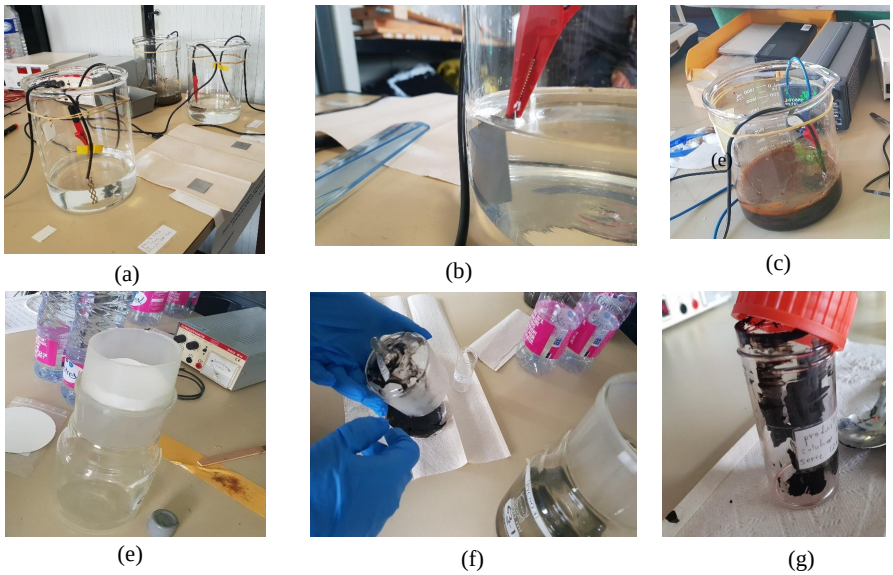

Figure 5.29 – Experimental setup (a) accelerated corrosion with electrolysis techniques on pure iron samples (b) iron plate in saline solution with 30 g/L NaCl (c) formation of corrosion products (d) and (e) screening and rinsing of corrosion products with distilled water to separate salt from products (f) and (g) gathering of products and drying them in the oven

of corrosion products, named "sample 1" and "sample 2", were obtained by filtering and cleaning the particles.

— Sample 1 was produced with a current density between 2 and 5 mA/cm^2,
— Sample 2 was produced with a current density between 1 and 2 mA/cm^2.

Both samples using pure iron plates with thicknesses of 1.0 and 0.5 mm. The experiment aimed to choose two reference samples for test is to investigate the effect of current intensity on the corrosion rate of the iron plates and to investigate the possible effect on the production of different types of corrosion products.
The samples were stored in an oven at 55° for three days to evaporate residual water. Finally, the corrosion products are gathered and prepared for the further tests.

X-ray Diffraction Analysis (XRD) characterization

To characterize the collected corrosion products, an X-ray Diffraction Analysis (XRD) test was conducted. XRD is a laboratory technique that analyzes materials and provides information on the crystallographic structure, chemical composition, and physical properties of a material. Therefore, the corrosion products were sent to the Institut Lavasier of Versailles University for XRD characterization.
The characterization of corrosion products for samples 1 and 2 was carried out through XRD in the 2 range of 10°-80° using a $K\alpha - Cu$ source. The samples were scanned for 5 hours in static mode, with correction for the X-fluorescence phenomenon. Figure 5.30 shows the XRD patterns for the two samples. The vertical axis represents the dimensionless count of diffracted

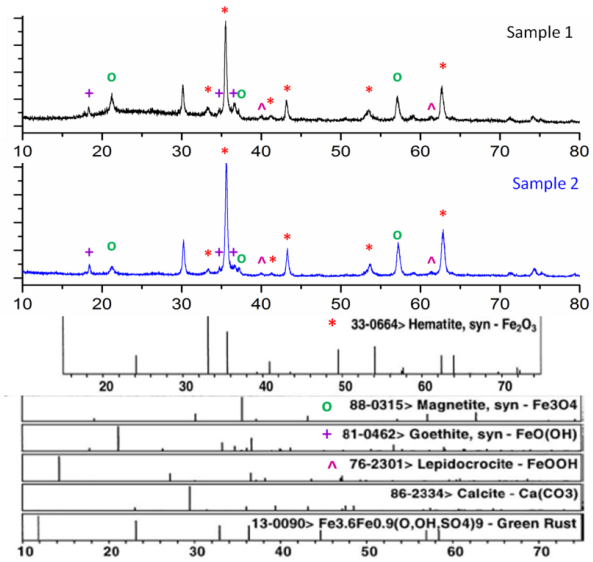

Figure 5.30 – XRD patterns for sample 1 and 2

Table 5.13 – Volumetric content of iron oxide phases for each sample

	Hematite %	**Magnetite %**	**Goethite %**	**Lepidocrocite %**
Sample 1	61	18	10	1
Sample 2	66	17	5	2

X-rays measured by the receptor for a given angle, according to Bragg's law. In compounds with multiple phases, the intensity of peaks associated with a specific phase is a function of the relative amount of each phase. Each peak corresponds to a specific crystallographic plane, which can be identified by Miller indices. The XRD patterns of the two samples show the same phases, with slightly higher crystallinity for sample 2.

Table 5.13 summarizes the XRD results for corrosion products of the two samples in terms of volumetric content for each identified compound. The volumetric content of each identified crystalline phase was estimated using the peak fitting module in origin. The presence of the same compounds with equivalent volumetric proportions confirms that the electrical current density accelerates corrosion, and thus, the type of corrosion products is independent of current intensity. Therefore, for each sample, four iron oxide phases were identified: Hematite (Fe_2O_3), Magnetite (Fe_3O_4), Goethite ($\alpha - FeOOH$), and Lepidocrocite ($\gamma - FeOOH$). Table 5.13 also shows that the hematite and magnetite are the main components of both samples 1 and 2 and the proportion of hematite being slightly higher in sample 2. The presence of hematite and magnetite indicate that iron oxidized in Fe^{2+} and Fe^{3+} are formed, which is coherent with studies about steel material corrosion in marine environment, mentioned in [10][211, 212].

Additionally, the composition of corrosion products (sample 1 and sample 2) being hematite (volumetric mass close to 5.15 $[g.cm^{-3}]$), magnetite (volumetric mass close to 4.90 $[g.cm^{-3}]$) and iron oxide (volumetric mass comprise between 3.8 and 4.1 $[g.cm^{-3}]$), the mean volumetric mass is considered as 5.00 $[g.cm^{-3}]$.

Investigation of magnetic permeability: materials preparation

In the second step, the samples were sent to Lab-STICC in the faculty of Sciences in Brest, France, where characterization methods for magneto-dielectric materials have been developed [216]. Through this method, it would be possible to determine the effective magnetic permeability of corrosion products.

The principle of this technique is elaborating massive samples shaped in APC7 format (ring with an outer diameter of 7 mm, an inner diameter of 3 mm, and a thickness of about 4 mm). Thus, the a APC7 dies would make to proper shape form corrosion product powders well as using a compressor device. Finally, by a reflection/transmission measurement device, proposed by Weir [214] and based on the idea of Nicolson and Ross [215], the real and imaginary parts of complex magnetic permeability and dielectric permittivity of material could be calculated, as a function of frequency. As described, we collected the corrosion products and mixed them with

Table 5.14 – Volumetric proportions of corrosion products, epoxy powder and pores in each pellets after compression

Pallet	Volumetric concentration of corrosion products (%)	Volumetric concentration of epoxy powder (%)	Volumetric concentration of pores (%)
S1 - 80/20	49.00	12.19	38.81
S1 - 70/30	-	-	-
S1 - 60/40	-	-	-
S1 - 50/50	34.28	34.48	31.23
S1 - 40/60	28.77	42.93	28.30
S2 - 80/20	49.25	12.25	38.50
S2 - 70/30	45.82	19.62	34.56
S2 - 60/40	40.00	26.97	33.03
S2 - 50/50	35.41	35.61	28.98
S2 - 40/60	31.02	46.28	22.71

epoxy resin and air to create composite material rings, as shown in Figure 5.31a. The mixing were prepared by mixing the corrosion products with epoxy resin and void in different volumetric ratios: 80%/20%, 70%/30%, 60%/40%, 50%/50%, and 40%/60%. After compression, Table 5.14 summarizes the volumetric proportions of corrosion products, epoxy powder, and pores in each ring associated with samples S1 and S2. The process was carried out in a related die, illustrated in Figure 5.31b, rings the APC7 format, referred to as pellets. APC7 pellets are shaped under 3 KN from these mixtures (*i.e.* a compression stress of approximately 120 MPa).
Then, the compression of the powder mixing (composite) were made by applied compression load of 3 KN (approximated compression stress: 20 MPa) through an uni-axial press in Figure 5.31c. The elaborated APC7 pellets have different mixture percentages and in powder form. In Table 5.15, sample 1 with 70/30 and 60/40 volumetric ratios, broke after the formation. So, their

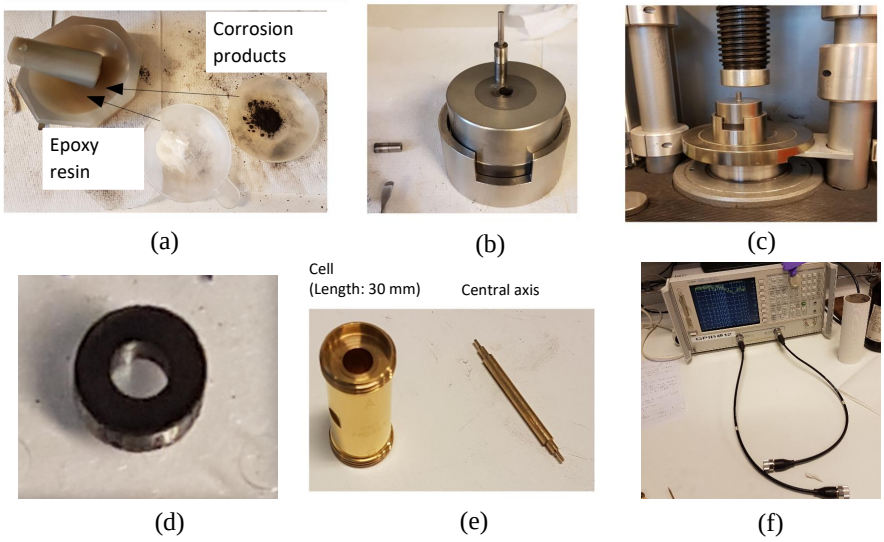

Figure 5.31 – (a) Sample preparation with epoxy resin mixing (b) and (c) APC7 die to produce sample rings (d) produced ring sample (pellet) (e) co-axial cell 30 mm (f) VNA with co-axial cables

characterization were impossible. Final produced pellet sample is illustrated in Figure 5.31d. In the next step, the pellets inserted separately to coaxial cell to investigate their associated relative permeability.

Investigation of magnetic permeability: coaxial cell characterization

In this study, we are only interested in the effective value of relative permeability μ'. The output analysis of VNA would provide transmission coefficient S21 and reflection coefficient S11. The complex permittivity $\epsilon = (\epsilon' - j\epsilon'')$, complex permeability $\mu = (\mu' - j\mu'')$ and microwave absorption properties of mixing corrosion products through different mixture ratios, with epoxy resin, have been evaluated as a function of frequency between 10 MHz and 6 GHz. The effective value of the desired physical characteristic can be deduced using the adapted Bruggemann model [216] as:

$$\sum_i \frac{C_i}{1 + \frac{A_i - A}{A} \cdot N} = 0 \tag{5.4}$$

- C_i the concentration of i^{th} component,
- A_i considered as parameter of (ϵ' or μ') of the i^{th} component
- A considered as parameter of (ϵ' or μ') of the composite material,
- N a depolarization (or demagnetizing) factor depending on the shape of characterized material.

The VNA is an AGILENT 8753 ES type which transmits electromagnetic waves. A central axis with a length of 30 mm is introduced in the central hollow of APC7 pellets and both are introduced in a copper cylindrical cell. Both extremities of the cell are connected to APC7 coaxial cables plugged to a VNA.
The complex scattering parameters that correspond the reflection (S_{11} or S_{22}) and transmission (S_{21} or S_{12}) for each of the samples, has been measured by coaxial cell. The complex permittivity and permeability were then determined from the measured scattering parameters, the coefficient of K is calculated from reflection and transmission coefficients:

$$K = \frac{(S_{11}^2 - S_{21}^2) + 1}{2S_{11}} \tag{5.5}$$

Using the K, the amount of reflection coefficient of the interference between material sample and air, referred as Γ, would be simply defined as:

$$\Gamma = K \pm \sqrt{K^2 + 1} \tag{5.6}$$

Thus, the transmission coefficient T would be:

$$T = \frac{(S_{11} + S_{21}) - \Gamma}{1 - (S_{11} + S_{21})\Gamma} \tag{5.7}$$

Then, the relation between ϵ and μ and the Γ would be:

$$\frac{\mu}{\epsilon} = \left(\frac{1+\Gamma}{1-\Gamma}\right)^2 \tag{5.8}$$

Analysis parameters are:

- Starting frequency: 10 MHz,
- End frequency: 6 GHz,
- Number of points: 401,
- IF bandwidth: 300 Hz.

The Figure 5.32 shows an example of the complex magneto-dielectric spectrum obtained for one sample pellet (mixture of 80%/20% corrosion products/epoxy resin volumetric ratios) in the frequency range 10 MHz to 6 GHz.
Results show that the value of real part of permeability μ' (blue curve) remains constant from the 10 MHz to 400 MHz range. It is then assumed that this value corresponds to that of the

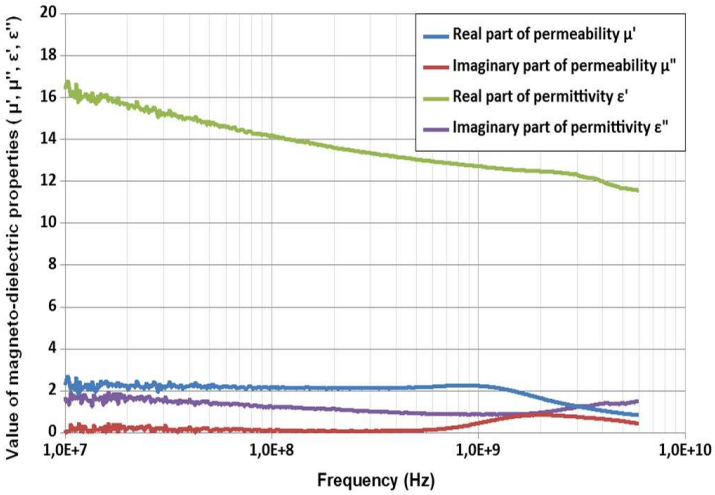

Figure 5.32 – Complex magneto-dielectric spectrum obtained after analysis of the pellet with 80%/20% (corrosion products/epoxy) volumetric ration in the frequency range 10 MHz to 6 GHz

Table 5.15 – Values of μ' at 100, 200, 300, 400 and 500 MHz for each pellets

pellet (corrosion products/epoxy)%	μ'- at 100 MHz	μ'- at 200MHz	μ' - at 300 MHz	μ'- at 400MHz	μ'- at 500MHz
Sample 1 - 80/20	2.18	2.16	2.16	2.19	2.22
Sample 1 - 70/30	-	-	-	-	-
Sample 1 - 60/40	-	-	-	-	-
Sample 1 - 50/50	1.74	1.73	1.73	1.74	1.76
Sample 1 - 40/60	1.61	1.60	1.59	1.60	1.61
Sample 2 - 80/20	2.88	2.88	2.92	3.01	3.11
Sample 2 - 70/30	2.77	2.77	2.82	2.91	3.01
Sample 2 - 60/40	2.40	2.41	2.44	2.50	2.57
Sample 2 - 50/50	2.24	2.22	2.23	2.28	2.34
Sample 2 - 40/60	2.10	2.08	2.09	2.14	2.19

material in static conditions. Complex permeability (red curve) reaches its maximum at 1,6 GHz, which corresponds to resonance frequency of composite. The shape of μ' and μ" spectrum indicates that magnetic losses mainly occur by spin resonance, the slight increase of μ' starting at 500 MHz can indicate looses by domain-wall relaxation in a lesser proportion. Values of $\epsilon^{'}$ and $\epsilon^{"}$ (green and purple curves respectively) are elevated at 10 MHz and tends to decrease with the increase of frequency. High values of $\epsilon^{"}$ at low frequencies can be attributed to the high porosity (38.5%) of the pallet but also the possible presence of remaining water in corrosion products powder (incomplete drying), which could also influence the value of $\epsilon^{'}$. Analysis of complex permittivity of the two batches of corrosion products is then debatable.

The values of μ' of each pellet at 100, 200, 300, 400, and 500 MHz are indicated in Table 5.15. For all of the pellets, the results spectram analysis, are provided in Figure 5.33 to 5.36

Using Bruggemann model [216] and the Eq. 5.4, the effective value of μ' for the two batches of corrosion products was obtained as:

— Sample 1: $\mu' = 4.13 \pm 0.16$

— Sample 2: $\mu' = 5.52 \pm 0.29$

Finally, the average value for these two samples would lead to an approximate amount of 5. This value is known as the relative permeability of the mixture of corrosion products, obtained for pure iron used in this study.

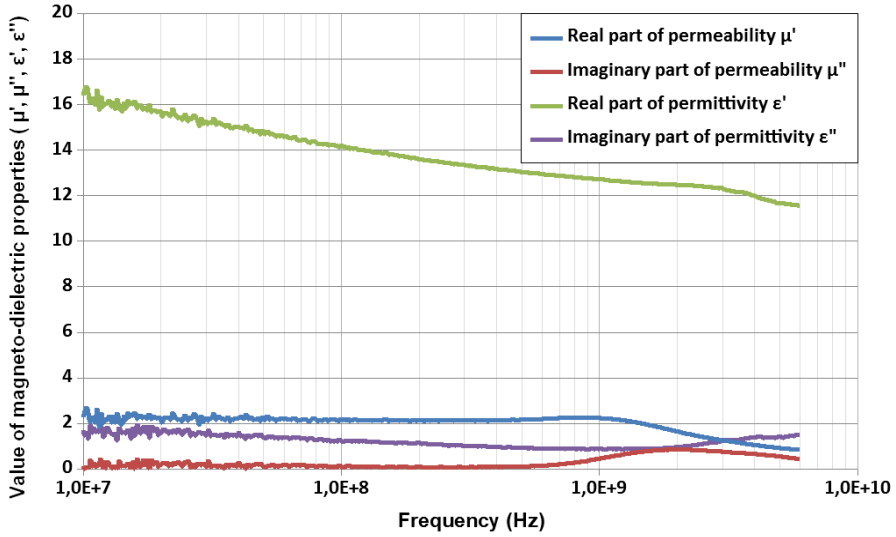

(a) S1 – 80/20 pallet in the frequency range 10 MHz to 6 GHz

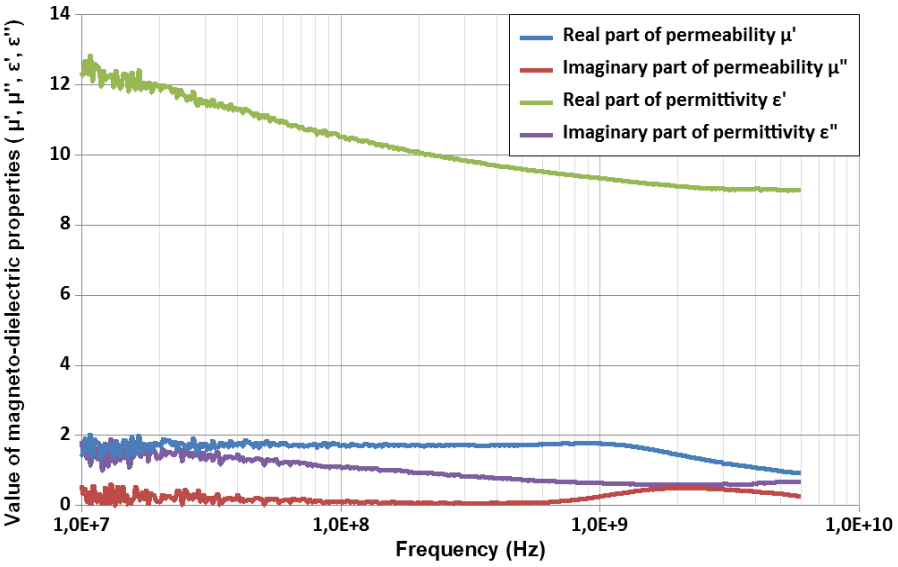

(b) S1 – 50/50 pallet in the frequency range 10 MHz to 6 GHz

Figure 5.33 – Complex magneto-dielectric spectrum obtained after analysis of pellets S1 – 80/20 and S1 – 50/50

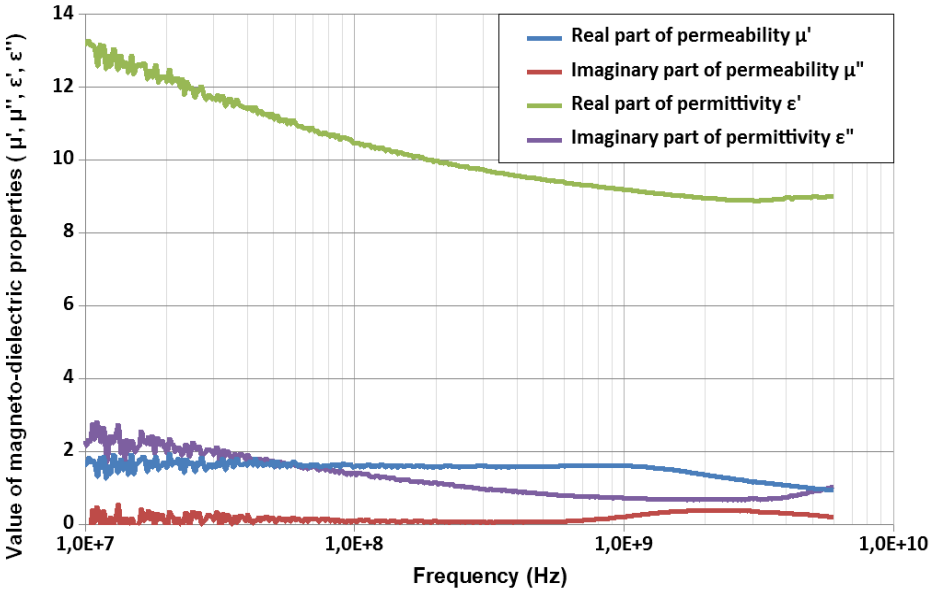

(a) S1 – 40/60 pallet in the frequency range 10 MHz to 6 GHz

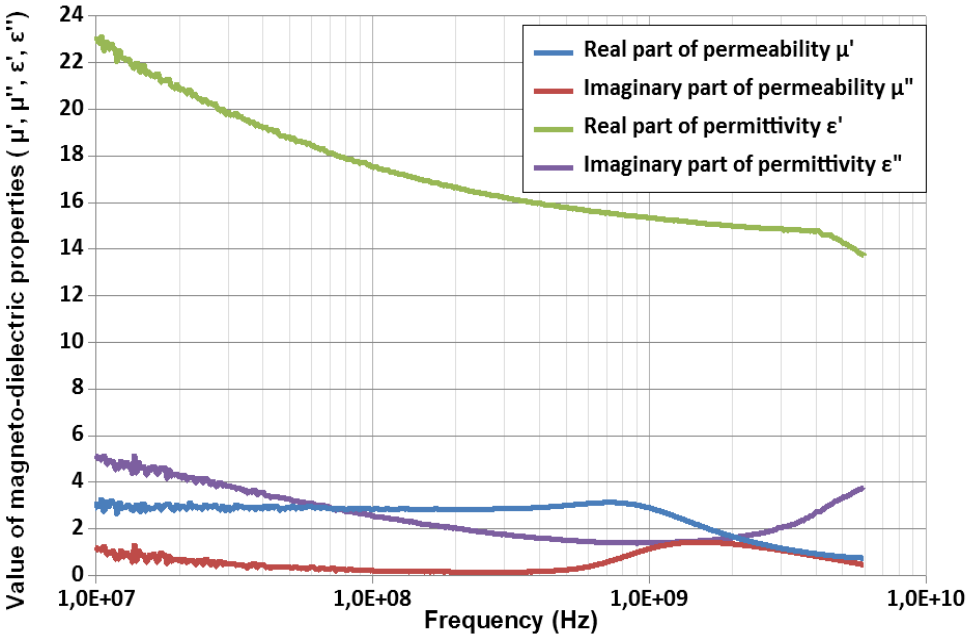

(b) S2 – 80/20 pallet in the frequency range 10 MHz to 6 GHz

Figure 5.34 – Complex magneto-dielectric spectrum obtained after analysis of pellets S1 – 40/60 and S2 – 80/20

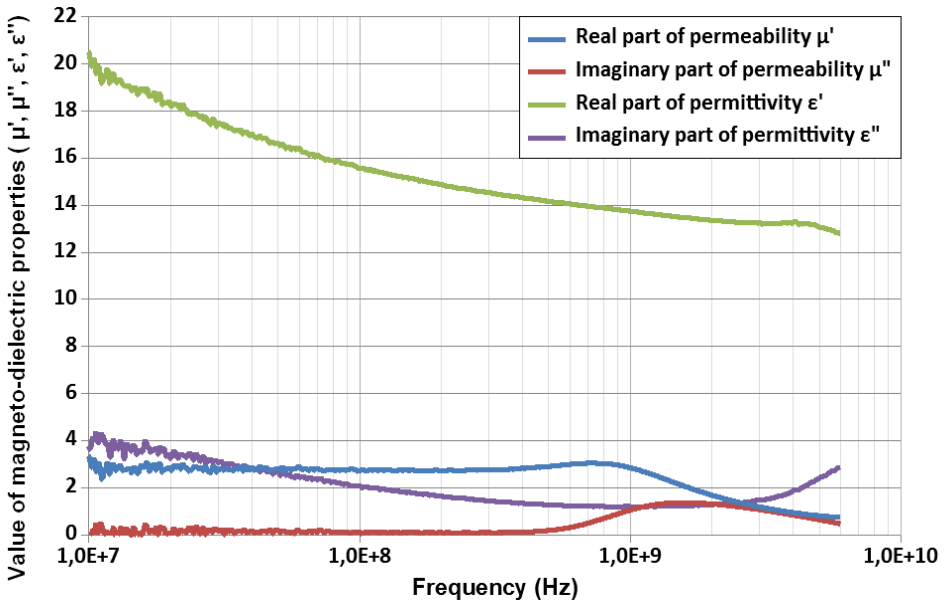

(a) S2 – 70/30 pallet in the frequency range 10 MHz to 6 GHz

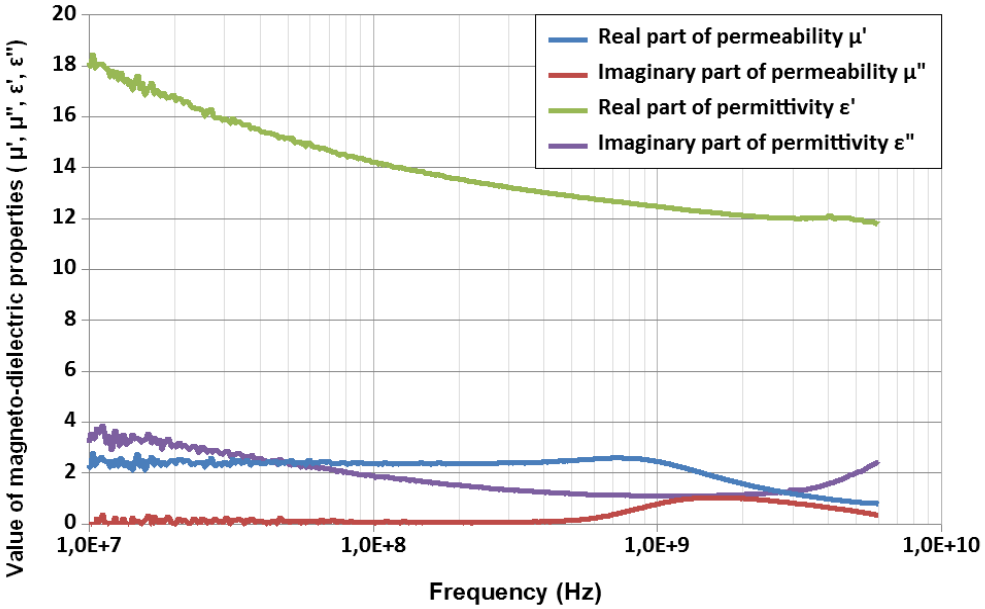

(b) S2 – 60/40 pallet in the frequency range 10 MHz to 6 GHz

Figure 5.35 – Complex magneto-dielectric spectrum obtained after analysis of pellets S2 – 70/30 and S2 – 60/40

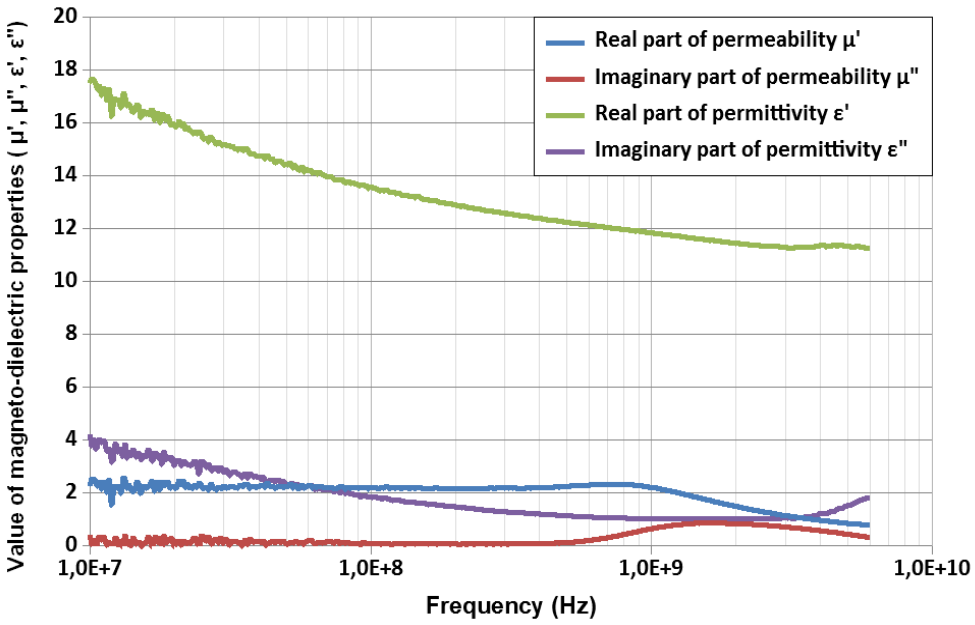

(a) S2 – 50/50 pallet in the frequency range 10 MHz to 6 GHz

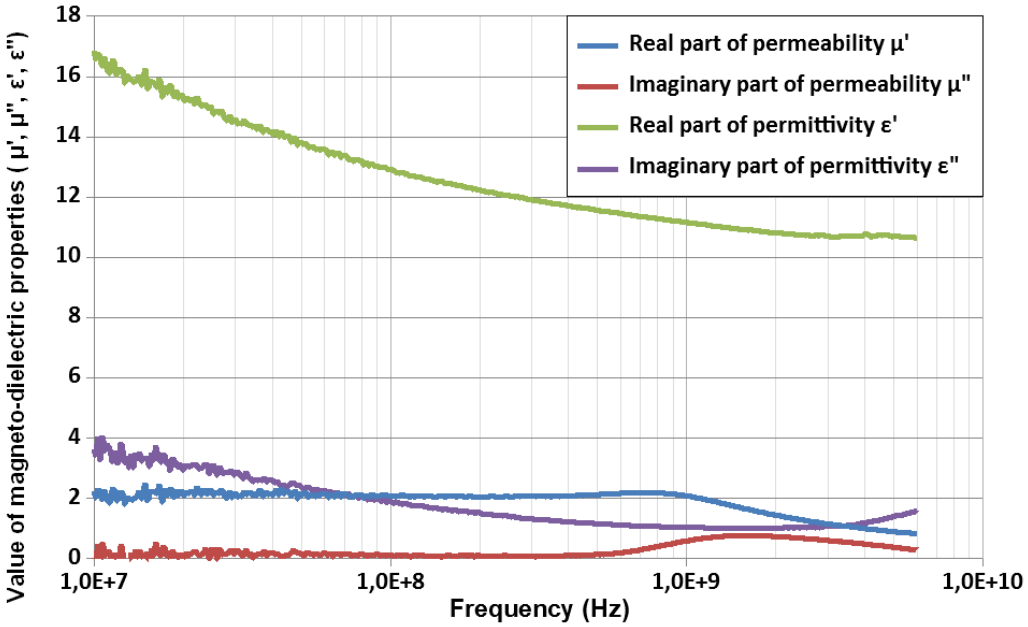

(b) S2 – 40/60 pallet in the frequency range 10 MHz to 6 GHz

Figure 5.36 – Complex magneto-dielectric spectrum obtained after analysis of pellets S2 – 50/50 and S2 – 40/60

BIBLIOGRAPHY

[1] D. Hobbs, "Concrete deterioration: causes, diagnosis, and minimising risk," *International Materials Reviews*, vol. 46, no. 3, pp. 117–144, 2001.

[2] P. Thoft-Christensen, "Deterioration of concrete structures," 2002.

[3] M. L. S. Rivetti, J. Netto, M. Junior, and D. V. Ribeiro, "Corrosion inhibitors for reinforced concrete," *Corrosion inhibitors, principles and recent applications*, pp. 35–58, 2018.

[4] G. Glass and N. Buenfeld, "Chloride-induced corrosion of steel in concrete," *Progress in Structural Engineering and Materials*, vol. 2, no. 4, pp. 448–458, 2000.

[5] Y. Veyret and A. Ciattoni, *Géo-environnement*. Armand Colin, 2011.

[6] F. Qu, W. Li, W. Dong, V. W. Tam, and T. Yu, "Durability deterioration of concrete under marine environment from material to structure: A critical review," *Journal of Building Engineering*, vol. 35, p. 102074, 2021.

[7] J. Liu, Q. Qiu, X. Chen, F. Xing, N. Han, Y. He, and Y. Ma, "Understanding the interacted mechanism between carbonation and chloride aerosol attack in ordinary portland cement concrete," *Cement and Concrete Research*, vol. 95, pp. 217–225, 2017.

[8] X.-m. Zhang, Z.-y. Chen, H.-f. Luo, Z. Teng, Y.-l. Zhao, and Z.-c. Ling, "Corrosion resistances of metallic materials in environments containing chloride ions: A review," *Transactions of Nonferrous Metals Society of China*, vol. 32, no. 2, pp. 377–410, 2022.

[9] R. Foley, "Role of the chloride ion in iron corrosion," *Corrosion*, vol. 26, no. 2, pp. 58–70, 1970.

[10] A. Poursaee, "Corrosion of steel in concrete structures," in *Corrosion of steel in concrete structures*, pp. 19–33, Elsevier, 2016.

[11] Z. Ai, J. Jiang, W. Sun, X. Jiang, B. Yu, K. Wang, Z. Zhang, D. Song, H. Ma, and J. Zhang, "Enhanced passivation of alloy corrosion-resistant steel cr10mo1 under carbonation—passive film formation, the kinetics and mechanism analysis," *Cement and Concrete Composites*, vol. 92, pp. 178–187, 2018.

[12] W. Feng, A. Tarakbay, S. A. Memon, W. Tang, and H. Cui, "Methods of accelerating chloride-induced corrosion in steel-reinforced concrete: A comparative review," *Construction and Building Materials*, vol. 289, p. 123165, 2021.

[13] M. Montemor, A. Simoes, and M. Ferreira, "Chloride-induced corrosion on reinforcing steel: from the fundamentals to the monitoring techniques," *Cement and concrete composites*, vol. 25, no. 4-5, pp. 491–502, 2003.

[14] M. G. Stewart, "Reliability safety assessment of corroding reinforced concrete structures based on visual inspection information," *ACI Structural Journal*, vol. 107, no. 6, p. 671, 2010.

[15] A. Zaki, H. K. Chai, D. G. Aggelis, and N. Alver, "Non-destructive evaluation for corrosion monitoring in concrete: A review and capability of acoustic emission technique," *Sensors*, vol. 15, no. 8, pp. 19069–19101, 2015.

[16] A. James, E. Bazarchi, A. A. Chiniforush, P. P. Aghdam, M. R. Hosseini, A. Akbarnezhad, I. Martek, and F. Ghodoosi, "Rebar corrosion detection, protection, and rehabilitation of reinforced concrete structures in coastal environments: A review," *Construction and Building Materials*, vol. 224, pp. 1026–1039, 2019.

[17] M. Dixit and A. K. Gupta, "A review of different assessment methods of corrosion of steel reinforcement in concrete," *Iranian Journal of Science and Technology, Transactions of Civil Engineering*, vol. 46, no. 2, pp. 735–752, 2022.

[18] M. Arooj and G. Yadav, "Comparison of destructive and non-destructive testing of concrete-a review," *Int. J. Eng. Res. Technol*, vol. 6, no. 11, pp. 62–68, 2017.

[19] P. Lehner and K. Hrabová, "Relationship of time-dependent parameters from destructive and non-destructive tests of structural concrete," *Mathematics*, vol. 10, no. 3, p. 460, 2022.

[20] G. Villain, Z. M. Sbartaï, X. Dérobert, V. Garnier, and J.-P. Balayssac, "Durability diagnosis of a concrete structure in a tidal zone by combining ndt methods: laboratory tests and case study," *Construction and Building Materials*, vol. 37, pp. 893–903, 2012.

[21] X. Dérobert and G. Villain, "Em characterization of concretes focused on water and chloride contents in the frame of multi-linear experimental designs," in *2016 16th International Conference on Ground Penetrating Radar (GPR)*, pp. 1–5, IEEE, 2016.

[22] R. Du Plooy, S. P. Lopes, G. Villain, and X. Derobert, "Development of a multi-ring resistivity cell and multi-electrode resistivity probe for investigation of cover concrete condition," *NDT & E International*, vol. 54, pp. 27–36, 2013.

[23] G. Villain, A. Ihamouten, R. Du Plooy, S. P. Lopes, and X. Dérobert, "Use of electromagnetic non-destructive techniques for monitoring water and chloride ingress into concrete," *Near Surface Geophysics*, vol. 13, no. 3, pp. 299–309, 2015.

[24] R. Du Plooy, G. Villain, S. Palma Lopes, A. Ihamouten, X. Derobert, and B. Thauvin, "Electromagnetic non-destructive evaluation techniques for the monitoring of water and chloride ingress into concrete: a comparative study," *Materials and structures*, vol. 48, pp. 369–386, 2015.

[25] R. Huan and W. Yeih, "Detection of the corrosion damage in reinforced concrete members by ultrasonic testing," 1997.

[26] S. Sharma and A. Mukherjee, "Nondestructive evaluation of corrosion in varying environments using guided waves," *Research in Nondestructive Evaluation*, vol. 24, no. 1, pp. 63–88, 2013.

[27] N. J. Carino, M. Sansalone, and N. N. Hsu, "A point source-point receiver, pulse-echo technique for flaw detection in concrete," in *Journal Proceedings*, vol. 83, pp. 199–208, 1986.

[28] Y. Tian, P. Zhang, K. Zhao, Z. Du, and T. Zhao, "Application of ag/agcl sensor for chloride monitoring of mortar under dry-wet cycles," *Sensors*, vol. 20, no. 5, p. 1394, 2020.

[29] B. Spencer Jr, J.-W. Park, K. Mechitov, H. Jo, and G. Agha, "Next generation wireless smart sensors toward sustainable civil infrastructure," *Procedia engineering*, vol. 171, pp. 5–13, 2017.

[30] S. Das and P. Saha, "A review of some advanced sensors used for health diagnosis of civil engineering structures," *Measurement*, vol. 129, pp. 68–90, 2018.

[31] H. Reinisch, M. Wiessflecker, S. Gruber, H. Unterassinger, G. Hofer, M. Klamminger, W. Pribyl, and G. Holweg, "A multifrequency passive sensing tag with on-chip temperature sensor and off-chip sensor interface using epc hf and uhf rfid technology," *IEEE Journal of Solid-State Circuits*, vol. 46, no. 12, pp. 3075–3088, 2011.

[32] S. E. Watkins, T. M. Swift, and M. J. Molander, "Rfid instrumentation in a field application," in *2007 IEEE Region 5 Technical Conference*, pp. 400–403, IEEE, 2007.

[33] Y. Duroc, "From identification to sensing: Rfid is one of the key technologies in the iot field," *Sensors*, vol. 22, no. 19, p. 7523, 2022.

[34] M. Shetty and A. Jain, *Concrete Technology (Theory and Practice), 8e.* S. Chand Publishing, 2019.

[35] P. K. Mehta, "Concrete. structure, properties and materials," 1986.

[36] W. Jin and C. Meyer, "Department of civil engineering and engineering mechanics," in *Materials Science of Concrete: The Sidney Diamond Symposium*, vol. 59, p. 367, Wiley-American Ceramic Society, 1998.

[37] L. Aljerf, "Effect of thermal-cured hydraulic cement admixtures on the mechanical properties of concrete," *Interceram-International ceramic review*, vol. 64, no. 8, pp. 346–356, 2015.

[38] P. K. Mehta, *Concrete in the marine environment*. Crc Press, 1991.

[39] V. C. Johanses, P. C. Taylor, and P. D. Tennis, *Effect of cement characteristics on concrete properties*. No. Engineering Bulletin 226, 2006.

[40] N. EN, "1-1 (2005) eurocode 2: Calcul des structures en béton-partie 1-1: règles générales et règles pour les bâtiments," *Association Française de Normalisation (AFNOR)*, 1992.

[41] Y. Chen, K.-J. Wang, and D. Liang, "Mechanical properties of pervious cement concrete," *Journal of Central South University*, vol. 19, no. 11, pp. 3329–3334, 2012.

[42] V. Murthy, *Geotechnical engineering: principles and practices of soil mechanics and foundation engineering*. CRC press, 2002.

[43] A. M. Neville *et al.*, *Properties of concrete*, vol. 4. Longman London, 1995.

[44] V. Baroghel-Bouny, *Concrete design for a given structure service life: durability management with regard to reinforcement corrosion and alkali-silica reaction: state of the art and guide for the implementation of a predictive performance approach based upon durability indicators*. Association française de génie civil, 2007.

[45] W. Heyen and L. Halsey, "Effect of moisture condition on concrete core strengths," 2019.

[46] V. B. Bouny, "Texture and moisture properties of ordinary and high-performance cementitious materials," in *International RILEM Conference on Concrete: from Material to Structure*, pp. 144–165, RILEM Publications SARL, 1996.

[47] C. Andrade, J. Sarrıa, and C. Alonso, "Relative humidity in the interior of concrete exposed to natural and artificial weathering," *Cement and concrete research*, vol. 29, no. 8, pp. 1249–1259, 1999.

[48] Z. C. Grasley, D. A. Lange, M. D. D'Ambrosia, and S. Villalobos-Chapa, "Relative humidity in concrete," *Concrete international*, vol. 28, no. 10, pp. 51–57, 2006.

[49] M. Thomas, "The durability of concrete for marine construction: Materials and properties," in *Marine Concrete Structures*, pp. 151–170, Elsevier, 2016.

[50] D. Song, F. Yang, M. Guo, S. Zhao, J. Hao, Z. Chen, J. Sun, Y. Xu, and J. Jiang, "Surface modification of rusted rebar and enhanced passivation/anticorrosion performance in simulated concrete pore solutions with different alkalinity," *Metals*, vol. 9, no. 10, p. 1050, 2019.

[51] C. G. Berrocal, K. Lundgren, and I. Löfgren, "Corrosion of steel bars embedded in fibre reinforced concrete under chloride attack: state of the art," *Cement and Concrete Research*, vol. 80, pp. 69–85, 2016.

[52] S. Ahmad, "Reinforcement corrosion in concrete structures, its monitoring and service life prediction—-a review," *Cement and concrete composites*, vol. 25, no. 4-5, pp. 459–471, 2003.

[53] N. Holmes, A. Byrne, and B. Norton, "First steps in developing cement-based batteries to power cathodic protection of embedded steel in concrete," *SDAR* Journal of Sustainable Design & Applied Research*, vol. 3, no. 1, p. 3, 2015.

[54] R. R. Hussain, "Influence of chloride ions and hot weather on isolated rusting steel bar in concrete based on ndt and electro-chemical model evaluation," *NDT & E International*, vol. 44, no. 2, pp. 158–162, 2011.

[55] C. Newton and J. Sykes, "A galvanostatic pulse technique for investigation of steel corrosion in concrete," *Corrosion Science*, vol. 28, no. 11, pp. 1051–1074, 1988.

[56] Y. Zhao and W. Jin, *Steel corrosion-induced concrete cracking*. Butterworth-Heinemann, 2016.

[57] C. Alonso, C. Andrade, X. Nóvoa, M. Izquierdo, and M. Pérez, "Effect of protective oxide scales in the macrogalvanic behaviour of concrete reinforcements," *Corrosion science*, vol. 40, no. 8, pp. 1379–1389, 1998.

[58] H.-M. Lee, H.-S. Lee, S.-h. Min, S. Lim, and J. K. Singh, "Carbonation-induced corrosion initiation probability of rebars in concrete with/without finishing materials," *Sustainability*, vol. 10, no. 10, p. 3814, 2018.

[59] M. G. Stewart and J. Peng, "Life cycle cost assessment of climate change adaptation measures to minimise carbonation-induced corrosion risks," *International Journal of Engineering under Uncertainty: Hazards, Assessment and Mitigation*, vol. 2, no. 1-2, pp. 35–46, 2010.

[60] A. K. Singh and G. Das, "Migration of chloride ion in the pore solution of reinforced concrete steel bar," *IRJET*, vol. 3, no. 12, pp. 786–795, 2016.

[61] U. M. Angst, B. Elsener, C. K. Larsen, and Ø. Vennesland, "Chloride induced reinforcement corrosion: Electrochemical monitoring of initiation stage and chloride threshold values," *Corrosion Science*, vol. 53, no. 4, pp. 1451–1464, 2011.

[62] Y. Zhao and W. Jin, *Steel corrosion-induced concrete cracking*. Butterworth-Heinemann, 2016.

[63] C. Rémazeilles and P. Refait, "On the formation of β-feooh (akaganéite) in chloride-containing environments," *Corrosion Science*, vol. 49, no. 2, pp. 844–857, 2007.

[64] K. Y. Ann and H.-W. Song, "Chloride threshold level for corrosion of steel in concrete," *Corrosion science*, vol. 49, no. 11, pp. 4113–4133, 2007.

[65] C. Hansson, "The impact of corrosion on society," *Metallurgical and Materials Transactions A*, vol. 42, no. 10, pp. 2952–2962, 2011.

[66] V. Baroghel-Bouny, T. Nguyen, and P. Dangla, "Assessment and prediction of rc structure service life by means of durability indicators and physical/chemical models," *Cement and Concrete Composites*, vol. 31, no. 8, pp. 522–534, 2009.

[67] L. Basheer, J. Kropp, and D. J. Cleland, "Assessment of the durability of concrete from its permeation properties: a review," *Construction and building materials*, vol. 15, no. 2-3, pp. 93–103, 2001.

[68] K. Stanish, R. D. Hooton, and M. Thomas, "Testing the chloride penetration resistance of concrete: a literature review," 1997.

[69] D. Conciatori, H. Sadouki, and E. Brühwiler, "Capillary suction and diffusion model for chloride ingress into concrete," *Cement and Concrete Research*, vol. 38, no. 12, pp. 1401–1408, 2008.

[70] M. Williams, "The mathematics of diffusion: By j. crank. clarendon press, oxford, £ 13.50, 1975, 414 pp," 1977.

[71] T. Zhang and O. E. Gjørv, "Diffusion behavior of chloride ions in concrete," *Cement and Concrete Research*, vol. 26, no. 6, pp. 907–917, 1996.

[72] K. Krabbenhøft and J. Krabbenhøft, "Application of the poisson–nernst–planck equations to the migration test," *Cement and Concrete Research*, vol. 38, no. 1, pp. 77–88, 2008.

[73] C. Andrade, M. Sanjuán, A. Recuero, and O. Río, "Calculation of chloride diffusivity in concrete from migration experiments, in non steady-state conditions," *Cement and concrete research*, vol. 24, no. 7, pp. 1214–1228, 1994.

[74] X. Lu, "Application of the nernst-einstein equation to concrete," *Cement and Concrete Research*, vol. 27, no. 2, pp. 293–302, 1997.

[75] C. ASTM *et al.*, "Standard test method for electrical indication of concrete's ability to resist chloride ion penetration," *Annual Book of ASTM Standards*, vol. 4, no. 7, 2012.

[76] N. Build, "443. concrete, hardened: accelerated chloride penetration," *Nordtest method*, 1995.

[77] ASTM, "Standard test method for determining the penetration of chloride ion into concrete by ponding," 2002.

[78] B. Díaz, X. Nóvoa, and M. Pérez, "Study of the chloride diffusion in mortar: A new method of determining diffusion coefficients based on impedance measurements," *Cement and Concrete Composites*, vol. 28, no. 3, pp. 237–245, 2006.

[79] N. Nordtest, "Concrete, hardened: accelerated chloride penetration," *Nordtest NT Build*, vol. 443, 1995.

[80] D. Harvey, "Analytical chemistry 2.0—an open-access digital textbook," *Analytical and bioanalytical chemistry*, vol. 399, no. 1, pp. 149–152, 2011.

[81] B. Park, "A statistical comparison of the gravimetric, mohr, and fajans methods for chloride," *Journal of Chemical Education*, vol. 35, no. 10, p. 516, 1958.

[82] A. Robert, "Dielectric permittivity of concrete between 50 mhz and 1 ghz and gpr measurements for building materials evaluation," *Journal of applied geophysics*, vol. 40, no. 1-3, pp. 89–94, 1998.

[83] X. Dérobert, J. Iaquinta, G. Klysz, and J.-P. Balayssac, "Use of capacitive and gpr techniques for the non-destructive evaluation of cover concrete," *Ndt & E International*, vol. 41, no. 1, pp. 44–52, 2008.

[84] F. N. Kusenberger, J. R. Barton, *et al.*, "Detection of flaws in reinforcing steel in prestressed concrete bridge members," 1981.

[85] K. Komlos, S. Popovics, T. Nürnbergerová, B. Babal, and J. Popovics, "Ultrasonic pulse velocity test of concrete properties as specified in various standards," *Cement and Concrete Composites*, vol. 18, no. 5, pp. 357–364, 1996.

[86] J.-K. Zhang, W. Yan, and D.-M. Cui, "Concrete condition assessment using impact-echo method and extreme learning machines," *Sensors*, vol. 16, no. 4, p. 447, 2016.

[87] R. Stratfull, "The corrosion of steel in a reinforced concrete bridge," *Corrosion*, vol. 13, no. 3, pp. 43–48, 1957.

[88] S. Yin, P. B. Ruffin, and T. Francis, *Fiber optic sensors*. CRC press, 2017.

[89] G. Gautschi and G. Gautschi, *Piezoelectric sensors*. Springer, 2002.

[90] J. R. Matthews, *Acoustic emission*, vol. 2. CRC Press, 1983.

[91] J. Hulimka and M. Kałuża, "Basic chemical tests of concrete during the assessment of structure suitability—discussion on selected industrial structures," *Applied Sciences*, vol. 10, no. 1, p. 358, 2020.

[92] "Nf p18-420: "méthodes d'essais des bétons - essai de grattage"." AFNOR, 1996. Accessed: January 31, 2023.

[93] J.-M. Torrenti, *Essais pour les bétons*. Eyrolles, 2016.

[94] B. Elsener, C. Andrade, J. Gulikers, R. Polder, and M. Raupach, "Half-cell potential measurements—potential mapping on reinforced concrete structures," *Materials and Structures*, vol. 36, no. 7, pp. 461–471, 2003.

[95] R. Arndt and F. Jalinoos, "Nde for corrosion detection in reinforced concrete structures–a benchmark approach," *Proceedings of Non-destructive Testing in Civil Engineering*, 2009.

[96] R. Vedalakshmi, L. Balamurugan, V. Saraswathy, S.-H. Kim, and K. Ann, "Reliability of galvanostatic pulse technique in assessing the corrosion rate of rebar in concrete structures: Laboratory vs field studies," *KSCE Journal of civil engineering*, vol. 14, no. 6, pp. 867–877, 2010.

[97] J. Xu and W. Yao, "Detecting the efficiency of cathodic protection in reinforced concrete by use of galvanostatic pulse technique," in *Advanced Materials Research*, vol. 177, pp. 584–589, Trans Tech Publ, 2011.

[98] H.-W. Song and V. Saraswathy, "Corrosion monitoring of reinforced concrete structures-a," *Int. J. Electrochem. Sci*, vol. 2, no. 1, pp. 1–28, 2007.

[99] C. Andrade Perdrix, M. Keddam, X. Nóvoa, M. C. Pérez, C. M. Rangel, and H. Takenouti, "Electrochemical behaviour of steel rebars in concrete: Influence of environmental factors and cement chemistry," 2001.

[100] M. Ohtsu and T. Yamamoto, "Compensation procedure for half-cell potential measurement," *Construction and Building Materials*, vol. 11, no. 7-8, pp. 395–402, 1997.

[101] L. Sadowski, "Methodology for assessing the probability of corrosion in concrete structures on the basis of half-cell potential and concrete resistivity measurements," *The scientific world journal*, vol. 2013, 2013.

[102] Ş. Erdoğdu, I. Kondratova, and T. Bremner, "Determination of chloride diffusion coefficient of concrete using open-circuit potential measurements," *Cement and Concrete Research*, vol. 34, no. 4, pp. 603–609, 2004.

[103] F. Bernal Castillo, G. Roa-Rodríguez, C. Cabrera Cabrera, N. Sierra-Melo, and W. Aperador, "Determination of the probability and rate of corrosion on reinforced concrete specimens through a remote corrosion monitoring system," *Tecciencia*, vol. 10, no. 19, pp. 27–31, 2015.

[104] M. A. Ismail, H. Soleymani, and M. Ohtsu, "Early detection of corrosion activity in reinforced concrete slab by ae technique," in *Proceedings of the 6th Asia-Pacific Structural Engineering and Construction Conference (APSEC 2006), Kuala Lumpur, Malaysia*, vol. 56, 2006.

[105] M. Stern and A. Geary, "A theoretical analysis of the shape of polarization curves," *J. Electrochem. Soc*, vol. 104, no. 1, pp. 56–63, 1957.

[106] C. Andrade, M. C. Alonso, and J. A. Gonzalez, "An initial effort to use the corrosion rate measurements for estimating rebar durability," in *Corrosion rates of steel in concrete*, ASTM International, 1990.

[107] K. C. Clear, "Measuring rate of corrosion of steel in field concrete structures," *Transportation research record*, no. 1211, 1989.

[108] W. Yeih and R. Huang, "Detection of the corrosion damage in reinforced concrete members by ultrasonic testing," *Cement and concrete research*, vol. 28, no. 7, pp. 1071–1083, 1998.

[109] S. Sharma and A. Mukherjee, "Longitudinal guided waves for monitoring chloride corrosion in reinforcing bars in concrete," *Structural Health Monitoring*, vol. 9, no. 6, pp. 555–567, 2010.

[110] D. Li, S. Zhang, W. Yang, and W. Zhang, "Corrosion monitoring and evaluation of reinforced concrete structures utilizing the ultrasonic guided wave technique," *International Journal of Distributed Sensor Networks*, vol. 10, no. 2, p. 827130, 2014.

[111] M. Goueygou, B. Piwakowski, A. Fnine, M. Kaczmarek, and F. Buyle-Bodin, "Nde of two-layered mortar samples using high-frequency rayleigh waves," *Ultrasonics*, vol. 42, no. 1-9, pp. 889–895, 2004.

[112] D. Aggelis, E. Kordatos, D. Soulioti, and T. Matikas, "Combined use of thermography and ultrasound for the characterization of subsurface cracks in concrete," *Construction and Building Materials*, vol. 24, no. 10, pp. 1888–1897, 2010.

[113] N. J. Carino, "The impact-echo method: an overview," *Structures 2001: A Structural Engineering Odyssey*, pp. 1–18, 2001.

[114] C.-C. Lin, P.-L. Liu, and P.-L. Yeh, "Application of empirical mode decomposition in the impact-echo test," *Ndt & E International*, vol. 42, no. 7, pp. 589–598, 2009.

[115] Y. Zhang and Z. Xie, "Ensemble empirical mode decomposition of impact-echo data for testing concrete structures," *Ndt & E International*, vol. 51, pp. 74–84, 2012.

[116] G. Monfore, "The electrical resistivity of concrete," tech. rep., 1968.

[117] D. A. Whiting and M. A. Nagi, "Electrical resistivity of concrete-a literature review," *R&D Serial*, vol. 2457, p. 1078, 2003.

[118] E. Hammond and T. Robson, "Comparison of electrical properties of various cements and concretes," *The Engineer*, vol. 199, no. 5156, p. 114, 1955.

[119] S. Feliu, C. Andrade, J. González, and C. Alonso, "A new method for in-situ measurement of electrical resistivity of reinforced concrete," *Materials and structures*, vol. 29, no. 6, pp. 362–365, 1996.

[120] J. H. Bungey and M. G. Grantham, *Testing of concrete in structures*. Crc Press, 2006.

[121] Y. Dong and F. Ansari, "Non-destructive testing and evaluation (ndt/nde) of civil structures rehabilitated using fiber reinforced polymer (frp) composites," in *Service life estimation and extension of civil engineering structures*, pp. 193–222, Elsevier, 2011.

[122] M. Fares, Y. Fargier, G. Villain, X. Derobert, and S. P. Lopes, "Determining the permittivity profile inside reinforced concrete using capacitive probes," *NDT & E International*, vol. 79, pp. 150–161, 2016.

[123] Ł. Sadowski, "New non-destructive method for linear polarisation resistance corrosion rate measurement.," *Archives of Civil & Mechanical Engineering (Oficyna Wydawnicza Politechniki Wroclawskiej)*, vol. 10, no. 2, 2010.

[124] Y. P. Virmani, K. C. Clear, and T. J. Pasko Jr, "Time-to-corrosion of reinforcing steel in concrete slabs. volume 5. calcium nitrite admixture or epoxy-coated reinforcing bars as corrosion protection systems. report for july 1980-december 1982," tech. rep., Federal Highway Administration, Washington, DC (USA), 1983.

[125] K. Reichling, M. Raupach, J. Broomfield, J. Gulikers, V. L'Hostis, S. Kessler, K. Osterminski, I. Pepenar, U. Schneck, G. Sergi, *et al.*, "Full surface inspection methods regarding reinforcement corrosion of concrete structures," *Materials and Corrosion*, vol. 64, no. 2, pp. 116–127, 2013.

[126] A. Legat, "Monitoring of steel corrosion in concrete by electrode arrays and electrical resistance probes," *Electrochimica Acta*, vol. 52, no. 27, pp. 7590–7598, 2007.

[127] M. Fares, G. Villain, S. Bonnet, S. P. Lopes, B. Thauvin, and M. Thiery, "Determining chloride content profiles in concrete using an electrical resistivity tomography device," *Cement and concrete composites*, vol. 94, pp. 315–326, 2018.

[128] M. Fares, G. Villain, Y. Fargier, M. Thiery, X. Dérobert, and S. P. Lopes, "Estimation of water content gradient and concrete durability indicators using capacitive and electrical probes," in *International Symposium Non-Destructive Testing in Civil Engineering (NDT-CE)*, 2015.

[129] S. Kabir and A. Zaki, "Detection and quantification of corrosion damage using ground penetrating radar (gpr)," *PIERS Proceeding*, 2011.

[130] U. Halabe, "Condition assessment of reinforced concrete structures using electromagnetic waves [ph. d. thesis]," 1990.

[131] M. Soutsos, J. Bungey, S. Millard, M. Shaw, and A. Patterson, "Dielectric properties of concrete and their influence on radar testing," *NDT & e International*, vol. 34, no. 6, pp. 419–425, 2001.

[132] C. Maierhofer, "Nondestructive evaluation of concrete infrastructure with ground penetrating radar," *Journal of materials in civil engineering*, vol. 15, no. 3, pp. 287–297, 2003.

[133] Z. M. Sbartaï, S. Laurens, J.-P. Balayssac, G. Ballivy, and G. Arliguie, "Effect of concrete moisture on radar signal amplitude," *ACI materials journal*, vol. 103, no. 6, p. 419, 2006.

[134] G. Klysz, J.-P. Balayssac, and S. Laurens, "Spectral analysis of radar surface waves for non-destructive evaluation of cover concrete," *NDT & E International*, vol. 37, no. 3, pp. 221–227, 2004.

[135] Z. Sbartaï, S. Laurens, J.-P. Balayssac, G. Arliguie, and G. Ballivy, "Ability of the direct wave of radar ground-coupled antenna for ndt of concrete structures," *NDT & e International*, vol. 39, no. 5, pp. 400–407, 2006.

[136] C. L. Barnes, J.-F. Trottier, and D. Forgeron, "Improved concrete bridge deck evaluation using gpr by accounting for signal depth–amplitude effects," *NDT & E International*, vol. 41, no. 6, pp. 427–433, 2008.

[137] W. L. Lai, T. Kind, and H. Wiggenhauser, "Detection of accelerated reinforcement corrosion in concrete by ground penetrating radar," in *Proceedings of the XIII Internarional Conference on Ground Penetrating Radar*, pp. 1–5, IEEE, 2010.

[138] S.-X. Hong, W. L. Lai, and R. Helmerich, "Monitoring accelerated corrosion in chloride contaminated concrete with ground penetrating radar," in *2012 14th International Conference on Ground Penetrating Radar (GPR)*, pp. 561–566, IEEE, 2012.

[139] S. Hong, W.-L. Lai, and R. Helmerich, "Experimental monitoring of chloride-induced reinforcement corrosion and chloride contamination in concrete with ground-penetrating radar," *Structure and infrastructure engineering*, vol. 11, no. 1, pp. 15–26, 2015.

[140] Z. Wang, Y. Gu, and Y. Wang, "A review of three magnetic ndt technologies," *Journal of Magnetism and Magnetic Materials*, vol. 324, no. 4, pp. 382–388, 2012.

[141] M. Mosharafi, S. Mahbaz, M. Dusseault, and P. Vanheeghe, "Magnetic detection of corroded steel rebar: Reality and simulations," *NDT & E International*, vol. 110, p. 102225, 2020.

[142] R. M. Bozorth and H. J. Williams, "Effect of small stresses on magnetic properties," *Reviews of Modern Physics*, vol. 17, no. 1, p. 72, 1945.

[143] R. M. Bozorth, *Ferromagnetism*. 1993.

[144] G. Dobmann *et al.*, "Magnetic ndt technology for characterizing materials–a state of the art survey," in *Proc National Seminar on Non-Destructive Evaluation, Hyderabad, India*, pp. 7–9, Citeseer, 2006.

[145] A. Doubov, "A study of metal properties using the method of magnetic memory," *Metal Science and Heat Treatment*, vol. 39, no. 9/10, pp. 401–402, 1997.

[146] J.-W. Kim, S. Park, and D.-J. Moon, "Hidden damage detection for main cables of suspension bridges incorporating dc magnetization with a search coil-based bh loop measurement," in *EWSHM-7th European Workshop on Structural Health Monitoring*, 2014.

[147] S. Shams, A. Ghorbanpoor, S. Lin, and H. Azari, "Nondestructive testing of steel corrosion in prestressed concrete structures using the magnetic flux leakage system," *Transportation Research Record*, vol. 2672, no. 41, pp. 132–144, 2018.

[148] A. Ghorbanpoor, G. Steber, and T. Shew, "Evaluation of steel in concrete bridges: The magnetic field disturbance (mdf) system. final report," tech. rep., 1991.

[149] G. Dobmann, "Magnetic leakage flux techniques in ndt- a state-of-the-art survey of the capabilities for defect detection and sizing," *Electromagnetic methods of nondestructive testing(A 87-18976 06-38). New York, Gordon and Breach Science Publishers, 1985,*, pp. 71–95, 1985.

[150] S. Lukyanets, A. Snarskii, M. Shamonin, and V. Bakaev, "Calculation of magnetic leakage field from a surface defect in a linear ferromagnetic material: an analytical approach," *NDT & e International*, vol. 36, no. 1, pp. 51–55, 2003.

[151] J. W. Wilson, G. Y. Tian, and S. Barrans, "Residual magnetic field sensing for stress measurement," *Sensors and Actuators A: Physical*, vol. 135, no. 2, pp. 381–387, 2007.

[152] R. Langman and P. Mutton, "Estimation of residual stresses in railway wheels by means of stress-induced magnetic anisotropy," *NDT & E International*, vol. 26, no. 4, pp. 195–205, 1993.

[153] O. David-West, D. Amafabia, G. Haritos, and D. Montalvao, "A review of structural health monitoring techniques as applied to composite structures," *Structural Durability & Health Monitoring*, 2017.

[154] D. Cullar, D. Estrin, M. Strvastava, *et al.*, "Overview of sensor network," *Computer*, vol. 37, no. 8, pp. 41–49, 2004.

[155] H. Sohn, C. R. Farrar, F. M. Hemez, D. D. Shunk, D. W. Stinemates, B. R. Nadler, and J. J. Czarnecki, "A review of structural health monitoring literature: 1996–2001," *Los Alamos National Laboratory, USA*, vol. 1, 2003.

[156] J. Ou and H. Li, "Structural health monitoring in mainland china: review and future trends," *Structural health monitoring*, vol. 9, no. 3, pp. 219–231, 2010.

[157] W. Ostachowicz, R. Soman, and P. Malinowski, "Optimization of sensor placement for structural health monitoring: A review," *Structural Health Monitoring*, vol. 18, no. 3, pp. 963–988, 2019.

[158] S. Mustapha, Y. Lu, C.-T. Ng, and P. Malinowski, "Sensor networks for structures health monitoring: Placement, implementations, and challenges—a review," *Vibration*, vol. 4, no. 3, pp. 551–585, 2021.

[159] J. Meyer, R. Bischoff, G. Feltrin, and M. Motavalli, "Wireless sensor networks for long-term structural health monitoring," *Smart Structures and Systems*, vol. 6, no. 3, pp. 263–275, 2010.

[160] X. J. Gao, J. Zhang, Y. Z. Yang, and S. Lu, "Preparation of chloride ion selective electrode and its potential response to different chloride solutions representing concrete environments," in *Materials science forum*, vol. 675, pp. 537–540, Trans Tech Publ, 2011.

[161] M.-H. Yun, J.-W. Yeon, J. Hwang, C. S. Hong, and K. Song, "A calibration technique for an ag/agcl reference electrode utilizing the relationship between the electrical conductivity and the kcl concentration of the internal electrolyte," *Journal of applied electrochemistry*, vol. 39, no. 12, p. 2587, 2009.

[162] M. Jin, J. Xu, L. Jiang, G. Gao, H. Chu, C. Xiong, H. Gao, and P. Jiang, "Electrochemical characterization of a solid embeddable ag/agcl reference electrode for corrosion monitoring in reinforced concrete," *Electrochemistry*, vol. 82, no. 12, pp. 1040–1046, 2014.

[163] H. Suzuki, T. Hirakawa, S. Sasaki, and I. Karube, "An integrated three-electrode system with a micromachined liquid-junction ag/agcl reference electrode," *Analytica chimica acta*, vol. 387, no. 1, pp. 103–112, 1999.

[164] M. Jin, S. Gao, L. Jiang, Y. Jiang, D. Wu, R. Song, Y. Wu, and J. He, "Continuous monitoring of steel corrosion condition in concrete under drying/wetting exposure to chloride solution by embedded mno2 sensor," *Int. J. Electrochem. Sci*, vol. 13, pp. 719–738, 2018.

[165] F. Pargar, D. A. Koleva, and K. Van Breugel, "Determination of chloride content in cementitious materials: from fundamental aspects to application of ag/agcl chloride sensors," *Sensors*, vol. 17, no. 11, p. 2482, 2017.

[166] Y. S. Femenias, U. Angst, F. Caruso, and B. Elsener, "Ag/agcl ion-selective electrodes in neutral and alkaline environments containing interfering ions," *Materials and Structures*, vol. 49, no. 7, pp. 2637–2651, 2016.

[167] J. Rammal, F. Salameh, O. Tantot, N. Delhote, S. Verdeyme, S. Rioual, F. Gallée, and B. Lescop, "A microwave sensor for zinc corrosion detection," *Journal of Applied Physics*, vol. 122, no. 11, p. 114501, 2017.

[168] R. Jamal, D. Nicolas, T. Olivier, V. Serge, G. François, and R. Stéphane, "New passive ceramic sensor for corrosion detection," in *2014 44th European Microwave Conference*, pp. 167–170, IEEE, 2014.

[169] M. Raupach, J. Gulikers, and K. Reichling, "Condition survey with embedded sensors regarding reinforcement corrosion," *Materials and corrosion*, vol. 64, no. 2, pp. 141–146, 2013.

[170] R. Baessler, J. Mietz, M. Raupach, and O. Klinghoffer, "Corrosion monitoring sensors for durability assessment of concrete structures," in *Smart Structures and Materials 2000: Smart Systems for Bridges, Structures, and Highways*, vol. 3988, pp. 32–39, SPIE, 2000.

[171] T. RILEM, "154-emc (2000): Electrochemical techniques for measuring metallic corrosion recommendations. test methods for on site measurement of resistivity of concrete," *Materials and Structures*, vol. 33, pp. 603–611, 2000.

[172] R. Myrdal, *The electrochemistry and characteristics of embeddable reference electrodes for concrete*. Woodhead Publishing, 2014.

[173] J. E. Ramón, I. Martínez, J. M. Gandía-Romero, and J. Soto, "Improved tafel-based potentiostatic approach for corrosion rate monitoring of reinforcing steel," *Journal of Nondestructive Evaluation*, vol. 41, no. 4, p. 70, 2022.

[174] B.-Y. Chang and S.-M. Park, "Electrochemical impedance spectroscopy," *Annual Review of Analytical Chemistry*, vol. 3, pp. 207–229, 2010.

[175] R. Polder, C. Andrade, B. Elsener, Ø. Vennesland, J. Gulikers, R. Weidert, and M. Raupach, "Test methods for on site measurement of resistivity of concrete," *Materials and Structures*, vol. 33, no. 10, pp. 603–611, 2000.

[176] C. Andrade and C. Alonso, "Test methods for on-site corrosion rate measurement of steel reinforcement in concrete by means of the polarization resistance method," *Materials and Structures*, vol. 37, no. 9, pp. 623–643, 2004.

[177] V. Dertimanis and E. Chatzi, "Sensor networks in structural health monitoring: From theory to practice," 2020.

[178] S. Banerji, A. Bagchi, and S. Khazaeli, "Str-991: Energy harvesting methods for structural health monitoring using wireless sensors: A review," 2016.

[179] H. Singh and K. Sharma, "Survey on impedance measurement technique based structural health monitoring," 2016.

[180] B. M. Phares, *Health monitoring of bridge structures and components using smart structure technology*, vol. 2. Wisconsin Highway Research Program, 2005.

[181] X. Yuan, X. Zhang, Y. Huang, J. Jie, Q. Wei, M. Tan, and Y. Yu, "Development of an electrochemical sensor for chloride ion detection using ion-sensitive field-effect transistor array," *Int. J. Electrochem. Sci*, vol. 16, p. 150911, 2021.

[182] M. Song, *Wireless Corrosion Monitoring for Reinforced Concrete Structures and Concrete Repair*. PhD thesis, Columbia University, 2012.

[183] B. A. Sundaram, K. Ravisankar, R. Senthil, and S. Parivallal, "Wireless sensors for structural health monitoring and damage detection techniques," *Current Science*, pp. 1496–1505, 2013.

[184] J. I. Aguirre, *EPCglobal: a universal standard*. PhD thesis, Massachusetts Institute of Technology, 2007.

[185] T. J. Lesthaeghe, S. Frishman, S. D. Holland, and T. J. Wipf, "Rfid tags for detecting concrete degradation in bridge decks," 2013.

[186] S. Tedjini, N. Karmakar, E. Perret, A. Vena, R. Koswatta, E. Rubayet, *et al.*, "Hold the chips: Chipless technology, an alternative technique for rfid," *IEEE Microwave Magazine*, vol. 14, no. 5, pp. 56–65, 2013.

[187] D. K. Cheng *et al.*, "Fundamentals of engineering electromagnetics," 1993.

[188] N. Wahlström, "Target tracking using maxwell's equations," 2010.

[189] J. D. Jackson, "Electrodynamics," *The Optics Encyclopedia*, 1975.

[190] J. Hey, "On the biot–savart law of electromagnetism applied to the atomic circulation current," *Journal of Physics A: Mathematical and Theoretical*, vol. 54, no. 16, p. 165302, 2021.

[191] C. Hughes, J. Isaacson, A. Perry, R. F. Sun, and J. Turner, "Creating superposition: Stern–gerlach," in *Quantum Computing for the Quantum Curious*, pp. 29–40, Springer, 2021.

[192] E. M. Purcell and D. J. Morin, *Electricity and magnetism*. Cambridge University Press, 2013.

[193] J. Crangle and G. Goodman, "The magnetization of pure iron and nickel," *Proceedings of the Royal Society of London. A. Mathematical and Physical Sciences*, vol. 321, no. 1547, pp. 477–491, 1971.

[194] T. Oguchi, K. Terakura, and N. Hamada, "Magnetism of iron above the curie temperature," *Journal of Physics F: Metal Physics*, vol. 13, no. 1, p. 145, 1983.

[195] J. D. Jackson, "Classical electrodynamics," 1999.

[196] H. González, S. Juárez, P. Kielanowski, and M. Loewe, "Multipole expansion in magnetostatics," *American Journal of Physics*, vol. 66, no. 3, pp. 228–231, 1998.

[197] A. Hubert and R. Schäfer, *Magnetic domains: the analysis of magnetic microstructures*. Springer Science & Business Media, 2008.

[198] D. C. Jiles and D. L. Atherton, "Theory of ferromagnetic hysteresis," *Journal of applied physics*, vol. 55, no. 6, pp. 2115–2120, 1984.

[199] C. Richter and B. A. van der Pluijm, "Separation of paramagnetic and ferrimagnetic susceptibilities using low temperature magnetic susceptibilities and comparison with high field methods," *Physics of the Earth and Planetary Interiors*, vol. 82, no. 2, pp. 113–123, 1994.

[200] N. A. Spaldin, *Magnetic materials: fundamentals and applications*. Cambridge university press, 2010.

[201] G. Bertotti, *Hysteresis in magnetism: for physicists, materials scientists, and engineers*. Gulf Professional Publishing, 1998.

[202] V. Neu, U. Hannemann, S. Fähler, B. Holzapfel, and L. Schultz, "Effect of rare earth content on microstructure and magnetic properties of smco and ndfeb thin films," *Journal of applied physics*, vol. 91, no. 10, pp. 8180–8182, 2002.

[203] Z. W. Liu, "New developments in ndfeb-based permanent magnets," in *Key Engineering Materials*, vol. 510, pp. 1–8, Trans Tech Publ, 2012.

[204] S. Ruoho, M. Haavisto, E. Takala, T. Santa-Nokki, and M. Paju, "Temperature dependence of resistivity of sintered rare-earth permanent-magnet materials," *IEEE Transactions on Magnetics*, vol. 46, no. 1, pp. 15–20, 2009.

[205] S. Nordebo and A. Gustafsson, "A quasi-static electromagnetic analysis for experiments with strong permanent magnets," *arXiv preprint arXiv:1407.0875*, 2014.

[206] H. Rahimi, A. Ghasemi, R. Mozaffarinia, and M. Tavoosi, "On the magnetic and structural properties of neodymium iron boron nanoparticles," *Journal of Superconductivity and Novel Magnetism*, vol. 29, no. 8, pp. 2041–2051, 2016.

[207] S. Celozzi, R. Araneo, and G. Lovat, *Electromagnetic shielding*, vol. 192. John Wiley & Sons, 2008.

[208] T. Sumner, J. Pendlebury, and K. Smith, "Convectional magnetic shielding," *Journal of Physics D: Applied Physics*, vol. 20, no. 9, p. 1095, 1987.

[209] C. R. Paul, R. C. Scully, and M. A. Steffka, *Introduction to electromagnetic compatibility*. John Wiley & Sons, 2022.

[210] O. Loukil, *Etude expérimentale et numérique de la dégradation d'éléments structurels en béton armé par corrosion sous courant imposé*. PhD thesis, Université Paris-Est, 2017.

[211] R. Vera, M. Villarroel, A. Carvajal, E. Vera, and C. Ortiz, "Corrosion products of reinforcement in concrete in marine and industrial environments," *Materials Chemistry and Physics*, vol. 114, no. 1, pp. 467–474, 2009.

[212] S. J. Oh, D. Cook, and H. Townsend, "Characterization of iron oxides commonly formed as corrosion products on steel," *Hyperfine interactions*, vol. 112, no. 1, pp. 59–66, 1998.

[213] M. S. Zhdanov, *Foundations of geophysical electromagnetic theory and methods*. Elsevier, 2017.

[214] W. B. Weir, "Automatic measurement of complex dielectric constant and permeability at microwave frequencies," *Proceedings of the IEEE*, vol. 62, no. 1, pp. 33–36, 1974.

[215] A. Nicolson and G. Ross, "Measurement of the intrinsic properties of materials by time-domain techniques," *IEEE Transactions on instrumentation and measurement*, vol. 19, no. 4, pp. 377–382, 1970.

[216] A. Chevalier, J.-L. Mattei, and M. Le Floc'H, "Propriétés hyperfréquences de matériaux composites à base de poudres de ferrites doux," in *JCMM 1998: 5èmes Journées de Caractérisation Microonde et Matériaux*, 1998.

[217] D. Souriou, S. Kadkhodazadeh, X. Dérobert, D. Guilbert, and A. Ihamouten, "Experimental parametric study of a functional-magnetic material designed for the monitoring of corrosion in reinforced concrete structures," *Remote Sensing*, vol. 14, no. 15, p. 3623, 2022.

[218] K. Bhargava, A. Ghosh, Y. Mori, and S. Ramanujam, "Analytical model for time to cover cracking in rc structures due to rebar corrosion," *Nuclear engineering and Design*, vol. 236, no. 11, pp. 1123–1139, 2006.

[219] K. Tuutti, *Corrosion of steel in concrete*. PhD thesis, Lund University, 1982.

[220] Y. Shiroyanagi, E. Anliker, Q. Hasse, H. Hu, M. Kasa, I. Kesgin, and Y. Ivanyushenkov, "Magnetic field calculation of planar scus using ansys maxwell," 2021.

[221] T. Waghmare, P. Choube, A. Dakre, A. Suryawanshi, and P. Holambe, "Design of internal permanent magnet brushless dc motor using ansys," *JournalNX*, vol. 2, no. 4, pp. 1–7, 2016.

[222] ANSYS, "Ansys maxwell documentation." `https://www.ansys.com/products/electronics/ansys-maxwell/documentation`, 2023. Accessed April 27, 2023.

[223] J. M. Camacho and V. Sosa, "Alternative method to calculate the magnetic field of permanent magnets with azimuthal symmetry," *Revista mexicana de física E*, vol. 59, no. 1, pp. 8–17, 2013.

[224] D. C. S. Baird, *Solution of electrodynamics Jackson, third edition*. West Texas A and M University, 2008.

[225] S. M. Kay, *Fundamentals of statistical signal processing: estimation theory*. Prentice-Hall, Inc., 1993.

[226] M. Bezerra, W. Kort-Kamp, M. Cougo-Pinto, and C. Farina, "How to introduce the magnetic dipole moment," *European journal of physics*, vol. 33, no. 5, p. 1313, 2012.

[227] L. Maciel, F. Gomide, and R. Ballini, "A differential evolution algorithm for yield curve estimation," *Mathematics and Computers in Simulation*, vol. 129, pp. 10–30, 2016.

[228] S. Ruder, "An overview of gradient descent optimization algorithms," *arXiv preprint arXiv:1609.04747*, 2016.

[229] J. C. Meza, "Steepest descent," *Wiley Interdisciplinary Reviews: Computational Statistics*, vol. 2, no. 6, pp. 719–722, 2010.

[230] N. I. Gould and S. Leyffer, "An introduction to algorithms for nonlinear optimization," in *Frontiers in numerical analysis*, pp. 109–197, Springer, 2003.

[231] J. V. Burke and M. C. Ferris, "A gauss—newton method for convex composite optimization," *Mathematical Programming*, vol. 71, no. 2, pp. 179–194, 1995.

[232] J. J. Moré, "The levenberg-marquardt algorithm: implementation and theory," in *Numerical analysis*, pp. 105–116, Springer, 1978.

[233] S. Roweis, "Levenberg-marquardt optimization," *Notes, University Of Toronto*, vol. 52, 1996.

[234] J. C. Lagarias, J. A. Reeds, M. H. Wright, and P. E. Wright, "Convergence properties of the nelder–mead simplex method in low dimensions," *SIAM Journal on optimization*, vol. 9, no. 1, pp. 112–147, 1998.

[235] T. Richard, *Capteur sans électronique pour la surveillance sans fil de la santé des infrastructures maritimes*. PhD thesis, Nantes, 2020.

[236] E. D. Ningsih, H. Rifai, and L. Dwiridal, "Magnetic susceptibility properties of portland cement," in *Journal of Physics: Conference Series*, vol. 2309, p. 012015, IOP Publishing, 2022.

COLLEGE ED MATHEMATIQUES
DOCTORAL STIC
PAYS DE LA LOIRE

Nantes Université

Titre : Contrôle de santé des structures en béton armé à partir des équations de Maxwell : inversion et traitement des signaux magnétiques

Mot clés : Contrôle Non Destructif (CND), Matériau Magnétique Fonctionnel (FMM), Corrosion

Résumé : Dans les environnements marins, la durabilité des structures en béton armé est généralement dégradée par la corrosion due à la pénétration d'agents agressifs. Cette thèse vise à proposer une nouvelle méthode de SHM magnétique, utilisant un dispositif intégré dans le béton de couverture, comme solution technologique pour surveiller la pénétration des agents agressifs. Ce nouveau dispositif est appelé Functional Magnetic Materials (FMM) car il est composé de matériaux magnétiques et ferromagnétiques. Il propose un dispositif autonome et peu coûteux qui génère des observables magnétiques (OM) passives mesurables à distance avec des interrogateurs externes. En raison de l'évolution de la corrosion de la partie réactive du FMM par le front d'ions chlorure, l'OM générée est modifiée en conséquence. Ceci permet de corréler l'état de corrosion du FMM en fonction des variations de l'OM et d'estimer également la probabilité de contamination du béton. L'objectif principal de cette thèse est de développer une méthode de traitement du signal, basée sur l'estimation de la variation du moment dipolaire magnétique en fonction de la variation de l'OM, à travers un modèle analytique de Biot Savart et avec une méthode d'inversion. Pour atteindre cet objectif, par modélisation numérique du FMM, la plage de variation de l'OM et la tendance ont été évaluées comme modèle de référence. Ensuite, via la solution analytique, la quantité de moments dipolaires magnétiques a été estimée en fonction des variations de l'OM. Enfin, la méthode proposée a été étudiée expérimentalement, en utilisant une variété de dalles en béton et différents états de corrosion pour la partie réactive. Les résultats obtenus montrent que la méthode proposée apparait comme une nouvelle solution de pronostic ND appliquée à la corrosion.

Title: Check the health statement of reinforced concrete structures, using Maxwell's equations,inversion and magnetic signal processing

Keywords: Non Destructive testing (NDT), Functional Magnetic Materials (FMM), Corrosion

Abstract: In marine environments, the reinforced concrete structures' durability is typically degraded by corrosion due to aggressive agent ingress. This thesis aims to propose a novel magnetic SHM method, using an embedded device in the cover concrete, as a technological solution for monitoring the ingress of aggressive agents. This novel device is referred as Functional Magnetic Materials (FMM) since it is made of magnetic and ferromagnetic materials. It suggests an autonomous and low-cost device that generates passive Magnetic Observable (MO) remotely measurable with external interrogators. Due to the corrosion evolution of the FMM reactive part by chloride ion front, the generated MO is changed consequently. This makes it possible to correlate the corrosion state of FMM as a function of MO variations and to estimate the probability of concrete contamination, as well. The main objective of this thesis is to develop a forward method, based on estimated magnetic dipolar moment variation as a function FMM corrosion, through an analytical model of Biot Savart and with optimization and inversion method. To reach this objective, by numerical modeling of FMM, the MO variation range and the tendency were evaluated as a reference model. Next, through the analytical solution, the amount of magnetic dipolar moments was estimated as a function of MO variations. Then, the proposed method was investigated experimentally, using a variety of concrete slabs and different corrosion states for the reactive part. The obtained results show that the proposed method appears as a new preventive ND method for the rebar corrosion application.